Piezoelectrically actuated bistable composite laminates for structural morphing

Giddings, Pete

Award date:
2010

Awarding institution:
University of Bath

Piezoelectrically actuated bistable composite laminates for structural morphing

Peter Francis Giddings

Doctor of Philosophy

University of Bath

Department of Mechanical Engineering

August 2010

Abstract

This thesis describes the experimental and finite element studies undertaken to develop a piezoelectrically actuated morphing structure based on bistable composite laminates. An adaptive bump mechanism is proposed as a demonstrator and the need for robust finite element models of bistable composites, Macro Fibre Composite (MFC) actuators and morphing structures combining these two technologies are identified as key research objectives. The developed models will be used to predict laminate deformation and actuation behaviour.

Laminate deformation and shape for both deformation states of bistable laminates is accurately predicted to within 12.5% by a finite element model including measured ply thickness data. The observed deformation states exhibit approximately opposing cylindrical curvatures about different axes of curvature. Regions of localised curvature reversal within bistable composite structures are also predicted by the model and these effects are correlated with variations in the through thickness stress components.

The actuation capability of a piezoelectric MFC actuator is predicted by finite element analysis, creating a homogenised solid model that includes three-dimensional compliance, dielectric and piezoelectric matrices. Prediction of actuation capability and changes in actuator compliance caused by changing electrical boundary conditions are in excellent agreement with experimental measurement.

The developed finite element models for bistable laminates and MFC actuators are combined to predict the cured shape and snap-through voltage of two MFC actuated cross-ply bistable laminates. Predicted snap-through voltage agrees with experimental measurements to within 5%.

Laminate deflection induced by changes in ambient temperature is measured to examine the influence of temperature dependent elastic constants and coefficient of thermal expansion of epoxy resin on laminate deflection. Additionally, the blocking force, free-deflection and deflection creep-rate for an MFC-actuated bistable laminate are experimentally characterised to determine operational actuation capabilities.

Finally, a finite element model based on insights gained in the preceding work is used to design an adaptive bump. Qualitative prediction of device behaviour and prediction of cured shape for the resulting prototype design are both excellent; however snap-through voltage is less well modelled by the presented work.

Acknowledgements

I would like to thank Alicia Kim, Paul Weaver and Martyn Cantrell for their academic supervision and guidance to ensure successful completion of the project. My thanks go to David Billington and Paul Hudson at Great Western Research and Airbus UK for their roles in providing the funding underpinning this studentship. I am also indebted to Chris Arnold and Dr Aki Salo for their help with manufacture of experimental rigs and undertaking motion capture measurements.

My academic supervisor Dr Chris Bowen has been a collaborative, knowledgeable and supportive mentor and allowed me the freedom to explore my own ideas throughout this project, thanks Boss.

I would particularly like to thank all of my friends and of course my Mum, Dad and sisters who have provided support, tolerance and distraction as the need arose throughout my research. It is difficult to express how much I appreciate all the nursing that was provided to help me become a doctor.

Most especially I'd like to thank Geraldine, travel companion and closest confidante throughout the last two years of my work.

Thesis structure

This section summarises the technical content of each chapter and describes the structure of this work to aid clarity and assist the reader in finding information of specific interest.

Chapter 1 gives motivation for the work and selection of novel and advantageous research objectives based on a literature survey of structural morphing. A survey of potential enabling technologies is presented and a physical description of the fundamental physics of bistable composite laminates and piezoelectric ceramic actuators is presented. This fundamental information is presented to allow more specific discussion of the particular areas discussed in each subsequent chapter.

The research work presented in Chapters 2-6 forms part of a research effort aimed at developing a design tool for piezoelectrically actuated morphing structures. Each Chapter assesses the relevant published literature identifying key areas of uncertainty in current understanding before presenting the work undertaken to gain insight into these areas. Finally in Chapter 7 the knowledge acquired during this incremental development is implemented in the prototype-design of a lab-scale demonstrator of an adaptive bump. The specifics of each chapter are now described.

Chapter 2 develops a finite element model of bistable composite laminates using experimentally determined ply-thicknesses to accurately predict cured shape in each of the stable deformation states. These predictions are validated against full-field surface profile measurements with excellent agreement between experimental measurements and predicted laminate deflection.

Chapter 3 describes a homogenised solid model of a commercially available macrofibre composite (MFC) actuator, including three dimensional matrices describing the stiffness, piezoelectric constants and relative permittivity of the actuator. Comparison with experimental validation shows that this model accurately predicts actuation properties of driven actuators and the changes in effective stiffness of passive actuators under varying electrical boundary conditions.

Chapter 4 addresses the issue of modelling the integration of MFC actuators within bistable composite laminates. The finite element models presented in Chapters 2 and 3 are integrated and extended to predict both the MFC drive-voltage required to induce snap-through and the cured shape of two piezoelectrically actuated bistable laminates. These

predictions are validated against measurements of snap-through voltage and surface profile of the modelled laminates.

Chapter 5 measures the response of a bistable laminate to changes in ambient temperature in order to assess validity of linear material models for prediction of composite laminates response to an imposed thermal load. The finite element model presented in Chapter 2 is extended to include gravitational loading and predictions of laminate profile at a range of ambient temperatures compared to the experimental values.

Chapter 6 describes experimental characterisation of the blocking force and free deflection of a piezoelectrically actuated bistable composite laminate. Analytical equations based on engineers beam theory are presented to describe the observed linear voltage-force characteristic. Piezoelectric deflection creep of the laminate is measured and compared with analytical predictions to determine the creep time constant of the system.

Finally, Chapter 7 extends the finite element model presented in Chapter 4 to design an adaptive bump mechanism based on a bistable laminate embedded within a rigid host structure. A suitably sized composite component is designed around a commercially available MFC actuator and predictions of cured shape and snap-through voltage for the resulting structure are compared with experimental measurements.

Chapter 8 summarises key findings and conclusions of this thesis and identifies areas of interest for future work.

Contents

Table of Figures

Chapter 1 - Introduction

This Chapter sets out the motivation for investigating structural morphing within the civil aviation industry and defines a 'morphing structure' and what it intends to achieve in section 1.1.

Section 1.2 presents a literature review on morphing aerodynamic surfaces, beginning with large scale morphing schemes followed by work relating to medium and small scale structures. It is concluded that a small scale morphing scheme, specifically an adaptive bump for aerodynamic drag reduction is an interesting and novel area of study.

Section 1.3 highlights the potential applications for multistable structures to reduce actuation requirements for adaptive structures and surveys the literature relating to morphing applications for two multistable technologies. Section 1.3.1 and 1.3.2 describe multistable copper beryllium sheets and bistable composite laminates respectively and assesses the literature relating to their application in morphing structures. It is concluded that bistable composite laminates represent the most promising multistable skin material for the manufacture of an adaptive bump. In section 1.3.3 the physical processes which cause the formation of a bistable composite laminate during manufacture are explained in preparation for more specific discussions relating to the work carried out in Chapters 2, 4 and 5.

As discussed in section 1.2 the application of smart technology within morphing structures is vital in realising the full potential of morphing structures to reduce system complexity and aircraft weight. Section 1.4 therefore compares the typical operational capabilities of commercially available smart material actuators in terms of their achievable strain and stress, Young's modulus, maximum operational frequency and density. It is concluded that piezoelectric macro-fibre composite (MFC) actuators are the most suitable smart actuation technology for use within an adaptive bump for aerodynamic flow control.

The atomic origins of the piezoelectric effect and a discussion of the structure and behaviour of poled ferroelectric ceramic materials are presented in section 1.5. This discussion of basic physical principles presents the necessary information to begin the more detailed discussion of MFC structure and modelling found in Chapter 3 and piezoelectric creep that follow in Chapters 6.

Section 1.6 presents a summary of the identified gaps in the literature and the chosen research aim of developing experimentally validated modelling techniques for use as a design tool. This design tool is then used to develop an adaptive bump based on a piezoelectrically actuated bistable composite laminate.

1.1 Aims of Research

The key research aims of this thesis are set out below to aid the reader in understanding:

- Design and prototype a small-scale morphing structure capable of reducing fuel consumption for civilian aircraft.
- Develop a design tool for piezoelectrically actuated morphing structures.
- Develop modelling techniques or procedures to accurately predict the cured shape of bistable composite laminates.
- Gain insight and understanding of modelling techniques appropriate for prediction of actuation capabilities for piezoelectric macro-fibre composite actuators.
- Determine and implement appropriate modelling techniques to predict cured shape and snap-through voltage of piezoelectrically actuated bistable composite laminates.

1.2 Aerospace morphing and motivation

A morphing structure is one that is capable of radical and unconventional shape change. Within aerospace applications, morphing structures have been proposed as a method of improving particular aerodynamic performance and introducing new control functionality. This work focuses on the use of morphing structures within civil aviation applications where the development of continuous aerodynamic surfaces capable of altering shape, either in the plan-form or thickness profile are of particular interest [1] to achieve one or more of the following design objectives [2]:

(i) Improve aircraft performance to expand its flight envelope;

(ii) Replace conventional control surfaces for flight control to improve performance and stealth;

(iii) Reduce drag to improve range and minimise costs;

(iv) Reduce vibration or control flutter.

In contrast to morphing structures, modern aerodynamic surfaces are rigid structures with discrete sections which move relative to one another in order to alter the aerodynamic properties of the whole surface. An example of this type of surface would be the trailing edge of a commercial airliner where flaps move relative to the main wing to alter wing camber.

These fixed surfaces operate efficiently at or near design conditions but performance degrades rapidly when conditions vary from the narrow range of cruise conditions in civil aviation, increasing fuel consumption and limiting flight speed [3, 4]. This sensitivity to operating conditions decreases mission capability in military applications where operating conditions vary widely compared to civil applications and the consequences of reduced capability are more severe [5].

In order to expand the range of operational conditions in which aerodynamic control surfaces achieve performance goals they must be able to adapt their shape to best suit current conditions [1], hence the interest in ‘morphing’. The envisaged benefits of morphing technology are as old as flight itself, with the Wright brothers choosing to control the Wright Flyer through wing warping [6]. This iconic aircraft used manually applied

mechanical load to deform a semi-rigid wing to provide roll and yaw control during the first powered flights.

More recent military aviation projects have emphasised the use of smart materials such as shape memory alloys (SMA) and piezoelectric actuators to effect shape change of aerodynamic surfaces to further improve aircraft performance and operational envelope [7]. These performance oriented projects seek to expand aircraft operational capabilities through radical alteration of wing plan form and large scale morphing of the airframe itself. An example of plan form morphing is the variable sweep wings of the F-111A fighter jet [5].

Further efforts have been made to control the profile of aerodynamic surfaces, as part of the Mission Adaptive Wing program run by the American Air Force Research Laboratory [2, 5, and 7] as well as active control of morphing missile-control fins [8]. Unfortunately the advances made in these projects are offset by significant increases in mechanical complexity and weight.

The operational requirements within the civil aviation sector differ from those within military projects. Flight missions are much more tightly defined and operating conditions are more tightly bounded, hence dramatic changes in aircraft configuration are not required [4].

Reduced environmental impact and cost reduction are important design outcomes due to mounting pressure on airlines and the aviation industry as a whole to reduce its environmental impact, and more specifically, its use of fossil fuels [3, 9]. With alternative fuel technologies not ready for full-scale implementation [10, 11] the short and medium term response to these challenges must come from increasingly efficient use of current fuel sources. As noted by Green [4], the areas most likely to produce greatest gains in efficiency are reduction of aerodynamic drag and structural weight. Preliminary investigations into including regions of variable profile within otherwise rigid host structures for control surfaces [12] and drag reduction [13] have demonstrated that morphing technology could play an important role in achieving these design goals.

In the following section published work investigating the use of morphing structures as aerodynamic flow control devices will be presented.

1.3 Aerospace morphing – Literature survey

The following section presents a summary of the published work relating to prototype testing of morphing structures within fixed wing aerospace applications. Many research institutes and universities have undertaken studies to assess the potential of a wide range of morphing structures as aerodynamic flow control devices. In sections 1.2.1-1.2.3 the published work has been subdivided as suggested by Ramarakhyani [14] according to the scale of the proposed morphing structure.

Large scale morphing structures designed to radically alter the shape or profile of the entire surface are presented in section 1.3.1. Medium and small morphing scale schemes which aim to alter the profile of a region or a local area of a surface are then discussed in sections 1.3.2 and 1.3.3 respectively.

1.3.1 Large scale morphing

Large scale morphing schemes encompass changes to the geometry of entire flight surfaces caused by alterations in wing plan-form and sweep angle. Fuselage shape change could also be included within morphing concepts though to date no published work has addressed this area. Fig. 1.1*a* shows the NextGen corporation folding wing concept as an example of plan-form morphing [15], with the variable wing sweep of the F-111 fighter jet seen in Fig.1.1*b* and 1.1*c*.

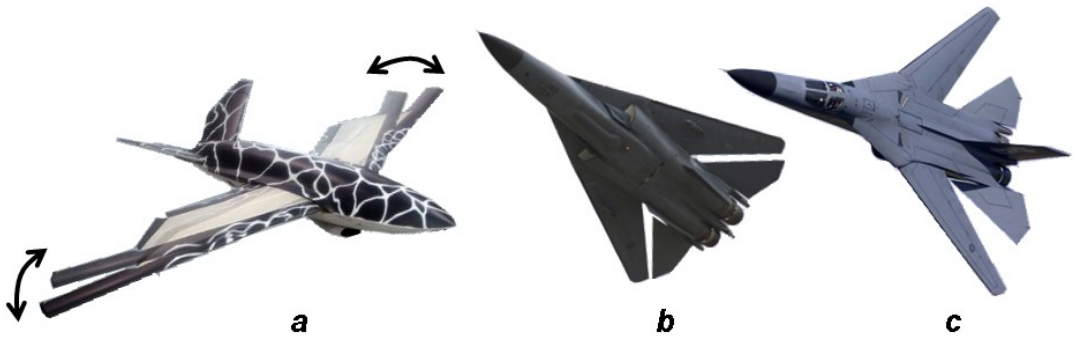

Fig.1.1: Next Gen folding wing concept for plan-form morphing (a) and variable sweep wings of the General Dynamics F111-A in swept (b) and extended (c) configuration. ***(****figure adapted from [15]****)***

These large-scale projects aim to increase the operational envelope of a single aircraft for widely varying flight cycles or multiple mission types [5, 15]. Although increases in mechanical complexity, cost and system weight have yet to be mitigated, large scale morphing structures have been flown in military aircraft such as the F111-A for many years [2, 5, 7]. Due to the operational and fuelling costs of increased weight and complexity large scale morphing structures are currently unlikely to be adopted by the civil aviation industry.

1.3.2 Medium scale morphing

A medium-scale morphing structure creates geometric change within one region of an aerodynamic surface in order to control the air flow behaviour over the surface. Examples of medium scale morphing structures include a morphing trailing edge (as in Fig. 1.2) used to increase wing camber [2, 16, 17], other flow-control devices such as leading edge devices [18], spoilers [13] or winglets [19].

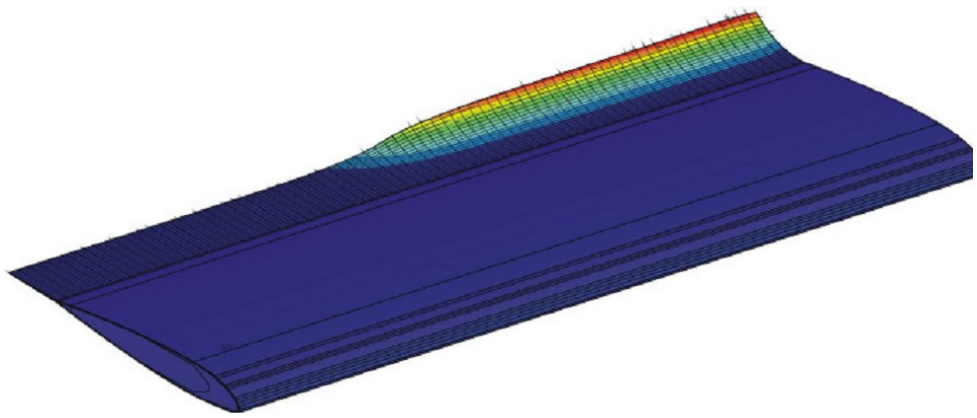

Fig.1.2: Piezoelectrically actuated trailing edge showing transition region between active and passive structures (*figure adapted from [20]***).**

Morphing flow-control devices such as leading or trailing-edges are proposed as replacements for discrete control components in order to enhance control when compared to traditional hinged designs. As observed by Kudva in his 2004 review of the DARPA Smart Wing project [7], wind tunnel testing of a morphing trailing-edge increased roll moment by approximately 17% in comparison to a traditional design using discrete hinged sections over a 15˚ range of flap deflection. This prototype model was actuated by piezoelectric rotary motors attached to curved beams which deflected the flexible skinned trailing edge structure; as noted by the investigators [20] the rotary motor and gearbox used significantly increased total system weight. This potential improvement of control authority

makes the development of medium-scale morphing projects very attractive to both academic researchers and industry.

It is important to note that these potential advantages are accompanied by increased technical challenges, such as actuation force requirements as well as risks to reliability and durability of safety critical structures [21]. As has been seen in the development of large scale morphing structures [5], the use of mechanical actuation systems to create morphing structures increases weight significantly compared to traditional fixed designs. Hence research into smart-materials and actuation is vital to meet the challenges associated with medium scale morphing projects.

Work presented by Daynes [22] has shown a morphing trailing edge flap based on pre-stressed bistable laminates. Symmetric or unsymmetric cross-ply laminates exhibit multiple cylindrical deformation states after manufacture when fibres are pre-stressed before the curing process begins [23]. When this pre-stress is released after the laminate is fully cured, a residual stress field remains which causes out of plane deformation in the laminates.

Aeroelastic calculations of structural deformation of a bistable trailing edge flap were presented [24] and extended with the inclusion of mechanical actuation of the flap to achieve 10˚ flap deflection [22]. Wind tunnel testing showed that morphing was achieved under aerodynamic loads; however no data was presented to suggest that the proposed scheme improved aerodynamic performance of the aerofoil.

While traditional actuation methods were employed in the wind tunnel testing, the novel application of bistable composites to reduce required actuation load shows the potential of multistable structures in morphing applications.

Smart actuation technologies such as shape memory alloy and piezoelectric actuators can provide compact mechanical actuation or combine structural and actuation capabilities to help reduce weight and complexity of morphing designs.

Shape memory alloy (SMA) technology has received attention as an active skin for aerodynamic control surfaces [25, 26], but the delay in structural response caused by heat conduction within the SMA metal was found to prevent SMA technology providing a viable operational solution. Boeing have filed patents relating to SMA actuated winglets which change configuration to reduce drag during different phases of the flight cycle and so structural response time is not a limiting factor [27, 28]. By using bending plates and torque

tubes to effect both span-wise and stream-wise bending of the structure [27] the proposed scheme has been shown effective during both validation and flight testing.

SMA wires embedded directly into composite laminates or other host structures have been suggested as actuators for morphing structures [29, 30] but to date the manufacture of these material systems remain problematic [31-33]. Implementation of embedded SMA wires within composite structures is not currently a feasible actuation technology although published results warrant further research [32, 34, 35].

Some studies have already implemented and tested prototypes using piezoelectric actuators [7, 20, 36], however the piezoelectric devices are used as conventional mechanical actuators, and hence do not take full advantage of the weight and complexity reduction that smart actuation may offer. In the short term this incremental approach to the use of novel actuation technologies may provide small improvements in performance but the additional mass and complexity remain serious disadvantages.

More recent work from Vos [12, 37] has designed, built and flown a sub-scale unmanned air-vehicle (UAV) with morphing trailing edge flaps using pre-compressed piezoelectric beams as actuators (as in Fig. 1.3). This work included a two dimensional semi-analytical model that produced excellent agreement with the observed flap deflections under test conditions. Wind tunnel testing and flight testing were both performed with increased roll control authority and a 3.5% weight saving demonstrated as compared to a hinged flap design actuated by an electromechanical servo actuator.

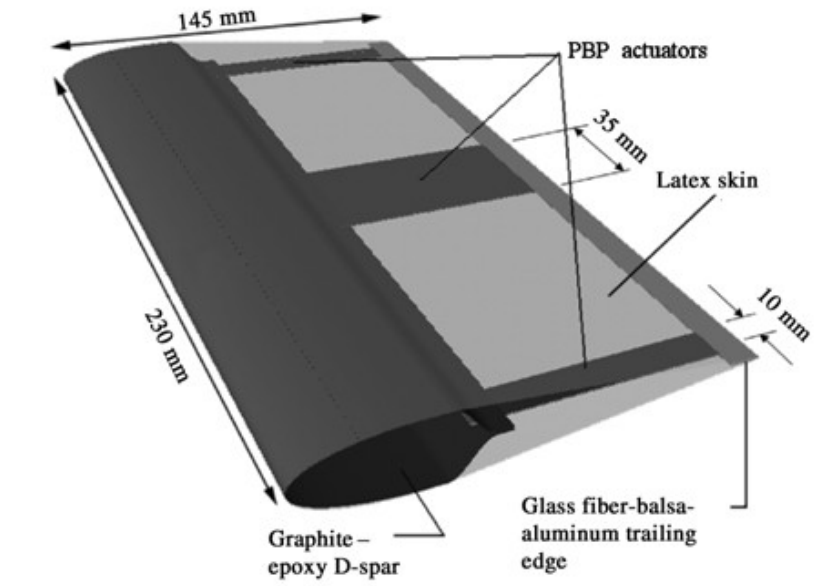

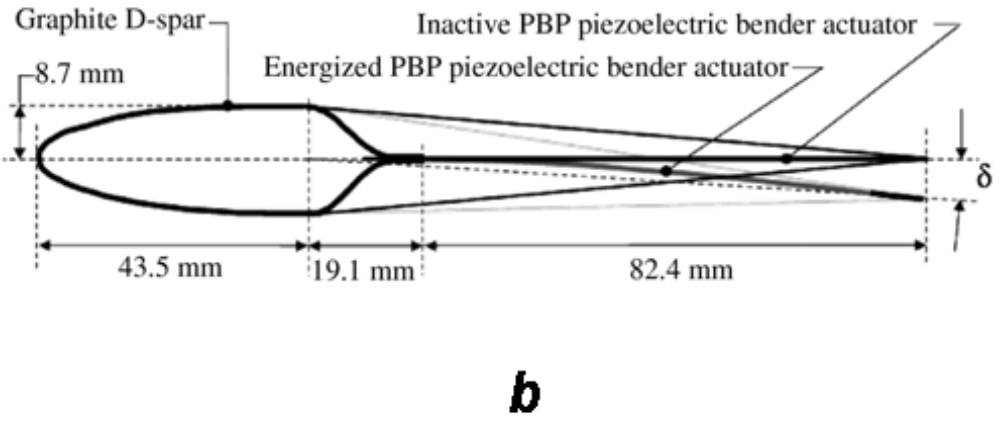

Fig.1. 3: Piezoelectrically actuated trailing edge concept for an unmanned aerial vehicle (UAV) as proposed by Vos et al. [12] showing dimensions and mechanism detail of morphing section. ***(****figure adapted from [12]****).***

As represented in the literature, schemes involving SMA actuation have been shown feasible and advantageous for morphing structures which do not require rapid structural response. Preliminary studies into the use of piezoelectric smart actuators have shown weight reductions and increased control authority compared to traditional mechanically actuated devices in sub-scale prototypes. To date no full scale testing has been undertaken of piezoelectrically actuated medium scale morphing devices and it is unclear if these

emergent technologies will prove capable of generating the required displacements, actuation forces and reliability required for applications within civil aircraft.

1.3.3 Small scale morphing

Small scale morphing applications, such as active gap-optimisation or localised skin profiling [38], aim to influence the aerodynamic conditions in the immediate vicinity of the morphing structure via alterations to surface geometry.

Several investigators have published work detailing the aerodynamic advantages of small scale flow-control devices within aviation structures. Natarajan [38] showed a theoretical investigation of leading edge bumps as a replacement for a vertical drag-rudder. This preliminary study showed that bumps of between 0.3% and 0.4% of chord length were effective in generating sufficient yaw moment with minimal loss of lift. Yaw is defined as the rotation of the aircraft about the vertical axis. Chord length is the length of the straight line (the chord) which runs from the tip of the trailing edge, passes through the centre of curvature of the leading edge and ends when it intersects the leading edge surface, as indicated in Fig. 1.4.

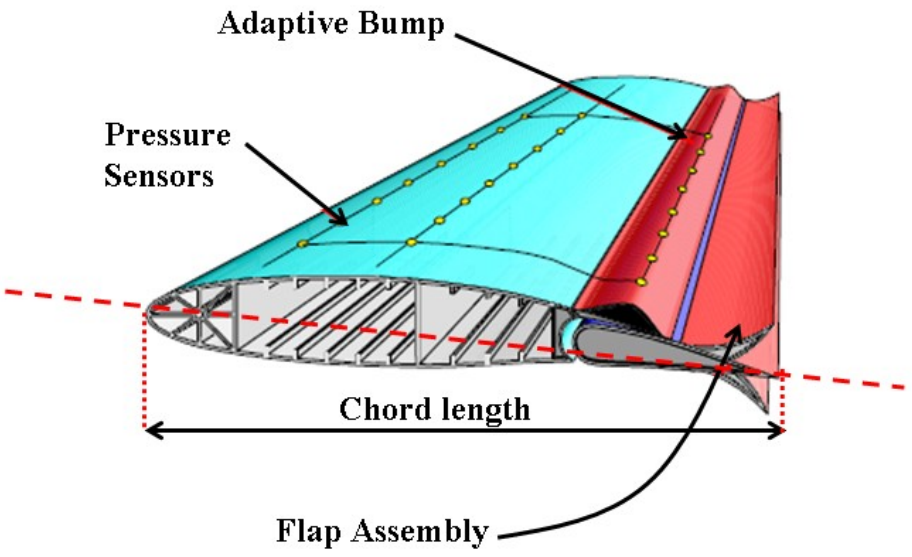

Fig.1.4: Adaptive trailing edge system proposed by Bein [13], showing the chord of the aerofoil and chord length measurement. *(figure adapted from [13])*.

In his review of adaptive wing technology Stanewsky [1] reports work conducted as part of the Euroshock-II project detailing potential drag reduction caused by inclusion of bumps on the surface of an aerofoil with a height equal to 0.035% chord length. This study found

Mach number dependent drag reduction of up to 23% across an aerofoil similar to that of the Airbus A340. It was noted that a smaller bump with a height equal to 0.017% of chord length performed better at lower lift coefficients, whilst the 0.035% bump became more effective as lift increased. This dual dependence of bump performance on Mach number and lift coefficient during service led Stanewsky to conclude:

"The effectiveness of bumps is, however, dependent on free-stream conditions so that an adaptive bump is needed for maximum performance gains."

An additional benefit of the inclusion of a bump is a 10% increase in the allowable lift coefficient achievable before the onset of buffeting occurs; this enables a higher cruise Mach number and reduced journey times. It may therefore be concluded that the inclusion of an adaptive bump which is able to significantly change bump height may allow both a reduction in drag and an increase in aircraft operational envelope.

It was found that the bump location for optimum drag reduction and buffet suppression were significantly different, which suggests that a position adaptive system or multiple fixed morphing sections may provide the largest improvements in aircraft performance. It was however noted that a bump located for optimum drag reduction would also delay the onset of buffet conditions.

Previous research investigating adaptive bumps for aerodynamic control has centred on two concepts, namely prismatic bumps and localised bumps. Prismatic bumps such as those investigated by Bein [13] extend across significant span-wise lengths and aim to alter airflow over a large region of the wingspan as seen in Fig 1.4. Both Bein and Barbarino have developed physical demonstrators of prismatic bumps, although the prototype shown by Barbarino was a standalone demonstrator (Fig. 1.5) unlike the fully integrated design of Bein.

The prototype presented by Bein [13] utilised a flexible skin which was deformed by a tube spring driven by internal pressure exerted by pneumatic actuator, an additional actuator utilising SMA actuation was also presented. Characterisation of the SMA actuator found that the proposed tube spring concept would not generate sufficient displacement for use in the adaptive bump design. A functional demonstrator measuring 3.2m × 0.9m × 0.6m was manufactured, and using the pneumatically actuated tube springs a maximum deflection of 15mm (1.6% of chord length) at the centre point of the bump was achieved. No values for the operational response time of the actuator or the demonstrator were given.

Barbarino [39] also used SMA actuation to create a smaller bump prototype in which a traditional aluminium sheet was deformed using a pre-strained SMA tape mounted beneath the adaptive skin (Fig 1.5a). System operational response time was observed to be 240s from initial position to a maximum deflection of 3.42mm when the skin material was 7075 T6 aluminium. Reduced deflection was observed when a stiffer stainless steel skin was used.

Barbarino measured achievable deflection for a range of SMA pre-strain, SMA ribbon thickness and applied actuation load and presented finite element and analytical models which agreed well with experimental measurement for maximum deflection. As noted by Barbarino [39], the small deflection achieved, slow response time and lack of imposed aerodynamic loading means that this work should only be viewed as a proof of concept study with much development work required before this prototype can considered ready for flight testing.

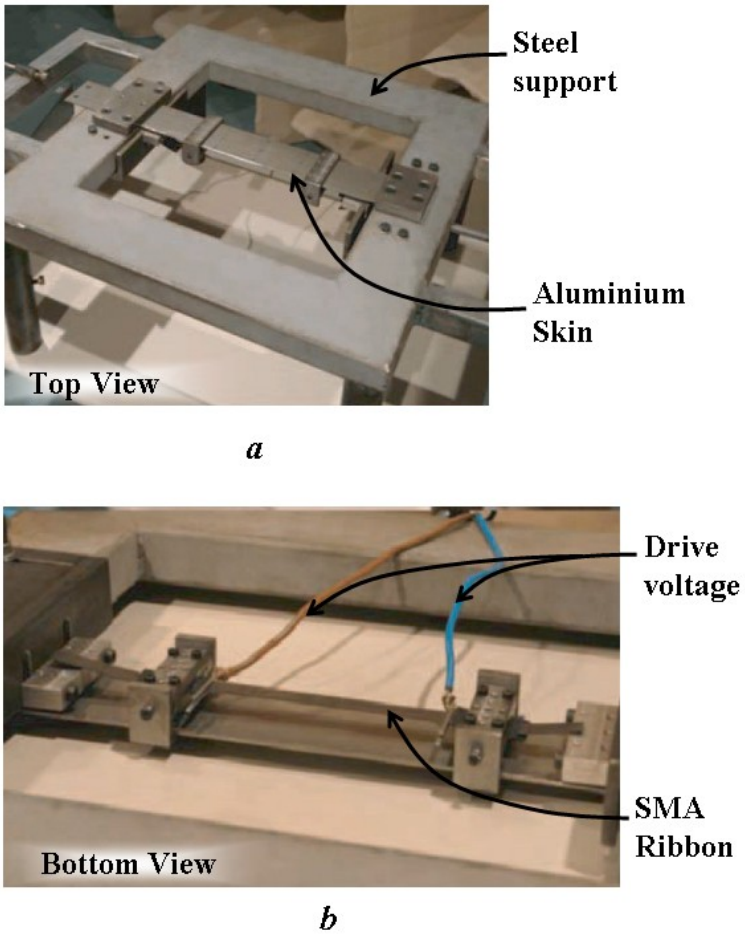

Fig.1.5: SMA actuated adaptive bump demonstrator showing top view of adaptive skin (a) and bottom view showing SMA ribbon (b) (*figure adapted from Barbarino [39]***).**

Physical prototyping and wind tunnel testing of a morphing leading edge was presented by Pinkerton [40] in a study which used piezoelectric unimorph actuators (THUNDER) to raise and lower a prismatic bump on the leading edge of a sub-scale airfoil to reduce aerodynamic drag.

Using a table-top wind tunnel a total of 60 different combinations of wing profile, angle of attack and air speed were tested to establish the potential drag reduction of a morphing leading edge bump.

Unfortunately due to experimental setup no quantitative data for the reduction in aerodynamic drag could be determined; however measurement of wake velocity suggests that drag reduction occurred. As noted by the investigators this conclusion is based on the assumption that wake velocity is inversely proportional to drag.

While quantitative data was not available to support drag reduction claims, this study remains the only prototype testing of a piezoelectrically actuated small scale morphing scheme presented in the literature.

In addition to preliminary wind tunnel testing, Pinkerton [40] identified several key issues related to the implementation of piezoelectric actuators in flow control devices. Decrease in actuation strain with increased aerodynamic loading, hysteresis and creep of the piezoelectric material are all notable challenges in implementing piezoelectric actuation in tightly controlled structural actuation applications.

Localised bumps are those for which span-wise and chord-wise dimensions are of the same order of magnitude, hence airflow is only affected within that specific region of wingspan. Natarajan [38] suggested the use of leading edge bumps for yaw control however no demonstrator or prototype was constructed. This extensive theoretical study suggests that the use of localised bumps may create novel control capabilities for aircraft in addition to the proposed drag reduction benefits outlined by Stanewsky [1].

The author is unaware of any experimental study of actuated localised bumps presented in the literature at the time of this review; therefore this interesting area of research represents a notable gap in current understanding.

1.3.4 Selection of the morphing structure

Given the potential gains in aerodynamic performance and control of small scale morphing structures their investigation would seem valuable to the civil aviation industry. The potential drag reduction and improvements in the cruise range for civil aircraft [1] make an adaptive bump particularly attractive.

The early stage research discussed in section 1.3.3 also demonstrates the feasibility of small scale morphing structures using SMA actuation of isotropic skins. Considering promising preliminary work presented by Pinkerton [40], it is clear that further investigation into the use of piezoelectrically actuated small scale morphing structures is of considerable merit in aerodynamic control applications where high-speed actuation response is necessary.

As shown by Daynes [22] in his development of a bistable trailing edge flap, multistable skins present significant advantages to engineers seeking to produce morphing structures. While the pre-stressed composite laminates used by Daynes proved effective in a medium scale morphing structure, direct integration with host structures during manufacture presents significant challenges due to constraints imposed by the pre-stressing process. Therefore to make use of the reduced actuation power requirements [22] and potential drag reductions [1] a bistable morphing bump could provide an alternative multistable technology.

With the gap in current understanding and the potential benefits for reduced aerodynamic drag and expanded operational envelope this work aims to develop modelling tools and gain experimental insight in order to allow design of a piezoelectrically actuated adaptive bump based on bistable composite laminates.

The following section will describe two technologies proposed for use within morphing aerospace structures, pre-stressed copper beryllium metal sheets and bistable composite laminates including a discussion of the physical processes which cause bistability in cross-ply composite laminates.

1.4 Multistable skins

This section discusses the work relating to two technologies for creating multistable sheets. As discussed in section 1.3.3 and 1.3.4 these unconventional materials exhibit two or more structurally stable deformation states [41]. Fig 1.6 shows two examples of multistable structures, $[-30/60]_T$ and $[0/90]_T$ bistable composite laminates exhibit two stable deformation states. Each of the observed states is a local minimum of the total potential energy of the laminate and hence is structurally stable.

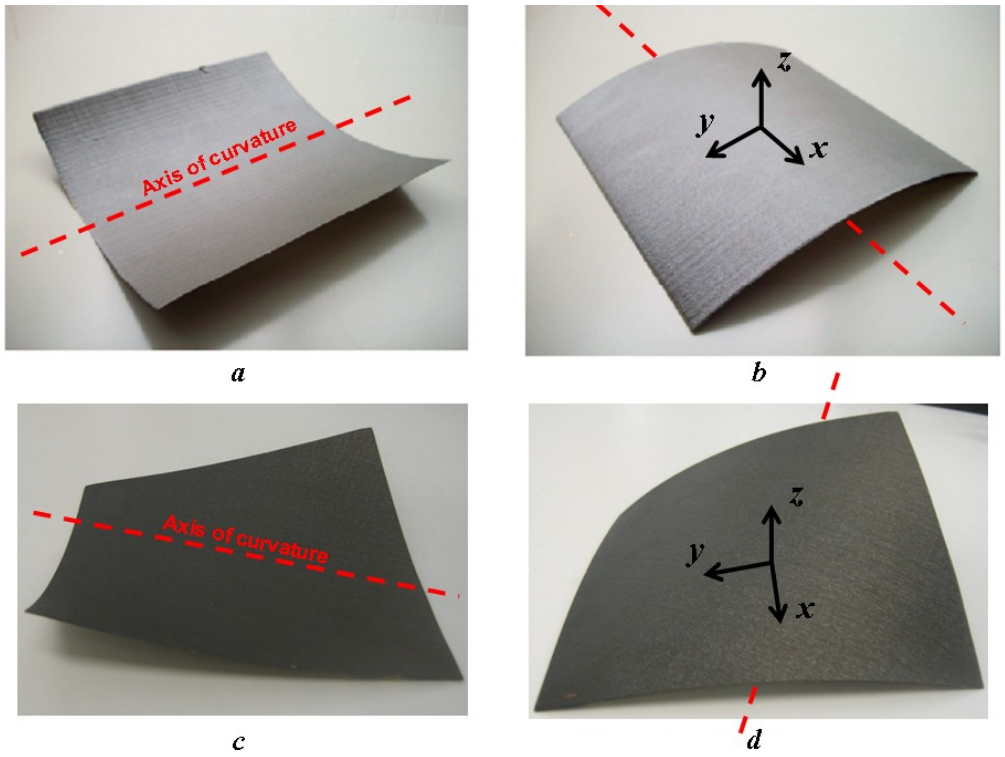

Fig.1.6: Two stable deformation states of $[0/90]_T$ (*a* and *b*) and $[-30/60]_T$ laminates (*c* and *d*), dashed line indicates axis of major curvature for each deformation state.

By switching between the discrete deformation states significant deflection can be achieved and maintained without continuous actuation and power demand [42]. In the drive to reduce actuation load, mechanical complexity and total system weight of morphing structures, these unique qualities make multistable structures extremely attractive.

In the following section early stage research into multistable copper-beryllium alloy sheets is presented before a review of the research relating to morphing structures based on bistable composite laminates is presented in section 1.4.2. Finally the physical processes which cause the formation of bistable composite laminates is presented in section 1.4.3.

1.4.1 Pre-stressed copper beryllium sheets

Work undertaken by Seffen [43, 44] outlines the development and analysis of copper beryllium alloy sheets manufactured with pre-stressed dimples within the sheet. These pre-stressed sheets exhibit various discrete deformation states including cylindrical curvature (Fig. 1.7a) and localised bumps (Fig. 1.7b) when different combinations of dimples are changed from concave to convex curvature.

The curvature of each dimple may be individually reversed between two stable states and doing so changes the global stress state within the sheet and hence the global deformation State As in Fig. 1.7.

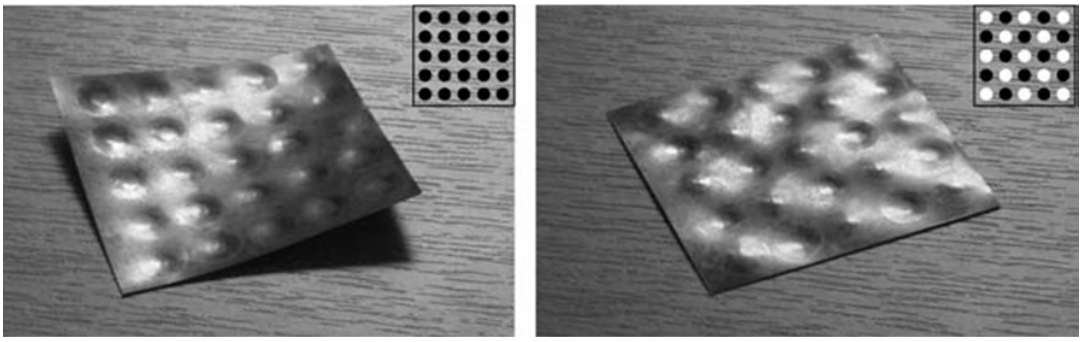

a *b*

Fig.1.7: Two global deformation states exhibited by pre-stressed sheet with legend showing orientation of localised dimples, black showing concave and white convex. (*figure adapted from[44]***)**

Despite extensive analysis of the metallic sheets, no work has been presented which proposes schemes of actuating the sheets between these global deformation states or assesses the feasibility of doing so. While pre-stressed metallic sheets may prove to be the basis of future morphing structures, significant development of actuation schemes suitable for use with these structures must be undertaken before they can be implemented in morphing structures.

1.4.2 Bistable composite laminates – Literature survey

Another interesting technology proposed as a method of realising adaptive structures for use within morphing structures are bistable composite laminates. Thin composite laminates whose lay-up is asymmetric about the laminate mid-plane have been shown to exhibit two or more structurally stable deformation states [41]. In the case of the commonly used example of a $[0_n/90_n]_T$ carbon fibre/epoxy laminate these two deformation states are observed as approximately cylindrical states where curvature is of opposing sign and about different axes [41]. Fig. 1.8 shows the two stable states of the $[0/90]_T$ laminate as well as their respective axes of curvature.

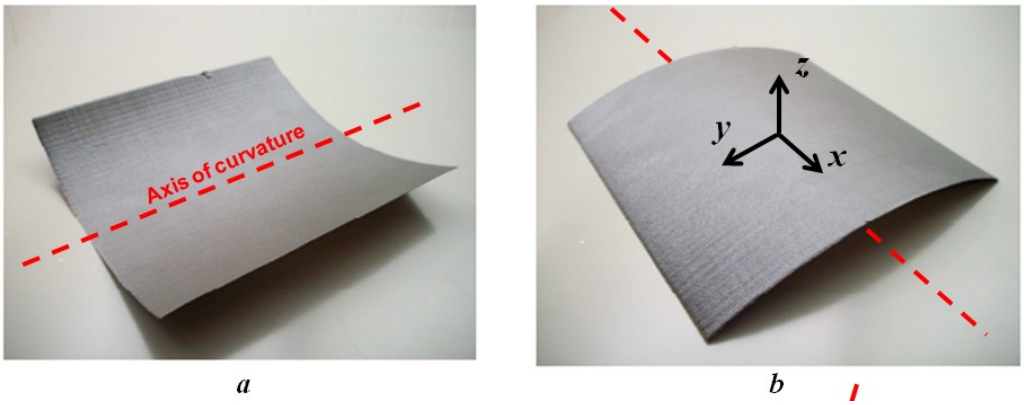

Fig.1.8: Two stable shapes of $[0/90]_T$ laminate, dashed line indicates axis of major curvature for State A (*a*) and State B (*b*).

These discrete stable states are the result of a residual stress field created during cooling from elevated cure temperatures used in their manufacture as a result of anisotropic thermal expansion coefficients of the composite plies [45-47].

A bistable laminate may be actuated between these two stable states by an applied actuation load. Transition between the two states is marked by a sudden and discontinuous change in structural shape without further increase in load; this is called 'snap-through'. Once snap-through has occurred the laminate will remain within the second structural state without continued actuation, or can be snapped back to the original configuration by application of an appropriate actuation load.

Bistable composite laminates have been proposed as a method of generating novel morphing structures within a range of engineering sectors such as aerospace, wind-power generation and automotive [36, 48, 49] because of their ability to sustain significant changes in shape without the need for a continuous power supply [42, 50-52].

In addition, the maximum deflection within a single stable state can be controlled by application of an actuation strain as shown by Bowen [42] which together with the potential for integration with rigid composite host structures makes them ideal candidates for creating a variable height adaptive bump.

The study of bistable components within non-adaptive host structures has received limited attention from investigators. Mattioni [53] presented analytical and finite element modelling and preliminary experimental measurements for a cross-ply laminate with a single boundary integrated with a host structure, shown in Fig. 1.9a. Integration with host structures presents particular challenges to analytical tools as the elasticity of the host structure must also be accounted for. Additional concepts for the use of bistable composites within morphing structures were presented which showed the breadth of potential applications for bistable composites.

Diaconu [49] presented more advanced finite element models of a morphing trailing edge flap structure, shown in Fig. 1.9b, however no experimental characterisation was presented to validate model predictions.

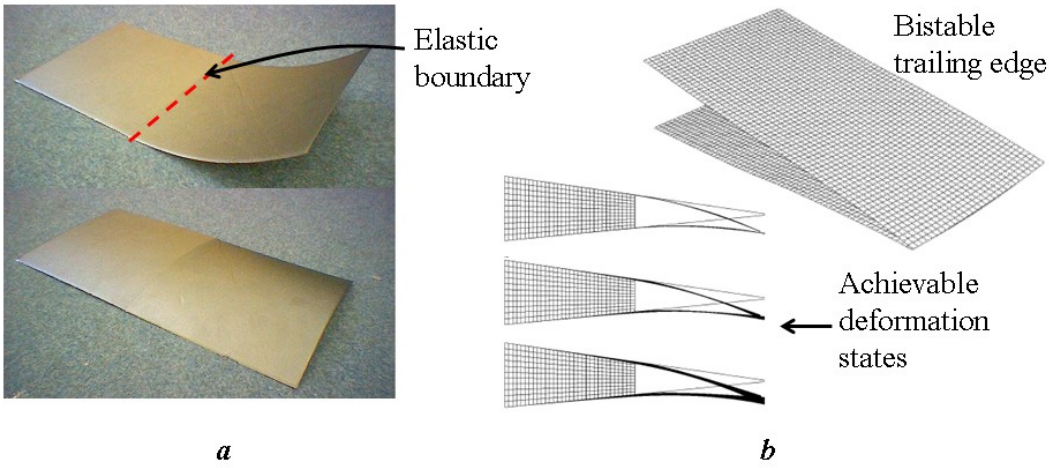

Fig.1.9: Cross ply bistable laminate with a single elastic boundary constraint (a) and proposed multistable trailing edge flap (b) ***(figure adapted from [54] and [49]).***

With limited experimental characterisation and modelling of bistable laminates with a single edge bonded to a host structure, the potential of bistable laminates fully embedded within rigid host structures has not yet been explored. The potential for realising various stable configurations through variations in lay-up of multistable composite laminates may help realise the goal of an adaptive bump without significant loss of structural rigidity.

Therefore, this work will seek to gain insight and develop understanding of the use of multistable composite laminates in the design of an adaptive bump for aerodynamic control purposes.

Therefore the finite element modelling and experimental characterisation of a bistable segment connected to host structure at all edges is an interesting topic of study and may lead to a feasible method for creating a localised adaptive bump for aerodynamic flow control.

In the following section the physical processes which cause the formation of bistable composite laminates during high temperature curing are described in preparation for more detailed discussions of the finite element analysis and experimental characterisation which follow in Chapter 2 & Chapters 4-7.

1.4.3 Bistable composite laminates – Formation

During the manufacture of composite laminates uncured pre-preg plies are layered together in the desired lay-up sequence on a flat plate coated in release film. This pre-preg material consists of carbon fibres bound together by part cured epoxy resin.

In its part cured state the epoxy is comprised of separate polymeric chains [47]. Epoxy resins cure via a chemical reaction between two constituent polymeric compounds which causes inter-atomic bonds to form between the polymeric chains forming a tightly bound three-dimensional network of inter-polymer bonds [55]. The matrix is said to be fully cured once no more cross-linking occurs; at this stage the laminate can be cooled and is ready for further processing. This cross linking process causes the resin to change from the pliable part-cured state of the composite pre-preg to a fully cross linked solid state.

Curing can be achieved at room temperature but high temperature curing achieves higher degrees of cross-linking and reduces alterations in properties during service [56]. For a typical aerospace epoxy resin the cure temperature would be 180˚C with a cure time of four hours. Curing takes place with the laminate contained in a vacuum bag and subjected to external atmospheric pressure to improve compaction and resin impregnation as well as reducing the occurrence of porosities within the laminate.

As temperature is increased from room temperature during the early stages of the curing process the resin system (thermally) expands more than the fibres. At this time, matrix viscosity and degree of cure are both low so there is little adhesion between fibre and resin. As the resin cures it adheres to the fibre surface and as cure temperature is held constant little additional thermal expansion occurs [57].

Once fully cured, the laminate is cooled back to room temperature creating thermal strain in both fibre and resin. For many fibre-reinforced polymer composites the coefficients of thermal expansion (CTE) parallel and perpendicular to the fibre direction differ by an order of magnitude [58]. Typical values of CTE for a unidirectional ply of carbon fibre/epoxy composite are -0.9×10^{-6} K^{-1} parallel to the carbon fibre direction compared to 30×10^{-6} K^{-1} in the transverse direction [59].

In addition to this thermal component of residual strain the cross-linking process increases resin viscosity and simultaneously reduces total volume [47, 56]. In epoxy resin systems the chemical shrinkage is typically 1.5% [55] and so would be expected to cause significant residual stresses in the cooled laminate. As identified in Chapter 5 the residual stress caused

by chemical shrinkage can be measured as a remnant curvature of bistable laminates when heated back to curing temperature.

Fig 1.10 illustrates the mismatch in thermal strain through the thickness of a $[0/90]_T$ laminate caused by variation in fibre angle between adjacent unidirectional plies. Once the epoxy has cured individual layers are bonded to one another to form the complete laminate. Hence continuity in the strain resultants must be maintained through the thickness of the laminate as relative movement of adjacent plies is not permitted.

In an asymmetric layup such as a $[0/90]_T$, where the sequence of plies above the laminate centre line is not mirrored by ply sequence below it, the resulting asymmetry thermal strain causes an out of plane deformation of the laminate.

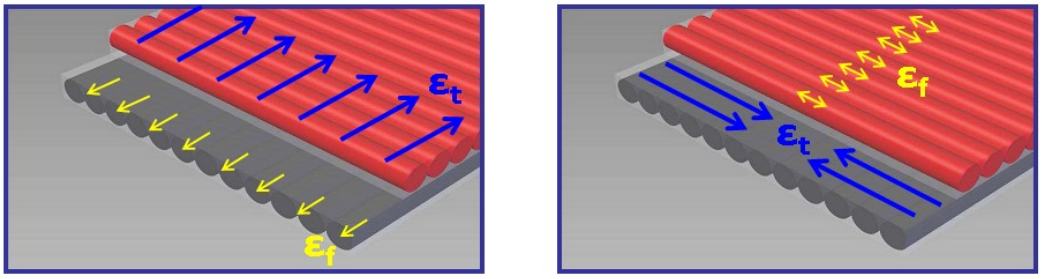

Fig.1.10: Mismatch in thermal strain in fibre (ε_f) and transverse directions (ε_t) between adjacent plies within a $[0/90]_T$ asymmetric composite laminate caused by anisotropy in coefficient of thermal expansion.

Fig. 1.11 shows finite element predictions of the incremental change in an asymmetric $[0/90]_T$ laminate profile as cooling progresses from cure temperature (T = 180°C) towards room temperature (T = 20°C).

The initial deformation forms a shallow saddle which subsequently becomes unstable as laminate temperature decreases and a cylindrical shape is adopted. This dominant cylindrical curvature develops further as laminate temperature approaches room temperature.

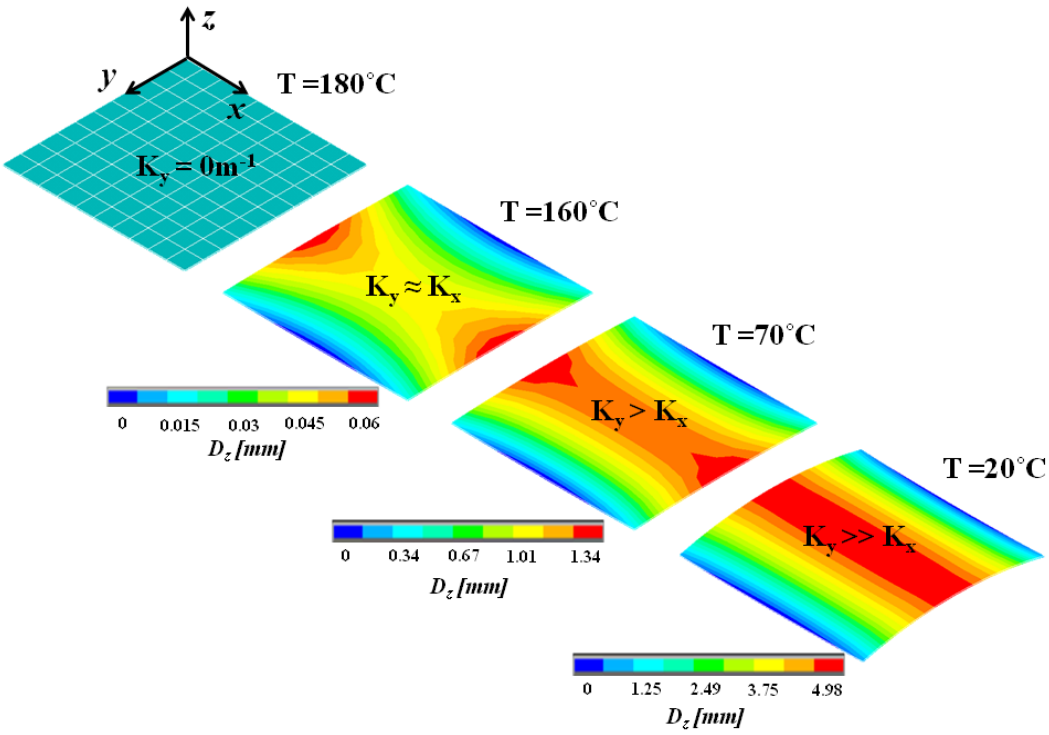

Fig.1.11: Finite element model prediction of laminate deflection [mm] in bistable M21/T800 $[0/90]_T$ laminate measuring 75mm × 75mm at various laminate temperatures showing development of cylindrical curvature. k_x and k_y are curvatures in the x and y-directions respectively.

The formation of two discrete deformation states as seen in Fig. 1.12b and 1.12c occurs only in asymmetric laminates whose edge length to thickness ratio is greater than a critical value. Thicker laminates whose edge-thickness ratio is below this value exhibit a single stable 'saddle' shape which is the superposition of the two cylindrical curvatures seen in bistable laminates as seen in Fig. 1.12a.

The critical value of edge-thickness ratio varies depending on the CTE and elastic constants of the composite plies as well as the exact layup sequence, though for the commonly used carbon/epoxy $[0/90]_T$ laminates the critical edge-thickness ratio has been predicted as 84 [60]. This dependence on laminate geometry limits the achievable thickness of bistable laminates of a given size.

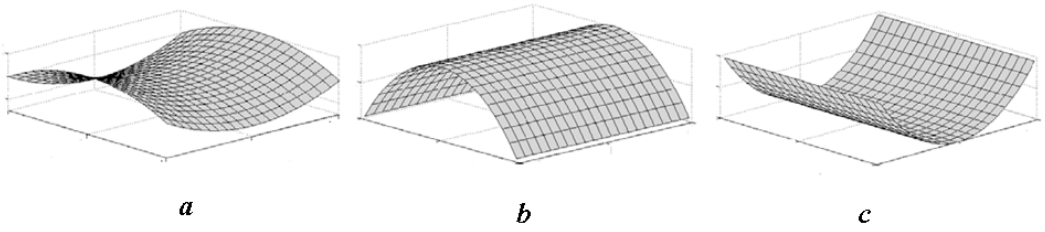

Fig.1.12: Saddle shape of thick asymmetric cross-ply laminates (a), two approximately cylindrical shapes adopted by thin laminates (b) and (c).

The formation of these discrete cylindrical deformation states is driven by the minimisation of total strain energy within the laminate [45]. Each deformation state represents a local minima in the total strain energy of the laminate, though not necessarily the global minimum [45]. The saddle shape observed in thicker asymmetric laminates does not represent a minimum in laminate strain energy in thin laminates and is therefore unstable. It is the principle of strain energy minimisation which allows the prediction of the cured shape of bistable laminates using the analytical methods discussed in Chapter 2.

1.5 Smart actuation

The potential of bistable composite laminates to amplify actuator displacement [42] within morphing structures and promising preliminary results in medium scale applications [19, 22] indicates that bistable composites may be suitable for use within a small scale morphing structure. In order for this emergent technology to be accepted within the civil aviation industry a suitable actuation technology must be developed which is capable of fulfilling force, displacement and frequency-response demands imposed by aerodynamic loads.

While several morphing concepts have been successfully prototyped using traditional actuation methods [5, 25] the improvements in aerodynamic performance comes at the expense of significant weight increase due to increased actuation complexity [7].

Smart actuation technologies such as shape memory alloys and piezoelectric ceramics have already been shown capable of producing significant weight savings as well as reducing system complexity compared to traditional actuation schemes [12, 37]. Therefore in section 1.5.1 the typical actuation capabilities of commercially available smart actuators will be assessed and the most suitable technology for the actuation of an adaptive bump will be selected.

1.5.1 Selection of smart actuation technology

This section aims to assess the typical range of actuator capabilities of commercially available smart actuators and select the technology most suited for the actuation of an adaptive bump for aerodynamic flow control.

Table 1.1 shows the typical range of actuation properties for smart structural actuators which use shape memory alloys, monolithic and piezoelectric polymer materials as the driving element taken from Huber [62] as well as piezoelectric macrofibre composite actuators (MFCs) taken from the manufacturers (Smart Materials GmbH, Dresden) data sheet .

Table 1.1: Typical actuation properties of structural actuators based on smart materials taken from [61] except subscript *a* denotes values taken from [62].

Material	Young's Modulus [GPa]	Maximum Free Strain [$\times 10^{-6}$]	Maximum actuation stress [MPa]	Maximum operational frequency [Hz]
Shape memory alloy (e.g. Nitinol)	30 - 90	7000 – 70,000	100 - 700	0.02 – 1
Low Strain monolithic Piezoceramic (e.g. PZT-5A)	50-80	50 - 200	1 - 3	5×10^{5} - 2×10^{7}
PVDF Shape memory polymer	2 - 10	200 - 1000	0.5 - 5	1×10^{5} - 1×10^{7}
MFC Actuator (Smart Materials 8557-P1)	30.3_{a}	1800_{a}	4.5_{a}	$1\times10^{7}{}_{a}$

It has been demonstrated that shape memory alloy (SMA) actuators are able to generate the necessary deflections and force for actuation of small and medium scale morphing structures [17, 25, 40]. However severe limitations in maximum operational frequency limit its use to applications not subject to rapidly changing operational requirements. As can be seen in table 1.1 shape memory alloy actuators are not able to operate at frequencies in excess of 1Hz and so are unsuitable for structures which must react to the rapidly changing aerodynamic conditions and control inputs which characterise aviation control surfaces [7].

By contrast both table 1.1 shows that polymer piezoelectric actuators are capable of high frequency actuation at frequencies of up to 10 kHz; which is sufficient for aerodynamic control applications. Despite high maximum operational frequency, piezoelectric polymers have a low Young's modulus which limits the achievable actuation strain when actuating a

high stiffness structure [63] as the actuator must deform the total stiffness of structure and actuator together as shown by [61]:

$$S = k_1 S_A / k_2 \tag{1.1}$$

where S is the observed actuation strain, S_A the free strain of the actuator, k_1 the actuator stiffness [Nm^{-1}] and k_2 is the transformed reduced stiffness of the layer to which the actuator is bonded [Nm^{-1}] [61].

As can be seen from table 1.1 the Young's modulus of a piezoelectric polymer actuator is well below that of an M21/T800 268gsm unidirectional carbon epoxy laminate, which has Young's modulus of 172GPa along the fibre direction and 8.9GPa in the transverse direction [64]. Because of this large mismatch on actuator and structural stiffness piezoelectric polymer actuators are not well suited to actuating high stiffness aerospace composite structures.

The remaining technology presented in table 1.1 is piezoelectric ceramic actuators. Although piezoelectric ceramic actuators are able to generate adequate actuation stress and achieve operational bandwidth requirements they are not able to generate large strains. Table 1.1 shows a typical free-strain value for monolithic ceramic actuators is only 2×10^{-4} which is two orders of magnitude below strains achieved by high strain SMA devices. Low free-strain and challenges in integrating rigid ceramic plates within flexible morphing structures makes the use of monolithic piezoelectric actuators within an adaptive bump design impractical.

Piezoelectric ceramics have also been used in fibre composite actuators which comprise piezoelectric ceramic fibres embedded in an epoxy matrix, with copper interdigitated electrodes bonded to top and bottom surfaces as seen in Fig. 1.13.

Active fibre composites as seen in Fig. 1.13 comprise extruded cylindrical fibres embedded within a polymer matrix. Improvements in achievable actuation strain and dielectric properties [65] have been made by use of rectangular cross-section fibres. Fibre composite actuators using these rectangular fibres are called macro-fibre composite (MFC) actuators. These novel composite actuators are capable of generating maximum actuation strain 1.8×10^{-3} which is an order of magnitude higher than monolithic piezoelectric ceramic actuators.

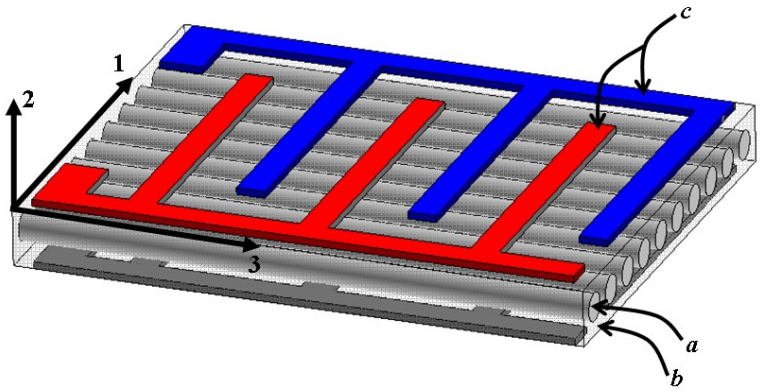

Fig.1.13: Schematic of active fibre composite (AFC) actuator showing unidirectional PZT fibre alignment (*a*), epoxy matrix (*b*), interdigitated electrodes (*c*) and orientation of MFC material coordinate system ***(****figure adapted from [65]****).***

Reported actuator stiffness of 30.3GPa along the fibre direction means that MFC actuators more closely match the stiffness of composite laminates increasing achievable actuation strain when actuating composite structures. In fact, it has been demonstrated by several investigators [42, 51, 66] that actuation strain created by MFC actuators is sufficient to cause snap-through in thin bistable composite laminates.

Proven ability for structural actuation at frequencies of up to 2 kHz [65] and maximum operational frequency of 20 kHz (table 1.1) is equal to the range achievable by either polymer or monolithic piezoelectric actuators.

Additional advantages include conformability for ease of integration with curved structures, damage tolerance [67, 68] and low density of 1400kgm^{-3} [62] compared to 1900 kgm^{-3} and 7500 kgm^{-3} for piezoelectric polymer and shape memory alloy respectively [62].

At present piezoelectric actuation using macro fibre composite actuators represents the most promising smart technology for actuation of an adaptive bump for aerodynamic control. The development of a finite element model suitable for predicting the actuation behaviour of MFC actuators is presented in Chapter 3 together with a literature review and introduction of the relevant technical areas.

In section 1.6 the physical origins of the piezoelectric effect as it relates to structural actuation will be discussed before the ‘poling’ process used to create ceramic actuators is explained and the nomenclature specific to piezoelectric systems defined.

1.6 Piezoelectric ceramics

Within piezoelectric materials the electric dipole moment (D) within the atomic structure changes under the action of an applied stress state (T) [69].

Described in more physically descriptive terms, the application of mechanical stress to a poled piezoelectric ceramic will cause an electric field to propagate through the material in a direction parallel to the applied stress as seen in Fig. 1.14a. This is the 'direct' piezoelectric effect and is utilised in piezoelectric transducers for sensor applications such as sonar and acoustography [70-73]. The field produced is proportional to stress and field direction switches under compressive or tensile stress as show by equation 1.2 [63]:

$$E = -gT \tag{1.2}$$

where E is the electric field strength [Vm^{-1}], g the piezoelectric voltage constant [$Vm^{-1}Pa^{-1}$] and T the applied stress [Pa].

Piezoelectric materials also exhibit a 'converse' effect whereby a strain (S) is produced within the poled ceramic under the action of an applied electric field (E) as in Fig. 1.14b. The strain observed is proportional to the applied field and switches between compressive or tensile strain according to field direction as in equation 1.3 [63]:

$$S = dE \tag{1.3}$$

where S is the material strain, d the piezoelectric strain constant of the material in the direction of the applied field [pmV^{-1}] and E the applied electric field [Vm^{-1}].

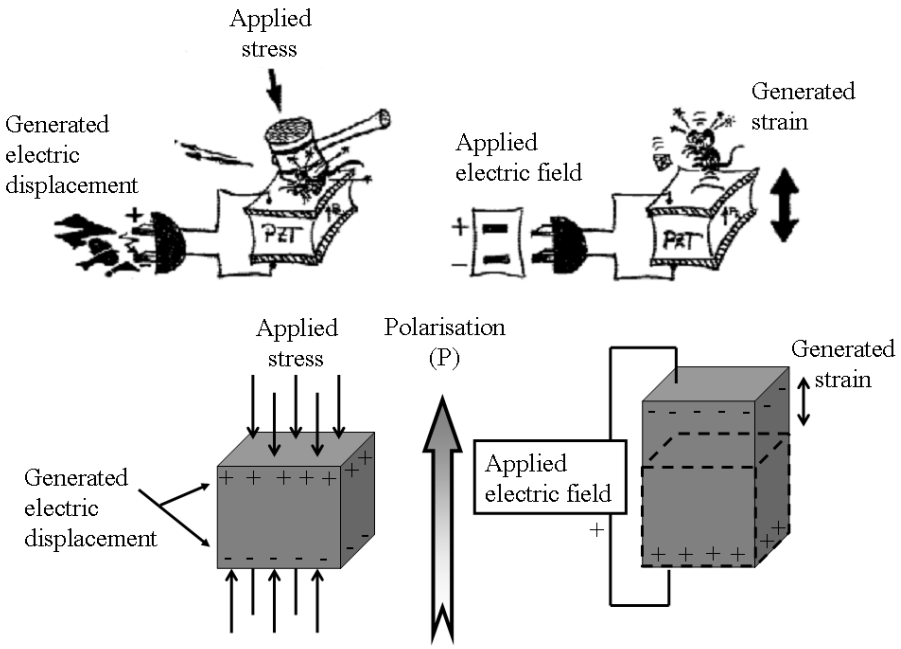

Fig.1.14: Net electric displacement within a piezoelectric solid under action of applied stress (a) and strain observed by same solid under influence of applied electric field (b) (*figure adapted from [74]*).

It is the converse effect that is of use to engineers seeking to create piezoelectric actuators [75].

The following section will explain the atomic origins of the piezoelectric effect before section 1.6.2 explains the use of piezoelectric 'poling' to create bulk piezoelectric material suitable for actuator applications. Section 1.6.3 will then describe the structure of the macro fibre composite (MFC) actuator selected as the actuation technology for the proposed adaptive bump structure in section 1.4.

1.6.1 Atomic origins of piezoelectricity in ceramic materials

The word 'piezo' is derived from the Greek word meaning to press, although the discovery of the effect dates from a much more recent era. Piezoelectricity was first observed in Rochelle salt crystals, quartz and other minerals in 1880 by Pierre and Jacques Curie [76]. Following Curie's work, the mechanisms of piezoelectric behaviour are now better understood. What follows is a brief introduction to the physical causes of piezoelectricity in ceramics which stemmed from the Curie's initial discovery.

The phenomenon of piezoelectricity can only be fully explained when the material is examined at the atomic level. At this level, an ionically bonded piezoelectric ceramic is composed of charged atoms (ions) of several different elements arranged in repeating patterns that together form a lattice. The lattice, being a repeated pattern, is therefore divisible into some smaller repeated portions. The smallest repeating portion of the crystal lattice is called the unit cell [74].

In piezoelectric ceramics the unit cell may be divided into one of the following structural groups: tungsten-bronze group, oxygen octahedral (Perovskite) group, pyrochlore group and the bismuth layer-structure group [74]. These groups define the chemical composition of the lattice and how the constituent elements are arranged and have a large effect on the piezoelectricity of the bulk ceramic. Of particular interest to engineers seeking to build effective and high strain piezoelectric actuators is the Perovskite group [74]; this group includes the most commonly used actuator material, namely lead zirconate titanate (PZT) which exhibit high piezoelectric induced strains (high piezoelectric d and g constants in equations 1.2 and 1.3).

In order to explain the basis of piezoelectricity in Perovskite ceramics, PZT will be used as the example throughout the following explanation, although similar principles apply to many other piezoelectric ceramics.

1.6.2 Unit cell structure of PZT

The unit cell of PZT exhibits an octahedral structure, as shown in Figure 1.15a. Six O^{2-} ions create a single unit of a corner-linked octahedral network that gives the structure its name. In addition to the six 0^{2-} ions, eight Pb^{2+} ions occupy interstitial sites (A-sites) which form the outer cuboid. It is important to keep in mind that Fig. 1.15 shows only one unit of a continuous network of oxygen octahedra and so, the A-sites occupied by Pb^{2+} ions form the boundary between one unit cell and the next. Within the octahedral cage of the unit cell is the Ti^{4+} or Zr^{4+} ion (B-site ion) that is vital to the piezoelectric effect.

At high temperatures the ceramic exists as a symmetric, cubic phase (Fig. 1.15a). Since the central Ti^{4+} ion is positioned directly at the centre of the cell, there is no net electric displacement about the centre of the cell so the cubic phase has no net dipole and hence is not piezoelectric. As the ceramic cools below some critical temperature the central Ti^{4+} ion is displaced (Fig. 1.15b), this critical temperature where the unit cell becomes polarised is called the Curie temperature (T_c).

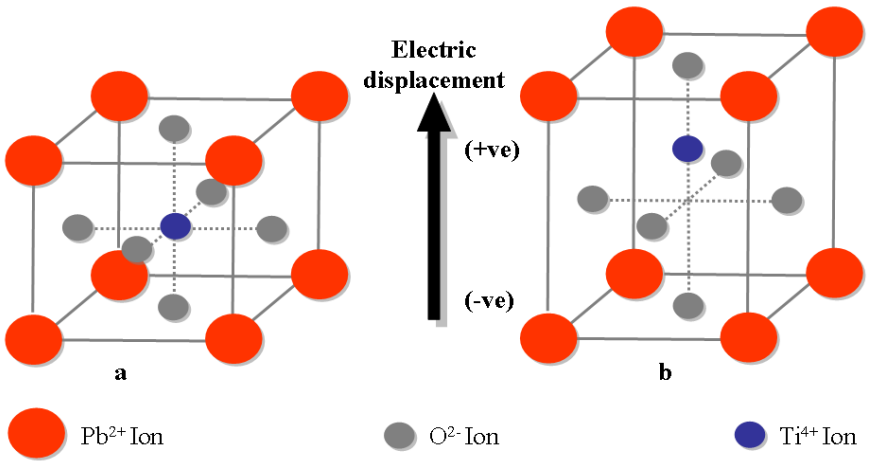

Fig.1.15: Unit cell of PZT with Pb^{2+}, Ti^{4+} and O^{2-} ion locations shown (a) symmetrical cubic above T_c (b) non centro-symmetrical tetragonal below T_c.

In order for PZT to exhibit piezoelectricity, the unit cell must be non centro-symmetric, meaning that there is at least one axis of the unit cell along which the arrangement of the ions is asymmetric about the centre of the cell. In addition, that asymmetry must generate an electric dipole moment within the cell.

Within a unit cell of overall neutral charge (like PZT) an electric dipole moment is defined as a non-zero summation of the products of each ion's charge and its location vector with

respect to the cell centre [77]. The dipole moment is therefore a measure of asymmetry in charge distribution within the cell, the greater the dipole moment, the greater the asymmetry in charge distribution.

When PZT is cooled from elevated temperatures to temperatures below T_c a distortion of the unit cell occurs that displaces the Ti^{4+} ion from its central location. Fig. 1.15b shows the tetragonal phase of the PZT unit cell with the Ti^{4+} clearly displaced towards the top of the cell.

This displacement creates an asymmetric charge distribution about the mid-plane of the cell and, hence a net electric dipole within the cell. The direction in which the central ion is displaced is called the polarisation direction or polar axis (P_s). In addition to the tetragonal form, PZT can also exist in the rhombohedral form which is also asymmetric. Fig. 1.16 shows the B-site ion displacement and associated polarisation directions (P_s) for rhombohedral and tetragonal phases.

As seen in Fig. 1.16a there are 6 equivalent polar axes for the tetragonal phase, corresponding to the Ti^{4+} ion moving toward each O^{2-} ion. Fig. 1.16b shows the rhombohedral phase of the Perovskite unit cell with the Ti^{4+} ion moving toward one of the A-site ions that form the outer cuboid. Hence there are 8 equivalent polar axes for the rhombohedral phase of the unit cell.

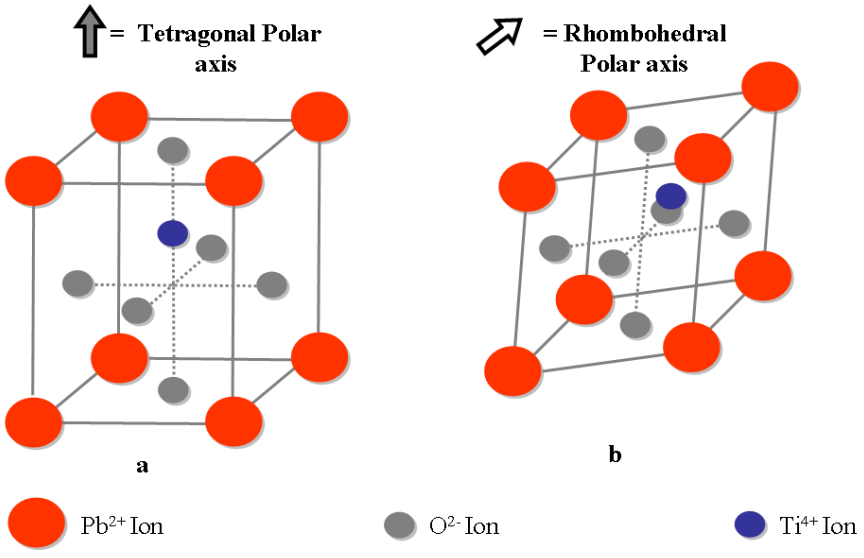

Fig.1.16: Tetragonal (a) and rhombohedral (b) distortion of Perovskite unit cell.

1.6.3 Unit cell deformation under applied electric field

Upon application of an electric field an asymmetric Perovskite unit cell will exhibit a strain along the polarisation direction of the cell. The generated strain is caused by changes in the relative positions of ions within the unit cell as seen in Fig. 1.17. For the tetragonal case the positively charged Ti^{4+} ion is drawn along the polarisation axis in the direction of the applied electric field to minimise the net electric dipole under the new electrical conditions.

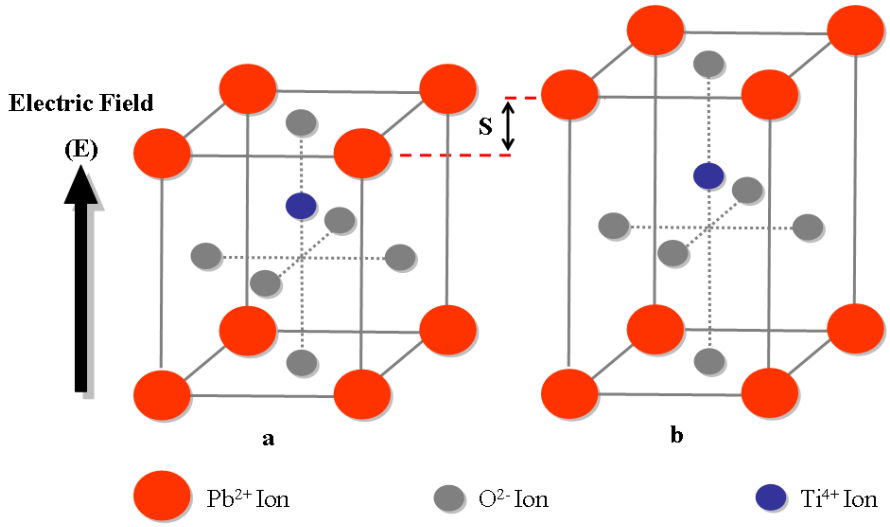

Fig.1.17: PZT unit cell before (a) and after (b) electric field application with unit cell strain (S) shown.

However, the movement of the positively charged Ti^{4+} ion toward the Pb^{2+} ions introduces a resistive electrostatic force caused by the repulsion of like charges which deforms the octahedral cage and hence the unit cell. This deformation of the octahedral cage (*S* in Fig. 1.17) is the cause of the strain in the unit cell.

The magnitude of the strain generated is approximately proportional to the applied field magnitude and can be either compressive or extensional depending on the applied field direction [78]. The constitutive equation for a perfectly elastic piezoelectric ceramic which predicts the strain generated by an applied field is [63]:

$$S = s^E T + dE \qquad \textbf{(1.4)}$$

where S is the induced strain, s^E the constant field (or short-circuit) stiffness [Nm^{-1}], T the applied stress [Pa], d the piezoelectric constant [pmV^{-1}] and E the electric field strength [Vm^{-1}].

In addition to the piezoelectric strain, the application of an electric field will generate a mechanical strain caused by electrostriction. Electrostriction occurs weakly in all materials and produces a mechanical strain that is proportional to even powers of field strength but unlike piezoelectric strain is independent of field direction [79].

The interactions between the piezoelectric, electrostrictive, thermal and other effects influencing the final configuration of the unit cell may be studied in great detail by considering the appropriate formulations for the free energy of the unit cell. The free energy of a thermodynamic system is the sum of its internal energy at some initial condition and the energy added to the system via mechanical, thermal or electrical processes [63].

However for the purposes of this work it is sufficient to remember the explanation of the piezoelectric effect and apply the equations given above. The coupled field finite element models developed in Chapter 3 and used in Chapters 4 and 7 will use these equations when calculating the stress state within the elements representing piezoelectric material. The interested reader can learn more about the thermodynamics governing piezoelectric behaviour in crystals by referring to Ikeda [63], Xu [77] and the texts cited therein.

In this section the atomic origins of the piezoelectric strain observed in Perovskite ceramics have been explained in terms of a single unit cell. However in order for this atomic strain to be of use within a structural actuator an entire volume of ceramic must exhibit the same strain. The following section describes the structure of polycrystalline PZT and the process of aligning the polarisation direction of all unit cells within a volume to form a 'poled' ceramic.

1.6.4 Structure of sintered ceramics

The origins of piezoelectricity are a spontaneous polarisation of the Perovskite unit cell which creates a net electric dipole relative to the centre of the cell. However samples of piezoelectric ceramics do not exhibit piezoelectricity immediately after sintering or other high temperature manufacturing techniques. This lack of piezoelectric behaviour in bulk ceramic stems from structural changes of the ceramic as it cools from elevated sintering temperature through the Curie temperature to room temperature.

During cooling, each individual unit cell undergoes the distortion discussed in section 1.6.1, creating either tetragonal or rhombohedral unit cells. However, the polar axes within the unit cells are not aligned throughout the material. Regions of cells sharing the same

polarisation direction are formed; these homogeneous regions of like-polarised cells are called domains.

As observed by Xu [77], the phenomenon of domain growth within a ceramic is well documented but not clearly understood. It is hypothesised and generally accepted that domains form so as to minimise the free energy within the material due to mechanical, electrical and thermal effects [75, 77].

This free energy minimisation process causes a sample of piezoelectric material to exhibit no net electric dipole moment. The orientation of the domains formed tends to introduce a higher degree of symmetry in the ceramic, preventing a net polarisation of the sample and hence the development of piezoelectric strains [80]. This can be thought of as the individual domain dipoles 'cancelling-out' any opposing domain dipoles [79].

The presence of dissimilarly oriented domains within a single crystal suggests the existence of some boundary between domains, called a domain wall. Domain walls are thin regions of the crystal lattice (at the scale of a few unit cells [77]) where the dipole direction changes rapidly between the directions of adjacent domains. There is no discrete switching point, rather a rapid but continuous change over the domain wall region from the dipole direction of one domain to that of the adjacent domain.

1.6.5 Aligning domains – Poling

In order to make use of the piezoelectric effect within a structural actuator, entire volumes of ceramic must be made to strain in response to applied electric field. As commercially available MFC actuators use polycrystalline PZT as the piezoelectric element the domains within the ceramic must be altered so that the sample as a whole displays piezoelectric behaviour. This is achieved through alignment of the randomly oriented domains formed by spontaneous polarisation via a 'poling' process as seen in Fig. 1.18.

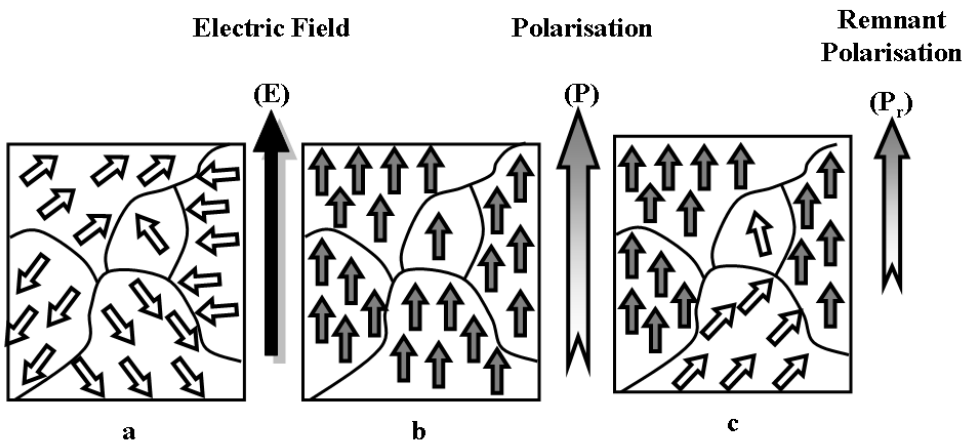

Fig.1.18: Poling of randomly oriented domains (a), under strong DC electric field (b) resulting in remnant polarisation (c).

Poling reorients domains via a combination of heat and applied electric field. The procedure used during a typical 'poling' process would be:

(i) Ceramic sample is heated towards the Curie temperature (80˚C is typical)

(ii) Strong dc-field is applied (e.g. ~2kV/mm) for an extended period of time

(iii) Sample is cooled to room temperature with the electric field still applied

(iv) Poling field is removed to complete 'poling' process

The strong DC field causes domains to alter the direction of spontaneous polarisation so that P_s has the largest possible component in the direction of the field. Individual domains can have their poling direction changed by switching to one of the other 14 possible poling directions (6 for the tetragonal phase and 8 for the rhombohedral phase as in Fig. 1.16) to best match poling direction to the applied field.

PZT is a solid solution ceramic comprised of cells of lead zirconate and lead titanate, in lead zirconate the central Ti^{4+} ion seen in Fig. 1.15 is replaced by a Zr^{4+} ion. In solutions with higher proportions of titanium, the ceramic exists in the tetragonal phase [71]. In solutions with more zirconium present the ceramic exists in the rhombohedral phase.

It has been observed that for compositions with approximately equal proportions of lead zirconate and lead titanate the relative permittivity (ε_r) and coupling factor (a measure of efficiency of conversion from mechanical to electrical energy), show large peaks [80] as seen in Fig. 1.19. In addition to increased electromechanical coupling, the ceramic is more readily poled as the material may switch phase to better align the polar axis with the applied field.

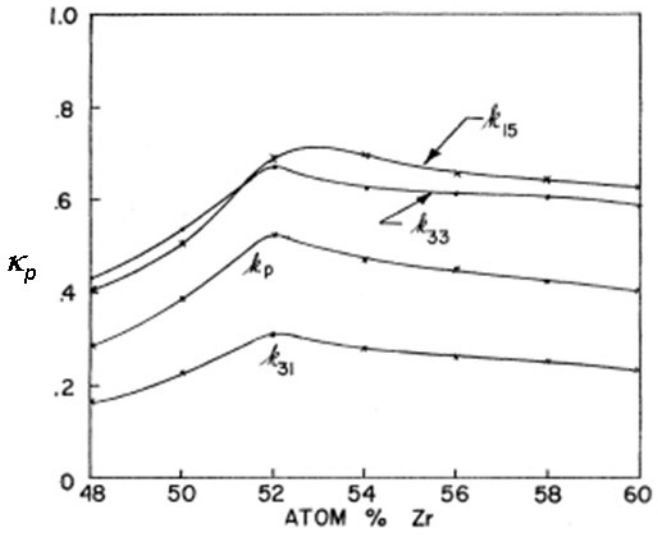

Fig.1.19: The effect of composition on the electromechanical coupling factor kp, and directional coupling factors k_{15}, k_{33} and k_{31} in PZT ceramics ***(figure adapted from:[81])*.**

Domains within PZT ceramics comprised of both tetragonal and rhombohedral forms can switch between 14 domain orientation states (8 rhombohedral, 6 tetragonal) allowing closer alignment with applied field than would be possible in a single phase material [80]. Therefore the compositions of many commercially available PZT piezoelectric ceramics are equal mixtures of zirconate and titanate phases. The region in which this improvement in polarisation is observed is called the 'morphotropic phase boundary' (MPB). This boundary identifies the composition at which a particular ceramic will exist in tetragonal or rhombohedral form. Fig. 1.20 shows a phase diagram for PZT with the morphotropic phase boundary indicated.

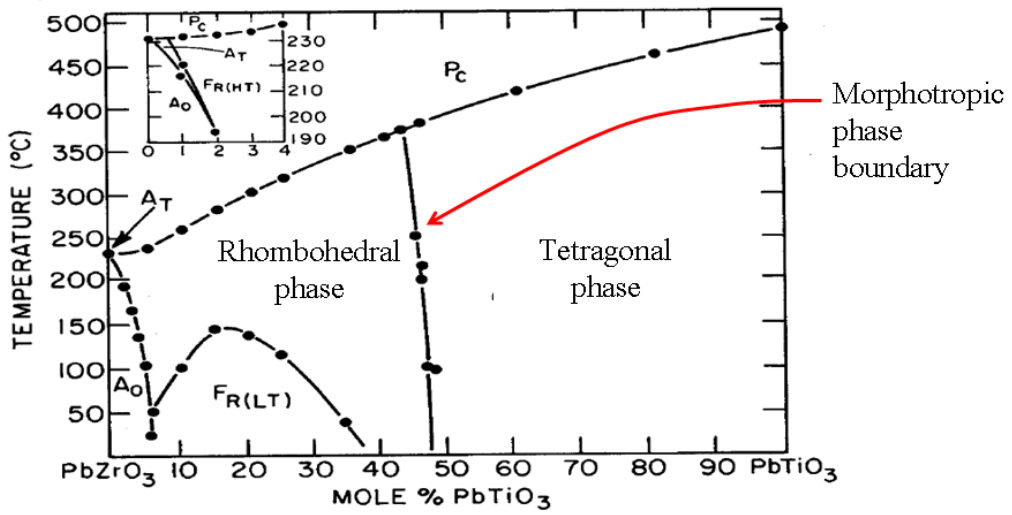

Fig.1.20: Phase diagram for PZT system, showing paraelectric cubic phase (P_c), tetragonal, and rhombohedral with morphotropic phase boundary indicated (*figure adapted from [74]*).

Domain walls can also move to enable domains whose poling direction is well aligned with applied field to grow while those with misaligned polar axis shrink in a process called domain wall motion. This process does not occur instantaneously leading the net polarisation of the solid to change with time, ultimately leading to creep in the ceramic material [82]. A more detailed discussion of piezoelectric creep as it relates to MFC actuators is presented in Chapter 6.

The alignment of domains is never complete because elastic stresses generated during domain switching can leave some domain orientations unstable without an applied field [77]. Hence, after the field is removed at room temperature some of the reoriented domains return to their original state [74], the remaining polarisation after the field is removed is the remnant polarisation (P_r).

P_r values in PZT can be as high as eighty three percent for the tetragonal phase and eighty six percent in the rhombohedral phase [74]. To achieve such complete poling extremely high electric field values of three to four times the coercive field (the minimum field required to reorient domains from the remnant to zero polarisation) must be applied to the sample.

The application of heat introduces thermal energy into the material which causes a reduction in the displacement of the B-site ion. The reduction of dipole moment reduces the coercive field [77] and can increase remnant polarisation (P_r) when protocols of equal field are compared [79].

After poling a ceramic will show significantly different mechanical and piezoelectric properties compared to its virgin state. Due to the improved alignment of polarisation direction of each domain (P_r) the ceramic will exhibit highly anisotropic piezoelectric constants ($[d_{ij}]$). Strain along the poling direction will be greatest for a given voltage while a smaller strain of opposing sign will be created in the two transverse directions [79].

Additionally a poled piezoelectric ceramic will exhibit a greater degree of anisotropy in its mechanical properties, as well as changes in its physical dimensions. Elongation along the poling axis is usual as poling aligns the strain observed in the unit cell seen in Fig. 1.14. As a result of this anisotropy of properties it is necessary to include the full three dimensional compliance matrix ($[s_{ij}]$) when modelling poled piezoelectric materials as will be shown in Chapter 3.

Due to the anisotropic physical properties of the material and the three dimensional nature of both electrical and mechanical fields which influence piezoelectric behaviour, a particular notation and coordinate system is used when analysing anisotropic piezoelectric materials. The notation and coordinate system used throughout this thesis for describing piezoelectric constants is described in the following section.

1.6.6 Piezoelectric constants coordinate system

The magnitude of the piezoelectric constant (d_{ij}) is different depending upon the direction of measurement. The d_{ij} coefficients represent the strain generated within the material per unit applied electric field. Measurement directions are defined within a coordinate system with the 3-axis parallel to the poling direction and the 1 and 2-axes forming the two orthogonal directions as in Fig. 1.21. In ceramics of the Perovskite class the properties in directions 1 and 2 are identical because the unit cell is axisymmetric about the poling axis.

When specifying the piezoelectric constant (d_{ij}) the first subscript denotes the direction of applied electric field and the second denotes the direction in which the strain is measured. For example the observed strain in the 1-direction in response to applied field in the 3-direction is described by the d_{31} constant.

Fig. 1.21 shows a Perovskite unit cell with poling direction (P_s) and applied field (E) directions, the resulting orientation of the d_{31} and d_{33} constants are also indicated.

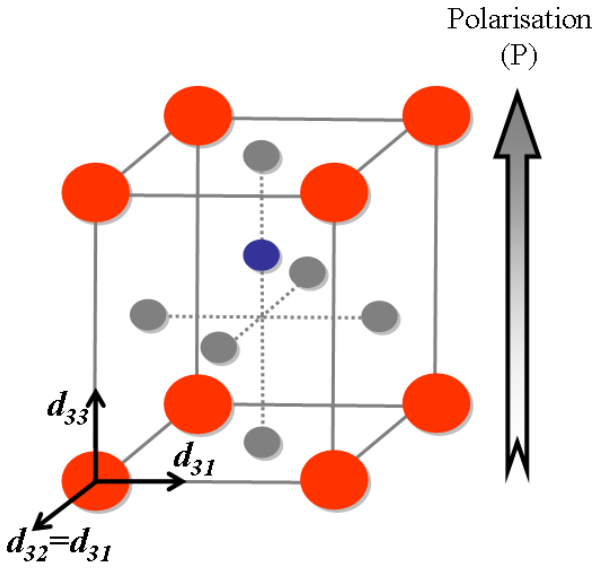

Fig.1.21: Perovskite unit cell with polar axis and piezoelectric constant coordinate system.

1.6 Summary

In this Chapter the strong motivation for development of morphing structures from economic and legislative drivers within the civil aviation industry has been described. Reduced fuel consumption through decreased aerodynamic drag and lower structural weight were identified as two key operational advantages of morphing structures in reducing fuel consumption.

With the aim of reduced fuel consumption in mind, a survey of the available literature relating to morphing concepts for aerodynamic surfaces has been presented. This body of work was subdivided into large, medium and small scale schemes with the proposed advantages and presented experimental prototypes discussed.

It was concluded that small scale morphing structures have not been fully explored in the literature and were most likely to be industrially viable over the medium term. In particular, the potential of a localised adaptive bump for drag reduction and increased cruise speed was highlighted as an interesting and novel area for research.

Potential smart actuation technologies were surveyed and the typical range of actuation properties compared. Piezoelectric macrofibre composite (MFC) actuators were chosen as the most suitable for the adaptive bump application based on high maximum operational frequency, achievable actuation strain and ease of integration within morphing structures.

Based on the available literature the development of an adaptive bump for aerodynamic drag reduction based on bistable composite laminates actuated by piezoelectric macro fibre composite actuators is the chosen focus of this thesis.

The physical principles which govern the formation of bistable composite laminates and the atomic origins of piezoelectric ceramics and the fundamental concepts relating to poled ceramic materials were introduced in preparation for more specific technical discussions presented in each of the relevant chapter introductions.

The following chapter presents work undertaken to develop a finite element model for prediction of the cured shape of bistable composite laminates. Experimental measurements of laminate composition will be used to include variations in ply thickness in the FE model to improve prediction accuracy. This model will form the basis of subsequent developments towards the research aim of this thesis which is a design tool for MFC actuated multistable structures.

1.7 Reference list

1. Stanewsky, E. (2001). "Adaptive wing and flow control technology." *Progress in Aerospace Sciences*, 37(7), 583-667.
2. Sanders, B., Crowe, R., and Garcia, E. (2004). "Defense Advanced Research Projects Agency - Smart Materials and Structures Demonstration Program overview." *Journal of Intelligent Material Systems and Structures*, 15(4), 227-233.
3. Green, J. E. (2003). "Civil aviation and the environmental challenge." *Aeronautical Journal*, 107(1072), 281-300.
4. Green, J. E. (2006). "Civil aviation and the environment - the next frontier for the aerodynamicist." *Aeronautical Journal*, 110(1110), 469-486.
5. Gilbert, W. W. (1981). "Mission adaptive wing system for tactical aircraft." *Journal of Aircraft*, 18(7), 597-602.
6. Culick, F. E. C. (2003). "The Wright brothers: First aeronautical engineers and test pilots." *AIAA Journal*, 41(6), 985-1006.
7. Kudva, J. N. (2004). "Overview of the DARPA Smart Wing Project." *Journal of Intelligent Material Systems and Structures*, 15(4), 261-267.
8. Barrett, R., Gross, R. S., and Brozoski, F. (1996). "Missile flight control using active flexspar actuators." *Smart Materials & Structures*, 5(2), 121-128.
9. McMasters, J. H., and Cummings, R. M. (2004). "From farther, faster, higher to leaner, meaner, greener: Further directions in aeronautics." *Journal of Aircraft*, 41(1), 51-61.
10. Haglind, F., Hasselrot, A., and Singh, R. (2006). "Potential of reducing the environmental impact of aviation by using hydrogen Part I: Background, prospects and challenges." *Aeronautical Journal*, 110(1110), 533-540.
11. Bradley, T. H., Moffitt, B. A., Mavris, D. N., and Parekh, D. E. (2007). "Development and experimental characterization of a fuel cell powered aircraft." *Journal of Power Sources*, 171(2), 793-801.
12. Vos, R., De Breuker, R., Barrett, R., and Tiso, P. (2007). "Morphing wing flight control via postbuckled precompressed piezoelectric actuators." *Journal of Aircraft*, 44(4), 1060-1068.
13. Bein, T., Hanselka, H., and Breitbach, E. (2000). "An adaptive spoiler to control the transonic shock." *Smart Materials & Structures*, 9(2), 141-148.
14. Ramrakhyani, D. S., and Lesieutre, G. A. (2005). "Aircraft Structural Morphing Using Tendon-Actuated Compliant Cellular Trusses." *Journal of Aircraft*, 42(6), 1615-1621.
15. "NextGen Bat Wing Concept." (2007). http://www.nextgenaero.com/success_mfx2.html. Accessed: Jan. 5, 2010.
16. Sanders, B., Cowan, D., and Scherer, L. (2004). "Aerodynamic performance of the Smart Wing control effectors." *Journal of Intelligent Material Systems and Structures*, 15(4), 293-303.
17. Perry, B., Cole, S. R., and Miller, G. D. (1995). "Summary of an Active Flexible Wing Program." *Journal of Aircraft*, 32(1), 10-15.
18. Bourdin, P., Gatto, A., and Friswell, M. I. (2008). "Aircraft control via variable cant-angle winglets." *Journal of Aircraft*, 45(2), 414-423.

19. Gatto, A., Mattioni, F., and Friswell, M. I. (2009). "Experimental investigation of bistable winglets to enhance wing lift takeoff capability." *Journal of Aircraft*, 46(2), 647-655.

20. Maucher. C.K, Grohmann. B.A. (2007). "Actuator design for trailing edge flap.". ww.noliac.com/files/billeder/pdf/actuator_design_for_the_active_trailing_edge.pdf. Accessed: 5th Jan 2010.

21. Jha, A. K., and Kudva, J. N. (2004). "Morphing aircraft concepts, classifications, and challenges." *Smart Structures and Materials 2004: Industrial and Commercial Applications of Smart Structures Technologies*, 5388, 213-224.

22. Daynes, S., Nall, S. J., Weaver, P. M., Potter, K. D., Margaris, P., and Mellor, P. H. (2010). "Bistable Composite Flap for an Airfoil." *Journal of Aircraft*, 47(1), 334-338.

23. Daynes, S., Potter, K. D., and Weaver, P. M. (2008). "Bistable prestressed buckled laminates." *Composites Science and Technology*, 68(15-16), 3431-3437.

24. Daynes, S., Weaver, P. M., and Potter, K. D. (2009). "Aeroelastic Study of Bistable Composite Airfoils." *Journal of Aircraft*, 46(6), 2169-2174.

25. Bartley-Cho, J. D., Wang, D. P., Martin, C. A., Kudva, J. N., and West, M. N. (2004). "Development of high-rate, adaptive trailing edge control surface for the Smart Wing Phase 2 wind tunnel model." *Journal of Intelligent Material Systems and Structures*, 15(4), 279-291.

26. Martin, C. A., Bartley-Cho, J., Flanagan, J., and Carpenter, B. F. (1999). "Design and fabrication of Smart Wing wind tunnel model and SMA control surfaces." *Proceedings of SPIE - The International Society for Optical Engineering*, 3674, 237-248.

27. Sankrithi, M., and Frommer, J. B. 2008. The Boeing Company. US-Patent reference: 11/763,701[US 2008/0308683], 1-13

28. Marks, P. (2009). "Morphing winglets make for greener aircraft." *New Scientist*, 201(2692), 22-23.

29. Hufenbach, W., Gude, M., and Kroll, L. (2002). "Design of multistable composites for application in adaptive structures." *Composites Science and Technology*, 62(16), 2201-2207.

30. Dano, M. L., and Hyer, M. W. (2003). "SMA-induced snap-through of unsymmetric fiber-reinforced composite laminates." *International Journal of Solids and Structures*, 40(22), 5949-5972.

31. Bettini, P., Riva, M., Sala, G., Di Landro, L., Airoldi, A., and Cucco, J. (2009). "Carbon Fiber Reinforced Smart Laminates with Embedded SMA Actuators-Part I: Embedding Techniques and Interface Analysis." *Journal of Materials Engineering and Performance*, 18(5-6), 664-671.

32. Zhou, G., and Lloyd, P. (2009). "Design, manufacture and evaluation of bending behaviour of composite beams embedded with SMA wires." *Composites Science and Technology*, 69(13), 2034-2041.

33. Kirkby, E. L., O'Keane, J., de Oliveira, R., Michaud, V. J., and Manson, J. A. E. (2009). "Tailored processing of epoxy with embedded shape memory alloy wires." *Smart Materials & Structures*, 18(9).

34. Riva, M., Bettini, P., Di Landro, L., Sala, G., and Airoldi, A. (2009). "Carbon Fiber-Reinforced Smart Laminates with Embedded SMA Actuators-Part II: Numerical Models and Empirical Correlations." *Journal of Materials Engineering and Performance*, 18(5-6), 672-678.

35. Todoroki, A., Kumagai, K., and Matsuzaki, R. (2009). "Self-deployable Space Structure using Partially Flexible CFRP with SMA Wires." *Journal of Intelligent Material Systems and Structures*, 20(12), 1415-1424.

36. Barlas, T. K., and van Kuik, G. A. M. (2010). "Review of state of the art in smart rotor control research for wind turbines." *Progress in Aerospace Sciences*, 46(1), 1-27.

37. Barrett, R., and Vos, R. (2008). "Post-buckled precompressed subsonic micro-flight control actuators and surfaces." *Smart Materials & Structures*, 17(5).

38. Natarajan, A., Kapania, R. K., and Inman, D. J. (2004). "Aeroelastic optimization of adaptive bumps for yaw control." *Journal of Aircraft*, 41(1), 175-185.

39. Barbarino, S., Ameduri, S., Lecce, L., and Concilio, A. (2009). "Wing Shape Control through an SMA-Based Device." *Journal of Intelligent Material Systems and Structures*, 20(3), 283-296.

40. Pinkerton, J. L., and Moses, W. R. (1997). "*A Feasibility Study to Control Airfoil Shape Using THUNDER*." *Rep. No. NASA-97-tm4767*, NASA, Langley Research Centre, NASA Technical Reports Server.

41. Hyer, M. W. (1981). "Some Observations on the Cured Shape of Thin Unsymmetric Laminates." *Journal of Composite Materials*, 15(MAR), 175-194.

42. Bowen, C. R., Butler, R., Jervis, R., Kim, H. A., and Salo, A. I. T. (2007). "Morphing and shape control using unsymmetrical composites." *Journal of Intelligent Material Systems and Structures*, 18(1), 89-98.

43. Seffen, K. A. (2007). "Hierarchical multi-stable shapes in mechanical memory metal." *Scripta Materialia*, 56(5), 417-420.

44. Seffen, K. A. (2006). "Mechanical memory metal: a novel material for developing morphing engineering structures." *Scripta Materialia*, 55(4), 411-414.

45. Hyer, M. W. (1981). "Calculations of the Room-Temperature Shapes of Unsymmetric Laminates." *Journal of Composite Materials*, 15(JUL), 296-310.

46. Kim, K. S., and Hahn, H. T. (1989). "Residual-Stress Development During Processing of Graphite Epoxy Composites." *Composites Science and Technology*, 36(2), 121-132.

47. White, S. R., and Hahn, H. T. (1992). "Process Modeling of Composite-Materials - Residual-Stress Development During Cure .1. Model Formulation." *Journal of Composite Materials*, 26(16), 2402-2422.

48. Schultz, M. R. (2008). "A concept for airfoil-like active bistable twisting structures." *Journal of Intelligent Material Systems and Structures*, 19(2), 157-169.

49. Diaconu, C. G., Weaver, P. M., and Mattioni, F. (2008). "Concepts for morphing airfoil sections using bi-stable laminated composite structures." *Thin-Walled Structures*, 46(6), 689-701.

50. Hufenbach, W., Gude, M., and Czulak, A. (2006). "Actor-initiated snap-through of unsymmetric composites with multiple deformation states." *Journal of Materials Processing Technology*, 175(1-3), 225-230.

51. Schultz, M. R., and Hyer, M. W. (2003). "Snap-through of unsymmetric cross-ply laminates using piezoceramic actuators." *Journal of Intelligent Material Systems and Structures*, 14(12), 795-814.

52. Schultz, M. R., Hyer, M. W., Williams, R. B., Wilkie, W. K., and Inman, D. J. (2006). "Snap-through of unsymmetric laminates using piezocomposite actuators." *Composites Science and Technology*, 66(14), 2442-2448.

53. Mattioni, F., Weaver, P. M., and Friswell, M. I. (2009). "Multistable composite plates with piecewise variation of lay-up in the planform." *International Journal of Solids and Structures*, 46(1), 151-164.

54. Mattioni, F., Weaver, P. M., Potter, K. D., and Friswell, M. I. (2008). "Analysis of thermally induced multistable composites." *International Journal of Solids and Structures*, 45(2), 657-675.

55. Hull, D., and Clyne, T. W. (1996). "An Introduction to composite materials." Cambridge University Press, Cambridge, UK. ISBN:0-521-23991-5

56. Barbero, E. J. (1999). "Introductio nto composite materials design." Taylor and Francis, London, UK. ISBN: 1-56032-701-4

57. Weitsman, Y. (1979). "Residual thermal stresses due to cool-down of epoxy resin composites." *Journal of Applied Mechanics*, 46, 563-567.

58. Kulshreshtha, A. K., and Vasile, C. (2003). "Handbook of polymer blends and composite." Rubber and Plastics Research Association, Shrewsbury, UK.

59. Cairns, D. S., and Adams, D. F. (1983). "Moisture and thermal expansion properties of unidirectional composite materials and the epoxy matrix." *Journal of Reinforced Plastics and Composites*, 2(4), 239-255.

60. Jun, W. J., and Hong, C. S. (1990). "Effect of residual shear strain on the cured shape of unsymmetric cross-ply thin laminates." *Composites Science and Technology*, 38(1), 55-67.

61. Huber, J. E., Fleck, N. A., and Ashby, M. F. (1997). "The selection of mechanical actuators based on performance indices." *Proceedings of the Royal Society of London Series A-Mathematical Physical and Engineering Sciences*, 453(1965), 2185-2205.

62. "MFC Brochure 2010 V3."(2010). http://www.smart-material.com/media/Publications/MFC-brochure_2010_V3.1.pdf Accessed June 15, 2010.

63. Ikeda, T. (1990). "Fundamentals of Piezoelectricity." Oxford University Press, Oxford, UK. ISBN: 0-198-56339-6

64. Desailloud, M. (2004). "Modulus harmonisation of HS & IM tape composite materials." *Rep. No. ESAC_RP0306315*, Airbus Section 530.

65. Williams, B. R., Inman, D. J., and Wilkie.W, K. (2006). "Nonlinear Response of the Macro Fiber Composite Actuator to Monotonically Increasing Excitation Voltage." *J Int Mat Sys Struct*, 17(7), 601.

66. Gude, M., and Hufenbach, W. (2006). "Design of novel morphing structures based on bistable composites with piezoceramic actuators." *Mechanics of Composite Materials*, 42(4), 339-346.

67. Gall, M., Thielicke, B., and Schmidt, I. (2009). "Integrity of piezoceramic patch transducers under cyclic loading at different temperatures." *Smart Materials & Structures*, 18(10), 104009.

68. Sodano, H. A., Park, G., and Inman, D. J. (2004). "An investigation into the performance of macro-fiber composites for sensing and structural vibration applications." *Mechanical Systems and Signal Processing*, 18(3), 683-697.

69. Tressler, J. F. (1998). "Piezoelectric sensors and sensor materials." *Journal of Electroceramics*, 2(4), 257-272.

70. Kell, R. C. (1963). "Modern applications of ferroelectricity." *British Journal of Applied Physics*, 14(5), 249-255.

71. Jaffe, H., and Berlincourt, D. A. (1965). "Piezoelectric transducer materials." 1372-1386.

72. Mason, W. P. (1935). "Electromechanical representation of piezoelectric crystal used as transducer." *Institute of Radio Engineers -- Proceedings*, 23(10), 1252-1263.

73. Daniel, I. M., Wooh, S. C., Sandhu, J. S., and Hamidzada, W. A. (1988). "Acoustographic nondestructive evaluation of composite materials." *Review of Progress in Quantitative Nondestructive Evaluation*, 7A, 325-332.

74. Haertling, G. H. (1999). "Ferroelectric ceramics: History and technology." *Journal of the American Ceramic Society*, 82(4), 797-818.

75. Damjanovic, D., and Newnham, R. E. (1992). "Electrostrictive and piezoelectric materials for actuator applications." *Journal of Intelligent Material Systems and Structures*, 3(2), 190-208.

76. Katzir, S. H. A. U. (2003). "The Discovery of the Piezoelectric Effect." *Archive for History of Exact Sciences*, 57(1), 61-91.

77. Xu, Y. (1991). "Ferroelectric Materials." Noth-Holland, Amsterdam.

78. Cady, W. G. (1964). Crystallography in *Piezoelectricty*. Dover Publications Inc, New York, 9-38. ISBN: 0-488-61094-2

79. Jaffe, B., Cook, W. R. (1971). "Piezoelectric ceramics." Academic Press, London, UK. ISBN: 1-878-907170-3

80. Cross, L. E. (2000). "Domain and phase change contributions to response in high strain piezoelectric actuators." *Fundamental Physics of Ferroelectrics 2000*, 535, 1-15.

81. Berlincourt, D. A., Cmolik, C., and Jaffe, H. (1960). "Piezoelectric properties of polycrystalline lead titanate zirconate compositions." *Institute of Radio Engineers -- Proceedings*, 48(2), 220-229.

82. Jung, H., and Gweon, D. G. (2000). "Creep characteristics of piezoelectric actuators." *Review of Scientific Instruments*, 71(4), 1896-1900.

Chapter 2 - Cured shape prediction of bistable composite laminates including laminate composition.

This chapter aims to develop a modelling approach to predict the cured shape of bistable composites. As part of the work leading to design of an adaptive bump structure (Chapter 7) a modelling technique which can aid in the design of an adaptive bump structure including integrated bistable segments is developed.

In section 2.1 of this chapter published work relevant to the prediction of cured shape for bistable laminates is summarised. It is concluded that finite element modelling techniques offer increased accuracy in cured shape prediction as well as the possibility to be extended to predict behaviour of fully integrated multistable structures. The need to investigate the influence of ply thickness and laminate composition on cured shape of bistable structures is identified.

In section 2.2.1 the experimental techniques and equipment used to characterise the laminate composition in terms of ply thickness and composition are described. Image correlation techniques as well as the laser profilometer used to measure the cured shape of two bistable laminates are presented in section 2.2.2. The observed laminate composition and measured ply thicknesses for a group of $[\theta,90\text{-}\theta]_T$ laminates are presented in section 2.2.3

Section 2.3 describes the development of a finite element model within commercial FE software Ansys V11.0 which accounts for experimentally observed variations in measured ply thickness for the composites manufactured. The model was solved using both idealised and experimentally measured ply thicknesses in order to compare model outputs.

Finite element predictions for cured shape using both idealised and observed laminate composition are presented and compared to experimental data in section 2.4.1. Section 2.4.2 highlights experimentally observed local reversals in laminate curvature and correlates these data with predicted variations in through thickness stress components within the laminate in those regions.

2.1 Introduction

In this section the previously presented analytical and finite element techniques for the prediction of the cured shape of bistable laminates are presented and their utility in the design of an adaptive bump structure assessed.

The phenomenon of bistability in thin asymmetric composite laminates was first analysed by Hyer [1]. The analytical technique developed by Hyer predicts the two discrete deformation states generated by the residual stress fields in square cross-ply laminates [1] as well as the structurally unstable saddle shape described in Chapter 1. In order to predict the two cylindrical deformation states, Hyer extended classical lamination theory [2] to include the geometric non-linearities associated with large deformations of highly curved structures.

A system of 14 non-linear equations was formulated to describe the total strain energy of the laminate in terms of two cylindrical curvatures. The first variation [3] of this system of non-linear equations was minimised using Rayleigh-Ritz minimisation techniques to find the local minima of the energy function and hence the stable states [1].

This early work inspired many investigators to extend Hyer's model first by accounting for in-plane shear stress within the strain energy formulation [4] and later extending the applicability of the model to laminates of arbitrary lay-ups [5]. Subsequent work directly approximated laminate mid-plane strain to simplify computation of total potential energy [6] while maintaining prediction accuracy.

Whilst significant steps have been taken to improve tools and techniques available for the analysis of bistable laminates, the challenges related to analysis of bistable segments integrated with host structures have only recently begun to be addressed [7]. By integrating bistable segments within host structures, variations of lay-up in the plan-form are created. The analysis of the elastic boundary conditions imposed on the bistable segment and the deformation created within the host create significant challenges for analytical tools.

Mattioni [7] presented an analytical model capable of accounting for the influence of a single elastic boundary on an otherwise free laminate. This study removed the assumption of previous analytical models [1, 5, 6] of constant laminate curvature and included a fourth order polynomial approximation to curvature within the model formulation.

The resulting predictions were verified against finite element models with good agreement. While no comparison with experimental data was presented the qualitative prediction of a single elastic boundary demonstrates that in future analytical tools may provide useful insight into integrated bistable segments. Mattioni noted that:

"the integration of bi-stable patches within bigger structures could be a potential solution for the realisation of new structural systems where the requirement of flexibility and stiffness must be combined together."

Despite advances made since Hyer's initial model [1], discrepancies exist between presented analytical models and experimental results [8, 9], even for simple laminates. As observed by several investigators [8, 10], regions of locally reversed curvature occur near the corners and edges of bistable laminates as seen in Fig. 2.1. These localised effects cannot be predicted using analytical techniques based on Hyer's model [8], yet can significantly influence the cured shape of bistable laminates.

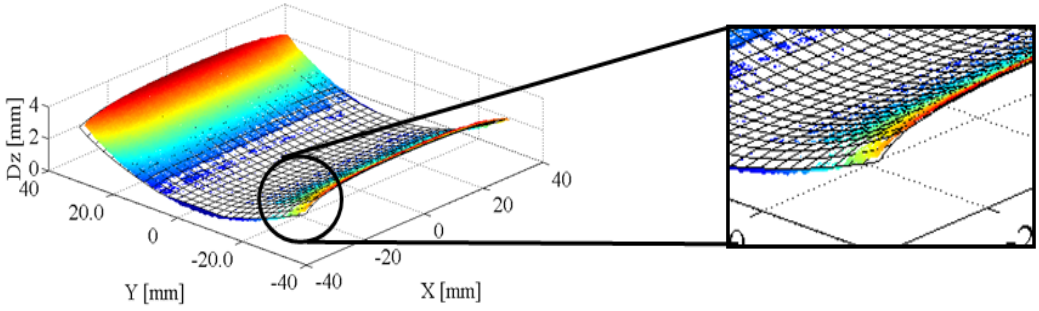

Fig.2.1: Cured shape of $[0/90]_T$ laminate in deformation State B with expanded view of corner region showing localised reversal of cylindrical curvature.

Finite element (FE) techniques have been used to predict the cured shape of bistable laminates with some success, and are capable of predicting edge and corner effects shown in Fig. 2.1 [8, 11, 12], although no explanation of the likely cause of the phenomenon has been proposed.

The presented modelling techniques also require significant user intervention to converge the model to the cylindrical states. Small variations in ply thickness [11], or viscous forces [7] are applied during the solution process to induce the solution algorithm to converge to the chosen deformation state. While these methods are successful in allowing FE codes to predict stable states, the necessity for user intervention and prior knowledge of deformation states limits their use in design activities.

While small variations in ply thickness have been used as a method of forcing solution convergence, to date no finite element analysis has been presented which accounts for variations in laminate composition which occur during manufacture.

Experimental data shows that significant differences in the cured shape and maximum deflection of the two stable states exist [10], however the analytical and finite element analyses predict equal curvature, and hence equal laminate deflection, in both stable states. Whilst the predicted laminate deflections are generally in close agreement with experimental data for a single state, no work to date has been able to predict non-equal curvature of stable states.

Composite laminates will inevitably contain imperfections from the manufacturing process. Common imperfections from the idealised models used to predict their behaviour include; variations in ply thickness, compaction, fibre fraction and ply-angle. It has been shown that small variations in ply-angle can alter the behaviour of bistable laminates during post-cure cooling [13]. However, little is known relating variations in composition and architecture to laminate behaviour.

Considering the gap in the presented literature relating to the influence of laminate composition on the cured shape of bistable composite laminates the aim of this chapter is to characterise the composition and architecture of the $[\theta/90\text{-}\theta]_T$ class of bistable laminates and make full-field measurements of their cured shape.

As described above, the analytical methods based on the Hyer extension to classical laminate theory are not currently able to predict the shapes of completely integrated bistable segments. Furthermore experimentally observed reversals in curvature near to the corners and edges of bistable laminates and the unequal deformation observed in the two stable states are not captured by these methods. Finite element analysis has been shown capable of predicting the behaviour of integrated bistable segments as well as the localised effects which analytical methods cannot. Therefore this chapter will focus on the development of a finite element model of bistable laminates using commercial FE software Ansys V11.0 (Canonsburg, Pennsylvania, USA).

The proposed model will allow the full three dimensional stress fields in regions of localised reversal of curvature observed near corners and edges of thin bistable laminates to be studied. Measured laminate composition such as ply-thickness, determined by optical microscopy will be included in the model formulation to represent imperfections within the

manufactured composites with the aim of accurately predicting laminate deflection in both stable states.

In the following section the methods used in the characterisation of laminate composition and cured shape are described.

2.2 Experimental techniques

This section presents the experimental techniques used to determine the laminate composition and cured shape of two bistable composite laminates. Section 2.2.1 describes the lay-up and curing procedure used to manufacture the experimental laminates. Section 2.2.2 describes the optical microscopy conducted to measure laminate composition and presents the measured ply-thickness. Motion capture techniques and laser profilometry measurements used to determine cured shape are described in section 2.2.3.

2.2.1 Laminate composition and cured shape measurement

Two sample laminates were manufactured from 268gsm T800/M21 pre-preg material, the first measuring 75mm×75mm with a $[0/90]_T$ lay-up and the second measuring 150mm×150mm with a $[-30/60]_T$ lay-up.

Pre-preg material was cut by hand to a size 10mm larger than the desired laminates on each side. These plies were then laid onto an aluminium table covered in release film before the second plies were added on top. A further layer of release film was added before two layers of breather material were laid down and the laminates sealed within a vacuum bag as seen in Fig. 2.2.

The breather layers were included to ensure even vacuum could be drawn throughout the bagged area. Once the laminates were sealed within this vacuum bag, the table was placed inside an autoclave and cured using a single-dwell cure cycle with a curing temperature of 180˚C as specified for the M21 resin system. Laminate temperature during the cure cycle was monitored using a thermocouple embedded between the composite plies.

After curing, the laminates were trimmed to the desired sizes, removing resin-poor areas and defects introduced by thermocouple placement from the edges of the laminate.

Since the laminates were placed on a flat metallic surface within the autoclave, the side in contact with the surface has a smooth finish while the opposite side has a thin textured layer of resin which bleeds from the top ply and cures on the surface. The presence of this thin resin layer will be included within the model to be discussed in section 2.3.

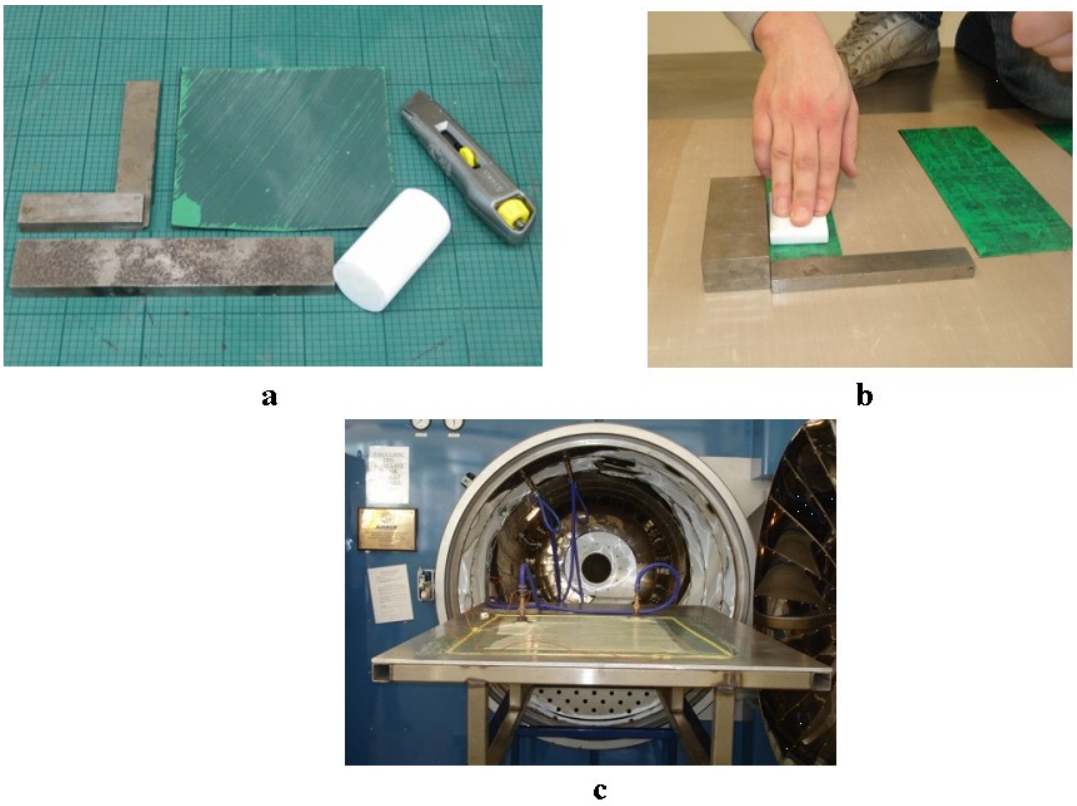

Fig.2.2: Photographs showing equipment used to cut pre-preg segments (a), lay-up and compaction (b) and completed vacuum bag ready for the autoclave (c).

2.2.2 Measurement of laminate composition

To characterise the resin layer and mean ply thickness, three optical microscopy specimens measuring 15mm×10mm were prepared from the material trimmed from the edges of both laminates. These samples were then set in epoxy resin and digitally photographed using a Nikon Eclipse Iv150 optical microscope with a Q-imaging 3.3RTV digital camera attachment. Images were taken at three points along the length of each sample and the mean ply-thickness across all specimens calculated using Image (U.S Institutes of Health, Bethesda, USA) image processing software. The standard deviation of ply-thickness was also calculated.

Fig. 2.3 shows typical images from optical microscopy of a $[0/90]_T$ laminate. The nominal thickness of the initial composite pre-preg was 0.25mm, suggesting an 'idealised' laminate thickness of 0.5mm. The thickness of the total laminate and individual plies differ from idealised values in the range ±6%. An uneven layer of resin on the uppermost surface of the laminate is also visible in Fig. 2.3, the lower face is pressed against the composite tool during curing and is therefore has very little surface texture. The observed resin layer varies

randomly in thickness between negligible thickness and 0.08mm over the entire surface of the laminate.

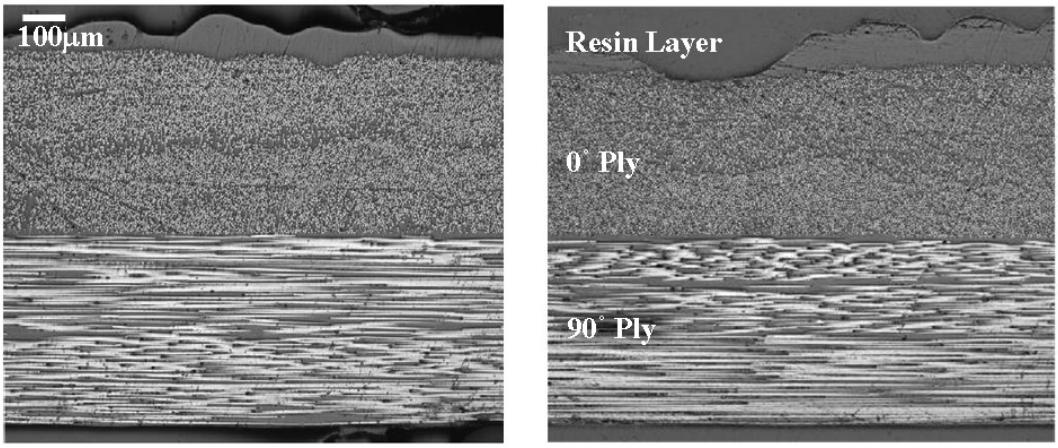

Fig.2.3: Two sample images showing composition for T800/M21 $[0/90]_T$ laminate. White scale bar in (a) is 100μm.

By measuring laminate composition of cross-ply bistable laminates and incorporating this information into a finite element model this chapter aims to clarify the role of imperfections introduced during manufacture and their influence on the cured shape of bistable laminates. Observed discrepancies in the maximum laminate deflection between the two stable states [10, 14] have yet to be predicted using finite element techniques. However recent work by Betts [15] has used an extended analytical model to demonstrate that ±2% variation in ply thickness results in ±4.6% variation in predicted laminate deflection in the two stable states.

Table 2.1 shows the mean and standard deviation of ply thickness and total laminate thickness for a range of manufactured laminates with ply angles of $[\theta/\theta+90]_T$. The mean values presented in Table 2.1 were used to specify layer thickness values within the element formulation of the 'improved model' (i.e. the model which incorporates experimentally measured values of ply-thickness).

Table 2.1: Mean and standard deviation (σ) of ply and total laminate thickness for $[\theta/\theta+90]_T$ laminates made from 268gsm M21/T800.

	Idealised	Improved	
	Thickness (mm)	**Thickness (mm)**	**σ**
θ˚ ply	0.25	0.255	0.013
θ +90˚ ply	0.25	0.233	0.018
Resin layer	0	0.027	0.021
Total	0.5	0.515	0.045

Section 2.2.3 below describes the laser profilometry techniques used to measure the cured shape of the 75mm x 75mm laminate and the image correlation techniques used to characterise the 150mm x 150mm laminate.

2.2.3 Measurement of cured shape

Cured shape of the 75mm x 75mm $[0/90]_T$ sample at room temperature of 22˚C was assessed via laser profilometry, generating 3D-coordinates defining the laminate surface. A Scantron Proscan 2000 laser profilometer was used to record laminate surface height relative to a datum-plane at nodes on a 300 μm step grid to maximise the number of data points across the laminate while ensuring data files remained below the maxim,um size imposed by the acquisition software. using the laser profilometer measurement resolution of 1μm was achieved over the measurement range. These raw data were then normalised against the datum plane to create the surface coordinates of the deformed laminate in both stable states.

Surface data was read into Matlab 2007a and an interpolated surface generated using a spline based method [16] available within the Matlab interpolation options.

The cured shape of the $[-30/60]_T$ laminate at room temperature of 22˚C was measured using Peak Motus® (Peak Performance, Colorado, USA); Motion capture system to provide a non-contact measurement of the spatial coordinates of 147 reference-points applied to the laminate seen in Fig 2.4a and 2.4b.

Three digital video camera recorders (Sony DCR-TRV 900E, Sony Corporation, Japan) operating at 50 fields per second were set up in an umbrella configuration [17] around the

experimental area. As in Fig. 2.5 camera 1 was always positioned to view this area from a high position with the centre of the lens positioned 2.19 m away from the origin of the experimental volume at a height of 1.86 m.

The other two cameras indicated in Fig. 2.5 were repositioned between measurements of the two deformation states so that best possible viewing angle was always achieved without compromising the umbrella configuration. The height and locations of cameras varied so that cameras were not all in the same plane in accordance to recommendations by Nigg et al. [17] and all reference markers were visible to at least two of the cameras.

In order to calibrate the motion capture system a calibration object was manufactured to provide known coordinates to act as reference coordinates for calibration. A space frame cuboid measuring 200mm × 200mm × 100mm was constructed from 2mm welding rod into the structure shown inset of Fig. 2.5.

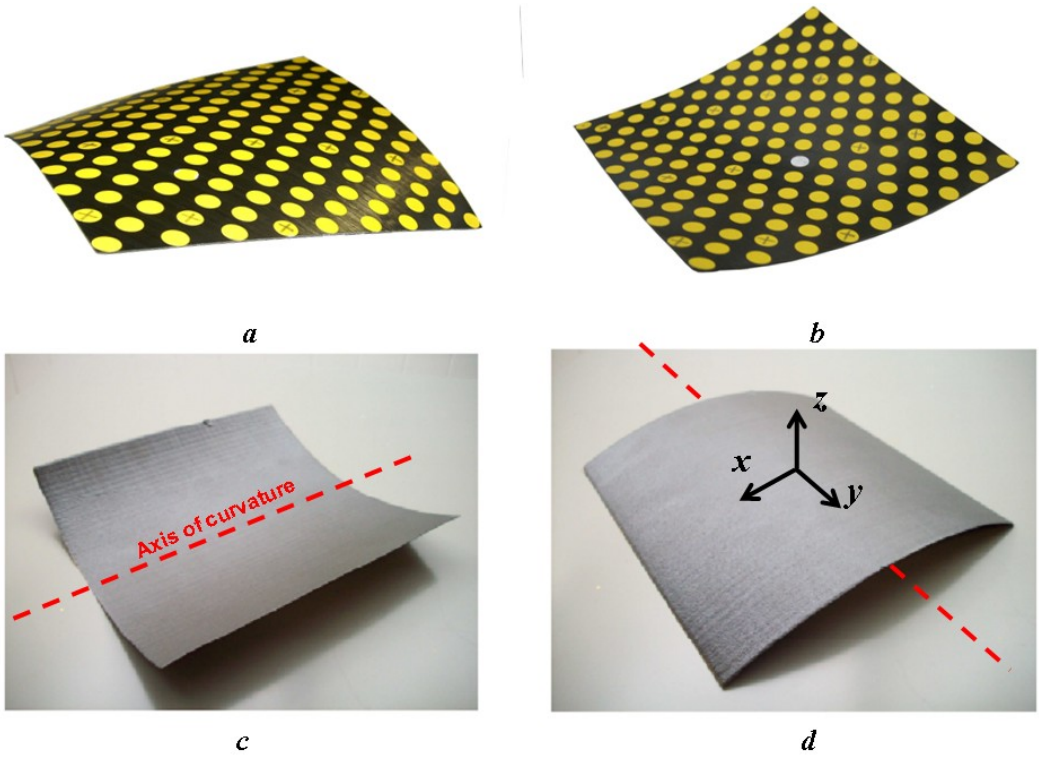

Fig.2.4: $[-30/60]_T$ laminate in stable State A (*a*) and State B (*b*) with reference markers for motion capture seen on the upper surface with $[0/90]_T$ laminate shown with global coordinate system in State A (*c*) and State B (*d*).

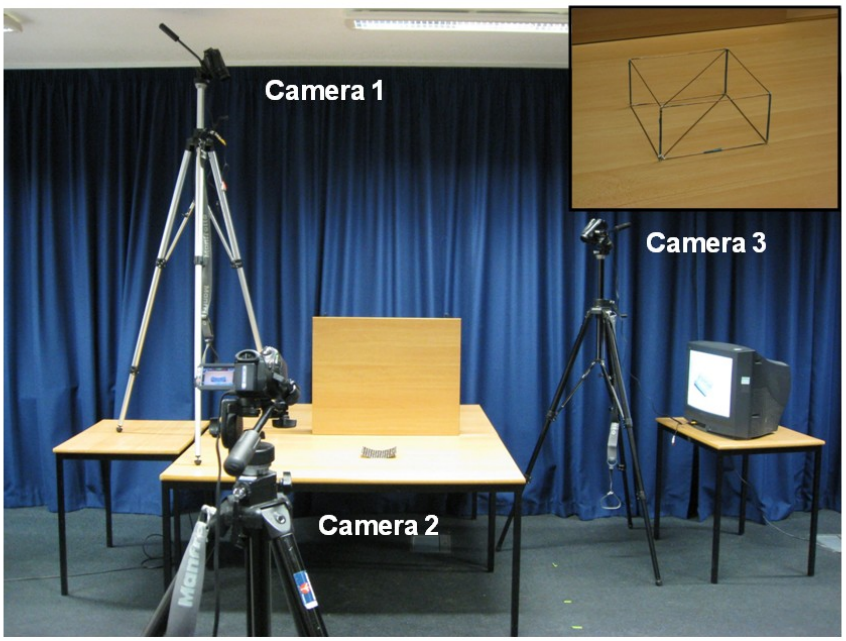

Fig.2.5: Camera setup used to generate images for measurement of cured shape, inset shows frame constructed for use as calibration object for Peak Motus® software.

The coordinates of the calibration object vertices were measured using vernier callipers and a measurement table. The camera views were restricted to a volume just slightly larger than the calibration frame to give a digitised area measuring 1440 × 1152 pixels. A video clip was taken of the calibration frame with the cameras in each setup before the frame was removed and the laminates positioned at the centre of the calibrated volume.

A short video clip was taken for each of the deformation states and these digital images transferred to Peak-Motus® motion analysis system (v. 8.5, Vicon, USA) to map the spatial coordinates of the reference markers. Before digitising the reference marker locations, the eight corners of the calibration wire frame were manually digitised from each camera view and for each camera set up. Following digitisation of the calibration frame, the centre of each of the 147 reference markers and the four corners of the each laminate were manually digitised from all three camera views.

Pixel locations for the reference markers were combined with the pixel locations of the calibration frame vertices for each camera view to transform the digitised pixel information to Cartesian co-ordinates of the laminate surfaces using Direct Linear Transformation method [18, 19]. Once the transformation was complete, the mean of the RMS error between the calibration co-ordinates and the respective digitised points of both camera set ups were 0.2 mm in each of the orthogonal co-ordinate directions.

Coordinates produced using motion capture techniques are irregularly spaced across the laminate surface, and are exported from Peak Motus® as three column-vectors *x, y* and *z*.

Irregularly spaced spatial-coordinates were imported into Matlab 2007a and the coordinates transformed so that the laminate centre point was located at the origin of the coordinate system. The coordinates were then rotated to match the coordinate system orientation of the finite element data to allow comparison.

Delaunay triangulation of the rotated coordinates was used to form an irregular surface-mesh before a continuous surface of the form $Z_i = f(X_i, Y_i)$ was fitted to this mesh using spline-based interpolation [16]. The matrix $[X_i, Y_i, Z_i]$ therefore describes the interpolated surface-approximation to the raw coordinates.

In the following section a finite element model is developed using commercial finite element software Ansys V11.0 to predict the cured shape of the experimental specimens.

2.3 Finite element modelling

Commercial finite element software Ansys V11.0 was used to predict the cured shape of bistable composite laminates and to include the influence of the observed variations in laminate composition described in section 2.2.2. Section 2.3.1 describes the model formulation and solution procedure used to generate coordinates describing the surface profile of two bistable laminates with lay-up of $[0/90]_T$ and $[-30/60]_T$ for comparison with the experimental data is described in section 2.3.2.

2.3.1 Model formulation

Predictions of cured shape for the manufactured laminates were made using the FE software Ansys V11.0. Models were created using 20-node brick elements SOLID186 [20] which allow layers to be defined through the element thickness to represent the different plies of the manufactured composite. SOLID186 elements use quadratic displacement functions to approximate displacement between nodes, improving solution accuracy for highly curved geometries. This is particularly important in view of the highly curved cured shape of the bistable composites. The material within a layer and the orientation of any anisotropic properties may be varied between layers to accurately model composites without increasing the number of elements used. This provides scope to model the $[0/90]_T$ and $[-30/60]_T$ lay-up as well as laminates with more complex lay-up.

The materials properties of the cured T800/M21 pre-preg material and resin layer are shown in Table 2.2 where subscripts *1* and *2* denote longitudinal and transverse direction in the plane of the fibre and *3* the thickness direction. Subscript *r* denotes properties of the bulk M21 resin system. The presented data was taken from an Airbus technical report [21] in which the elastic constants for cured unidirectional pre-preg tape identical to that used for this work was determined from experimental characterisation. Standardised coupon testing was conducted in accordance with Airbus standard procedures [21, 22] to generate the data presented in table 2.2. Material and processing parameters were identical to those used in the production of the materials data therefore further coupon testing to verify the data was deemed unnecessary.

Table 2.2: Elastic properties of 268gsm^{-1} T800/M21 material from Airbus technical report [21], * indicates values calculated using stress-strain relations described in [23].

Property [*unit*]	Value
E_1 [GPa]	172
E_2 & E_3 [GPa]	8.9
G_{12} & G_{23} [GPa]	4.2
G_{23}* [GPa]	0.0225
ν_{12} & ν_{13}	0.35
ν_{23}*	0.01
α_1 [1×10^{-7}]	-0.9
α_2 & α_3 [1×10^{-5}]	3
E_r [GPa]	1.5
ν_r	0.4
α_r [1×10^{-5}]	9
Density [kgm^{-3}]	1072

The mean-ply thicknesses determined by optical microscopy were entered as layer thicknesses with corresponding ply-orientations in the SOLID186 element definition. Measured values for ply thicknesses may be seen in table 2.1. To fully represent the architecture of the laminates the excess resin layer was included in the element definition with materials properties outlined in table 2.2.

As seen in fig 2.3, the excess resin layer was shown to be highly irregular and discontinuous, with thickness reducing to zero in many locations. The discontinuous nature of the layer must significantly influence the in-plane residual thermal stress state within the resin layer. Near the free-surface of a discontinuity the in-plane stress resultants normal to the free-surface within the resin layer must reduce to zero in order to satisfy equilibrium at the surface. Hence, mean in-plane stress of the layer must be reduced.

To date no relation between the extent of surface texture and the change in resulting residual thermal stresses has been published in and hence the reduction in mean in-plane stress resultants caused by local edge-effects was approximated by reducing the Young's modulus of the resin layer.

A micromechanical FE-model of the resin layer including a representative surface texture would be one method of predicting the influence of resin discontinuities however such work falls outside the scope of this thesis. Due to the lack of supporting research in the literature, this effect was approximated by reducing the Young's modulus of the resin layer by 50% to 1.5 GPa.

This approximation to resin modulus has proven reliable across several further test laminates but prediction accuracy on resin layer elastic modulus. The author suggests further investigation into the influence of surface texture on the development residual thermal stresses would be of interest.

A sensitivity analysis on the effect of resin elastic modulus was conducted, with deflection shown to be proportional to resin modulus with difference between predicted and experimentally measured values of maximum laminate deflection increasing to 19% with fully stiff resin layer from 6.8% when modelled using the approximated value.

Laminates were modelled and meshed using SOLID186 elements of aspect ratio 4.85 (element dimensions were 2.5mm×2.5mm×0.515mm) for all models. A global change in temperature of (ΔT) was applied to all nodes in the model to simulate a cool down from the 180˚C cure temperature to a temperature matching the relevant experimental conditions. It is important to note that the NLGEOM option of Ansys static solution was implemented to include geometric non-linearities in the calculation of laminate deformation; NLGEOM specifies the use of rotated element coordinate system in the formulation of the element stiffness matrix.

As seen in Fig. 2.6 when the laminate is deformed the local coordinate system of the element must rotate so that the *xy*-plane remains co-planar with the mid-plane of the deformed element. If the element *xy*-plane remains fixed, the in-plane stiffness of the element changes as a function of the element rotation which does not occur in the physical specimen.

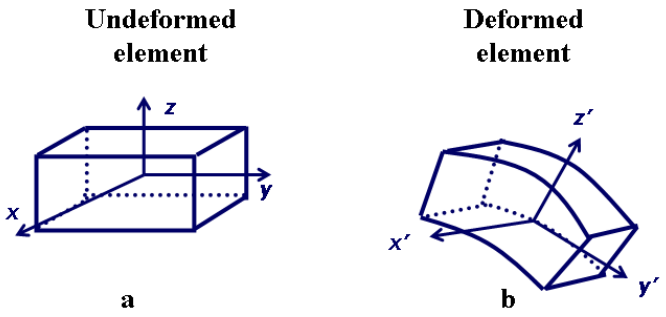

Fig.2.6: Element coordinate system shown with *xy*-plane co-planar with mid surface of layered element before deformation (a) and after bending deformation (b).

Two types of FE models were developed to demonstrate the improvements to prediction accuracy made by inclusion of measured laminate composition. Firstly an 'idealised model' was formulated which used the initial nominal ply-thickness (0.25mm) used to fabricate the laminates in the element definition and did not include the resin layer. The idealised model did not converge to the cylindrical states without a temporary mechanical force being applied during the first 0.1˚C of cooling.

The 'improved model' used the measured ply thickness from the optical microscopy shown in table 2.1 and included the presence of the resin rich layer (as indicated in Fig. 2.3) in the element definition. No external loads or imperfections were required since the through thickness discrepancy in ply thickness and the presence of the resin layer were sufficient imperfections to achieve convergence.

The stable cylindrical state with the largest value of maximum deflection was designated State A as shown in Fig 2.4a; this is the state where the resin-layer lies on the concave surface. State B shown in Fig. 2.4b is the secondary state, showing reduced maximum deflection and the resin layer on the convex surface. The 'improved model' converged to deformation State A without externally imposed imperfections or loads. This independent convergence to the experimentally observed dominant state improves upon work by previous investigators [8, 12, 24, 25] by reducing operator intervention during solution.

The laminate models were mechanically constrained from translation in all three orthogonal directions at the origin of the global coordinate system shown in Fig. 2.4d. Additionally the node at the point (0,0,0.515) was constrained from in-plane translation to ensure the laminate did not rotate about either the *x* or *y*-axis.

2.3.2 Model solution

With a mechanical constraint applied the model was solved with the temperature constraint in place to simulate cool down from curing temperature. A nonlinear static analysis was performed with the line search convergence control option activated using the LNSRCH command to enable Ansys to follow the correct load path during laminate snap-through.

Non-linear finite element analysis with Ansys V11.0 relies upon the Newton-Raphson iterative solution procedure to solve the set of non-linear equation generated by element discretisation [26]:

$$\left[K_i^T\right]\left\{\Delta u_i\right\} = \left\{F^A\right\} - \left\{F_i^{nr}\right\} \tag{2.1}$$

$$\left\{u_{i+1}\right\} = \left\{u_i\right\} + \left\{\Delta u_i\right\} \tag{2.2}$$

where K is the tangent coefficient matrix, u the vector of unknown degrees of freedom, F the vector of applied loads and F^{nr} the vector of restoring loads corresponding to internal forces within the element. Subscript i relates to values calculated for the current iteration [27] (cited in [26]).

For example in a structural analysis K^T is the tangent stiffness matrix [Nm^{-1}], u_i the displacement vector [m] and F^{nr} the restoring force vector [N] calculated from internal stresses within the deformed elements.

Beginning from a known initial condition (u_0 in Fig. 2.7), the tangent stiffness matrix K^T and restoring force vector F^{nr} are calculated and the first approximation to the change in displacement vector (Δu_i) computed and added to u_0. Using the resulting displacement vector (u_i) both K^T and F^{nr} are recalculated and a new value for Δu_i computed and added to u_i to produce u_{i+1} as seen in Fig. 2.7.

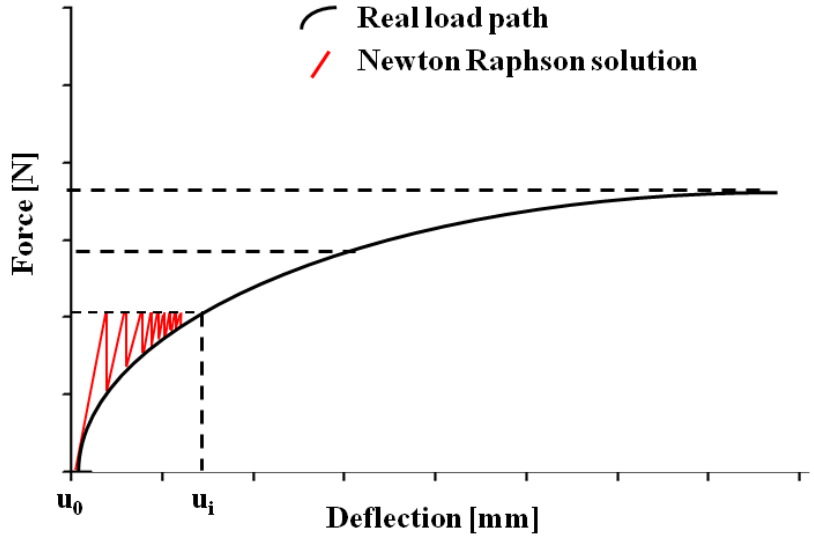

Fig.2.7: Incremental Newton-Raphson solution method showing iterative solution of non-linear equation.

The iterative solution process continues updating u_i until the resulting restoring force vector matches the vector of applied loads to within a specified tolerance as in [27]:

$$\|\{R\}\| < \varepsilon_R R_{ref} \tag{2.3}$$

where ε is the convergence tolerance, R a specified reference value and

$$\|\{R\}\| = \left(\sum R_i^{\,2}\right)^{1/2} \tag{2.4}.$$

When using line search convergence control the approximation to the change in displacement vector (Δu_i) is scaled by a scalar factor s so that:

$$\{u_{i+1}\} = \{u_i\} + s\{\Delta u_i\} \tag{2.5}$$

The scaling factor s is determined by finding the zeroes of the non linear equation:

$$g_s = \{u_i\}^T\left(\{F^a\} - \{F^{nr}(s\{\Delta u_i\})\}\right) \tag{2.6}$$

where g_s is the gradient of the total potential energy of the model with respect to s [27]. The zeroes of equation 2.5 correspond to minima in the potential energy of the model. Hence in models where potential energy varies rapidly with respect to applied load, as in

snap-through of a bistable composite, step size will reduce thus improving stability of convergence [28].

Once the parameter *s* has been determined using equation 2.6 the scaled value for Δu_{i+1} is calculated using equation 2.5 and used in the standard Newton-Raphson equation 2.1 for calculation of Δu_{i+2}. Although the additional computational cost of using the *LNSRCH* solution option slows convergence, solution stability is significantly improved compared to a standard Newton-Raphson solution.

After the initial thermal load step converged, the laminate remained in the first stable state (State A). To fully determine the shape profile of both states it was necessary to 'snap' the bistable laminate to the second stable state (State B). In order to achieve this within the FE model a displacement constraint was applied to the corner nodes of the laminate.

The corner nodes were constrained in the *z*-direction (as seen in Fig. 2.4d) so that displacement in that direction was of equal magnitude but of opposite sign to their displacement in State A (Fig. 2.4a). Displaced nodes were free to move in the *xy*-plane and laminate translation was constrained by the central constraint described above. Once the displaced solution converged, the displacement constraints were removed and the model relaxed into stable State B (Fig. 2.4b).

In each state through-thickness shear stresses (γ_{xz} and γ_{yz}) expressed in the rotated element coordinate system were read into a .CSV file and plotted against the corresponding nodal coordinate. The element coordinate system must be selected to correctly assess the stress acting through the laminate thickness and not those acting in the global coordinate system.

In order to compare FE predictions to experimentally measured laminate shapes the deformed nodal coordinates were calculated within ANSYS by summing undeformed nodal coordinates with the respective displacements in the three orthogonal directions. The APDL code file used to create, solve and post process the presented FE model of the $[0/90]_T$ laminate is shown in Appendix 1.

The surface fitting procedure described in section 2.2.3 was used to create a regularly spaced matrix of laminate surface coordinates as the calculated nodal coordinates were not regularly spaced in the global *xy*-plane.

This section has described the finite element model formulated to predict cured shape of bistable composite laminates and the data processing required to create appropriate data sets. In section 2.4.1 the predicted values of laminate deflection will be compared to the

measured values. Section 2.4.2 presents data which suggests that through thickness stress components play a key role in the formation of local reversals of curvature near the laminate edges.

2.4 Results

In this section experimental observations on the cured shape of the two bistable laminates described in section 2.2 will be presented and the presence of localised reversals of curvature will be highlighted. The experimental measurements of laminate deflection in both deformation states will be presented and compared with the finite element (FE) predictions of cured shape.

Section 2.4.2 will seek to explain the proposed link between variations in the through thickness stress components within the laminates and the observed reversals of curvature at the edges of the laminates. The importance of including full three-dimensional stress information within calculations of cured shape for bistable laminates is highlighted and the specific variations in through thickness stress and shear stress components which lead to the cured shape of test laminates is explained.

2.4.1 Cured shape and finite element prediction

The cured shapes of the $[0/90]_T$ laminate measuring 75mm×75mm and the $[-30/60]_T$ measuring 150mm×150mm were predicted using the FE model described in section 2.3. Fig 2.8 shows the observed cured shape of both the $[-30/60]_T$ and the $[0/90]_T$ laminate in States A and B. State A is defined as the state where the excess resin layer lies on the concave face, whereas in State B the resin layer lies on the convex face.

These two states are generally described as cylindrical shapes with constant curvature of opposite sign about unique axes of curvature. In reality their shape is only approximated by a constant curvature and it will be shown in this section that there exist significant deviations from this constant cylindrical curvature.

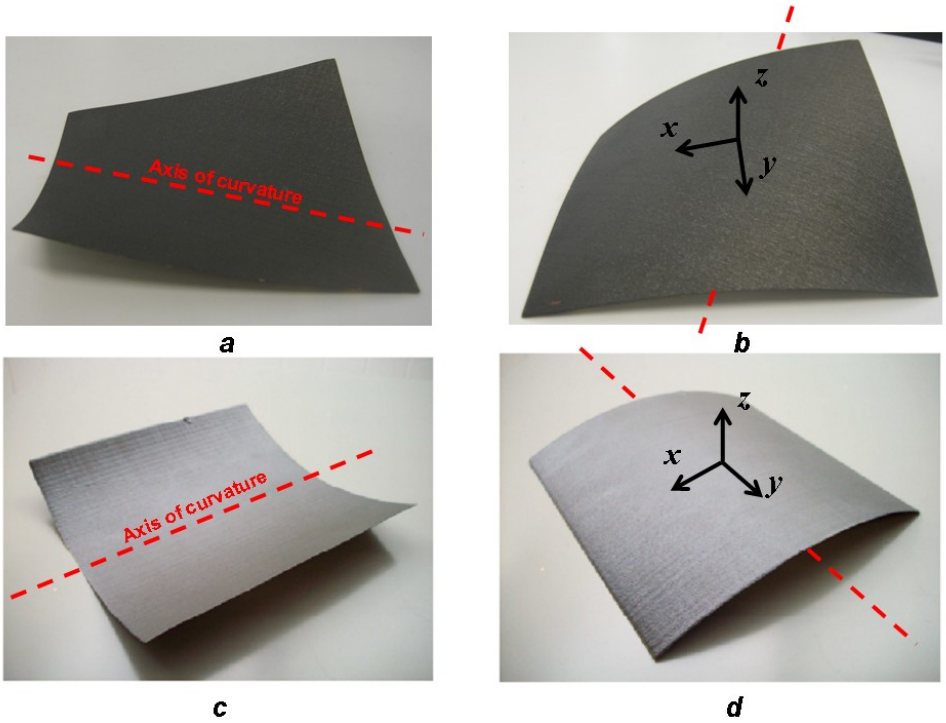

Fig.2.8: $[-30/60]_T$ bistable laminate shown in State A (a) and State B (b), $[0/90]_T$ laminate in State A (c) and State B (d).

Fig 2.9 shows the interpolated surface plot of laminate profile based on laser profilometry coordinates. The interpolated FE-predicted surface is overlaid as a mesh. Fig. 2.9 shows predicted shape is in good agreement with experimental measurement in terms of overall profile as well as capturing regions of reversed curvature near the edges and corners of the laminate which will be discussed in section 2.4.2. Maximum deflection (D_{max}) is also indicated in Fig. 2.9 and is defined as the maximum displacement in the z-direction relative to the centroid of the undeformed laminate.

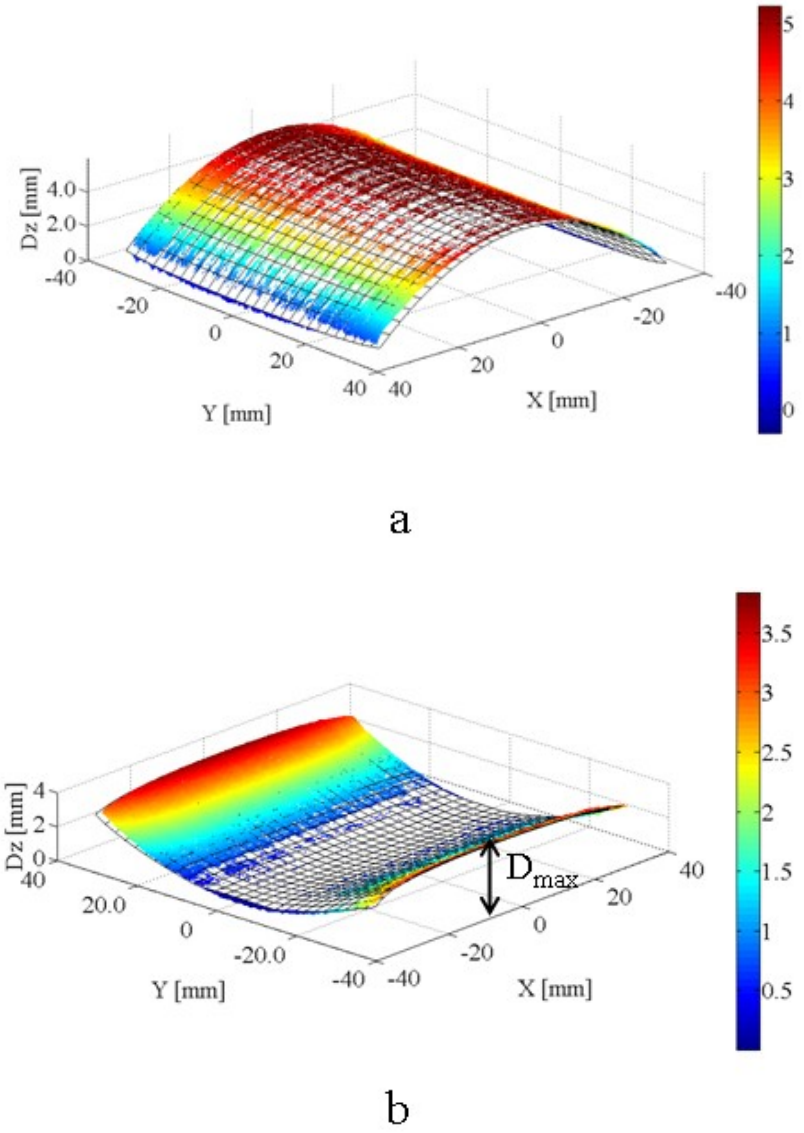

Fig.2.9: Surface plot of experimental measurements for cured shape of 75mm×75mm $[0/90]_T$ laminate in State A (a) and State B (b) with FE-predicted values overlaid as a mesh. Experimental surface is shaded according to laminate deflection D_z with maximum laminate deflection D_{max} indicated.

Fig 2.10 shows the interpolated surface based on the experimental measurement of the $[-30/60]_T$ laminate with the FE-predicted profile overlaid as a mesh. Agreement between FE predictions and experimental measurements for overall laminate shape is good and localised reversals of curvature near the corners of the laminate are well captured. However, at point A in Fig. 2.10 it can be seen that there exists some discrepancy between FE prediction and experimental measurement. Near to the point of maximum deflection the FE predicted surface shows less deformation than is observed in the experiment data.

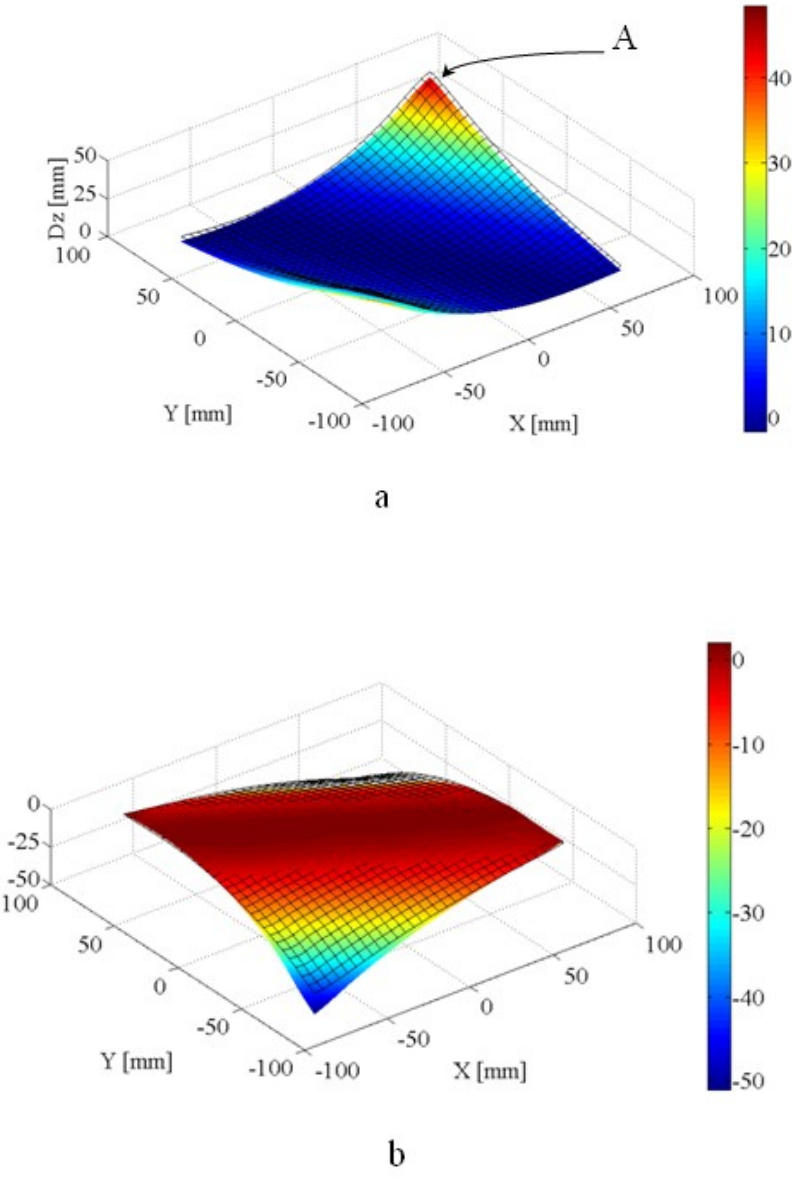

Fig.2.10: Interpolated surface plot of experimental measurements for State A cured shape of 150×150mm $[-30/60]_T$ laminate shaded according to laminate deflection D_z with FE-predicted values overlaid as a mesh.

Experimentally measured maximum deflection (D_{max}) in States A and B were not of equal magnitude in all laminates. States A and B should theoretically be of equal magnitude if the individual ply thicknesses were exactly 0.25mm. In both cases the observed deflection was the greatest in State A, in which the thermal contraction of the excess resin layer acts to increase D_{max} by increasing curvature. It was also observed during manufacture that all laminates cooled into State A immediately after curing.

Table 2.3 summarises all the experimental and modelling data and compares the measured maximum deflections of the $[0/90]_T$ and $[-30/60]_T$ laminates with those predicted by the 'idealised' and 'improved' FE models.

The 'improved model' which includes measured ply-thicknesses resin rich layer converged to State A without the use of temporary forces in the solution process as described in section 2.3, thus reducing user intervention in the FE-solution process. As seen in table 2.3 the inclusion of measured ply thickness values in the FE-model definition also improved prediction accuracy for maximum laminate deflection in both deformation states.

The difference in deflection between states A and B was well modelled by the inclusion of measured ply thicknesses within the FE-model. As seen in table 2.3, the variation in predicted laminate deflection using 'improved model' is in good agreement with the observed change in deflection between the two states for both laminates.

Table 2.3: Maximum deflection (D_{max}) for states A and B of 75×75mm^2 $[0/90]_T$ and 150×150mm^2 $[-30/60]_T$ laminates.

Bistable Laminate	Experimental Data [mm]		Idealised Model [mm]		Improved Model [mm]	
	State A	State B	State A	State B	State A	State B
$[0/90]_T$	5.12	3.55	3.76	3.76	4.98	3.53
$[-30/60]_T$	45.11	38.22	34.88	34.88	42.04	33.49

Peak error between FE predicted laminate deflection values using the 'improved model' and experiment is seen for the $[-30/60]_T$ laminate. FE predicted values for D_{max} being 6.8% and 12.4% below those measured for State A and State B respectively. Peak error for FE-predicted values of laminate deflection of the $[0/90]_T$ laminate are 2.7% and 0.05% for State A and B respectively. Laminate profile is very well predicted by the improved model for both laminates, with accurate reproduction of the local reversal of curvature near the edges and corners of the laminate.

By comparison, the 'idealised' FE-model underestimated D_{max} by 22.7% for State A and 8.7% for State B when forced to converge to the cylindrical deformation states. However as discussed in section 2.1, in order to converge to the cylindrical deformation states temporary mechanical forces were applied during model solution. Without this user intervention predicted laminate deflection values were underestimated by 71.9% for State A. More importantly no second stable state was predicted and laminate profile did not show a single axis of curvature but rather two superposed curvatures.

It was shown that the reduction in FE-predicted laminate deflection was not due to restricted degrees of freedom within the FE model since a further refinement of the mesh did not significantly increase predicted deflection. However, Betts [15] recently observed that a 2% discrepancy in individual ply thickness caused a change of up to 4.6% in predicted laminate deflection for cross-ply bistable laminates.

As shown in table 2.1, the standard deviation of ply thickness values is significant in comparison to the actual ply thickness. For example the first layer shows a mean ply thickness of 0.233mm with a standard deviation (σ in table 2.1) of 0.013mm (5% of total ply thickness). Assuming a normal distribution of ply thickness values, it is likely that 32% of laminate area will show variations in ply thickness of more than 5%. This spatial distribution of ply thickness variation may introduce additional residual stresses not accounted for in the FE model.

Furthermore this variability of laminate composition, and specifically resin layer thickness, may significantly alter the influence of the observed resin layer. The 50% reduction in Young's Modulus of the resin layer imposed to approximate changes to residual thermal stresses within the resin layer may prove important in further refinement of the proposed model. In the absence of any relevant micromechanical models in the literature the complex task of accurately assessing the influence of the resin layer should form part of future work in this area.

Due to the variability in laminate composition and the hand lay-up techniques used in manufacturing experimental samples it is likely that a combination of small inaccuracies in the values of ply thickness, sample geometry and materials properties have combined to create the observed maximum error of 12.4% in FE-predicted laminate deflection. In future work it may improve prediction accuracy to individually measure laminate composition for all experimental samples.

Despite peak errors of 12.4% between FE-modelling results and experimental measurements it has been shown that inclusion of laminate composition within FE-model definition improves qualitative prediction of laminate behaviour. Model predictions of convergence to State A during manufacture matches the experimentally observed behaviour without the need for user intervention to force convergence unlike previous studies [8, 12].

2.4.2 Edge and corner effects

Previous observations by Hyer [29] and Potter [10] have identified significant deviations from otherwise constant curvature near to the laminate edges and corners of bistable laminates as indicated in Fig. 2.12 and 2.15. In these regions the global curvature reverses to a greater extent than could be explained by the normal anticlastic curvature caused by Poisson's ratio effects. As shown in the preceding section similar localised effects were observed in the cured shape of the test laminates with the modelling capturing the local curvature reversal well. This section analyses the observed corner effects and correlates them with variations in the through thickness stress components.

Fig. 2.11a shows a surface plot of *xz*-shear stress (γ_{xz}) across the lowermost ply of the $[-30/60]_T$ laminate shown in Fig. 2.11b. Large variations in through thickness shear stresses are seen near to the corner regions and especially the (-75,-75,0) corner indicated in Fig. 2.11. These variations in shear stress occur in the same regions which experience rapid reversal of curvature causing the laminate to flatten near to the y = 75mm edge as indicated in Fig. 2.12.

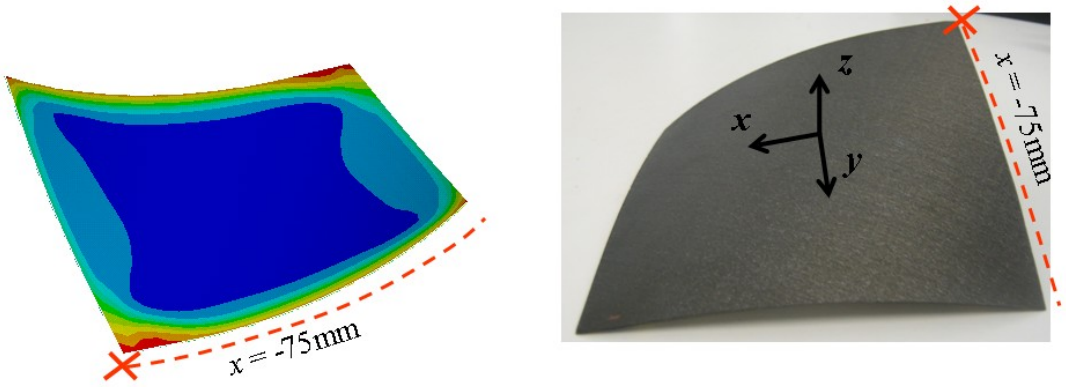

Fig.2.11: Surface plot of FE-predicted variation in γ_{xz} stress across the upper surface of the $[-30/60]_T$ laminate(a) and image from experimental laminate (b) x = -75mm line and (-75,-75,0) point marked by dashed line and × in both images. *(Laminate shown inverted in (a) for clarity).*

FE-predicted values for laminate deflection (*D)* along the x = -75mm edge of the $[-30/60]_T$ laminate are seen as a function of y-coordinate in Fig. 2.12 along with the corresponding values for *xz* and *yz*-shear stress components (γ_{xz} & γ_{yz}).

The edge plot in Fig. 2.12 shows the strong correlation between the observed reversal of curvature and the variation in through thickness shear stress components present within the lowermost ply of the laminate. Between y = -60mm and y = 60mm γ_{xz} and γ_{yz} remain approximately constant at around 45MPa and 10MPa respectively. However near to the free edges wide variations in both components is observed with γ_{xz} increasing and γ_{yz} decreasing in magnitude as they near the y = -75mm free-edge.

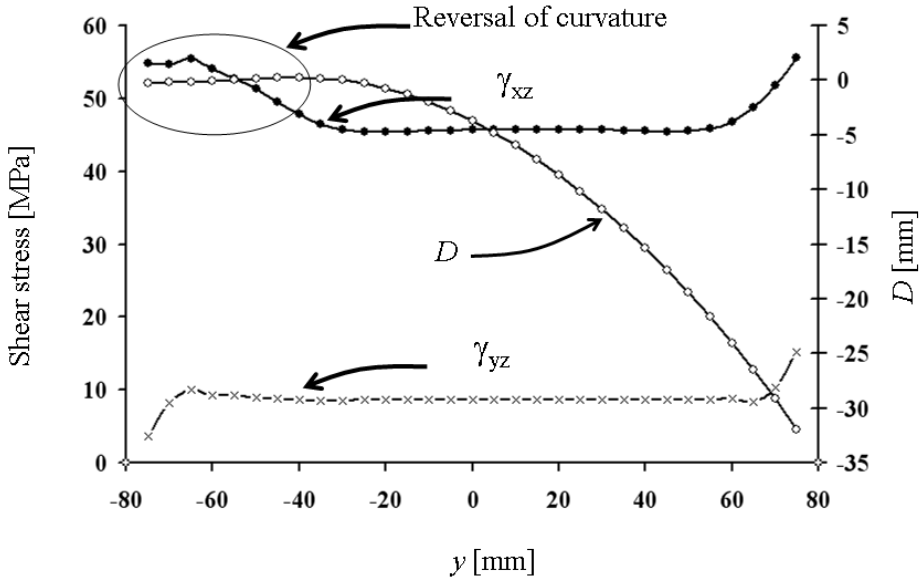

Fig.2.12: *xz* and *yz*-shear stresses (γ_{xz} & γ_{yz}) and deflection (*D*) along the x = -75mm free-edge of the $[-30/60]_T$ laminate as a function of *y*-coordinate.

Fig. 2.13 shows the variation of through thickness stress component (σ_z) along the y = -75mm free-edge of the $[-30/60]_T$ laminate as a function of *y*-coordinate. As observed previously a sharp increase in stress magnitude occurs near to the free-edges of the laminate, with both y = -75mm and y = 75mm edge experiencing σ_z values approximately 15% higher than those seen away from the edges.

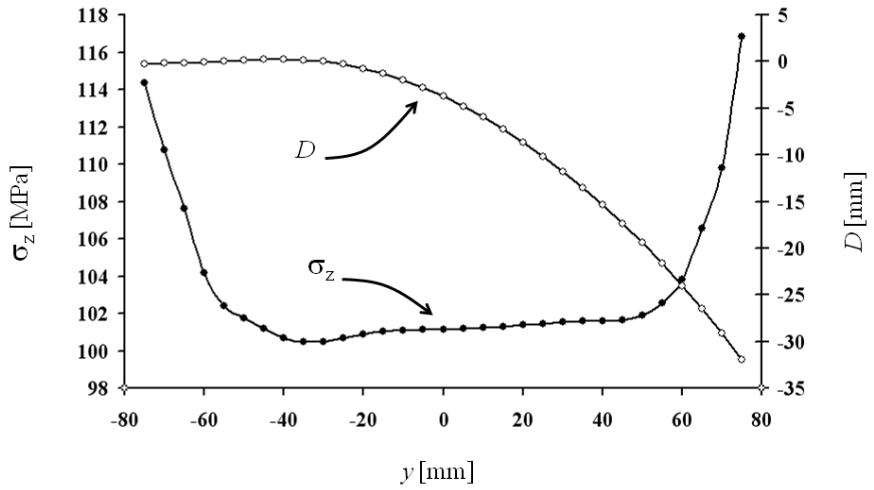

Fig.2.13: Through thickness stress component (σ_z) and deflection (D) along the x = -75mm free-edge of the $[-30/60]_T$ laminate as a function of y-coordinate.

It should be noted that at the y = 75mm free edge there is no observed reversal of curvature in the y-direction despite significant increases in magnitude of both through thickness shear components and σ_z.

Pronounced reversal of curvature near to the corners and edges of the $[0/90]_T$ laminate were also observed in the manufactured composite and correlate with variations in the through thickness shear stress components. Localised reversal of curvature was not most prominent at the corners of the $[0/90]_T$ laminate. However a significant edge effect was observed at both the y = -37.5mm and y = 37.5mm edges as seen in Fig. 2.9.

Fig. 2.14 shows a surface plot of the xz-shear stress component (γ_{xz}) within the uppermost ply of the laminate with significant variations seen in the regions near to the x = 37.5mm and x = -37.5mm edges. The laminate is shown inverted for clarity. Fig. 2.15a shows a graph of laminate deflection D and γ_{xz} stress along the y = 22.5mm line of the $[0/90]_T$ laminate with 2.15b showing a detailed view of the region near to the x = 37.5mm edge.

It is clear that the variations in through thickness shear stress occur at exactly the locations where maximum change in curvature is observed. Peak values for γ_{xz} were two orders of magnitude lower than those shown in Fig. 2.14. The yz-shear stress component (γ_{yz}) did not show similar variations in magnitude to those observed in γ_{xz}.

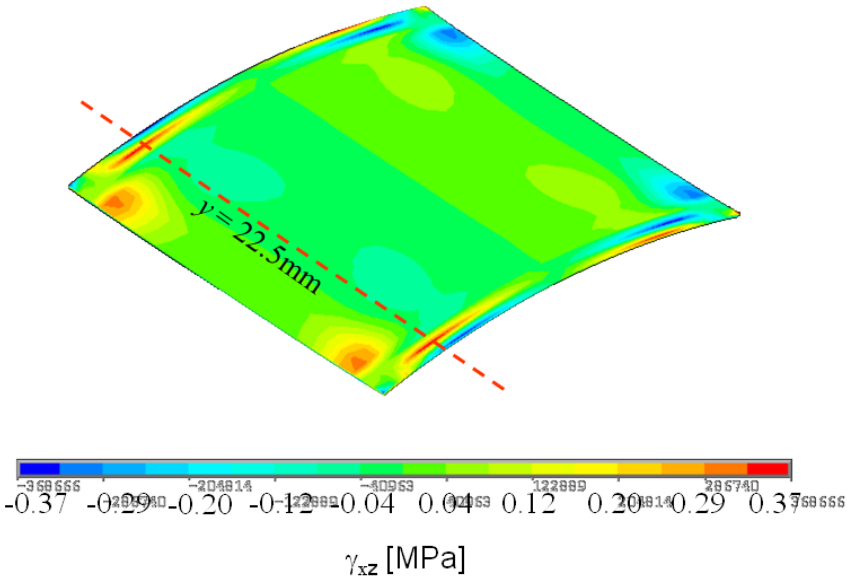

Fig.2.14: Surface plot of FE-predicted variation in γ_{xz} stress across the upper surface of the $[0/90]_T$ laminate. *(Laminate shown inverted for clarity).*

These variations in local through *xz*-shear stress correspond well to the observed reversal of curvature near the free-edges of the laminate, however in the $[0/90]_T$ laminate there were also significant variations in the through thickness stress σ_z which are thought to contribute to the observed edge effect.

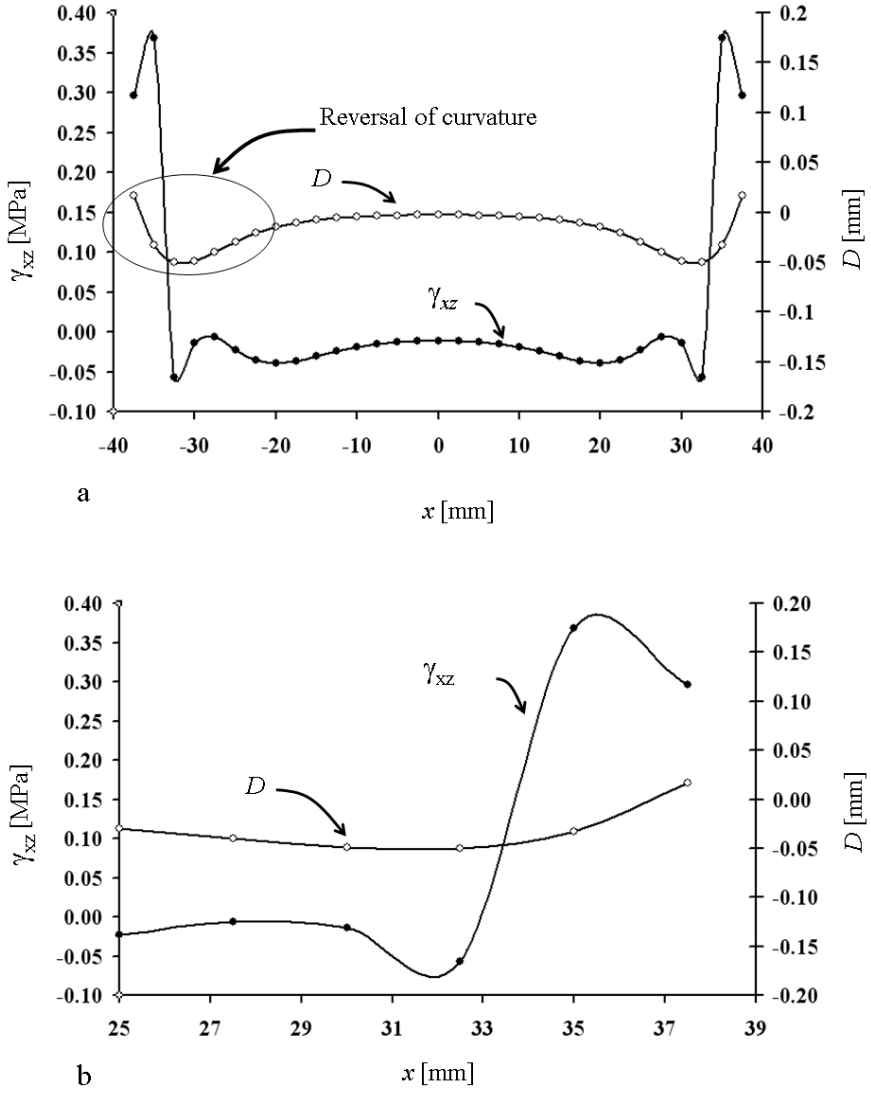

Fig.2.15: a) *xz*-shear stress (γ_{xz}) and laminate deflection (*D*) at the *y* = 22.5mm free-edge of the $[0/90]_T$ laminate as a function of *x*-coordinate. b) Expanded view of the region near to *x* = 37.5mm edge.

Fig. 2.16 shows a surface plot of the through thickness stress component (σ_z) within the uppermost ply of the laminate with significant variations seen in the regions near the *x* = 37.5mm and *x* = -37.5mm edges. Fig. 2.17a shows a graph of laminate deflection *D* and σ_z stress along the *y* = 0mm line of the $[0/90]_T$ laminate where maximum variations in this quantity are shown. Fig 2.17b shows a detailed view of the region near to the *x* = 37.5mm edge. Peak values for σ_z are two orders of magnitude higher than peak shear stress

magnitudes within the same laminate (Fig. 2.15) and hence it is thought that variations in the through thickness stress σ_z component are the dominant cause of the edge effect in the $[0/90]_T$ laminate.

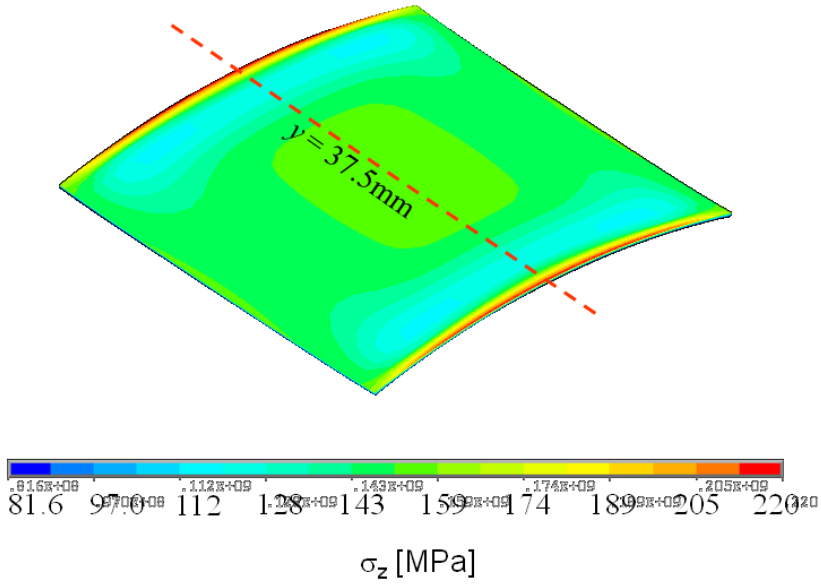

Fig.2.16: Surface plot of FE-predicted variation in σ_z stress component across the upper surface of the $[0/90]_T$ laminate. (*Laminate shown inverted for clarity***).**

In both $[-30/60]_T$ and $[0/90]_T$ laminates regions of significant variation in through thickness stress components correspond to the locations maximum reversal of curvature approaching the free-edges. It is logical to conclude that the observed regions of reverse curvature are a direct result of the rapid variation in stress state in these regions.

This phenomenon occurs because in-plane residual thermal stresses within the laminate must satisfy equilibrium at the free-edges. Therefore in-plane stress resultants normal to the free-surface must reduce to zero at the free-edge, however by doing so the overall stress state of the laminate in that region. The variations in through thickness and shear components observed in Fig. 2.11 – 2.17 occur in order to maintain equilibrium of forces within the laminate.

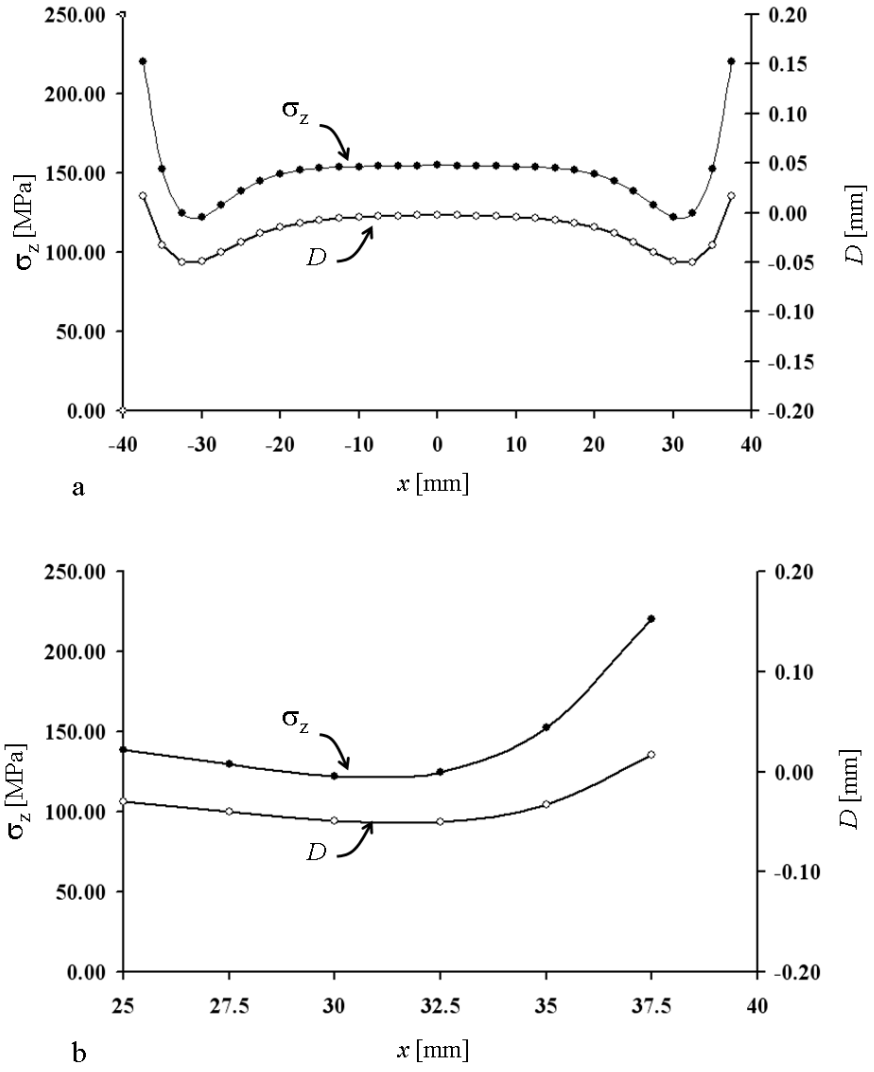

Fig.2.17: *xz*-shear stress (σ_z) and laminate deflection (*D*) along the *y*=37.5mm plane of the $[0/90]_T$ laminate as a function of *x*-coordinate (a) and expanded view of the region near to *x* = 37.5mm edge (b).

Finite element models using solid elements are well adapted to analysing this three dimensional stress State and in further work would allow more detailed assessment of the role that through thickness stresses play in the cured shape of bistable composites, including inter-laminar stresses. This detailed analysis of cured shape is not possible using analytical methods based on Hyer's non-linear extension to classical lamination theory as all through thickness stresses are considered equal to zero and therefore these edge effects are not predicted.

2.5 Conclusion

This chapter has characterised the composition and architecture of bistable laminates using optical microscopy in conjunction with digital image processing to aid in the design of morphing structures.

The key conclusions drawn from this chapter were as follows:

- Laminate composition for $[\theta/90\text{-}\theta]_T$ laminates was measured and both individual ply and total laminate thickness were seen to deviate by up to 6% from idealised values.
- A residual resin layer which cures on the surface of the laminate was identified with 0.027mm thickness and standard deviation of 0.021mm.
- A finite element model including the measured laminate composition was implemented to predict maximum laminate deflection to within 12.5% of experimental measurements.
- The presented FE model accurately predicts localised reversals of curvature which are closely correlated with variations in the through-thickness stress components σ_z, γ_{xz} and γ_{yz}.

The presence of an excess resin layer was identified and ply-thicknesses within two-ply cross ply laminates measured and compared to idealised laminate models. Both individual ply and total laminate thickness were seen to deviate by up to 6% from idealised values.

Cured shapes for a 75x75mm $[0/90]_T$ were measured using laser profilometry and those of a 150x150mm $[-30/60]_T$ laminate were determined via Peak Motus® motion capture software. Peak deflection (D_{max}) was not equal in both stable states, rather a dominant state was observed in which D_{max} was greater; this state corresponded with the excess resin layer being at the concave surface of the curved laminate. Localised reversal of curvature near the edges and corners of the laminates was observed with both effects strongest with the laminate in State B.

A Finite Element (FE) model including the observed laminate composition was described and implemented within commercial FE software ANSYS V11.0 to predict the cured shapes of the test laminates. This improved FE model captured the inequality in State A and B deflection and predicted values for maximum laminate deflection for both laminates

agreed with experimental measurements to within 12.5% as compared with errors ranging between 7 and 72% for FE models using idealised laminate composition.

The 'improved model' converged to the cylindrical State A without externally imposed imperfections or loads, in contrast to work by other investigators. This preferential adoption of State A after cooling from cure temperature was also observed in the experimental samples.

The improved FE-model accurately predicted the occurrence and magnitude of localised reversals of laminate curvature near to the edges and corners of the experimental samples. These edge effects were shown to be related to localised increases in the through thickness stress components. It is not possible to predict the observed edge effects using the laminated plate theory prevalent in the analysis of bistable laminates [1, 4, 30] and although promising work continues to be presented in the field of shell theories to predict bistable behaviour [9], these techniques are not yet established in this field.

The presented finite element model has significantly improved both qualitative and quantitative prediction of the cured shape of bistable laminates. In addition the often observed localised reversal of curvature has been linked with variations in the through-thickness stress components σ_z, γ_{xz} and γ_{yz}.

The FE-model described in this chapter is of interest as a design and scoping tool for multi-stable structures where accurate prediction of each stable state is of importance. Further work extending the FE model to include piezoelectric actuation and to allow multistable elements embedded within host structures is presented in Chapters 4 and 6 respectively.

2.6 Reference list

1. Hyer, M. W. (1981). "Calculations of the Room-Temperature Shapes of Unsymmetric Laminates." *Journal of Composite Materials*, 15, 296-310.
2. Hull, D. (1981). "An Introduction to Composite Materials." Cambridge University Press, Cambridge, England. ISBN: 0-521-38190-8
3. Strong, G. (1986). "Introduction to Applied Mathematics." Cambridge Press. ISBN: 0-961-40880-4
4. Jun, W. J., and Hong, C. S. (1990). "Effect of residual shear strain on the cured shape of unsymmetric cross-ply thin laminates." *Composites Science and Technology*, 38(1), 55-67.
5. Jun, W. J., and Hong, C. S. (1992). "Cured Shape of Unsymmetric Laminates with Arbitrary Lay-Up Angles." *Journal of Reinforced Plastics and Composites*, 11(12), 1352-1366.

6. Dano, M. L., and Hyer, M. W. (1998). "Thermally-induced deformation behavior of unsymmetric laminates." *International Journal of Solids and Structures*, 35(17), 2101-2120.

7. Mattioni, F., Weaver, P. M., and Friswell, M. I. (2009). "Multistable composite plates with piecewise variation of lay-up in the planform." *International Journal of Solids and Structures*, 46(1), 151-164.

8. Schlecht, M., Schulte, K., and Hyer, M. W. (1995). "A comparative study for the calculation of the temperature dependent shapes of unsymmetric laminates based on finite element analysis and extended classical lamination theory." *Mechanics of Composite Materials*, 31(3), 247-254.

9. Pirrera, A., and Weaver, P. M. (2009). "Geometrically Nonlinear First-Order Shear Deformation Theory for General Anisotropic Shells." *AIAA Journal*, 47(3), 767-782.

10. Potter, K., Weaver, P., Seman, A. A., and Shah, S. (2007). "Phenomena in the bifurcation of unsymmetric composite plates." *Composites Part A: Applied Science and Manufacturing*, 38(1), 100-106.

11. Portela, P., Camanho, P., Weaver, P., and Bond, I. (2008). "Analysis of morphing, multi stable structures actuated by piezoelectric patches." *Computers & Structures*, 86(3-5), 347-356.

12. Mattioni, F., Weaver, P. M., Potter, K. D., and Friswell, M. I. (2008). "Analysis of thermally induced multistable composites." *International Journal of Solids and Structures*, 45(2), 657-675.

13. Hamamoto, A., and Hyer, M. W. (1987). "Nonlinear Temperature-Curvature Relationships for Unsymmetric Graphite-Epoxy Laminates." *International Journal of Solids and Structures*, 23(7), 919-935.

14. Hyer, M. W. (1981). "Some Observations on the Cured Shape of Thin Unsymmetric Laminates." *Journal of Composite Materials*, 15, 175-194.

15. Betts, D. N., Salo, A. I. T., Bowen, C. R., and Kim, H. A. (2010). "Characterisation and modelling of the cured shapes of arbitrary layup bistable composite laminates." *Composite Structures*, 92(7), 1694-1700.

16. Sandwell, D. T. (1987). "Biharmonic Spline Interpolation of Geos-3 and Seasat Altimeter Data." *Geophysical Research Letters*, 14(2), 139-142.

17. Nigg, B. M., and Cole, G. K. (2007). "Optical methods." *Biomechanics of the musculo-skeletal system*, W. Herzog, ed., John Wiley and Sons, Chichester, 362-391.

18. Abdel-Aziz, Y. I., and Karara, H. M. (1971). "Direct linear transformation from comparator coordinates into object space coordinates in close-range photogrammetry." Proceedings of the ASP/IU symposium on close-range photogrammetry. ASP/IU symposium on close-range photogrammetry 1971. 1-116.

19. Wood, G. A., and Marshall, R. N. (1986). "Accuracy of DLT extrapolation in three-dimensional film analysis." *Journal of Biomechanics*, 19(9), 781-785.

20. Ansys Inc. 2007. Composite materials modelling guide, Ansys user help reference System V11.0.

21. Desailloud, M. (2004). "Modulus harmonisation of HS & IM tape composite materials." *Rep. No. ESAC_RP0306315*, Airbus Section 530.

22. Risse, L. (2003). "Module Harmonisation of unidirectional HS composite materials." *Rep. No. L00D03000275*, Airbus UK Ltd, Section 530.

23. Hyer, M. W. (1998). "Stress Analysis of Fibre Reinforced Composite Materials." WCB/McGrawhill, Boston, Mass. ISBN: 1-932-07886-X

24. Schultz, M. R., and Hyer, M. W. (2003). "Snap-through of unsymmetric cross-ply laminates using piezoceramic actuators." *Journal of Intelligent Material Systems and Structures*, 14(12), 795-814.

25. Schultz, M. R., Hyer, M. W., Williams, R. B., Wilkie, W. K., and Inman, D. J. (2006). "Snap-through of unsymmetric laminates using piezocomposite actuators." *Composites Science and Technology*, 66(14), 2442-2448.

26. Ansys Inc . 2007. Structures with geometric non-linearities. Chapter 3. Ansys Theory Reference V11.0.

27. Bathe, K. (1982). "Finite element procedures in engineering analysis." Prentice-Hall, London. ISBN: 0-133-01458-4

28. Schweizerhof, K. H., and Wriggers, P. (1986). "Consistent linearization in non-linear FE analysis." *Computer Methods in Applied Mechanics and Engineering*, 59(3), 261-279.

29. Hyer, M. W. (1982). "The Room-Temperature Shapes of 4-Layer Unsymmetric Cross-Ply Laminates." *Journal of Composite Materials*, 16, 318-340.

30. Schlecht, M., Schulte, K., and Hyer, M. W. (1995). "Advanced Calculation of the Room-Temperature Shapes of Thin Unsymmetric Composite Laminates." *Composite Structures*, 32(1-4), 627-633.

Chapter 3 - Finite element modelling of Macro Fibre Composite actuators

In this chapter work conducted to create a finite element model of a commercially available macrofibre composite (MFC) piezoelectric actuator within ANSYS V11.0 software will be described. The goal of this model will be to accurately predict the actuation capability of MFCs when bonded to composite structures. Homogenised properties describing device behaviour will be formulated by aggregation of micro-scale features of the actuator to form a representative solid model. Once validated, in the following chapter the MFC model will then be integrated with the bistable composite model described in Chapter 2 to predict piezoelectrically actuated snap-through without introducing unnecessary micro-scale details and therefore decreasing computational cost.

Section 3.1 describes the construction and key functional elements of the MFC actuator before surveying the published literature relating to finite element modelling of MFC actuation. In section 3.2 three-dimensional matrices describing device stiffness (E), Piezoelectric (d_{ij}) and relative permittivity (ε) will be formulated and used to define a set of material properties for an electromechanically coupled solid model of the active portion of the MFC.

In section 3.3, appropriate mechanical and electrical constraints of the MFC are identified and an FE model described to predict the deflection of an isotropic beam under MFC actuation. The derived materials properties are validated through comparison of FE predictions to experimental data for deflection of the actuated beam in section 3.4.

3.1 Introduction

MFC actuators consist of polycrystalline piezoelectric ceramic fibres embedded in an epoxy matrix, with copper interdigitated electrodes bonded to top and bottom surfaces. The piezoelectric ceramic used for the fibres in commercially available products is a lead zirconate titanate (PZT), usually PZT-5A since this is a 'soft' PZT which exhibits high piezoelectric d_{33} and d_{31} coefficients and therefore high strain per unit electric field. Research is being conducted into high-strain single crystal PMNT (Lead Magnesium Niobium Titanate) [1] as well as lead free piezoelectric ceramic fibres, although these technologies are not at present ready for market.

The actuators used in this work were sourced from Smart Materials GmbH (Dresden, Germany), with the high-strain type-P1 MFC actuators and comprise rectangular cross-section PZT fibres embedded within a structural epoxy. The ceramic fibres are machined from a tape-cast sheet of bulk ceramic of 0.2mm thickness [2, 3]. The flat upper and lower surfaces of these rectangular fibres improve electrical contact between fibre and electrode surfaces hence improving actuator performance as compared to fibres with circular cross section as used in an active fibre composite or AFC shown in Fig. 3.1 [3, 4]. Fig. 3.1 shows the fibres, resin and interdigitated electrodes which comprise the active portion of the AFC with fibre, resin and electrode components marked, in macrofibre composites the structure is identical, except PZT fibres are rectangular in cross section.

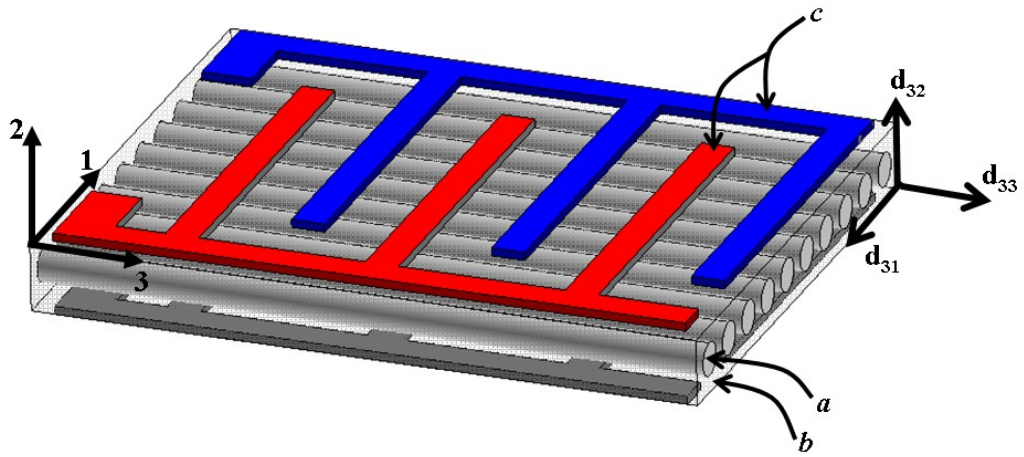

Fig.3.1: Schematic of an AFC actuator showing unidirectional PZT fibre alignment (a), epoxy matrix (b), interdigitated electrodes (c) and orientation of AFC material coordinate system (*figure adapted from Williams et al.[5]***).**

To enhance resistance to harsh environments and ensure electrical insulation of the active portion, the fibre composite and electrodes are encased between polymer films to create the finished actuator. When this encapsulation is included the final thickness of the MFC increases to approximately 0.3mm [6].

In order to generate the high strain per unit field of modern MFC actuators, it is necessary to align the poling direction of the ceramic along the fibre length and subsequently apply the electric field parallel to the poling direction. Aligning poling and field directions ensures that the desired actuation strain is generated via the d_{33} coefficient which is typically twice the d_{31} coefficient [7].

Fig 3.2 shows cross sectional view of an MFC with the direction of the applied electric field resulting from the interdigitated electrode arrangement. The applied electric field is only well aligned with the fibre direction for a portion of the electrode spacing with significant volumes of ceramic being poled, and excited by electric field not running parallel with the *3*-axis of the MFC coordinate system.

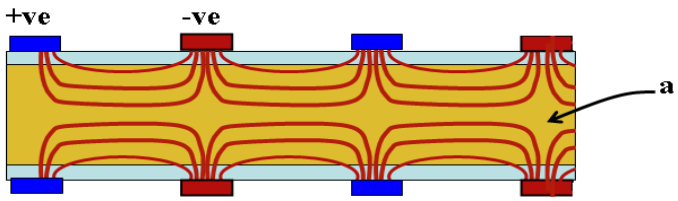

Fig.3.2: Electric field lines created within an MFC by excitation using interdigitated electrodes showing wide variability in field direction and dead-zones (a) which are not exposed to significant electric field underneath each electrode.

Efforts to model the microscopic behaviour of the constituent materials of the MFC are ongoing with several institutions producing interesting results using both finite element [8, 9] and analytical techniques [1, 10, 11]. While these efforts bring insight into the underlying mechanisms of MFC function and provide tools to aid in actuator design (optimising electrode placement and fibre shape etc.) the level of complexity inherent in this micromechanical modelling is too computationally expensive for integration within a larger macro-scale structural model such as a bistable composite. Therefore in this chapter, material properties which represent the actuation behaviour of the complete MFC actuator will be developed to create a solid model to predict MFC actuation performance.

In addition to increased actuation strain created by the interdigitated electrode pattern, this electrode arrangement also brings benefits in terms of damage tolerance. Because electric

field is applied at regular intervals along the fibre length, fractures in the fibre or electrode only reduce the functionality of a small region surrounding the defect and do not significantly reduce global actuator performance [5].

The materials properties of an MFC are anisotropic due to (i) the aligned unidirectional piezoelectric fibres and (ii) the anisotropic elasticity of poled ferroelectric materials such as PZT caused by alignment of their atomic structure as described in Chapter 1. Because of this anisotropy a full three dimensional formulation for these properties is necessary with appropriate values specified for each of the three orthogonal directions (1,2 and 3) shown in Fig. 3.1. The specification of these anisotropic materials properties will be described in section 3.2.

Electrical boundary conditions significantly influence the apparent stiffness of piezoelectric structures under mechanical loading [7]. When subjected to mechanical stress a piezoelectric solid will develop a potential difference (voltage) between opposite boundaries of the solid via the direct piezoelectric effect according to [12]:

$$D = dT + \varepsilon^T E \tag{3.1}$$

where D is the induced electric displacement [Cm^{-2}], d the piezoelectric charge constant [pmV^{-1}], T the applied stress [Nm^{-2}], ε^T the relative permittivity under constant stress [Fm^{-1}] and E the electric field strength [Vm^{-1}].

This potential difference and accompanying electric displacement causes a resistive stress within the volume via the converse piezoelectric effect according to [12]:

$$T = c^D S - hD \tag{3.2}$$

where T is the induced stress [Nm^{-2}], c^D the elastic stiffness at constant electric displacement [Nm^{-1}], D is the electric displacement [Cm^{-2}] and h the piezoelectric constant defined as:

$$h_{ij} = -\left(\frac{\partial T_i}{\partial D_j} \right)^s \tag{3.3}$$

As total mechanical stress within a solid is the sum of all imposed stress fields [13] this resistive stress increases the apparent stiffness of the material. This dependence of material stiffness upon the electrical boundary conditions requires that the relative permittivity (or

dielectric constant ε) of the material be included within the material properties definition to enable the full constitutive equations for a piezoelectric solid (equation 3.1) to be solved.

Under open circuit boundary conditions the boundaries of the volume are electrically isolated (Fig. 3.3) and so the potential difference is not dissipated, leading to the increase in apparent stiffness described above. By contrast, closed circuit boundary conditions electrically connect charge collecting surfaces, dissipating the developed potential difference, hence neither the induced electric field nor corresponding piezoelectric stress are generated.

Equation 3.4 shows the relationship between the closed circuit or constant field compliance (s^E) and open circuit or constant electric displacement compliance (s^D) both expressed in Pa^{-1} [13]. These two quantities are related via the square of the electromechanical coupling coefficient (k^2) which is defined as the ratio of stored electrical energy to supplied mechanical energy in the case of a piezoelectric solid subjected to mechanical loading.

$$1-k^2 = s^D \Big/ s^E \tag{3.4}$$

As k^2 is always positive and less than unity [13], it follows from equation 3.4 that the closed circuit compliance will always be greater than the open circuit compliance. Hence under the same loading a piezoelectric solid under closed circuit conditions would deform more than when under open circuit conditions, as shown in Fig. 3.3. Based on a typical value for piezoelectric coupling coefficient k for PZT-5A of ~0.7 [14], the open circuit stiffness of the MFC is approximately twice the closed circuit stiffness. This change in actuator stiffness leads to significantly smaller deformation of a beam with an MFC actuator under open circuit versus closed circuit electrical boundary conditions as illustrated in Fig. 3.3.

Despite significant interest in the use of MFC actuators in structural actuation schemes [15-17] little work has been presented which adequately captures the change in actuator stiffness caused by the dependence of actuator stiffness on electrical boundary conditions during actuation of bistable composites.

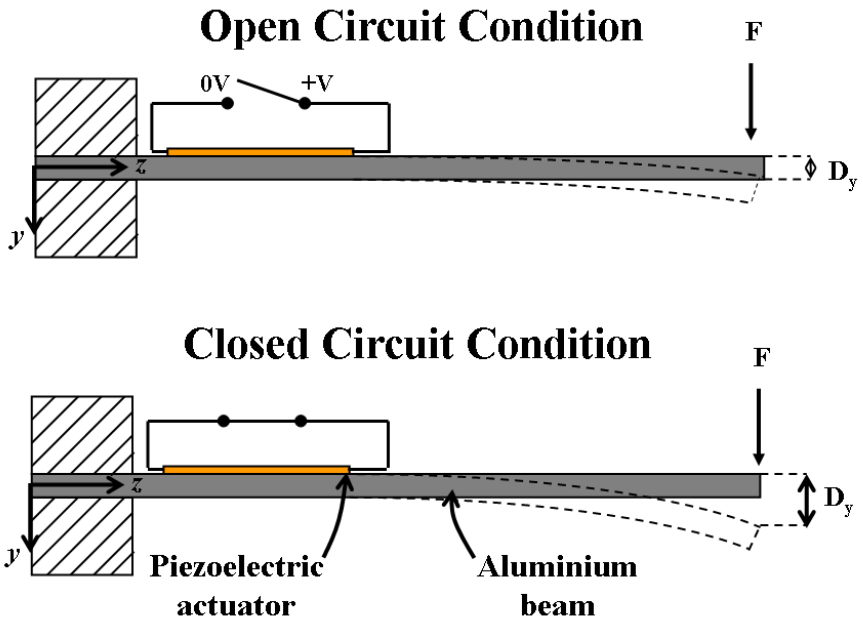

Fig. 3.3: Change in deflection of an isotropic beam with passive piezoelectric actuator bonded to its upper surface in response to applied mechanical load with actuator under open circuit and closed electrical boundary conditions.

Several investigators [16, 18] have chosen to approximate the piezoelectric strain by altering the coefficient of thermal expansion of the macro fibre composite model to create the appropriate actuation strains at a chosen temperature.

While such research efforts provide approximations to actuator behaviour, in order to achieve accurate representation of the electromechanical coupling inherent in piezoelectric devices the elastic and electrical conditions within a device must be coupled. In addition, thermal approximations are not appropriate for predicting the influence of electrical boundary conditions upon piezoelectric actuators (e.g. open and closed circuit conditions, as discussed in section 3.3.3) and would not allow design of combined control and actuation systems utilising MFC sensor capabilities, which requires prediction of voltage generated within the MFC in response to applied stress.

As discussed in Chapter 1, the design of an adaptive bump for aerodynamic flow control requires the use of finite element (FE) techniques. Therefore in order to integrate the actuator model with the structural FE model coupled field finite elements [19] which provide electromechanical coupling must be used to model the MFC actuator.

To date only three investigators have studied the use of coupled field finite elements to create a functional MFC model. Gude [19] created a simple homogenised MFC model and investigated the use of MFCs to induce snap-through in bistable laminates. Analytical and finite element models were presented to model MFC device behaviour but no validation of the MFC model was presented and no comparison of FE-predicted snap-through voltage was made to experimental values it is not possible to determine the validity of the presented model.

More recently Dano [21] presented a finite element analysis of MFCs used to compensate for thermal deformation of unsymmetric composite laminates. A full three dimensional stiffness matrix for the MFC was formulated including through thickness elastic constants determined by finite element analysis of a representative unit cell. The actuation performance of the MFC model was validated against experimental measurement of the induced deflection of an aluminium beam and a unidirectional carbon/epoxy plate measuring 250mm × 100mm × 0.79mm and 250mm × 100mm × 0.32mm respectively. Finite element predictions of beam deflection for both test cases were in good agreement with experimental data however no quantitative comparison of prediction error was presented.

More recently Binette [17] conducted experimental characterisation of laminate deflection for a composite sandwich panel subjected to thermal loading. Piezoelectric actuation via two MFC actuators was used to reverse the induced thermal deformation. This experimental work was conducted to validate a coupled field finite element model of an unsymmetric composite laminate under combined piezoelectric and thermal actuation. The coupled field MFC model was based on that presented by Dano [21] and shared the same set of material properties to represent MFC actuation response. System behaviour under isothermal piezoelectric actuation and combined thermal-piezo loading was predicted using the FE model developed.

Fig. 3.4a shows the experimental setup used by Binette with the two MFC actuators visible while Fig. 3.4b shows the radiant lamp and constraint arrangement. Laminate deflections were measured using a digital motion capture system similar to that described in Chapter 2, with the speckle pattern required for motion capture clearly visible in Fig 3.4a.

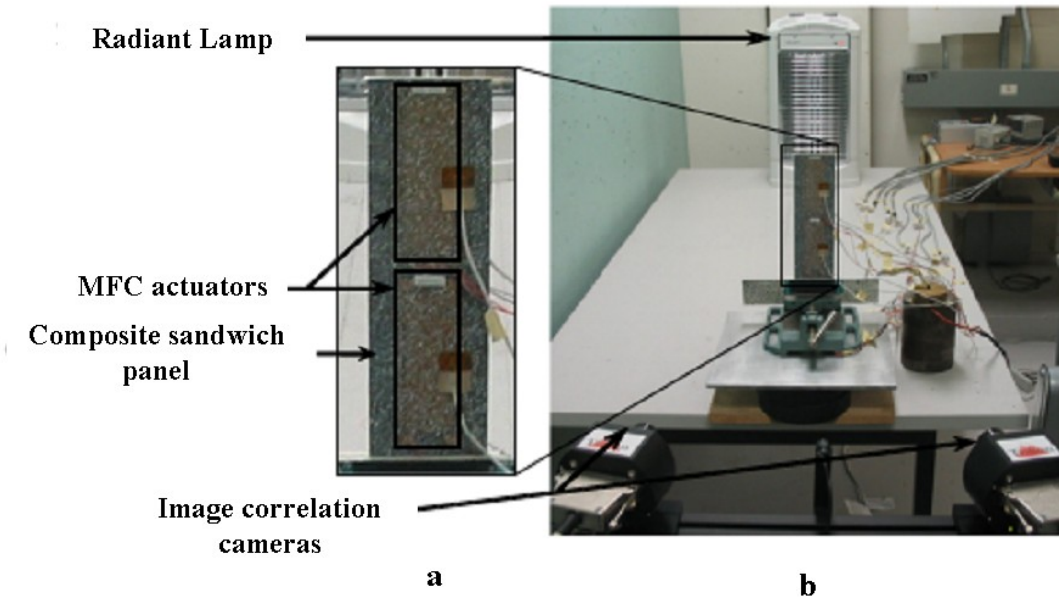

Fig.3.4: Experimental set up used by Binette [17] to characterise MFC actuation of composite sandwich panel with speckle pattern used for image correlation shown in *A* and camera setup and heat source shown in *B*. (*figure adapted from [17]*).

Though finite element predictions for laminate deflection under piezoelectric actuation agree with experimental results for deflections of less than 0.4mm, for measured laminate deflections of above 1mm predictive accuracy decreases significantly with errors compared to experiment of 9%. In the case of combined thermal and piezoelectric loading prediction accuracy varies between 4% and 31% at maximum MFC drive voltage. While the presented model from Dano [21] and Binette [17] provides insight into the behaviour and likely applications for MFCs as structural actuators, the lack of predictive accuracy at very low laminate deflections limits its utility as a design tool for morphing structures.

Relative permittivity (ε) was not considered in these models and no detail was given regarding constraint and boundary conditions for the electrical degree of freedom. Therefore actuator behaviour when deformed without applied actuation voltage would not be correctly predicted. The lack of an electrical constraint also allows electric field to propagate in directions other than the fibre direction as is the case within an MFC as seen in Fig 3.2. This breaks the uniform field assumption implicit in the use of homogenised piezoelectric constants. To date no presented work has presented a coupled field finite element model of an MFC actuator capable of fully capturing device actuation behaviour.

This chapter aims to formulate and validate a homogenous solid model of a commercially available MFC actuator to predict actuation characteristics under varying electrical

boundary conditions using the finite element software ANSYS V11.0 (Canonsburg, Pennsylvania, USA). To fully describe MFC actuation behaviour, three dimensional compliance $[c_{ij}]$, piezoelectric $[d_{ij}]$ and relative permittivity $[\varepsilon_{ij}]$ matrices will be formulated before deflection of an actuated isotropic beam is predicted and compared to experimental measurement to validate the proposed model.

3.2 MFC model formulation

In the following sections the formulation of three-dimensional matrices describing the effective compliance, piezoelectric coefficients and relative permittivity for the active portion of the MFC is presented.

3.2.1 Compliance matrix formulation

The three dimensional compliance matrix of the MFC was populated by converting the four linear elastic engineering constants as measured by Williams *et al.* [22] in Table 3.1 into equation 3.3. This equation was derived from the standard stress-strain relations for orthotropic materials presented in [13]. The resulting compliance matrix is of the standard form for a transversely isotropic material with a single axis of rotational symmetry parallel with the poling direction in PZT fibres [13].

$$[s_{ij}] = \begin{bmatrix} 1/E_1 & -\nu_{31}/E_1 & -\nu_{31}/E_3 & 0 & 0 & 0 \\ -\nu_{31}/E_1 & 1/E_1 & -\nu_{31}/E_3 & 0 & 0 & 0 \\ -\nu_{31}/E_3 & -\nu_{31}/E_3 & 1/E_3 & 0 & 0 & 0 \\ 0 & 0 & 0 & 1/G_{31} & 0 & 0 \\ 0 & 0 & 0 & 0 & 2(1+\nu_{31})/E_3 & 0 \\ 0 & 0 & 0 & 0 & 0 & 2(1+\nu_{31})/E_3 \end{bmatrix} \tag{3.3}$$

where E is the Young's modulus [GPa] , G the shear modulus [GPa], v the Poisson's ratio of the material and subscripts denote the orientation of each property with respect to the material coordinate system of Fig 3.1.

For comparison, the manufacturers (Smart Materials GmbH, Dresden) data sheet values for the MFC elastic constants are also presented in Table 3.1 and are in good agreement with measured values presented in [22]. The final s_{ij} matrix used to define the compliance of the MFC model is shown below.

$$[s_{ij}] = \begin{bmatrix} 0.065 & -0.0205 & -0.0106 & 0 & 0 & 0 \\ -0.0205 & 0.065 & -0.0106 & 0 & 0 & 0 \\ -0.0106 & -0.0106 & 0.034 & 0 & 0 & 0 \\ 0 & 0 & 0 & 0.165 & 0 & 0 \\ 0 & 0 & 0 & 0 & 0.173 & 0 \\ 0 & 0 & 0 & 0 & 0 & 0.173 \end{bmatrix} \times 10^{-9} m^2 N^{-1} \quad (3.4)$$

Table 3.1: Mechanical properties of Smart Materials Corp M8557-P1 MFC actuator taken from Williams *et al.* [22] and manufacturers data sheet [6].

	Williams *et al* 2004.	Smart Materials Corp.
E_{33} (*GPa*)	29.4	30.336
E_{11} (*GPa*)	15.2	15.857
G_{31} (*GPa*)	6.06	5.515
υ_{31}	0.312	0.31
υ_{13}	0.16	0.16

3.2.2 Piezoelectric matrix formulation

The effective piezoelectric constants for the device were determined in order to describe the average response of the MFC to an applied electric field. As described by several investigators [5, 8] the relationships between the piezoelectric properties of the constituent materials and the complete MFC are highly complex (due to non-uniform polarisation of PZT fibres and the composite structure of the actuator) and remain the subject of research efforts. While predictive models for free-strain behaviour have been shown to agree well with experiment [5,11], experimental measurement of device behaviour provides the best available data on which to base the FE model developed in this chapter.

Williams *et al*. [5] experimentally determined the free-strain behaviour of the same MFC actuator used in the present study (Smart Materials Corp M8557-P1) by bonding metal foil strain gauges to its surface and applying a range of excitation voltages to measure the effective piezoelectric constants of the device. The value for d_{33} (strain per unit electric field in poling direction) presented in [5] agrees with data presented by the manufacturer [6], however no value for d_{31} is reported by either source. The d_{31} constant is the strain per unit electric field in the *1*-direction shown in Fig 3.1.

Table 3.2: Piezoelectric coupling coefficients [d_{ij}] and relative permittivity (ε_{ij}) of Smart Materials M8557 MFC actuator.

	Smart Materials Corp M8557-P1 MFC actuator
d_{33} (pm/V)	467
d_{32} (pm/V)	-210
d_{31} (pm/V)	-210
ε_1^s	712
ε_2^s	1.7
ε_3^s	737

Williams *et al.* determined d_{33} and d_{31} values for an 'Active Fibre Composite' [5] whose construction and mode of operation are sufficiently similar to MFCs to assume the measured ratio of d_{31}/d_{33} to be equal in both devices [22]. The values for both d_{31} and d_{32} shown in table 3.2 were calculated by multiplying the measured piezoelectric d_{33} constant taken from Smart Materials product specification [6] by the d_{31}/d_{33} ratio of -0.449 measured by Williams *et al* [5]. The calculated values used to populate the piezoelectric coefficient [d_{ij}] matrix used in the present FE-model of the MFC are shown in Table 3.2 and the final matrix is shown below [12].

$$\left[d_{ij}\right] = \begin{bmatrix} -2.1 & -2.1 & 4.67 & 0 & 0 & 0 \\ 0 & 0 & 0 & 0 & 0 & 0 \\ 0 & 0 & 0 & 0 & 0 & 0 \end{bmatrix} \times 10^{-10}\, pmV^{-1} \tag{3.5}$$

3.2.3 Relative permittivity matrix formulation

To fully specify the electromechanical coupling within the MFC the relative permittivity of the active layer must be determined. This property is important in providing the relationship between charge Q [C], capacitance C [F] and voltage (V) for the MFC ($Q = CV$), and so determines the magnitude of the induced electric field when subjected to a mechanical stress. Experimental measurement of device dielectric properties such as capacitance would not enable accurate calculation of properties for the active layer as capacitance is influenced by all structures and materials through which electric field passes, such as the interdigitated electrode array. Extraction of the active layer properties from this combined capacitance measurement is not possible and hence active layer properties must be determined analytically.

In order to determine the relative permittivity (or dielectric constant) of the active layer of the MFC, a micromechanical mixing rule for ε_3 presented by Deraemaeker [10] and the standard mixing rule for dielectric volumes in series representing ε_2 as seen in [10]:

$$\varepsilon_{33}^{T} = \rho\varepsilon_{33}^{T_p} + (1-\rho)\varepsilon_{33}^{T_m} \tag{3.6}$$

$$\frac{1}{\varepsilon_{22}} = \left(\rho\varepsilon_{22}^{Tp}\right)\left(\frac{(1-\rho)\varepsilon_{22}^{Tm}}{\rho\varepsilon_{22}^{Tp} + (1-\rho)\varepsilon_{22}^{Tm}}\right) \tag{3.7}$$

where ε is the relative permittivity [Fm^{-1}]and ρ the volume fraction of PZT within the active layer. The first numeric subscript denotes direction of field application with the second showing the direction of mechanical strain. The superscript T indicates values are measured at constant stress with superscripts m and p denoting properties of the piezoelectric and matrix materials respectively.

In this work the piezoelectric material was modelled using coupled-field elements [19] within the commercial finite element software ANSYS (Version 11.0). ANSYS requires that relative permittivity matrix under constant strain (ε^S) be entered in the material model. The relative permittivity matrix of piezoelectric ceramics is generally reported under conditions of constant stress (ε^T), which is transformed using equation 3.8 [13]:

$$\varepsilon^S = \varepsilon^T(1-k^2) \tag{3.8}$$

where k is the electromechanical coupling coefficient [13]. The values of relative permittivity for the active layer predicted by equations 3.6 and 3.7 were then transformed into the constant stress values using the k-coefficient of PZT-5A prior to calculation of active layer properties shown in table 3.2.

The relative permittivity of PZT-5A data used to calculate MFC device ε was taken from Jaffe [14] with the value for the epoxy matrix taken from Deraemaeker [10].

The wide variation in the predicted relative permittivity values between the ε_1 and ε_2 (712 and 1.7 repectively) is caused by the different electrical conditions in the *1* and *2*-directions. For a field to propagate in the *2*-direction it must permeate through the epoxy layer and then the PZT fibre. This means that the low permittivity of the epoxy significantly reduces the effective permittivity of the active layer in this direction as seen in Fig. 3.5 which shows a representative volume element of the active layer of the MFC.

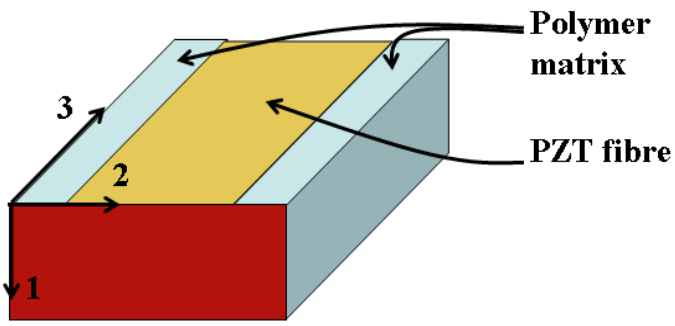

Fig. 3.5: Representative volume element of MFC actuator active layer showing PZT fibre and polymer matrix with coordinate system shown.

Because the electric field must propogate through the polymer and ceramic in parallel in both the *1* and *3*-directions of the MFC as seen in Fig.3.5, the small difference between the relative permittivity of the MFC ε_1 and ε_3 (shown in table 3.2 as 712 and 737 respectively) is a direct result of the difference in the ε_{33} and ε_{31} values for poled PZT-5A of 1700 and 1730 respectively [14].

The presented mixing rules combine the relative permittivity of the piezoelectric ceramic (PZT-5A) and the epoxy matrix according to ceramic volume fraction to determine the effective relative permittivity for the active layer of the MFC actuator used in the present study. In contrast to the assumptions made in traditional rule of mixtures [25] Deraemaeker applies a plane stress assumption so that the through-thickness stresses (σ_2) are assumed to

be zero. Furthermore, the electric field is assumed parallel to fibre direction and constant along the length of the fibre.

This plane stress assumption may limit the accuracy of the model in bending where through thickness effects could have role in device response. However, when validated against a micromechanical FE-model the predicted values for relative permittivity were in good agreement. Therefore in the absence of experimentally determined information relating to the relative permittivity of the active layer within the MFC actuator the chosen approximation represents the best available information.

3.3 MFC model validation

To validate the materials homogenised materials properties describing the MFC actuator which were determined in the preceding section, it was necessary to compare FE model predictions of actuator deflection with experimental data. Two MFC actuators were bonded to a simple aluminium cantilever with one connected to act as an actuator and the second remaining passive to allow testing of the influence of electrical boundary conditions.

In section 3.3.1 the experimental measurements of the deflection of an aluminium beam in response to MFC actuation are presented. This experiment was undertaken in order to validate finite element model predictions and has previously been used to allow characterisation of MFC actuation [21].

In section 3.3.2 the finite element model used to predict deflection of the experimental beam (Fig. 3.6) in response to MFC actuation is described. The solution procedure used to predict changes in the effective stiffness of a passive MFC actuator in response to changes in electrical boundary conditions will also be presented. Modelling these changes using thermal approximations to piezoelectric actuation as proposed by several investigators [16, 18] would not replicate this electromechanical coupling effect.

3.3.1 MFC actuated isotropic beam - Experimental setup

Two MFC actuators (Smart Materials Corp M-8557P1) were bonded to front and back surfaces of an aluminium beam measuring 330 × 75 × 1.97mm as in Fig. 3.6. The actuators and aluminium surfaces were cleaned using isopropryl alcohol and a thin coat of a two-part epoxy adhesive applied to both surfaces. The MFCs were then carefully located whilst ensuring no air-bubbles were trapped during placement. With the MFCs in place, the assembly was placed under 200N clamping force for 24hrs to allow the epoxy to cure. Both MFCs (labelled MFC-1 and MFC-2 in Fig. 3.6) were positioned so that the active area was positioned between z = 45mm and z = 130mm, with the poling direction of the PZT fibres (*3*-direction in Fig. 3.1) parallel with the z-axis.

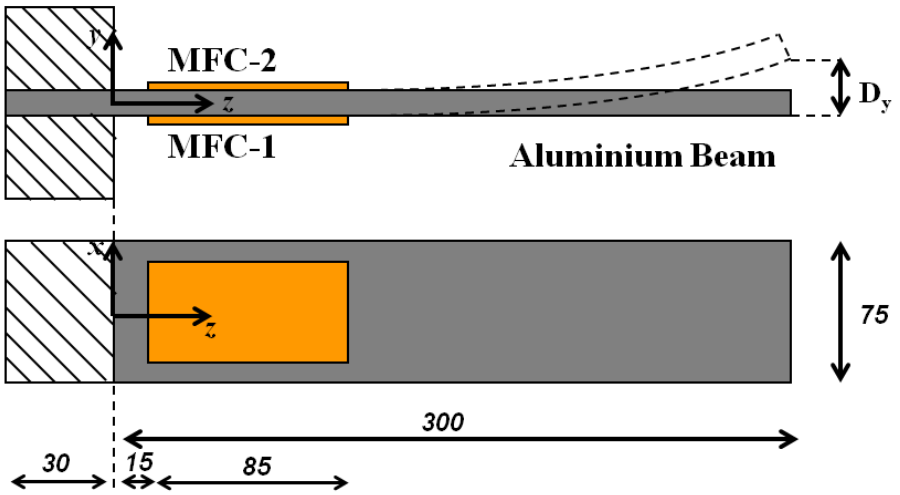

Fig.3.6: Experimental setup with aluminium beam, driven actuator (MFC-1) and passive actuator (MFC-2) with dimensions shown in *mm*.

As in Fig. 3.6 the beam was clamped so that the 75*mm* dimension (*x*-direction) was aligned vertically. This arrangement isolated beam deflection (D_y) from the influence of gravitational forces. A Nippon LAS5010v laser displacement sensor with a resolution of 10μm was used to measure cantilever deflection as a function of applied voltage. The active MFC (MFC-1) was driven from a signal generator with an attached Trek PZD700 Piezodriver which gave 200V output per volt input. Closed circuit boundary conditions were imposed on MFC-2 by connecting the positive and earth electrode terminals, while for open circuit conditions these terminals were insulated from one another.

Piezoelectric actuators are subject to slow creep under open loop control (constant voltage) [26] due to domain motion. To standardise the creep effects in the MFC response [27], all measurements at each voltage were taken after a 60 second settling period.

Beam deflection at z = 120mm as a function of MFC-1 drive voltage was measured for a range of drive voltages from 0 – 400V with measurements taken at 80V intervals. Deflection measurements were carried out with MFC-2 under closed circuit boundary conditions. A datum measurement of beam position was taken before voltage application and this value subtracted from the actuated beam position to calculate the deflection. These data are shown in section 3.3.3.

In order to measure the change in beam deflection due to changing electric boundary conditions of MFC-2 beam deflection in response to 400V MFC-1 drive voltage was measured at intervals of 30mm between z = 120mm and z = 300mm. Closed and open

circuit measurements were taken sequentially at each z = position. A separate datum measurement was taken for each measurement and both MFC-1 and MFC-2 were electrically discharged between measurements. A resting period of 60 seconds was allowed between each measurement so that any residual strain relaxation within either MFC could subside without influencing the measurements. Data of beam deflection for open and closed circuit conditions is presented in Fig.3.10 and Fig. 3.11 respectively.

The following section will now describe the development of the FE model used to test the representative solid model of the MFC actuator.

3.3.2 MFC actuated isotropic beam - Finite element model

The aluminium cantilever was modelled using 20-node quadratic brick SOLID186 elements with isotropic mechanical properties shown in Table 3.3. The two MFC actuators were represented by 20-node quadratic brick SOLID226 elements. SOLID226 elements are coupled field elements which solve the constitutive equations for an elastic piezoelectric solid (equation 3.1 and 3.2) to determine the deformation of the element under imposed electrical conditions and mechanical stress.

In addition to the improved solution accuracy of 20-node quadratic elements in modelling highly curved structures, when combining element types within a single model it is advisable to use 20-node elements throughout [19] to ensure that all nodes on adjacent elements are coincident. Attempting to merge nodes linked to a volume meshed with 8-node elements with 20-node elements connected with an adjacent volume can result in nodes losing connectivity with the model, introducing numerical errors and preventing model solution.

Once the model was appropriately meshed, the model consisted of a total of 4680 SOLID186 elements for beam and 340 SOLID226 elements within the MFC volume. All elements within the beam volume were of aspect ratio 2.6 and the element aspect ratio within the MFC vole was 8.33. Element density was sufficient to accurately capture beam behaviour as further refinement of the mesh did not significantly affect the predicted beam deflection.

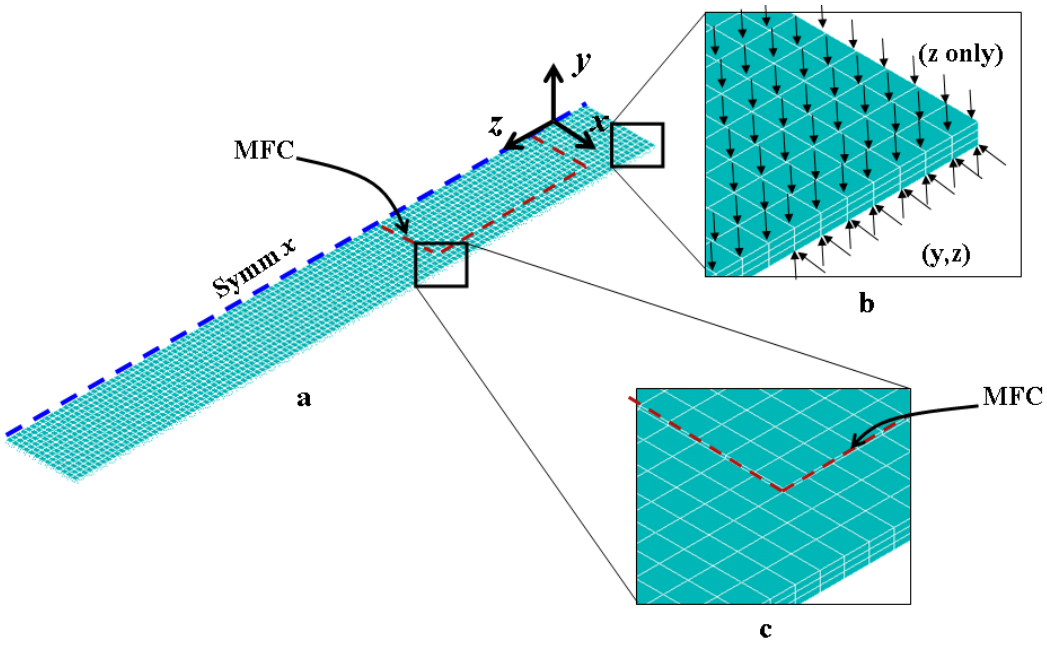

Fig.3.7: Finite element model used to predict beam deflection showing coordinate system and symmetric boundary constraint (a), mechanical constraint to model clamped end condition of experimental set up and mesh density of both MFC volume and beam (c).

The MFC model volumes were positioned on the front and back surfaces of the cantilever as in Fig. 3.6 with all coincident nodes on the contact surfaces merged to ensure stress transfer between cantilever and actuator volumes.

Table 3.3: Materials properties used to model aluminium validation beam

Property	Value
Young's Modulus [GPa]	70.7
Shear Modulus [GPa]	25.0
Poisson's Ratio	0.32

The clamped mechanical boundary condition was modelled by constraining all three translational degrees of freedom (*x, y,& z* in Fig. 3.3) for nodes lying in the range $-30mm < x < 0mm$ on the $y = 0mm$ plane. Nodes in the same range of *x*-coordinate on the $y = 0.197mm$ plane were constrained in the *y*-direction only.

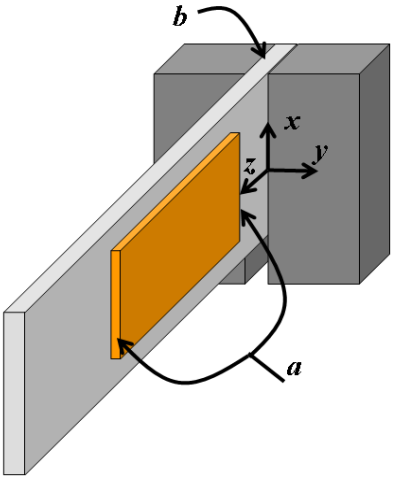

Fig.3.8: Finite element model constraint showing *x*= 35mm and 120mm faces of MFC (*a*), region of mechanical constraint (*b*) and the orientation of the model coordinate system.

In creating homogenous piezoelectric [d_{ij}] and permittivity [ε] matrices for the MFC actuator it is assumed that electric field is constant along and aligned with the z-axis. To ensure constant and well aligned electric field, the voltage degree of freedom for nodes of equal z-coordinate was coupled to create planes of equal voltage at 5mm intervals along the z-direction of the MFC volume.

In order to model MFC behaviour under closed circuit boundary conditions (i.e. two electrodes of MFC-2 are electrically connected) the induced potential difference as a result of a stress must be dissipated as occurs in the physical system; however it is inappropriate to constrain all voltage DOFs within the MFC volume as doing so reduces solution accuracy [19].

Furthermore, simply altering the voltage constraints at the x = 35mm and x = 120mm faces (Fig. 3.8) would not suppress the induced field throughout the volume but only near the extremities. To suppress induced field throughout the passive MFC volume (MFC-2 in Fig. 3.6) the piezoelectric coefficients (d_{33} and d_{31}) for that volume were reduced by a factor 1×10^{9}, hence d_{33} for closed circuit conditions was 467×10^{-21} m/V. This alteration of piezoelectric constants effectively modelled the suppressed induced field which characterises closed circuit electrical boundary conditions while maintaining solution accuracy.

In the following section the finite element predicted values of beam deflection will be compared to the experimentally measured values.

3.3.3 Validation results

Beam deflection as a function of MFC-1 drive-voltage is shown in Fig. 3.9 and clearly shows the linear trend predicted by engineering beam theory and observed by other investigators [21]. Predicted finite element values of cantilever deflection using the MFC materials properties had excellent agreement with experimental values to within 2%, it should be noted that for all, except the value for 160V, the error was within measurement uncertainty of ±10μm.

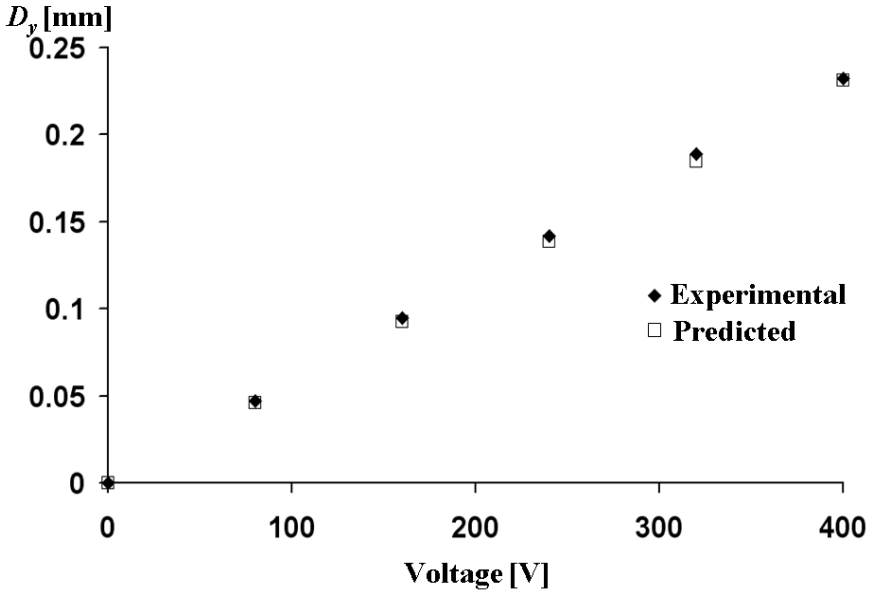

Fig.3.9: Beam deflection (D_y) as a function of MFC drive-voltage.

Fig. 3.10 and Fig. 3.11 show beam deflection (D_y) as a function of distance from the clamped region of the cantilever with a drive voltage of 400V applied to MFC-1 and MFC-2 under open and closed circuit boundary conditions respectively. FE-predictions of D_y are again accurate to within 2% compared with experimental values for both conditions. It should be noted that deviation from the linear relation within the experimental data around z =160mm is due to surface irregularities of the beam.

Prediction of closed circuit behaviour showed excellent quantitative agreement with experiment, with predicted cantilever gradient (dy/dz) over the range 120mm<z<300mm matching the measured value of 3.8μmV^{-1} exactly. In addition beam tip deflection was predicted to within 1% of the measured value of 0.905mm. As expected observed beam tip deflection decreased under open circuit boundary conditions as compared to closed circuit

values, with the predicted and observed values (0.873mm & 0.880mm respectively) matching to within 1%. However, beam gradient under open circuit boundary conditions was lower in the model by 2.6%, with FE prediction of $3.7\mu mV^{-1}$ as compared to the experimental value of $3.6\mu mV^{-1}$.

The introduction of relative permittivity properties to the homogenised MFC model has allowed the change in effective stiffness under varying electrical boundary conditions to be predicted. This important facet of actuator behaviour is not captured by the thermal approximations to piezoelectric actuation proposed by other investigators [16, 27, 28].

The small discrepancy between the measured and predicted beam deflection under open circuit conditions indicates that the model generates a larger than expected voltage (via the $V = Q/C$ relation) and electric field in MFC-2 due to the beam deflection. It is suggested that the relative permittivity in the model was too low, leading to increased induced field and hence piezoelectric strain within the MFC-2, increasing the cantilevers effective stiffness. Excellent agreement for closed circuit response indicates that both elastic and piezoelectric matrices are appropriately formulated.

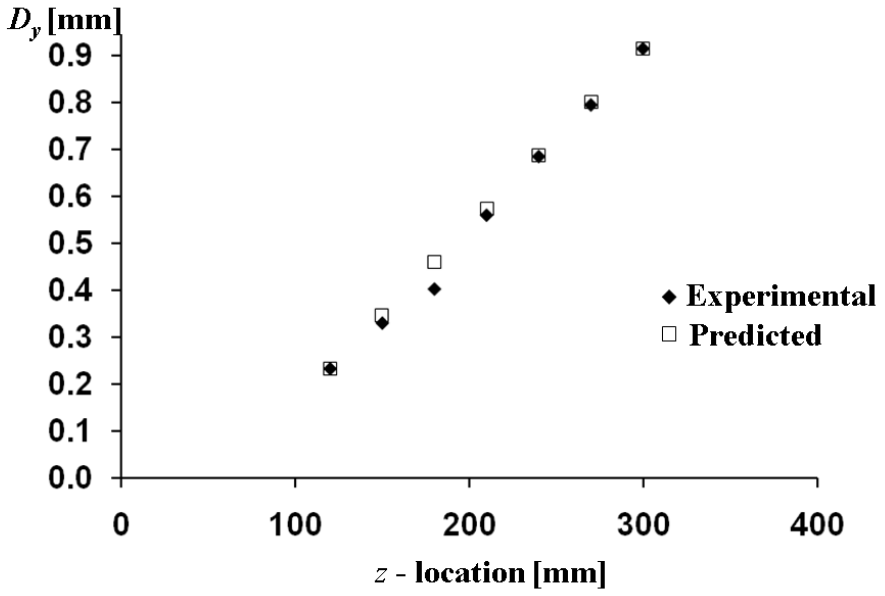

Fig.3.10: D_y as a function of z-location with MFC-2 under open circuit boundary conditions.

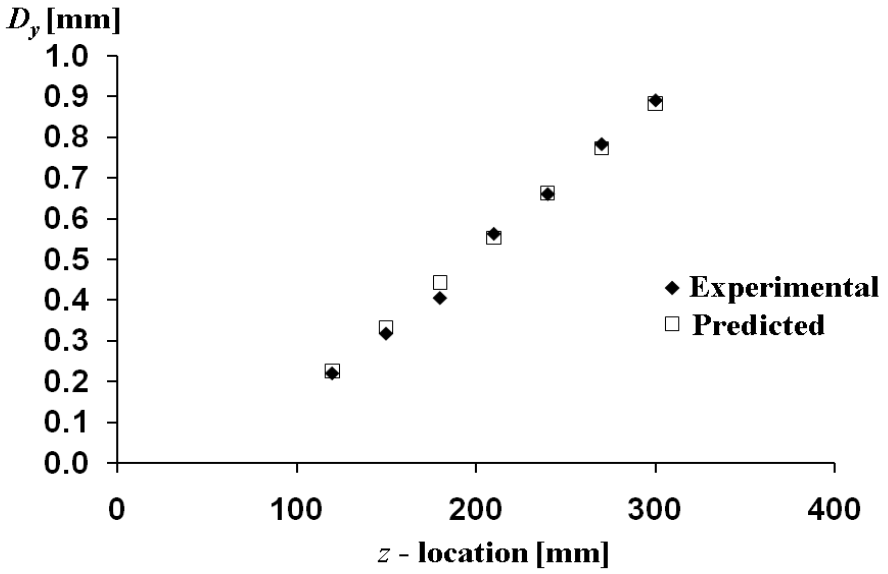

Fig.3.11: D_y as a function of z-location with MFC-2 under closed circuit boundary conditions.

3.4 Conclusion

In this chapter a homogenised finite element model of a commercially available MFC actuator has been developed and validated to allow prediction of actuator performance under combined electrical and stress fields.

The key conclusions drawn from work presented in this chapter are:

- A homogenised finite element model of an MFC actuator capable of predicting actuator performance under combined electrical and stress fields was presented.
- It is shown that inclusion of relative permittivity values within the coupled-field element definition allows accurate prediction of variations in effective MFC-stiffness under varying electrical boundary conditions.
- The MFC model was validated by prediction of tip deflection of an isotropic aluminium beam with prediction errors of 1% under a range of electrical boundary conditions.

Three dimensional piezoelectric and stiffness matrices for the MFC were calculated using experimentally determined orthotropic constants presented in the literature to create a homogenised material model of the MFC actuator.

In order to fully capture the electromechanical coupling of the MFC system the relative permittivity matrix was formulated using a rule of mixtures approximation presented by Deraemaeker [10]. The present work shows that inclusion of relative permittivity values within the coupled-field element definition allows accurate prediction of variations in effective MFC-stiffness under varying electrical boundary conditions; this important change in actuator behaviour is impossible to predict using thermal approximations.

This model was validated by comparing finite element predictions to experimental measurements of tip deflection of an isotropic beam with MFC actuators bonded to both top and bottom surfaces. Actuation strain was provided by a single MFC actuator with drive voltages up to 400V. Predicted values of tip deflection agreed with experiment to within 2.5% over this range.

To test the influence of relative permittivity on the effective stiffness of the MFC an additional actuator (MFC-2) was bonded to the rear-face of the test beam; the variation in

tip deflection was then compared whilst this additional MFC was subject to open and closed circuit electrical boundary conditions.

With MFC-2 under closed circuit boundary conditions both tip deflection gradient of the beam were predicted to within 1% of experimental measurement. Under open circuit conditions, the developed field within the MFC caused a reduction in beam gradient of 2.6% as opposed to the predicted reduction of 5.2%, although predicted beam tip deflection remained within 1% of experimental values.

From these data it may be concluded that the proposed FE model and the electrical constraints imposed upon it are appropriate for representing the actuation behaviour of commercially available MFCs. However, while good agreement with experiment is achieved, the influence of electrical boundary conditions is over estimated by the model, therefore it is likely that approximated relative permittivity values are higher than those of the real MFC.

The following chapter aims to gain understanding of the snap-through behaviour of a piezoelectrically actuated bistable laminate; by combining the insights described above with the knowledge gained of bistable composites presented in Chapter 2, a coupled field finite element model capable of predicting cured shape and snap-through will be developed.

3.5 Reference list

1. Lloyd, J. M., Williams, R. B., Inman, D. J., and Wilkie, W. K. (2004). "An analytical model of the mechanical properties of the Single Crystal Macro-Fiber Composite actuator." SPIE-INT SOC Optical Engineering, Bellingham. 6(2), 37-46.
2. Wilkie, W. K., Bryant, R. G., High, J. W., Fox, R. L., Hellbaum, R. F., Jalink, A., Little, B. D., and Mirick, P. H. (2000). "Low-cost piezocomposite actuator for structural control applications." SPIE-INT SOC Optical Engineering, Bellingham. 11(60). 323 - 334.
3. Williams, R. B., Grimsley, R. B., Inman, D. J., and Wilkie, W. K. (2002). "Manufacturing and mechanics-based characterization of macro fiber composite actuators." ASME, New Orleans, Louisiana, USA. 67. 79-89.
4. Huber, C., Spori, D. M., Melnykowycz, M. M., and Barbezat, M. (2005). "Active fibre composites: Optimization of the manufacturing process and their poling behavior." SPIE-INT SOC Optical Engineering, Bellingham. 7(3). 542 - 547.
5. Williams, B. R., Inman, D. J., and Wilkie.W, K. (2006). "Nonlinear Response of the Macro Fiber Composite Actuator to Monotonically Increasing Excitation Voltage." J Int Mat Sys Struct, 17(7), 601 - 608.
6. "MFC Brochure 2010 V3."(2010). http://www.smart-material.com/media/Publications/MFC-brochure_2010_V3.1.pdf Accessed: June 15, 2010.
7. Jaffe, B., and Cook, W. R. (1971). "Piezoelectric ceramics." Academic Press, London, UK. ISBN: 1-878-907170-3
8. Paradies, R., and Schlapfer, B. (2009). "Finite element modeling of piezoelectric elements with complex electrode configuration." Smart Materials & Structures, 18 (2). 025015.
9. Bowen, C. R., Bowles, A., Drake, S., Johnson, N., and Mahon, S. (1999). "Fabrication and finite element modelling of interdigitated electrodes." Ferroelectrics, 228(1), 257-269.
10. Deraemaeker, A., Nasser, H., Benjeddou, A., and Preumont, A. (2009). "Mixing Rules for the Piezoelectric Properties of Macro Fiber Composites." Journal of Intelligent Material Systems and Structures, 20(12), 1475-1482.
11. Bowen, C. R., Nelson, L. J., Stevens, R., Cain, M. G., and Stewart, M. (2006). "Optimisation of interdigitated electrodes for piezoelectric actuators and active fibre composites." Journal of Electroceramics, 16(4), 263-269.
12. Ikeda, T. (1990). "Fundamentals of Piezoelectricity." Oxford University Press, Oxford, UK. ISBN: 0-198-56339-6
13. Hyer, M. W. (1998). "Stress Analysis of Fibre Reinforced Composite Materials." WCB/McGrawhill, Boston, Mass. ISBN: 0-071-15983-5
14. Jaffe, H., and Berlincourt, D. A. (1965). "Piezoelectric transducer materials." Proceedings of the IEEE. 53 (10). 1372-1386.
15. Choi, S. C., Park, J. S., and Kim, J. H. (2007). "Vibration control of pre-twisted rotating composite thin-walled beams with piezoelectric fiber composites." Journal of Sound and Vibration, 300(1-2), 176-196.
16. Portela, P., Camanho, P., Weaver, P., and Bond, I. (2008). "Analysis of morphing, multi stable structures actuated by piezoelectric patches." Computers & Structures, 86(3-5), 347-356.

17. Binette, P., Dano, M. L., and Gendron, G. (2009). "Active shape control of composite structures under thermal loading." Smart Materials & Structures, 18(2). 025007.

18. Schultz, M. R., and Hyer, M. W. (2003). "Snap-through of unsymmetric cross-ply laminates using piezoceramic actuators." Journal of Intelligent Material Systems and Structures, 14(12), 795-814.

19. ANSYS Inc . 2007. Coupled field analysis guide. Ansys user help reference system V11.0.

20. Gude, M., and Hufenbach, W. (2006). "Design of novel morphing structures based on bistable composites with piezoceramic actuators." Mechanics of Composite Materials, 42(4), 339-346.

21. Dano, M. L., Gakwaya, M., and Julliere, B. (2008). "Compensation of thermally induced distortion in composite structures using macro-fiber composites." Journal of Intelligent Material Systems and Structures, 19(2), 225-233.

22. Williams, R. B., Inman, D. J., Schultz, M. R., Hyer, M. W., and Wilkie, W. K. (2004). "Nonlinear tensile and shear behavior of macro fiber composite actuators." Journal of Composite Materials, 38(10), 855-869.

23. Schultz, M. R., Wilkie, W. K., and Bryan, R. G. (2007). "Investigation of self-resetting active multistable laminates." Journal of Aircraft, 44(4), 1069-1076.

24. Skinner, D. P., Newnham, R. E., and Cross, L. E. (1978). "Flexible Composite Transducers." Materials Research Bulletin, 13(6), 599-607.

25. Jung, H., and Gweon, D. G. (2000). "Creep characteristics of piezoelectric actuators." Review of Scientific Instruments, 71(4), 1896-1900.

26. Jung, H., Shim, J. Y., and Gweon, D. G. (2001). "Tracking control of piezoelectric actuators." Nanotechnology, 12(1), 14-20.

27. Ren, L. B. (2008). "A theoretical study on shape control of arbitrary lay-up laminates using piezoelectric actuators." Composite Structures, 83(1), 110-118.

28. Schultz, M. R., Hyer, M. W., Williams, R. B., Wilkie, W. K., and Inman, D. J. (2006). "Snap-through of unsymmetric laminates using piezocomposite actuators." Composites Science and Technology, 66(14), 2442-2448.

Chapter 4 - Actuated composite model

Chapters 2 and 3 described the development and validation of finite element models to predict the cured shape of bistable composite laminates and actuation properties of macrofibre composite actuators respectively. This chapter builds on the insights gained in the preceding chapters by developing and validating a finite element model using Ansys V11.0 to predict snap-through of bistable composite laminates actuated by macrofibre composite (MFC) actuators bonded to the laminate. The developed model is an important intermediate step in the design of an adaptive bump based on bistable composites (Chapter 7).

Section 4.1 of this chapter outlines the relevant research efforts into prediction of snap-through behaviour of bistable composites and highlights the need for a correctly formulated coupled field model of the system for prototype design of morphing structures. Section 4.2 describes the experimental techniques used to measure snap-through voltage along with those used to measure the cured shape of two sample laminates. The finite element (FE) model and solution procedure used to ensure correct integration of the MFC and bistable composite models is described in section 4.3. Finally predicted values for actuated laminate shape and snap-through voltage are compared with experimental values in section 4.4.

4.1 Introduction

The use of piezoelectric macro fibre composites (MFCs) as structural actuators has received some attention [1, 2], much less work has been presented investigating their suitability for inducing snap-through in bistable composite laminates.

Analytical techniques based on the Rayleigh-Ritz minimisation techniques of Hyer [3] have met with some success in the prediction of snap-through for MFC actuated square composite laminates [4-6]. Analytically predicted values for snap-through voltage do not agree well with and experimental measurements although the reduced computational cost has allowed investigators to conduct parametric studies relating to the influence of moisture absorption [7] and laminate composition [8].

While these analytical methods enable efficient design space exploration, detailed mechanism design of laminates comprised of several segments of different lay-up combined into a single sheet remains beyond their scope. As discussed in Chapter 2, the potential demonstrated by segmented laminates [9, 10] makes finite element (FE) modelling of these structures a necessity to allow detailed design of adaptive structures. In addition to variations of lay-up the design tools capable of predicting cured shape of non-rectangular laminates are a necessity for effective mechanism design. To date, no such analytical model has been presented or reported.

If bistable mechanisms are to be viable within morphing structures, they must be integrated within host structures and so are subject to elastic boundary conditions imposed by the stiffness of the host. Despite advances made in this area [10], current analytical models based on Hyer's energy minimisation method are not able to predict the cured shapes of bistable composite laminates embedded within monostable host structures.

Therefore the remainder of this discussion will focus on investigations concerned with development of FE techniques used to predict snap-through behaviour of bistable composite laminates.

Following an attempt to model bistable composite laminates using the commercial FEA software Ansys (release V5.5.2) [11], Gude and Hufenbach attempted to model the snap-through of a bistable composite laminate using 8-node layered solid elements (SOLID46) to represent the composite laminate and 8-node coupled field brick elements (SOLID5) for the MFC actuator [12].

The $[0/90]_T$ composite laminate modelled was manufactured from an unidentified pre-preg material using T300 carbon fibre reinforcement and measured 150×150×0.5mm. A Smart Materials MFC-8557P1 actuator was bonded to its upper surface as seen in figure 4.1.

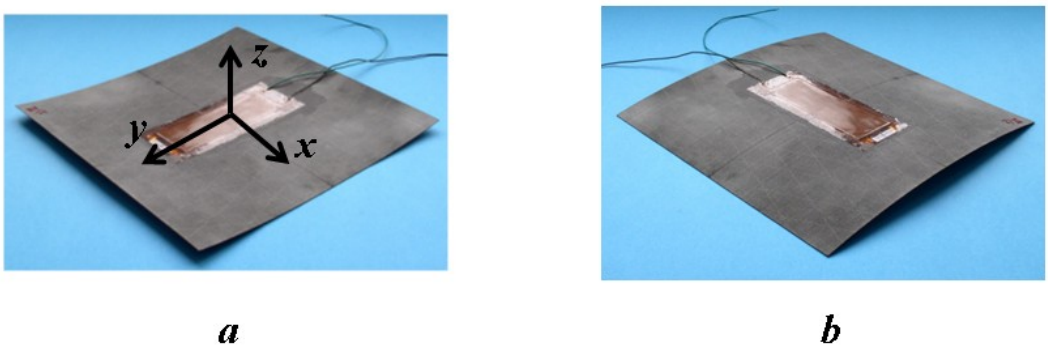

Fig.4.1: Bistable composite laminate with MFC actuator centrally bonded in State A showing global coordinate system (*a*) and State B (*b*). ***(figure adapted from [12])***

In this work [12] the element types used for both composite and MFC volumes are linear solid elements. Both element types approximate the displacement field between nodes using linear interpolation. This first order approximation to displacement introduces numerical errors in the analysis of highly curved structures [13]. As no details of mesh density are given in the work, it is not possible to determine if element size was reduced to minimise these errors. No details are given relating to the solution procedure and no materials properties are presented to support the model formulation.

Furthermore the SOLID46 element is unsuitable for modelling curved structures. When the SOLID46 element is deformed, as occurs in curved bistable laminates, the element stiffness matrix is formulated assuming the element coordinate system remains parallel to the original coordinate system of the undeformed element [13].

No predicted snap-through voltage is presented and no comparison between the FE solution and either experimental data or analytical predictions is made, the authors simply state that snap-through was predicted; therefore a basic qualitative agreement is likely to have been achieved.

It should however be noted that the analytical model presented by Gude [12] in addition to the finite element model does not agree well with experimental data contained within the work. Analytically predicted values for snap-through voltage deviate from those observed in experiment by 130% (1260V predicted against 526V observed).

More recently Portela *et al.* presented an analytical technique as well as a finite element model (FE) using commercial finite element software ABAQUS/EXPLICIT to predict snap-through voltage for an MFC-actuated bistable composite laminate [6]. The FE model approximates the behaviour of the MFC by applying a different thermal load to the MFC elements compared to the composite elements. By scaling the coefficient of thermal expansion of the MFC elements to match the strain per unit electric field value of the MFC (d_{33}) a correlation between temperature change within the MFC elements and drive voltage in the physical specimen is obtained.

In addition, data presented by Portela *et al.* predicts the effect of moisture on laminate curvature and snap-through voltage for a range of materials and actuator sizes. Portela et al. [6] suggest that for any given laminate there is an optimum size of actuator which is capable of initiating snap-through without significantly impacting on the cured shape of the composite laminate. This is supported to some extent by the FE analyses, though the work does not contain validating experimental data.

While the presented model [6] is based on a sound composite modelling procedure and rigorous non-linear solution protocols the behaviour of the MFC is not well captured. The strain per unit field perpendicular to the fibre direction (d_{31}) of the MFC is not considered in the model formulation which will lead to errors in predicted laminate deflection. Wilkie characterised MFC actuators in terms of strain per unit electric field and found d_{31}:d_{33} ratio for a similar unit to those used in Portela *et al* to be -0.449 [14]; this significant transverse strain is omitted from the FE model.

Additionally, thermal modelling of MFC actuators is not capable of predicting the change in effective stiffness caused by differing electrical boundary conditions as discussed in Chapter 3, hence design of morphing structures subject to electrical control would be impaired by the use of thermal approximations to MFC actuation.

It has been shown that piezoelectric actuators show displacement creep when under open loop control [15] it is therefore essential that any design tool be integrated into control systems simulation. Variation in control circuit resistance or capacitance would also impact the electrical boundary conditions imposed upon the MFC, and hence would alter effective actuator stiffness as shown in section 3.1. The ability to predict the voltage generated within MFC actuators under the action of applied mechanical stress is not possible using thermal approximations. This sensor capability of MFCs could be used as part of a closed loop control

scheme and hence coupled field finite element models capable of predicting sensor function of MFC actuators are essential.

Coupled field models may be coupled to control circuit simulations within the ANSYS package to fully model system response to electrical control signals, this would not be possible using the a thermal approximation to MFC characteristics.

Only a single experimental measurement of snap-through voltage is presented by Portela [6] with no explanation of which particular laminate was tested to achieve the observed snap-through of 390V. Without laminate descriptions, test conditions or experimental procedures being clarified it is not possible to determine the extent to which the presented model agrees with experimental data.

Despite unclear correlation with experimental data, the insights gained into possible effects of moisture absorption on bistable laminates and their snap-through behaviour are valuable contributions to the field.

In light of work from Gude [12] and Portela [6] it is suggested that currently no adequate finite element model exists to predict the actuation behaviour of MFC actuated bistable composite laminates. Therefore, this chapter will describe the formulation and validation of a coupled field finite element model to predict snap-through voltage and cured shape of MFC actuated bistable laminates using the commercial FE-software Ansys V11.0.

4.2 Experimental techniques

The following section will describe the manufacture of the active laminates (section 4.2.1) with the experimental techniques used to measure snap-through voltage and cured shape presented in section 4.2.2 and 4.2.3 respectively.

4.2.1. MFC actuated bistable composite laminates - Manufacture

Two cross-ply composite laminates were manufactured using Hexcel carbon fibre-epoxy pre-preg material cut and laid-up by hand and cured as described in section 2.2. A T700/M21 $[0/90]_T$ laminate measuring 170mm×170mm and a T800/M21 $[-30/60]_T$ laminate measuring 150mm×150mm were both manufactured from 268gsm unidirectional pre-preg material.

A Smart Materials 8557-P1 MFC actuator was bonded to the smooth surface, as the absence of the textured excess resin layer described in Chapter 2 ensured better bonding between MFC and the laminate. To ensure good adhesion, bond surfaces were roughened with emery paper and then cleaned with isopropryl alcohol before a thin layer of two-part epoxy was applied to both MFC and laminate. The MFC was positioned centrally on the laminate surface with PZT-fibre direction aligned with *y*-axis (Fig. 4.2); the active laminate was then placed between two flat aluminium plates under 200N clamping force for 24hr to allow the epoxy to cure.

The two stable states for the $[-30/60/0_{MFC}]_T$ laminate can be seen in Fig.4.2a and 4.2 b, as in Chapter 2, State A is defined by the resin layer being on the concave face. Stable states for the $[0/90/0_{MFC}]_T$ laminate can be seen in Fig. 4.2c and 4.2d with the axes of curvature for each stable state indicated as dashed lines.

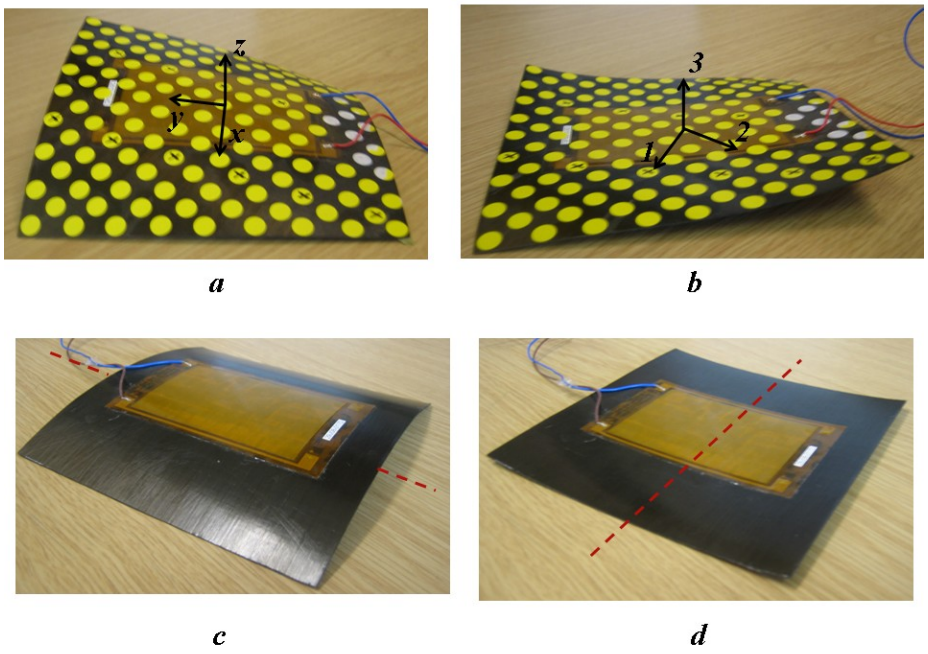

Fig.4.2: Cured shape of $[-30/60/0_{MFC}]_T$ laminate in State A (a) with global coordinate system (*a*) and State B showing local material coordinate system for uppermost 60˚ ply (*b*) and $[0/90/0_{MFC}]_T$ laminate in State A (c) and State B (d) with axis of curvature shown as dashed line.

4.2.2. MFC actuated bistable composite laminates – Snap-through measurement

A function generator was used to provide a DC step-input from zero volts up to the desired test voltage to a power amplifier (TREK PZD700 piezo driver). The system was manually calibrated to provide an output voltage of 200±0.1V for a 1V input signal. Actuation voltage was maintained for 60seconds after the step-input to account for the effects of piezoelectric creep [16].

After each test cycle (i.e. snap-through from State A to State B), voltage was reduced to zero and the laminate disconnected from the amplifier. The laminate was manually snapped into each stable state once before being reset to the starting condition and electrically discharged to ensure that no residual charge influenced system characteristics. The lowest snap-through voltage for both laminates was established via binary search in the range 0 - 1500V with 5V the smallest increment between test voltages.

During determination of MFC drive-voltage required to induce snap-through from State B into State A (states show in Fig 4.2) laminates rested on a polished steel table to ensure

laminate deflection was not impeded by frictional forces. Actuation voltage was applied via two single-core copper wires soldered to the MFC and secured to the table so that no additional mechanical load was imposed on the laminate.

4.2.3. MFC actuated bistable composite laminates – Cured shape

The cured shape of the laminates was measured using the motion capture techniques described in section 2.2.3 to provide full-field surface profiles for both the tested laminates.

The coordinate markings were placed on the laminate surface to which the MFC was bonded to maintain continuity between measurement of shape with and without MFC attachment, Fig.4.3 shows the laminate ready for measurement after MFC addition.

Camera position was varied between measurement of each stable state of both laminates so that as many reference markers as possible were visible to all three cameras. Camera position also varied to maintain the umbrella configuration advised by Nigg *et al* [17] to maintain measurement resolution. Once the system had been calibrated using 200mm × 200mm × 100mm calibration object the resolution of digitisation was calculated as 200μm for both the $[-30/60/0_{MFC}]_T$ and $[0/90/0_{MFC}]_T$ laminates within the Peak Motus software.

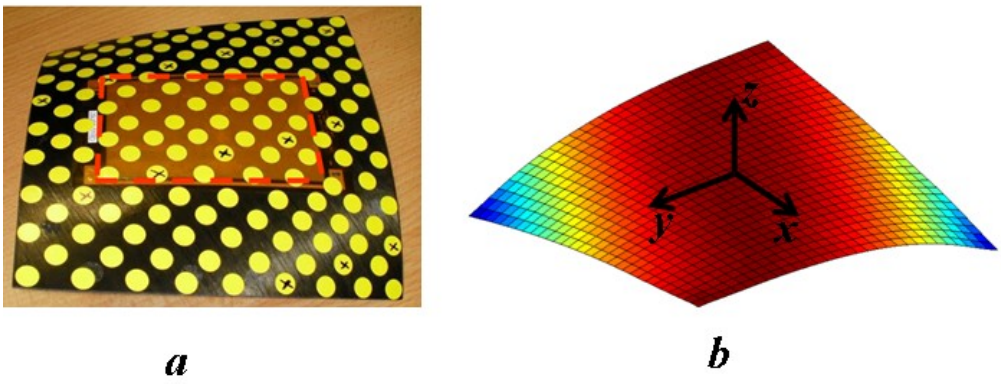

Fig.4.3: $[-30/60/0_{MFC}]_T$ laminate shown in State A with yellow reference markers, red dashed line indicates active area of MFC actuator (a) with the corresponding interpolated surface plot of State A laminate deflection generated from experimental coordinates (b).

As in section 2.2.3 the raw coordinates were exported to Matlab 2007a and rotated so that the coordinate system of the measured surface matched that shown in Fig. 4.3b. The interpolated surface was then constructed from the raw coordinates using the spline based interpolation method [18] for comparison with FE predictions.

4.3 Actuated composite model formulation

In order to predict cured shape and snap-through voltage for two piezoelectrically actuated bistable composite laminates the MFC model described in Chapter 3 was combined with the bistable composite model described in Chapter 2.

4.3.1 Active laminate model – Formulation

A non-linear large deflection finite element analysis was conducted to predict cured shape and snap-through voltage of two piezoelectrically actuated bistable composite laminates. Model convergence was controlled using the line search convergence control method described in Chapter 2 to improve numerical stability of the model [19, 20].

Formulation of this combined model was far more complex than the simple isotropic aluminium cantilever beam presented in Chapter 3 as it is necessary to capture:

(i) The bistable states of the unsymmetrical composite and the corresponding laminate curvature as a result of cooling the cured composite from elevated temperature

(ii) The influence of attaching the piezoelectric actuator on the curvature of the bistable composite – MFC combination and

(iii) The prediction of a snap-through event as a result of the application of a piezoelectric voltage to the MFC.

The $[-30/60/0_{MFC}]_T$ laminate was modelled using 20-node quadratic SOLID186 layered brick elements as described in section 2.3. The laminate was modelled as three volumes as seen in Fig 4.4a. A central strip measuring 57mm × 170mm was located underneath the MFC volume (point 1 in Fig. 4.4a) was meshed with 1360 elements while the two remaining volumes both measuring 56.5mm × 170mm (points 2 and 3 in Fig. 4.4a) were meshed with 816 elements each to create the mesh shown in Fig.4.4a. Maximum element aspect ratio within the composite laminate was 9.14. All coincident nodes within the laminate volume were then merged to ensure stress transfer during model solution.

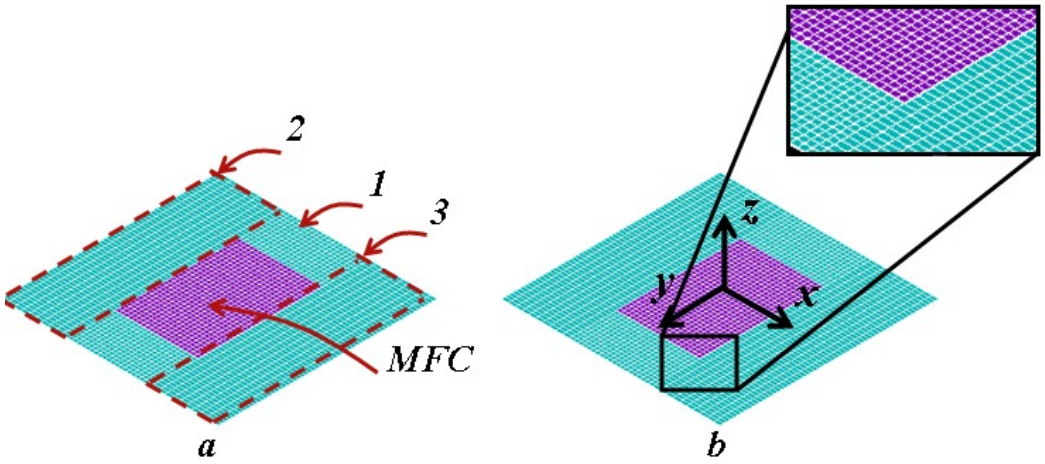

Fig.4.4: Meshed finite element model of $[-30/60/0_{MFC}]_T$ laminate showing three laminate volumes (1, 2 and 3) and centrally located MFC volume (a) overall mesh density and detail of coincident nodes near corner of MFC volume and global coordinate system (b).

To make use of the symmetry of the $[0/90/MFC]_T$ laminate, a symmetric boundary condition was imposed along the x = 0mm plane. This reduced the number of required elements by half with a strip measuring 29mm × 150mm meshed with 600 elements and a strip measuring 46.5mm × 150mm meshed with 600 elements modelling half the composite laminate.

The previously determined mean ply-thicknesses for laminates with ply angles of $[\theta/\theta+90]_T$ were used to approximate the laminates individual ply thicknesses. Table 4.1 shows the mean and standard deviation of ply thickness and total laminate thickness for a range of manufactured laminates with ply angles of $[\theta/\theta+90]_T$. The measured values presented in Table 4.1 were used to specify layer thickness values within the SOLID186 element formulation.

Table 4.1: Mean and standard deviation (σ) of ply and total laminate thickness for $[\theta/\theta+90]_T$ laminates made from 268gsm M21/T800.

	Idealised	Measured	
	Thickness (mm)	**Thickness (mm)**	**σ**
θ° ply	0.25	0.255	0.013
θ +90° ply	0.25	0.233	0.018
Resin layer	0	0.027	0.021
Total	0.5	0.515	0.045

Materials properties determined by batch testing undertaken by Airbus UK [21] for both T700/M21 and T800/M21 pre-preg material were used to define the composite material models with the values used shown in table 4.2.

Table 4.2: Elastic properties of 268gsm-1 T800/M21 material and T700/M21 * indicates values calculated using stress-strain relations described in [22].

Property [*unit*]	T700/M21	T800/M21
E_1 [GPa]	148	172
E_2 & E_3 [GPa]	7.8	8.9
G_{12} & G_{23} [GPa]	3.8	4.2
G_{23}* [GPa]	0.02	0.02
ν_{12} & ν_{13}	0.35	0.35
ν_{23}*	0.01	0.01
α_1 [1×10^{-7}]	-0.9	-0.9
α_2 & α_3 [1×10^{-5}]	3	3
E_r [GPa]	1.5	1.5
ν_r	0.4	0.4
α_r [1×10^{-5}]	9	9
Density [kgm^{-3}]	1072	1072

A volume measuring 85×57×0.3 mm was defined and ascribed the homogenised materials properties described in Chapter 2 (MFC model formulation)to represent the active area of the Smart Materials MFC8557P1 actuator. The actuator volume was located centrally on the upper surface of the laminate with MFC-fibre orientation aligned with the *y*-axis as indicated in Fig. 4.4b. This volume was meshed with 1200 SOLID226 elements with a maximum element aspect ratio of 9.33.

With all volumes meshed, coincident nodes on adjacent surfaces of laminate and MFC were merged along with coincident areas to ensure stress transfer between the laminate and MFC volumes. Due to the selection of higher order solid elements it is possible to accurately model bending deformation without multiple elements through the thickness [13] and hence as before in Chapters 2 and 3 a single element thickness was used.

With all volumes meshed and the MFC and laminate volumes merged, the laminate models were mechanically constrained from translation in all three orthogonal directions at the origin of the global coordinate system shown in Fig. 4.5a. Additionally the node at the point (0,0,0.515) was constrained from in-plane translation to ensure the laminate did not rotate about either the *x* or *y*-axis as shown in Fig. 4.5a.

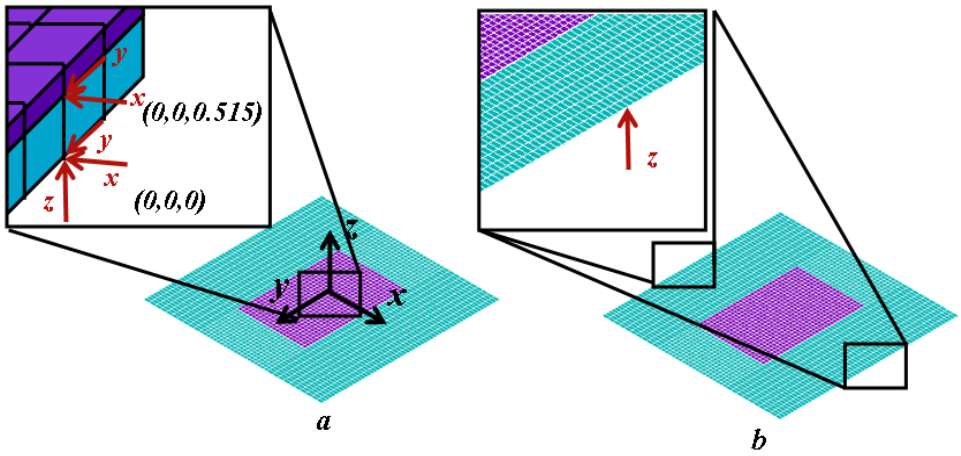

Fig.4.5: Meshed finite element showing mechanical constraint at origin of global coordinate system (a) and temporary mechanical constraint used to force model convergence to deformation State B (b).

Due to actuator orientation in the experimental sample (Fig. 4.2 b), the finite element model must converge to stable deformation State B before application of MFC drive-voltage. As noted in section 2.4.1 the bistable composite laminate model converges to stable State A when a temperature change is imposed upon the composite elements. In order to force the finite element solution to converge to the State B deformation state temporary displacement constraints were applied at locations of minimum State B deflection as indicated in Fig. 4.5b. As described in section 4.3.2 these temporary constraints were removed after completion of the thermal loadstep.

The stable cylindrical state with the largest value of maximum deflection was designated State A as shown in Fig 4.2a; this is the state where the resin-layer lies is on the concave surface. State B shown in Fig. 4.2b is the secondary state, showing reduced maximum deflection and the resin layer on the convex surface.

4.3.2. Active laminate model – Model solution

With the model mechanically constrained as described in section 4.3.1, the cool down of the composite laminate and attachment of the MFC actuator was modelled in a 4 step process:

(i) Temperature change of -160K applied to composite elements to ensure laminate converges to State B

(ii) Application of an offset voltage to compensate for thermal stress imposed on MFC volume

(iii) Removal of temporary displacement constraints (as shown in Fig. 4.5b)

(iv) Application of MFC drive-voltage until snap-through into State A

Fig. 4.6a shows the laminate model at the cure temperature of 180°C with Fig. 4.6b showing the highly curved State At laminate temperature of 20°C with the temporary displacement constraints described in section 4.3.1 still in place. Fig. 4.6b represents stage (I) of the solution process detailed above.

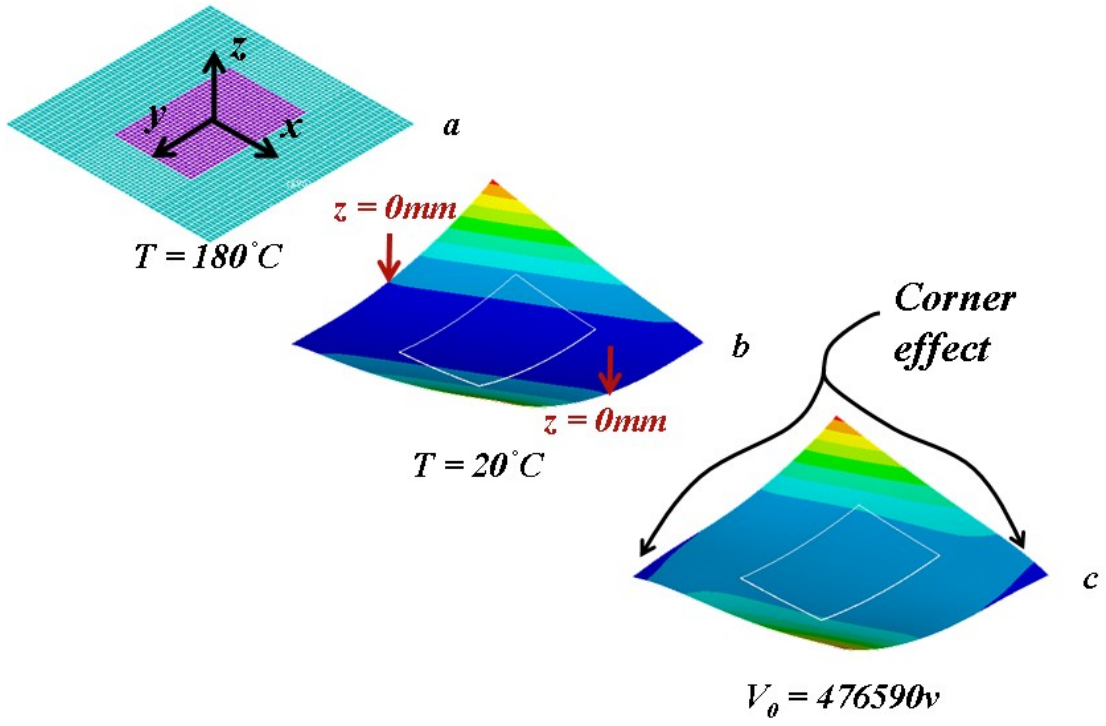

Fig.4.6: Finite element prediction of cured shape for $[-30/60/0_{MFC}]_T$ laminate at cure temperature of 180°C (a) room temperature of 20°C (b) and in stable deformation State B with offset voltage (V_0) applied (c).

Fig. 4.6c shows the laminate model after application of the offset voltage (V_0) and removal of the temporary displacement constraints, this represents stages (ii) and (iii) of the solution process. During application of MFC drive voltage (stage (iv) in the solution process) the laminate flattened as MFC drive-voltage and the resulting actuation strain increased before undergoing the sudden transition into deformation State A (snap-through).

To model the cool down from elevated curing temperature of the composite laminate a temperature difference was applied to the composite elements. The temperature constraint was applied only to composite (SOLID186) elements while the coupled field (SOLID226) elements within the MFC volume were not subject to the imposed temperature constraint. Since the MFC is attached to the bistable composite at room temperature the experimental samples do not undergo thermal loading. The temperature drop applied to the composite elements is determined by the change in temperature between the cure temperature of 180°C and the ambient temperature at which the laminate shape was measured of around 20°C.

As described in section 3.3.1 the electrical degree of freedom for the SOLID226 elements was coupled for nodes of equal *z*-coordinate at 5mm intervals along the *y*-axis. This constraint ensures that applied field remains well aligned with the poling direction of the MFC model and minimise variation in the field along the y-axis of the MFC volume.

During model development it was noted that solutions of bistable laminates with the MFC model integrated exhibited significantly reduced curvature and did not exhibit a second stable configuration but rather always adopted the State A configuration after application of the thermal load step. This phenomenon was attributed to the interaction of the MFC and laminate models under the action of the imposed thermal load not capturing the conditions within the physical specimen.

Within the FE model only composite elements were subjected to the imposed thermal load, nevertheless MFC-elements experienced significant elastic strain comprising the thermal strain of the composite and the mechanical strain caused by laminate deformation deforming the MFC volume. As nodes within the MFC volume are merged with those on the laminate surface before the temperature change is imposed, both mechanical and thermal strains were imposed upon the MFC model. This introduces an additional mechanical stress within the MFC volume which does not represent the experimental loading.

By contrast, under experimental conditions thermal strains experienced by the laminate during cool-down do not contribute to the stress field within the MFC as the MFC is only bonded to the laminate after it has cooled to room temperature. The additional thermal strains

resulted in a stress state within the MFC which was a superposition of the mechanical and thermal stresses caused by laminate cool down.

In order to compensate for the superposed thermal stress an 'offset voltage' was applied to the MFC. Via the converse piezoelectric effect the offset voltage created a stress field of equal magnitude but of opposite sign to that created by the imposed thermal strain.

The total thermal strain in the portion of laminate bonded to the MFC was calculated by considering the MFC as an elastic constraint resisting the thermal contraction. Observed strain in both laminate and MFC due to thermal contraction of the composite laminate must be equal, hence force equilibrium leads to:

$$\varepsilon_M = \frac{\varepsilon_T K_1}{K_1 + K_2} \tag{4.1}$$

where ε_M is the observed strain within the MFC, ε_T and K_1 are the unconstrained thermal contraction and transformed reduced stiffness of the layer to which the MFC is bonded while K_2 is the MFC stiffness; all properties are measured in the *y*-direction and are aligned with MFC-fibre orientation. Transformed reduced stiffness may be calculated from the orthotropic elastic constants of each layer using [22]:

$$\overline{Q_y} = Q_{11}\cos^4\theta + 2(Q_{12} + 2Q_{66})\sin^2\theta\cos^2\theta + Q_{22}\sin^4\theta \tag{4.2}$$

where $\overline{Q}_y$ is the transformed reduced stiffness in the *y*-direction of the global coordinate system [GPa], Q_{ij} is the reduced stiffness values measured in the material coordinate system [GPa] and θ the orientation of the material coordinate system with respect to the global coordinate system. In this case the global coordinate system whose first principal direction is the *y*-direction as shown in Fig 4.7.

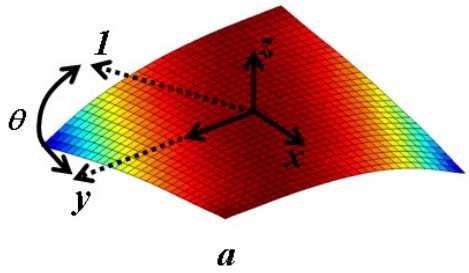

Fig.4.7: $[-30/60/0_{MFC}]_T$ laminate in deformation State B showing orientation material coordinate system of the uppermost 60° layer, showing angle θ between the *1*-direction of the local system and *y*-direction of the global system.

The offset voltage required to compensate for the imposed thermal strain may be calculated using:

$$V_O = \varepsilon_M S_E / d_{33} \tag{4.3}$$

where V_0 is the offset voltage [V], ε_M the observed strain in the MFC and S_E is the electrode separation in the FE model [m].

The volt degree of freedom for nodes on the y = 42.5mm face of the MFC model (indicated in Fig. 4.8) were coupled and forced to the offset voltage value while nodes on the y = -42.5mm face were constrained to zero volts. This created an effective electrode separation of 85mm in the FE model. Once the offset voltage was applied across the MFC model, the temporary displacement constraints discussed above were removed and the model remained in stable State B.

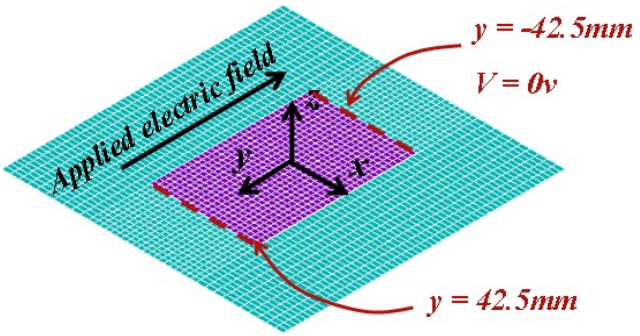

Fig.4.8: Finite element model of $[-30/60/0_{MFC}]_T$ laminate showing electrical constraint at y = -42.5mm and location of drive-voltage application at y = 42.5mm and the resulting direction of applied electric field.

Piezoelectric actuation was modelled by applying a voltage constraint (V_c) on nodes at y = 42.5mm to create a change in the electric field in the MFC equal to its maximum operational electric field strength ($3MVm^{-1}$). Values of ΔL, V_0 and V_c for the two modelled laminates are shown in table 4.3.

Table 4.3: Values for strain in MFC due to thermal load ε_M , offset voltage (V_0) and maximum drive voltage (V_c) for $[0/90/0_{MFC}]_T$ and $[-30/60/0_{MFC}]_T$ laminates.

	$[0/90/0_{MFC}]_T$	$[-30/60/0_{MFC}]_T$
ε_M	1.00×10^{-3}	2.61×10^{-3}
V_0 [V]	182038	476590
V_c [V]	-72962	221590

The voltage constraint was applied as a ramp change from the offset voltage (V_0), with several intermediate time steps specified between V_0 and V_c to ensure that the model followed the load path accurately. As specified for non-linear buckling analysis in situations where the arc-length method is not implementable [13], snap-through was identified as the lowest value of voltage constraint at which the no longer model converged to State B (i.e. snap-through into State A had occurred). The APDL code file used to create and solve the $[-30/60/0_{MFC}]_T$ model is presented in Appendix 2.

4.4 Results and discussion

This section will compare the cured shape and snap-through voltages predicted by the FE model described in section 4.3 to the experimental measurements described in section 4.2.

4.4.1 Cured shape

Predicted shape of a $[-30/60/0_{MFC}]_T$ active laminate (bistable composite laminates with MFC attached) is shown in Fig.4.9 with significant deviations from cylindrical curvature seen at points A and C. It is of note that the laminate adopts a saddle-shape after MFC addition with a significantly flattened section directly underneath the MFC itself (point B). This reduction in curvature underneath the MFC indicates that the bending stiffness of the actuator has a significant effect on the cured shape of the laminate.

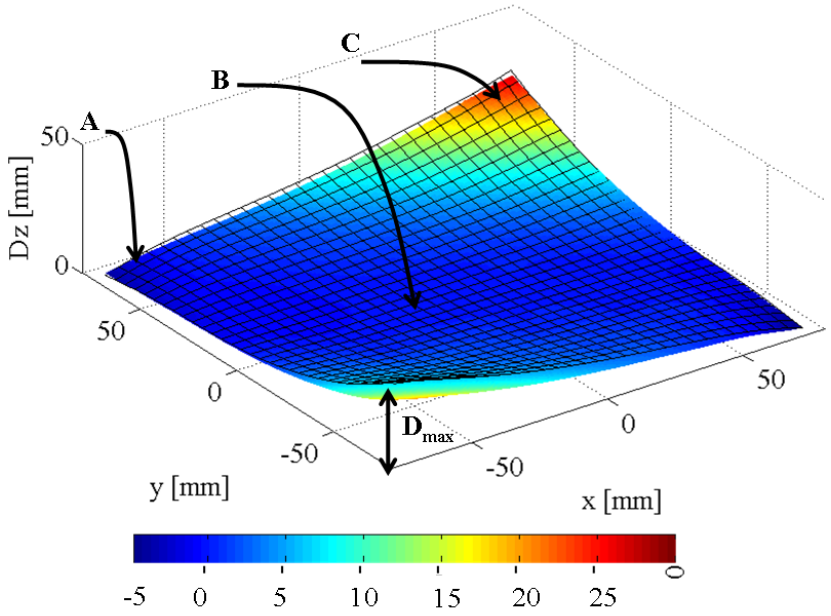

Fig.4.9: Interpolated surface plot of 149 experimentally measured surface coordinates showing the $[-30/60/0_{MFC}]_T$ laminate in State B with FE-predicted surface overlaid as mesh.

When comparing maximum deflections with respect to the laminate geometric centre (D_{max}) before and after MFC-bonding, the influence of MFC addition is clear with measured deflections of 38.2mm for the composite laminate and reducing to 22.5mm after MFC addition. Finite element prediction of composite laminate deflection of 33.49mm maximum deflection (D_{max}) is 12.3% lower than experimental measurement, whereas after MFC addition

D_{max} is predicted to be 25.2mm, 12.3% higher than experimentally measured laminate deflection.

Figure 4.10 shows interpolated surface plot of experimental measurement of laminate deflection for the $[0/90/0_{MFC}]_T$ laminate with the FE predicted values showing close agreement and capturing the significant reduction in laminate deflection in State B caused by the additional bending stiffness of the MFC.

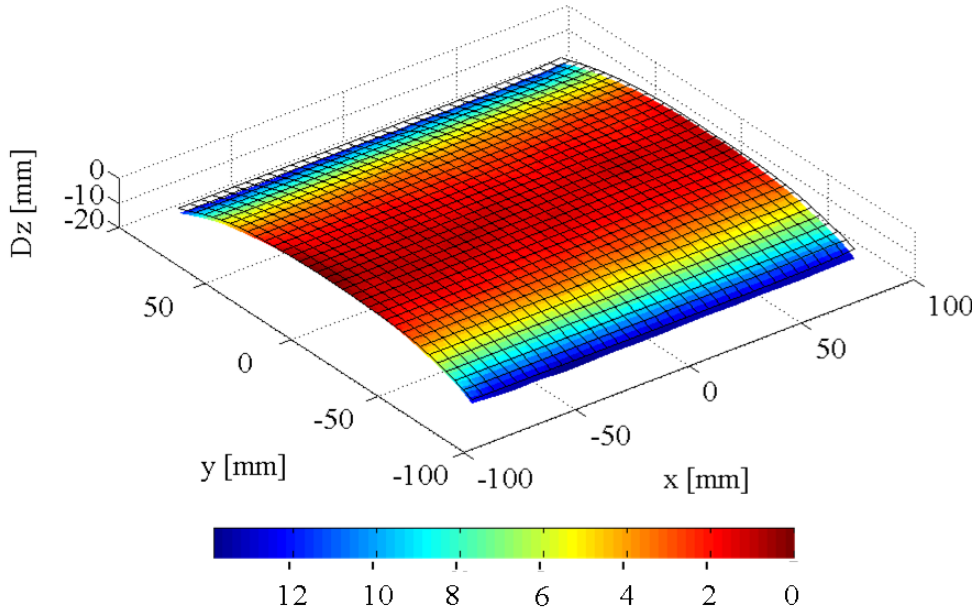

Fig.4.10: Interpolated surface plot based on 283 experimentally measured surface coordinates showing the $[0/90/MFC]_T$ laminate in State B with FE-predicted surface overlaid as mesh ***(****laminate shown inverted for clarity of presentation****).***

Maximum deflection for the $[0/90/MFC]_T$ laminate after MFC addition was predicted to be 10.73mm for State B, 16.0% lower than experimentally measured maximum deflection of 12.77mm. As seen in Fig. 4.9 the global curvature and the presence of a local reversal of curvature beneath the MFC is well predicted however the magnitude of laminate deflection is significantly lower in the FE model compared with experiment. Table 4.4 shows finite element predicted and experimentally measured maximum laminate deflections along with prediction error for both $[-30/60/0_{MFC}]_T$ and $[0/90/0_{MFC}]_T$ laminates. Due to equipment availability it was not possible to measure the cured shape of the $[0/90/MFC]_T$ laminate before MFC addition.

Table 4.4: Finite element predicted and experimentally measured maximum laminate deflection values with prediction error for both $[-30/60/0_{MFC}]_T$ and $[0/90/0_{MFC}]_T$ laminates.

Bistable Laminate	Experimental measurement [mm]		Finite element prediction [mm]			
	Before MFC addition	After MFC addition	Before MFC addition	Prediction error [%]	After MFC addition	Prediction error [%]
$[0/90/MFC]_T$	-	12.77	-	-	10.73	-16.0
$[-30/60/MFC]_T$	38.21	22.48	33.49	-12.3	25.20	12.1

The discrepancy between predicted and experimentally measured shape after MFC-bonding may be due to the offset voltage causing transverse actuation strain (strain in the x-direction of Fig. 4.8) via the d_{31} piezoelectric constant. This transverse actuation stress is not physically representative. The observed strain in the *x*-direction imposed on the MFC volume during cool down of the $[0/90]_T$ laminate is 0.105ppm (as calculated using equation 4.1), while the application of the offset voltage creates opposing strain of -18.2ppm. This large mismatch between the imposed thermal strain and the strain generated via application of offset voltage could lead to inaccuracies in predicted laminate deflection.

This discrepancy between small transverse thermal strain applied to the MFC volume and the large strain created by the actual applied offset voltage (V_0) is an unavoidable consequence of offsetting thermally induced stresses through longitudinal actuation via d_{33} coupling.

When using coupled field elements, varying the MFC element stiffness as proposed by Portela [6] does not negate the need for the offset voltage. The thermal strain imposed on the MFC elements during temperature change is still present when the element stiffness matrix is returned to representative values. This non-zero strain causes an opposing piezoelectric stress as observed in the present work.

By using the element death facility within Ansys V11.0 which artificially sets element stiffness to zero during specified sections of the solution, it is possible to erase the strain

history of an element without affecting links with other structures it is joined to. Once the affected elements are reactivated their stiffness matrices are calculated for their new deformed shape but the strain matrix remains empty. Implementation of this facility would allow accurate analysis of the MFC bonding process without the need for offset voltage, however element birth and death is not an option within the SOLID226 element formulation and so at present the use the offset voltage method is unavoidable within Ansys V11.0.

The additional bending stiffness of the MFC which reduces maximum laminate deflection after bonding is calculated based on the assumption of transverse isotropy in the MFC. The standard stiffness matrix formulation shown in equation 3.1 predicts the two through thickness shear moduli to be 5% lower than the in-plane shear modulus. Dano [1] used a representative volume element of the Smart Materials M8557-P1 actuator to calculate the through thickness shear moduli. These finite element predictions showed the through thickness shear moduli to be approximately half the in-plane shear modulus. This potential overestimation of the shear stiffness of the MFC volume may also contribute to the observed discrepancy between predicted and observed laminate deflection of the $[0/90]_T$ laminate although it is more likely that variations in laminate composition and ply-angle caused by hand lay-up are responsible for the prediction error in the $[-30/60]_T$ sample.

As discussed in Chapter 2, variations in laminate composition and ply orientation commonly seen during hand manufacture create significant variations in observed laminate deflection. Due to the high sensitivity of predicted deflection to laminate composition, it is likely that small deviations from the mean MFC thickness and PZT fibre volume fraction would also introduce errors. The combined effect of these unknown variations in laminate and MFC composition could account for a large part of the observed errors in predictions of laminate deflection.

For problems in which precise cured shape is vital the presented method predicts maximum laminate deflection to within 16% which would not allow precise aerodynamic analysis of morphing structures for aerospace applications. Despite limitations in quantitative prediction the model captures the cured shape and local reversals of curvature very well. The next section will compare predicted and experimentally measured snap-through voltages for the two actuated laminates.

4.4.2 Snap-through results

Finite element prediction of snap-through voltage was achieved for both laminates, with non-linear buckling analyses predicting behaviour prior to snap-through. The model to occur at 645V while experimental observation showed that a drive voltage of 670V induced snap-through predicted snap-through of the [0/90/MFC] T laminate. In the case of the $[-30/60/MFC]_T$ laminate predicted and observed snap-through voltages were 677V and 700V respectively.

The predicted snap-through voltages are in excellent agreement with the measured values with errors compared to experiment of less than 4.5% in both cases. This excellent predictive accuracy significantly improves upon previously presented models [6, 12] in which no correlation with experimental data was possible due to complete data not being available.

Delayed snap-through was observed at voltages immediately below monotonic snap-through voltage when drive-voltage applied for a prolonged time period. This was due to displacement creep of the MFC actuators [16] and could be compensated for in industrial applications using time varying input signals [15] and closed-loop control.

Due to the discontinuity of the voltage-deflection curve associated with snap-through (shown in Fig. 4.11) the Newton-Raphson solution procedure was not able to predict laminate response throughout the entire load cycle even with line search convergence control enabled. Under prediction of snap-through voltage by the FE-model is likely due to the inability of the presented model to fully track the discontinuous voltage-deflection curve for the laminate.

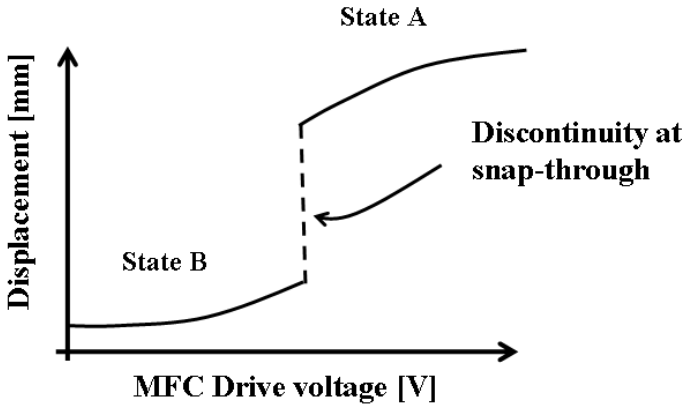

Fig.4. 11: Schematic of discontinuous voltage-deflection characteristic for snap-through between deformation State B and State A.

It has been observed [6] that bistable laminates deform continuously within a single deformation State as drive voltage is increased but the observed response to increasing actuation strain is not linear. Near to the snap-through voltage the gradient of voltage-deflection graph increases rapidly before a discontinuity occurs as the laminate snaps between the two stable states. It is not possible for line search to follow the discontinuous portion of this behaviour and therefore the model fails to converge, hence snap-through is predicted when the gradient first exceeds an internally specified maximum.

As reported in Portela [6] snap-through under MFC actuation occurs very soon after peak actuation stress, hence prediction accuracy of the presented model is not thought to be significantly affected. In order to fully track voltage-deflection behaviour of bistable laminates under MFC actuation implementation of non-linear stabilisation or the arc-length solution methods is necessary [6]. However neither non-linear stabilisation nor the arc-length solution methods are currently implementable with SOLID226 elements.

Therefore the presented model represents the most appropriate formulation within the Ansys V11.0 finite element software and has significantly extended modelling capability and accuracy of coupled field finite element models in the prediction of actuation behaviour of bistable composites.

4.5 Conclusion

This chapter has developed and experimentally validated using Ansys V.11.0 finite element software.

The key conclusions drawn from the work presented in this chapter are:

- A coupled field model of to predict cured shape and snap through voltage an MFC actuated bistable composite laminate is presented.
- Prediction of cured shape after MFC addition is in good agreement with experimental measurement with maximum error between prediction and measured values of 12.3%.
- Snap-through voltage for square bistable laminates was predicted to within 4.5% of experimentally measured values.

The MFC model presented in Chapter 3 of this thesis was integrated with the model for bistable composite laminates described in Chapter 2 to predict cured shape and snap-through behaviour of two cross-ply bistable laminates. Challenges associated with integration of coupled field elements with the composite structure have been addressed through application of an offset voltage to compensate for undesired thermal stresses within the MFC volume.

Prediction of cured shape after MFC addition is in good agreement with experimental measurement with maximum error between prediction and measured values of 12.3%. The change in cured shape caused by MFC addition and localised variation in curvature were predicted, and quantitative prediction of laminate deflection agrees with experiment sufficiently to aid prototype design.

Precise determination of cured shape remains a challenge as maximum error between predicted and measured values of laminate deflection of 2.8mm (12.3%) would prevent detailed design studies using the presented model. The presented model is based entirely on physically representative values for temperature and, as is common within commercial finite element analysis [24], quantitative prediction accuracy could easily be improved by combining empirical data to scale the imposed thermal load.

Detailed characterisation of laminate composition of each specimen could further enhance prediction accuracy however this would limit the use of the model as a predictive design tool.

Snap-through voltage for both $[0/90/0_{MFC}]_T$ and $[-30/60/0_{MFC}]_T$ laminates were predicted to within 4.5% of experimental measurements which is a significant improvement upon previously unvalidated attempts at predicting snap-through [6, 12]. By including correctly formulated homogenised MFC properties as well as appropriate electrical constraints the presented model improves and extends the applicability of finite element techniques available for mechanism design of morphing structures based on bistable composites beyond what has previously been possible.

This model fulfils the requirement of snap-through voltage prediction for piezoelectrically actuated bistable laminates for use as a design tool, and will be extended to predict the actuation behaviour of an adaptive bump structure based on integrated bistable segments in Chapter 7.

In the following chapter the response of bistable composite laminates to changes in ambient temperature will be experimentally characterised and the finite element model presented in Chapter 2 will be extended to predict laminate deflection.

4.6 Reference list

1. Dano, M. L., Gakwaya, M., and Julliere, B. (2008). "Compensation of thermally induced distortion in composite structures using macro-fiber composites." Journal of Intelligent Material Systems and Structures, 19(2), 225-233.
2. Choi, S. C., Park, J. S., and Kim, J. H. (2007). "Vibration control of pre-twisted rotating composite thin-walled beams with piezoelectric fiber composites." *Journal of Sound and Vibration*, 300(1-2), 176-196.
3. Hyer, M. W. (1981). "Calculations of the Room-Temperature Shapes of Unsymmetric Laminates." *Journal of Composite Materials*, 15, 296-310.
4. Schultz, M. R., and Hyer, M. W. (2003). "Snap-through of unsymmetric cross-ply laminates using piezoceramic actuators." *Journal of Intelligent Material Systems and Structures*, 14(12), 795-814.
5. Ren, L. B. (2008). "A theoretical study on shape control of arbitrary lay-up laminates using piezoelectric actuators." *Composite Structures*, 83(1), 110-118.
6. Portela, P., Camanho, P., Weaver, P., and Bond, I. (2008). "Analysis of morphing, multi stable structures actuated by piezoelectric patches." *Computers & Structures*, 86(3-5), 347-356.
7. Etches, J., Potter, K., Weaver, P., and Bond, I. (2009). "Environmental effects on thermally induced multistability in unsymmetric composite laminates." *Composites Part A-Applied Science and Manufacturing*, 40(8), 1240-1247.
8. Betts, D. N., Salo, A. I. T., Bowen, C. R., and Kim, H. A. (2010). "Characterisation and modelling of the cured shapes of arbitrary layup bistable composite laminates." *Composite Structures*, 92(7), 1694-1700.

9. Diaconu, C. G., Weaver, P. M., and Mattioni, F. (2008). "Concepts for morphing airfoil sections using bi-stable laminated composite structures." *Thin-Walled Structures*, 46(6), 689-701.

10. Mattioni, F., Weaver, P. M., and Friswell, M. I. (2009). "Multistable composite plates with piecewise variation of lay-up in the planform." *International Journal of Solids and Structures*, 46(1), 151-164.

11. Hufenbach, W., Gude, M., and Kroll, L. (2002). "Design of multistable composites for application in adaptive structures." *Composites Science and Technology*, 62(16), 2201-2207.

12. Gude, M., and Hufenbach, W. (2006). "Design of novel morphing structures based on bistable composites with piezoceramic actuators." *Mechanics of Composite Materials*, 42(4), 339-346.

13. ANSYS Inc . 2007. Structures with Geometric non-linearities. Chapter 3. Ansys Theory Reference V11.0

14. Williams, R. B., Inman, D. J., and Wilkie, W. K. (2006). "Nonlinear response of the macro fiber composite actuator to monotonically increasing excitation voltage." *Journal of Intelligent Material Systems and Structures*, 17(7), 601-608.

15. Jung, H., Shim, J. Y., and Gweon, D. G. (2001). "Tracking control of piezoelectric actuators." *Nanotechnology*, 12(1), 14-20.

16. Jung, H., and Gweon, D. G. (2000). "Creep characteristics of piezoelectric actuators." *Review of Scientific Instruments*, 71(4), 1896-1900.

17. Nigg, B. M., and Cole, G. K. (2007). "Optical methods." *Biomechanics of the musculo-skeletal system*, W. Herzog, ed., John Wiley and Sons, Chichester, 362-391.

18. Sandwell, D. T. (1987). "Biharmonic Spline Interpolation of Geos-3 and Seasat Altimeter Data." *Geophysical Research Letters*, 14(2), 139-142.

19. Schweizerhof, K. H., and Wriggers, P. (1986). "Consistent linearization for path following methods in nonlinear FE analysis." *Computer Methods in Applied Mechanics and Engineering*, 59(3), 261-279.

20. ANSYS Inc . 2007. Newton-Raphson Procedure. Chapter 15. Ansys Theory Reference V11.0

21. Desailloud, M. (2004). "Modulus harmonisation of HS & IM tape composite materials." *Rep. No. ESAC_RP0306315*, Airbus Section 530.

22. Hyer, M. W. (1998). "Stress Analysis of Fibre Reinforced Composite Materials." WCB/McGrawhill, Boston, Mass. ISBN: 0-071-15983-5

23. Potter, K., Weaver, P., Seman, A. A., and Shah, S. (2007). "Phenomena in the bifurcation of unsymmetric composite plates." *Composites Part A: Applied Science and Manufacturing*, 38(1), 100-106.

24. Bathe, K. (1982). "Finite element procedures in engineering analysis." Prentice-Hall, London. ISBN: 0-133-17305-4

Chapter 5 - Response of bistable composite laminates to thermal loads

In Chapter 4 a coupled field finite element model was developed and validated to predict snap-through behaviour of a piezoelectrically actuated bistable composite laminate and results compared to experimentally determined values. The presented model is shown to be accurate in predicting behaviour of multistable composite structures with integrated MFC actuators operating at room temperature, however before multistable components may be deployed in civil aviation applications their response to expected service conditions must be more fully understood.

In section 5.1 of this chapter the service conditions most likely to affect performance of multistable composite structures will be discussed and it is concluded that their response to thermal loading of passive bistable composite laminates is of particular importance. Therefore, in section 5.2 the experimental techniques used to measure laminate deflection when exposed to variations in ambient temperature are explained. In section 5.3 the finite element model presented in Chapter 2 is extended to predict the structural response of a bistable composite laminate under thermal and gravitation loading. Model outputs are compared to data collected from experimental characterisation and observed non-linearities in the temperature-deflection relationship discussed in section 5.4.

5.1. Introduction

Within the civil aviation industry any critical structures must gain certification of safety before use in flight. Therefore even if prototype testing proves that morphing structures are capable of appropriate deformation and of supporting likely service loads their performance under widely varying operating conditions must be established before they can be deemed suitable for use in civil aviation applications.

The ability of composite structures to withstand minor damage without a dangerous reduction in strength is a highly active area of research with ongoing efforts to more fully understand damage mechanisms [1, 2], modelling [3] and mitigation techniques [4-6]. Due to the large elastic strain within the laminate [7, 8] during snap-through and the sensitivity of structural response to changes in laminate composition (shown in Chapter 2) it is likely that prediction of damage mechanisms and their influence on morphing capabilities will require significant development of both damage models and careful implementation within bistable composite models.

While the damage tolerance of bistable structures is of vital importance to their viability within civil aviation structures, the potential range of application of pristine components must first be established. In order to establish potential operational range issues relating to moisture absorption and resistance to thermal load must first be addressed.

It is widely known that the epoxy resin systems commonly used in aerospace composite materials absorbs atmospheric moisture [9, 10] causing an isotropic expansion proportional to the moisture expansion coefficient [11, 12]. The resin expansion caused by moisture absorption relaxes the residual stress state caused by thermal contraction during post cure cooling from elevated temperature [13]. This relaxation of the residual thermal stress state in the laminate causes a reduction in the maximum laminate deformation in both stable states.

Etches [14] and Portela [15] have observed the reduction in laminate deformation caused by moisture absorption in bistable laminates as well as using finite element and analytical techniques to predict the influence of moisture absorption on both cured shape and snap-through load of bistable laminates.

The analytical model presented by Etches [14] was based on previous analytical models presented by Mattioni and provided acceptable agreement with experimental measurements of laminate deflection. More interestingly, the reduction in laminate deflection attributed to

moisture absorption was accurately predicted hence it may prove useful as a scoping tool for investigating the influence of environmental effects on bistable structures.

With preliminary studies able to predict the influence of moisture absorption on the curvature of bistable laminates in place, the challenges of limiting any detrimental effects on actuation performance can be tackled. However the related and more complex issue of the influence of imposed thermal loading on the cured shape and snap-through load of bistable laminates has yet to be investigated.

As the bistable components discussed within this work are formed through residual thermal stresses as discussed in Chapter 1, it is obvious that their response to thermal loading is one area which may limit their utility. For applications within the fuselage of a civilian aircraft, it is likely that the multi-stable structures will be exposed to wide ranging thermal conditions which may affect their stable shapes and load carrying capacity. For example, during a typical passenger jet flight cycle the temperature may vary in the range -60°C to 40°C [16], hence to operate reliably it is vital that the response of any integrated structures is well understood and may be accurately predicted.

In addition to these undesirable thermal effects, the potential use of thermal loading as an actuation method to produce 'thermally active laminates' has also been proposed by investigators; internal heat sources are embedded within composite structures formed using materials with different coefficient of thermal expansion (CTE) to provide actuation loads.

While thermally active metal laminates are common (bimetallic strips being widely used as temperature sensors in household thermostats) active composite laminates are less well understood. The concept of a thermally activated morphing laminate has been demonstrated in fibre-metal composites to produce a shape change within a simple plate structure [17] as seen in Fig. 5.1. Electrical resistance heating provided by a layer of low CTE carbon fibre reinforced polymer provides sufficient thermal load to induce bending when bonded to a metallic layer of high CTE [17, 18].

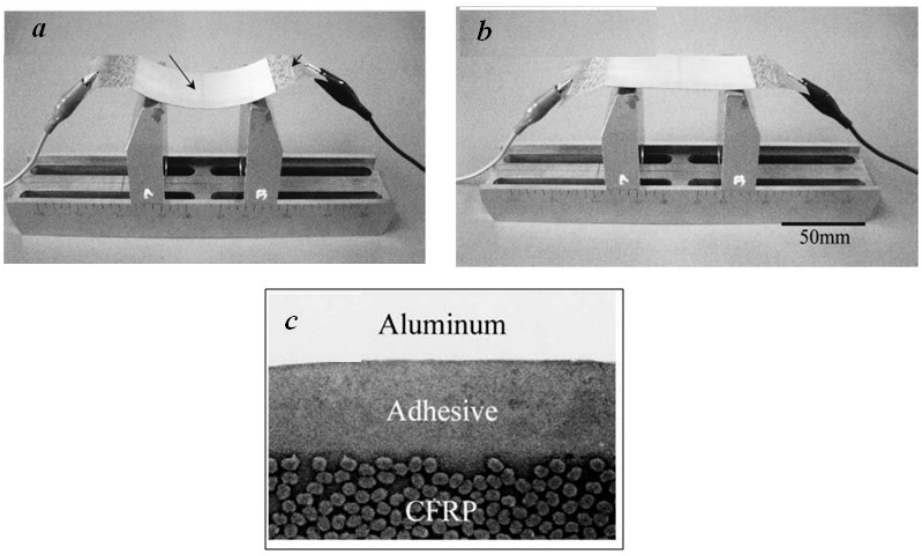

Fig.5.1: Thermally active laminate comprising high coefficient of thermal expansion (CTE) and low CTE carbon/epoxy fibre composite layer at room temperature (a) and 753K (b) with optical microscopy image of laminate cross section (c). (*figure adapted from [17]***).**

Recent work has also developed a thermally active fibre-composite laminate called CBCM (Controlled Behaviour Composite Material). This concept utilises Joule heating within electrically excited carbon yarns woven into standard composite plies to act as electrical heating elements. This internal heat source combined with the different thermo-mechanical properties of each composite ply within the laminate induces a change in shape of the structure [19]. These active laminates may be of interest to morphing structures designed to be deployed in non-time critical situations (such as transitioning between cruise and landing configurations) but for small scale control structures the low operating frequency limits their utility.

Analytical techniques have been developed with some success to predict the deformation of laminated plates [20, 21] and laminated strips [22] to imposed thermal loading, however these techniques are not able to predict the snap-through behaviour of bistable laminates or the complex deformation states resulting from the edge and corner effects described in Chapter 2.

The models put forth by Hyer [23], Dano [24] and other investigators [25-27] have been shown to provide adequate accuracy for prediction of maximum laminate deflection of bistable laminates at room temperature, however comparatively little work has been conducted to determine thermal loading characteristics of bistable laminates.

Hamamoto and Schlecht have both investigated the influence of resin system thermo-mechanical properties on the post-cure cooling of bistable laminates [28, 29]. With the changes in epoxy elastic constants, coefficient of thermal expansion and Poisson's ratio all being accounted for in the analysis of post cure cooling. Despite providing an insight into the likely influence of resin system properties on thermally induced deformation, laminate shape was only measured at room temperature so validation of the resin system model was not possible.

To date no work has been presented on the response of cured bistable laminates subjected to thermal loading. Section 5.2 of this chapter will describe experimental measurement of laminate deflection of a bistable $[0/90]_T$ laminate under imposed thermal loading. A finite element model which includes measured laminate composition as described in Chapter 2 and gravitational loading will then be presented in section 5.3. FE-model predictions of laminate deflection will be compared to experimental measurements in section 5.4. In addition, identified residual laminate curvature observed when laminate temperature is returned to cure temperature is discussed and proposed as a measure of the residual stress state caused by chemical shrinkage of the epoxy resin during the curing process.

5.2. Experimental techniques

In this section the motion capture techniques used to measure the deformation of a bistable laminate subjected to thermal loading caused by changes in ambient temperature are described.

A $[0/90]_T$ laminate of T800/M21 pre-preg material was manufactured and cured according to the manufacturers instructions as described in section 2.2. After cooling from cure temperature the laminate was trimmed to measure 250mm×80mm to remove resin rich areas as well as defects caused by thermocouple placement.

In order to measure deflection in response to changes in ambient temperature the laminate was balanced on a small metal block inside a Gallenkamp vacuum oven so that the front edge of the laminate lay on the *xz*-plane parallel with the plane of the oven door as shown in Fig 5.2.

Changes in laminate temperature were measured via a type-K thermocouple inserted in a separate two ply T800/M21 laminate located at the base of the oven. Though this approach may introduce small errors in laminate temperature caused by the different physical location of the thermocouple it is felt the reduction of mechanical load due to thermocouple wiring and placement from the test laminate would cause greater errors in deflection.

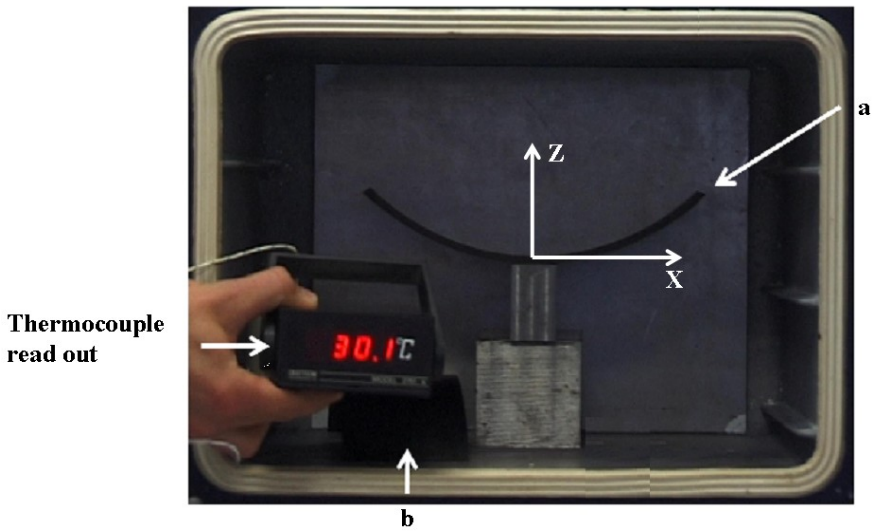

Fig.5.2: Test laminate (a) and secondary laminate with thermocouple (b) inside vacuum oven shown with digital thermocouple read-out and measurement coordinate system with y-direction perpendicular to xz-plane and positive toward the camera.

Measurement of laminate profile was carried out utilising standard motion analysis techniques described in Bowen *et al.* [30]. A digital video camera recorder (Sony DCR-TRV 900E, Sony Corporation, Japan) was positioned perpendicular to the *xz*-plane, in which the bending of the laminate occurred. The camera was located 2.46 m from the *xz*-plane at the height of the middle of the oven and operated at 50 fields per second.

A rectangular calibration object of 303 mm × 247 mm was located at the back of the oven (parallel to the *xz*-plane at *y*=-130mm) with the camera view restricted just outside the calibration object to provide known coordinates for system calibration. The calibration object dimensions were scaled to the front edge of the laminate using trigonometry to allow measurement of laminate edge coordinates.

The oven was then heated from room temperature to over 170°C over the course of 20 minutes. Due to the slow increase in temperature it is unlikely that any significant spatial variation from the measured laminate temperature is present in the test laminate. A video clip of the laminate was taken at 10°C intervals (from 30°C to 170°C) by briefly opening the oven door when the laminate had reached the required temperature.

These video clips were subsequently imported to Peak Motus® (v. 8.5, Vicon, USA) image analysis software to enable the deformed the edge of the laminate to be manually digitised. Digitisation was achieved by manually selecting 31 points in a random fashion along the *y*=0mm edge of the laminate. Two further points were selected at either end of the laminate to define the laminates corner locations.

Despite careful set up, a slight roll of the camera of -0.6° about the *y*-axis was noticed during digitisation. This small error in setup was corrected by rotating the co-ordinate system within Peak Motus® software to realign physical and digital coordinate systems.

The digitised area consisted of 1440 x 1152 pixels, resulting in an effective resolution of digitisation of approximately 0.6 mm in both horizontal and vertical directions. After the scaling and reconstruction, the raw co-ordinates of 33 points were exported to Microsoft Excel®. A fifth order polynomial trend line was fitted to the raw co-ordinates in order to recreate the profile of the laminate at each experimental temperature and the maximum laminate deflection relative to the origin of the coordinate system shown in Fig. 5.2 was logged.

5.3 Finite element model formulation

In order to assess the suitability of the linear coefficient of thermal expansion used to define composite material model, the finite element model discussed in Chapter 2 was extended to predict laminate behaviour in response to imposed temperature change. The extended model included both gravitational and thermal loading to match the experimental conditions described in the preceding section. Laminate deflection at each experimentally measured temperature was predicted to allow comparison with experimental results.

The composite laminate was modelled as previously described in Chapter 2 using SOLID186 20-node layered brick elements with the elastic constants of the carbon fibre pre-preg and layer thicknesses as shown in tables 2.1 and 2.2 respectively.

As the experimental laminate was symmetrical about the x=0 and y=-40mm planes a quarter of the laminate was modelled within Ansys to reduce computational time by imposing symmetry constraints upon the two boundaries shown in Fig. 5.3.

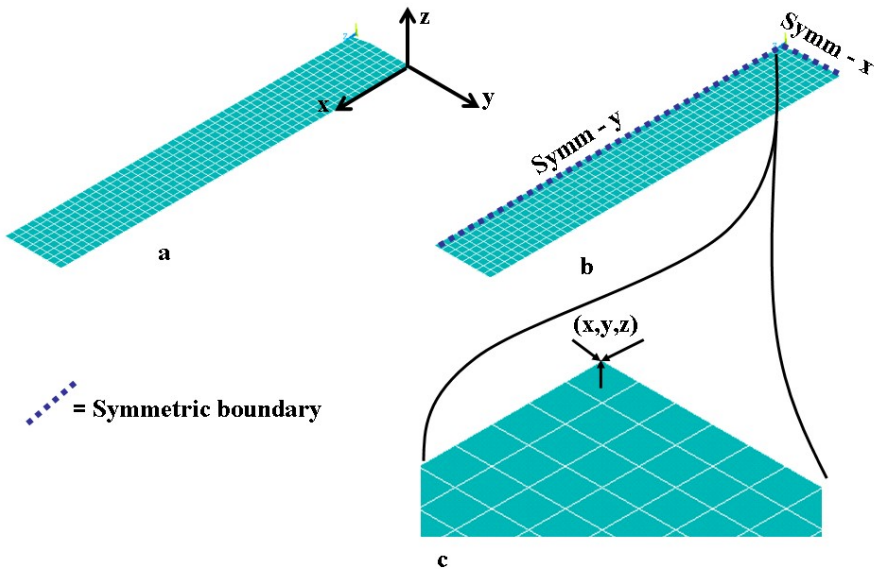

Fig.5.3: Finite element model of quarter laminate showing coordinate system and mesh density (a), boundaries with symmetry constraint (b) and central translational constraint (c).

When a symmetry boundary condition is imposed on a structural analysis both in-plane rotations as well as out of plane translations are constrained to zero as shown in Fig 5.4:

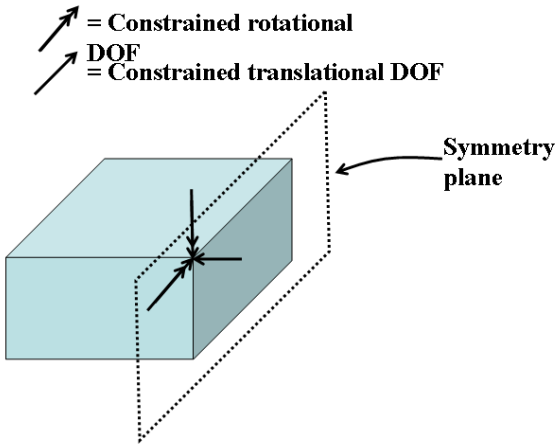

Fig.5.4: Showing vectors defining the rotational and translational degrees of freedom constrained to zero at a symmetric boundary mechanical condition.

Once the quarter model was constrained as shown in Fig.5.3 the volume was meshed with 400 SOLID186 elements measuring 5×5×0.516mm (aspect ratio 9.69). This element aspect ratio was decided upon after sensitivity analysis confirmed further reduction of element size resulted in variations in predicted edge deflections of less than 0.5%.

Since the laminate was held horizontally during experimental measurement (Fig. 5.2), gravity loading was applied to the laminate as an acceleration of $9.81 ms^{-1}$ acting on all nodes within the laminate in the positive *z*-direction.

With gravity loading applied, the temperature of all nodes (*T*) was constrained to match that of each experimental data point. Coordinates for all nodes at the *y*=0mm free-edge of the laminate (shown in Fig 5.2) were calculated by summing the undeformed nodal coordinates at T=22°C and nodal displacements in the *x* and *z*-directions at each experimental temperature.

These raw coordinates were then exported to Microsoft Excel® for comparison with experimental data. The maximum nodal displacement at each experimental temperature was plotted against laminate temperature and a linear trend line fitted to the data.

5.4. Bistable composites - Response to thermal load

The deformation of a bistable laminate in response to imposed temperature change was experimentally characterised and these data compared with laminate deflection predicted using the finite element model described in section 5.3.

5.4.1 Laminate deformation

Fig.5.5 shows laminate profile at each measured temperature in the range 30.3°C 169.9°C. These profiles are constructed from coordinates of 33 points along the x = 0mm edge of the laminate as described in section 5.2. As seen in Fig. 5.5 maximum laminate deflection (D_{max}) decreases as temperature increases, reducing curvature as temperature approaches the laminate cure temperature.

At low temperature, the section of laminate in the region x<0 region has a negative curvature in the x-direction. However as temperature increases above 150°C regions of positive curvature develop near to the x=-125mm free edge of the laminate as indicated at point (a) in Fig.5.5. A similar reversal of curvature also occurs near to the x=125mm free edge.

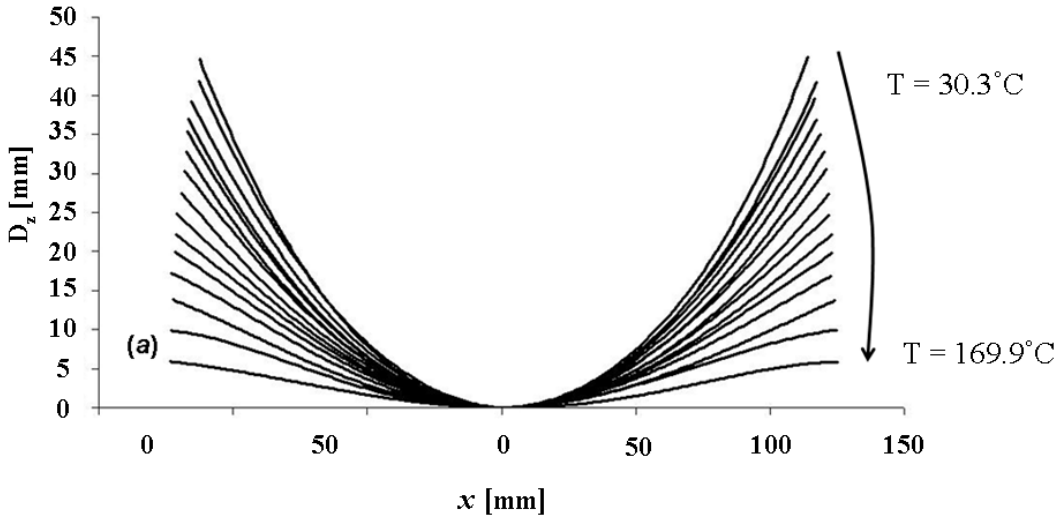

Fig.5.5: Laminate profile between 30.3˚C and 169.9˚C based upon 5th order polynomial trend lines fitted to 33 experimental data points. Region of reversed curvature indicated at point (a).

Epoxy resins are known to soften in the range of 50-120˚C [25] showing reduced coefficient of thermal expansion (CTE), elastic and shear moduli. At approximately 120˚C the CTE increases once more although the elastic and shear moduli continue to decrease. Though no specific information relating to the Hexcel M21 resin system used here has been published, data reported in [25] relate to a structural epoxy used in composite construction thought to be similar to M21. It is suggested that gravity loading in conjunction with the softened matrix cause the ends of the laminate to reverse curvature or "sag" toward the z=0mm plane.

Fig.5.6 shows the measured maximum deflection of the laminate (D_{max}) for each sample temperature along with the corresponding FE-predictions. A fifth order polynomial was fitted to the experimental data with an R^2 correlation coefficient of 0.99, however a linear trend line was adequate to achieve a similar correlation with the FE predicted data. The relationship between laminate temperature and D_{max} for the experimental data is more complex than the simple linear relationship predicted by the FE model.

As laminate temperature rises, D_{max} initially increases at similar rates in both experimental and FE data. However at approximately 50˚C the rate of change of deflection ΔD_{max} with respect to temperature reduces significantly. Between 50˚C and 120˚C ΔD_{max} remains approximately constant leading significant divergence of FE predicted deflection and experimental measurements. As the laminate temperature increases beyond 120˚C the ΔD_{max} increases once more as temperature approaches 169.9˚C.

The observed changes in rate of change of deflection with respect to temperature (ΔD_{max}) at 120˚C corresponds with the appearance of regions of reversed curvature near to the free-edges of the laminate discussed above and indicated in Fig.5.5.

The linear material model used to describe the composite pre-preg did not include temperature dependent variations in mechanical properties and hence variations in ΔD_{max} were not accurately predicted causing the observed discrepancy between FE-predictions of laminate deflection and experimental data.

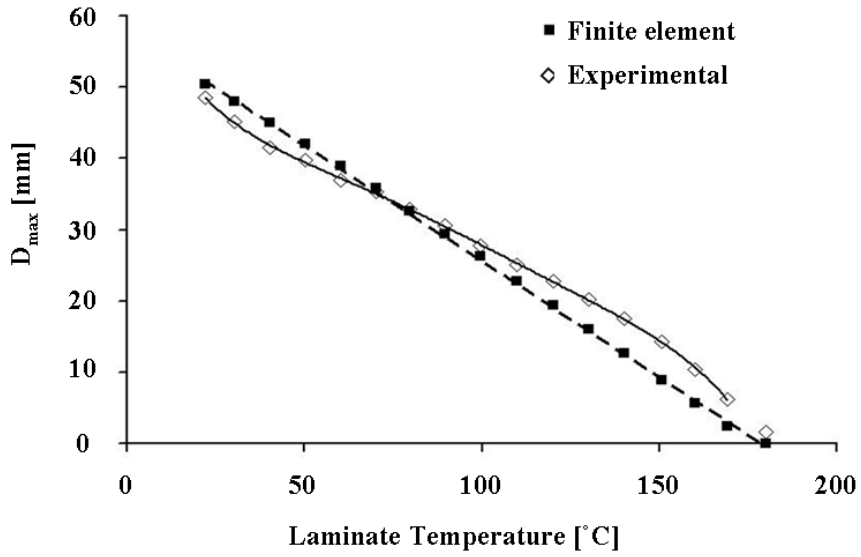

Fig.5.6: Experimentally measured and FE-predicted values for maximum laminate deflection (D_{max}) as a function of laminate temperature for 250×80mm^2 $[0/90]_T$ T800/M21 laminate. Experimental data is fitted using a 5th order polynomial trend line while a linear trend line is shown fitted to FE-data points.

Despite the observed non-linearities in the laminate's response to thermal loading the FE-predictions remain within 10% of experimental values in the range 22-109˚C. Thereafter percentage errors rise as laminate deformation approaches zero, however absolute error remains less than ±5mm over the entire temperature range.

Alteration of the coefficient of thermal expansion (CTE) used in the composite material model would allow FE-predicted laminate deflection to more closely match experimentally observed values. However as the observed non-linear deformation is the result of temperature dependent CTE and Young's modulus varying a single parameter would negatively impact prediction of cured shape. In future studies it may be possible to utilise two separate material models for the composite pre-preg: The first tailored to capture the residual stresses created during manufacture; the second having temperature dependent properties to allow more accurate prediction of laminate deflection under imposed changes in temperature.

5.4.2 Residual curvature

During measurement it was noted that although the laminate approached the cure temperature of 180˚C, the laminate curvature did not reduce to zero. This residual curvature may be related to the additional residual stresses introduced by chemical shrinkage of the resin system during the curing process which was described in Chapter 1.

The rate of change of D_{max} with respect to temperature was calculated for the experimental data by the finite difference method [31] between 150.7 and 169.9˚C. This value of ΔD_{max} was then used to extrapolate the experimental data set to predict laminate deflection at a laminate temperature of 180˚C using linear extrapolation [31].

Predicted laminate deflection (D_{max}) at 180˚C using this technique was 1.57mm. This residual deformation shows that a significant residual stresses remain present causing structural deformation within the laminate. The authors suggest that this residual deflection could serve as a convenient measure of the non-reversible residual stresses present within thin asymmetric composites. In order to accurately calculate the residual stress field the influence of gravitational and temperature dependent material properties would need to be accounted for and the detailed material characterisation required to undertake this task lies outside the scope of the present work.

It is likely that the residual stress field is comprised of superposed stresses resulting from chemical shrinkage, tool interaction [13, 32] and differential curing through the thickness of the laminate. A deeper understanding of the physical factors responsible for the observed residual deformation within unsymmetric composite laminates could enable more accurate prediction of their cured shape. In addition improvement in manufacturing techniques which control the factors which create undesired residual stresses could lead to reduce post cure distortion of precision composite parts.

5.4. Conclusions

In this chapter the deflection of a bistable laminate in response to changes in ambient temperature was characterised. The finite element model presented in Chapter 2 was extended to include gravitational loading and laminate deflection predicted and compared to experimental measurements.

The key conclusions drawn from the work presented in this chapter are:

- Laminate tip deflection shows a non-linear relationship to temperature with observed behaviour correlating well with published non-linear models of epoxy mechanical properties.
- The presented finite element model predicts laminate tip deflection to within 10% of experimentally measured values despite using a linear material model.
- A residual curvature is observed when laminate is heated to cure temperature, it is suggested that this curvature is caused by chemical, hygroscopic and mechanical residual stresses within the laminate.

The change in laminate deflection of a 250x80mm $[0/90]_T$ laminate when subjected to changes in ambient temperature was measured using motion capture techniques as described in section 5.2. Deflection reduced as laminate temperature increased however the rate of change of deflection was not linear; as laminate temperature increased above 50˚C significant non-linearities in the temperature-deflection relation were observed.

The observed behaviour correlates well with previously measured [28] temperature dependent mechanical properties of similar epoxy resin systems. In addition gravitational load in combination with reduced Young's modulus was shown to cause the extremities of the laminate to reverse curvature or "sag" at elevated temperature.

During experiment a residual curvature was noted even when laminate temperature neared cure temperature. The deflection at cure temperature was extrapolated from the experimental data to predict the degree of residual deflection. Using linear extrapolation a residual deflection of 1.57mm was predicted which indicates the presence of residual stresses which are not fully relaxed by reheating. It is known that the residual stress state within bistable laminates is a superposition of stress fields created by chemical, mechanical and thermal

effects during the cure cycle, and the presence of this residual curvature provides further supporting evidence.

In future work measurements of this residual deflection could be used to calculate the magnitude of residual stresses caused by chemical and mechanical effects such as tool interaction during the curing process.

The presented FE model predicts laminate deflection to within 10% over the range 20-110˚C despite using a simple linear material model. While the presented model is of use for first order design activities the observed discrepancies with experiment underline the importance of developing models that capture non-linear materials properties and manufacturing imperfections such as changes in ply thickness and resin rich areas. While implementation of non-linear material models are necessary for more accurate modelling of the thermal deflections of bistable laminates after the curing process, their implementation within finite element models used to predict the cured shape after manufacture require further validation studies. The large deflections induced by changes in ambient temperature are a clear indication that bistable composite structures must be designed to operate within relatively strict temperature ranges like those found at cruise altitude in a civil aircraft [16].

In the following chapter the actuation characteristics of MFC actuated bistable laminates will be experimentally characterised in terms of blocking force and free-deflection.

5.5 Reference list

1. Kashtalyan, M. Y., and Soutis, C. (2002). "Mechanisms of internal damage and their effect on the behavior and properties of cross-ply composite laminates." *International Applied Mechanics*, 38(6), 641-657.
2. Bartus, S. D. (2007). "A review: Impact damage of composite materials." *Journal of Advanced Materials*, 39(3), 3-21.
3. Garnich, M. R., and Akula, V. M. K. (2009). "Review of Degradation Models for Progressive Failure Analysis of Fiber Reinforced Polymer Composites." *Applied Mechanics Reviews*, 62(1).
4. Dickinson, L. C., Farley, G. L., and Hinders, M. K. (1999). "Translaminar reinforced composites: A review." *Journal of Composites Technology & Research*, 21(1), 3-15.
5. Trask, R. S., Williams, G. J., and Bond, I. P. (2007). "Bioinspired self-healing of advanced composite structures using hollow glass fibres." *Journal of the Royal Society Interface*, 4(13), 363-371.
6. Soutis, C., Duan, D. M., and Goutas, P. (1999). "Compressive behaviour of CFRP laminates repaired with adhesively bonded external patches." *Composite Structures*, 45(4), 289-301.
7. Schultz, M. R., Wilkie, W. K., and Bryan, R. G. (2007). "Investigation of self-resetting active multistable laminates." *Journal of Aircraft*, 44(4), 1069-1076.
8. Dano, M. L., and Hyer, M. W. (2002). "Snap-through of unsymmetric fiber-reinforced composite laminates." *International Journal of Solids and Structures*, 39(1), 175-198.
9. Zhou, J. M., and Lucas, J. P. (1999). "Hygrothermal effects of epoxy resin. Part I: the nature of water in epoxy." *Polymer*, 40(20), 5505-5512.
10. Vanlandingham, M. R., Eduljee, R. F., and Gillespie, J. W. (1999). "Moisture diffusion in epoxy systems." *Journal of Applied Polymer Science*, 71(5), 787-798.
11. Adamson, M. J. (1980). "Thermal expansion and swelling of cured epoxy resin used in graphite/epoxy composite materials." *Journal of Materials Science*, 15(7), 1736-1745.
12. Cairns, D. S., and Adams, D. F. (1983). "Moisture and thermal expansion properties of unidirectional composite materials and the epoxy matrix." *Journal of Reinforced Plastics and Composites*, 2(4), 239-255.
13. White, S. R., and Hahn, H. T. (1992). "Process Modeling of Composite-Materials - Residual-Stress Development During Cure .2. Experimental Validation." *Journal of Composite Materials*, 26(16), 2423-2453.
14. Etches, J., Potter, K., Weaver, P., and Bond, I. (2009). "Environmental effects on thermally induced multistability in unsymmetric composite laminates." *Composites Part A-Applied Science and Manufacturing*, 40(8), 1240-1247.
15. Portela, P., Camanho, P., Weaver, P., and Bond, I. (2008). "Analysis of morphing, multi stable structures actuated by piezoelectric patches." *Computers & Structures*, 86(3-5), 347-356.
16. Diaconu, C. G., Weaver, P. M., and Mattioni, F. (2008). "Concepts for morphing airfoil sections using bi-stable laminated composite structures." *Thin-Walled Structures*, 46(6), 689-701.

17. Asanuma, H., Haga, O., Ohira, J., Takemoto, K., and Imori, M. (2003). "Fabrication of CFRP/Al active laminates." *Jsme International Journal Series A-Solid Mechanics and Material Engineering*, 46(3), 478-483.

18. Asanuma, H., Haga, O., and Imori, M. (2006). "Development of high performance CFRP/metal active laminates." *Jsme International Journal Series A-Solid Mechanics and Material Engineering*, 49(1), 32-37.

19. Drobez, H., L'Hostis, G., Gautier, K. B., Laurent, F., and Durand, B. (2009). "A new active composite." *Smart Materials & Structures*, 18(2), 1-7.

20. Wu, Z., Cheng, Y. K., Lo, S. H., and Chen, W. J. (2007). "Thermal stress analysis for laminated plates using actual temperature field." *International Journal of Mechanical Sciences*, 49(11), 1276-1288.

21. Lo, S. H., Zhen, W., Cheung, Y. K., and Wanji, C. (2010). "Hygrothermal effects on multilayered composite plates using a refined higher order theory." *Composite Structures*, 92(3), 633-646.

22. Vargas, G., Arrese, A., Carbajal, N., and Mujika, F. (2009). "Analysis of In-plane and Out-of-plane Thermo-mechanical Stresses in Un-symmetric Cross-ply Curved Laminated Strips." *Journal of Composite Materials*, 43(25), 3157-3184.

23. Hyer, M. W. (1981). "Calculations of the Room-Temperature Shapes of Unsymmetric Laminates." *Journal of Composite Materials*, 15(JUL), 296-310.

24. Dano, M. L., and Hyer, M. W. (1998). "Thermally-induced deformation behavior of unsymmetric laminates." *International Journal of Solids and Structures*, 35(17), 2101-2120.

25. Schlecht, M., Schulte, K., and Hyer, M. W. (1995). "Advanced Calculation of the Room-Temperature Shapes of Thin Unsymmetric Composite Laminates." *Composite Structures*, 32(1-4), 627-633.

26. Ren, L. B., and Parvizi-Majidi, A. (2003). "Cured shape of cross-ply composite thin shells." *Journal of Composite Materials*, 37(20), 1801-1820.

27. Jun, W. J., and Hong, C. S. (1992). "Cured Shape of Unsymmetric Laminates with Arbitrary Lay-Up Angles." *Journal of Reinforced Plastics and Composites*, 11(12), 1352-1366.

28. Hamamoto, A., and Hyer, M. W. (1987). "Nonlinear Temperature-Curvature Relationships for Unsymmetric Graphite-Epoxy Laminates." *International Journal of Solids and Structures*, 23(7), 919-935.

29. Schlecht, M., Schulte, K., and Hyer, M. W. (1995). "A comparative study for the calculation of the temperature dependent shapes of unsymmetric laminates based on finite element analysis and extended classical lamination theory." *Mechanics of Composite Materials*, 31(3), 247-254.

30. Bowen, C. R., Butler, R., Jervis, R., Kim, H. A., and Salo, A. I. T. (2007). "Morphing and shape control using unsymmetrical composites." *Journal of Intelligent Material Systems and Structures*, 18(1), 89-98.

31. Stroud, K. A. (1987). "Engineering Mathematics." MacMillan Education Ltd, London, Uk. ISBN: 0-333-44886-3

32. White, S. R., and Hahn, H. T. (1992). "Process Modeling of Composite-Materials - Residual-Stress Development During Cure .1. Model Formulation." *Journal of Composite Materials*, 26(16), 2402-2422.

Chapter 6 - Actuation characteristics of piezoelectrically actuated bistable composite laminates

In this chapter the experimental techniques used to characterise the actuation response of a piezoelectrically actuated bistable composite laminate are described in terms of blocking force and free-deflection. The observed linear dependence of both blocking force and free-deflection on applied actuation voltage is explained in terms of the engineers beam bending equation and the implications of this result for MFC actuator simulation discussed.

In section 6.1 published work relevant to experimental characterisation of morphing structures utilising smart actuation will be discussed and a lack of experimental characterisation of MFC actuated structures is identified. The mechanisms which cause deflection creep in piezoelectric actuators are also discussed in preparation for a discussion of the observed creep in the MFC actuation response.

Section 6.2 will describe the experimental techniques used to characterise blocking force, free-deflection and creep of the actuated laminate while experimental results and the relevance of the engineers beam bending equation in explaining the observed behaviour is discussed in section 6.3.

6.1 Introduction

6.1.1 Actuation behaviour of MFC actuated smart structures

As is common when implementing any novel technology, there remain significant areas of uncertainty surrounding the behaviour of MFC actuators when integrated within host structures. MFC actuators have been proposed as smart strain sensors for structural health monitoring applications [1, 2] utilising the direct piezoelectric effect as well as actuators in vibration suppression schemes [3, 4] and in structural actuation applications [5, 6] via the reverse piezoelectric effect. To date few experimental investigations into their use as structural actuators [6-8] has been presented, although several investigators have conducted theoretical studies in this area [9, 10] which predict significant improvements in control authority and vibration attenuation

As discussed in Chapter 3, MFC actuators are at present the most attractive smart actuation technology for use within an adaptive bump for aerodynamic flow control. As such it is important that the actuation behaviour and structural response of actuated bistable laminates is fully characterised.

Despite preliminary experimental characterisation of MFC actuators bonded to isotropic beams [5, 8, 11] and some investigations into MFC-actuated snap-through of bistable laminates [11-14] the experimental characterisation of MFC performance as a structural actuator for large deflection systems has not yet been undertaken.

As described in Chapter 3, Dano [8] has presented experimental measurement of the deflection of an unsymmetric composite laminate in response to imposed piezoelectric actuation and thermal loading. Binette [15] extended this work using similar techniques, however laminate deflections were small and the geometric nonlinearities which create the large deflections observed in bistable laminates were not investigated.

Several investigators have undertaken simple testing the actuation behaviour of an MFC bonded to an isotropic beam [8, 16], but at the time of this report the authors are unaware of any presented work measuring the force production capabilities and actuation behaviour of piezoelectrically actuated bistable laminates.

In addition to studies characterising isotropic beams, systems have been proposed which combine piezoelectric and mechanical loading to achieve reversible snap-through and control the morphing of bistable composite structures [14]. By combining mechanical and

piezoelectric actuation these systems offer significant reversible deflections and shape change that can be achieved by maintaining a bistable composite structure in a single stable configuration [14]. This ability to create continuous shape change within a structurally stable state may also allow fine-scale adjustment of aerodynamic performance beyond what is possible using snap-through deformation alone.

Given the sensitivity of bistable composites to variations in laminate composition [17] it is likely that similar sensitivity to variations in actuator performance will be observed. Therefore it is of primary importance to experimentally characterise the actuation behaviour of MFC actuators in order to validate assumption of linear piezoelectric constants in the formulation of the finite element models presented in Chapters 3 and 4.

In order to examine the assumption of a linear material model for piezoelectric coefficient (d_{33} and d_{31}) this chapter aims to characterise a piezoelectrically actuated bi-stable carbon-fibre laminate in terms of free deflection, blocking force and load-deflection behaviour. The validity of a commonly used model for piezoelectric creep will also be assessed for MFC actuators bonded to bistable composite laminates by correlating experimental measurements of time-dependent displacement creep with analytically predictions.

6.1.2 Piezoelectric creep

It has previously been observed that piezoelectric actuators [18, 19] including MFC actuators exhibit deflection creep under prolonged DC-voltage excitation. This section describes the physical mechanisms which cause this creep in preparation for a discussion of the observed creep of the MFC actuated laminate in section 6.3.2.

The instantaneous strain observed in piezoelectric ceramics is well modelled by the usual constitutive equation [20] describing the intrinsic piezoelectric strain in a unit cell:

$$S = s^E T + dE \tag{6.1}$$

where S is the induced strain, s^E the compliance under constant field conditions [Pa^{-1}], T the applied stress [Pa], d the piezoelectric constant [pmV^{-1}] and E the applied electric field strength [Vm^{-1}]. It is well known that piezoelectric actuators, including MFCs display displacement creep under open loop voltage control [18, 19, 21]. However this phenomenon has yet to be observed in actuated composite structures or the deformation caused by piezoelectric creep correlated with previously presented analytical models [18].

Time-dependent displacement creep within piezoelectric ceramics is caused by 'extrinsic' effects occurring outside the Perovskite unit cell. Fig. 6.1 shows the unit cell of lead zirconate titanate (PZT) and the induced strain in the polarisation direction which is created by application of an electric field. The extension of the dipole shown in Fig. 6.1 is rapid and is an example of the 'intrinsic' mechanism of piezoelectric strain.

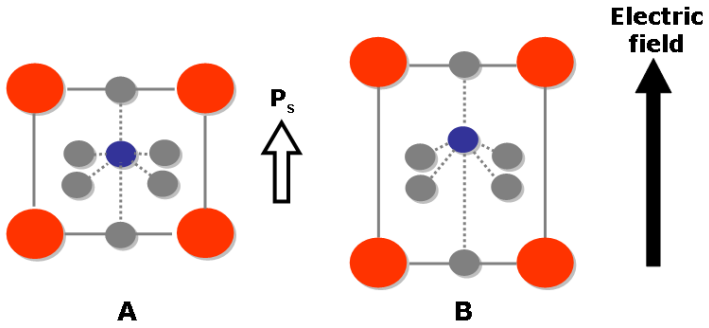

Fig.6.1: Induced strain in a tetragonal PZT unit cell with polarisation axis Ps before (A) and after application of applied electric field E (B).

'Extrinsic' effects occur at a scale larger than a single unit cell of the ceramic. The two principal effects which cause the creep response of piezoelectric ceramics being domain wall motion and localised phase transitions [22]. It is these extrinsic creep effects which cause the actuation response of MFC actuator under open loop control to differ from the predictions of equation 6.1.

Domains are regions of ceramic in which all of the unit cells share a common polarisation axis [20], as discussed in Chapter 3. Domain wall motion is characterised by the boundary between adjacent domains moving to cause a reduction in volume of domains with polarisation axes that are poorly aligned with the applied field. Adjacent domains whose polarisation axis is well aligned with applied field increase in volume as shown in Fig 6.2.

As polarisation axis becomes better aligned with applied electric field the induced strain of the ceramic under increases as reoriented domains exhibit a greater piezoelectric strain than prior to reorientation. This time dependent increase in induced strain is seen in the observed creep of piezoelectric ceramics under constant applied field [23].

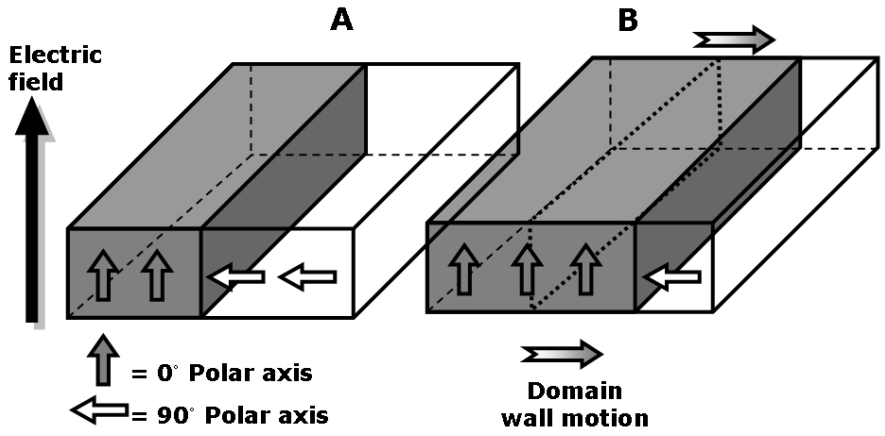

Fig.6.2: Polarisation of domains within PZT ceramic immediately after field application (a) and at time *t* (b) showing domain wall motion increasing size of well aligned domains.

Due to the tetragonal crystal structure of the PZT-5A material used in the MFC actuators (PZT-5A) studied here, this domain wall motion (as seen in Fig 6.2) is primarily the result of domain reorientation of 90° domains [23], which does not allow complete alignment of polarisation axis with applied field in all domains.

In addition to domain wall motion, domains whose polar axis remains significantly misaligned may also be reoriented by changing the phase of the material within that domain via localised phase changes [24]. By switching from the tetragonal crystal structure to the rhombohedral structure domains that may be better aligned by changes in polar axis of 109° or 71° [25] can achieve better alignment of polar axis and drive field. As discussed in Chapter 1 by switching phase a single unit cell may reorient the polar axis into one of 14 possible directions allowing more complete alignment with applied field direction.

Localised phase transition is most prevalent in PZT compositions which are close to the morphotropic phase boundary [26], and of approximately equal proportions of titanium-rich rhombohedral and zirconium-rich tetragonal unit cells. In these compositions the electric field provides the energy input required to cause phase transition.

Fig. 6.3 shows the change in polarisation direction between adjacent regions of tetragonal and rhombohedral ceramic. As the change in polarisation axis induced by phase transition is smaller than that induced by domain wall motion the contribution to creep is also smaller.

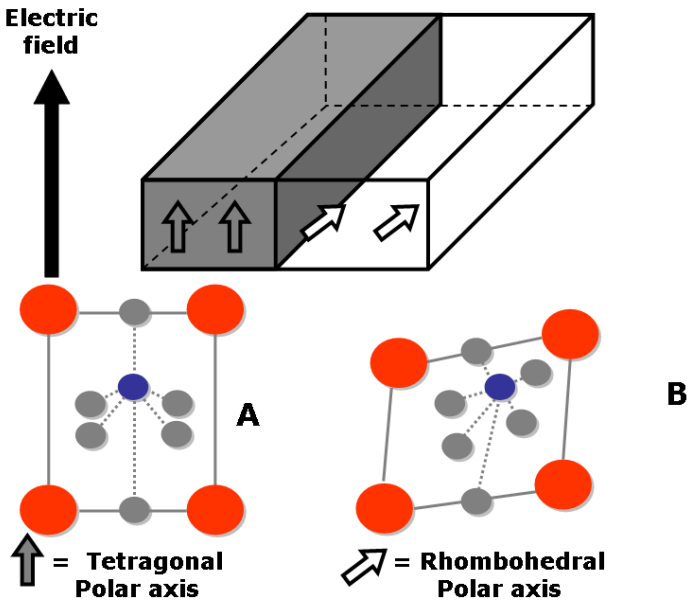

Fig.6.3: Shift in polar axes (P_s) of a PZT crystal, with regions composed of tetragonal (a) and rhombohedral (b) phases respectively.

Several models have been proposed that seek to quantify the extent of this time dependent creep with the model used by Jung [18] of equation 6.2 being most widely accepted for use in the prediction of creep response in PZT samples.

$$x(t) = x_0\left[1+\gamma \log(\frac{t}{0.1})\right] \tag{6.2}$$

where $x(t)$ is the piezoelectric actuator's displacement [m] for any fixed input voltage or electric field [Vm^{-1}], x_0 is a nominal constant displacement value (namely the displacement 0.1 s after applying the input voltage) [m] and γ is a creep factor which determines the logarithmic creep rate (percent change per time decade). While piezoelectric creep has been extensively studied in monolithic actuators [21, 27] to date the creep of composite structures actuated using Macro Fibre Composite actuators bonded to a bistable composite has not been characterised.

In section 6.2 of this chapter the experimental characterisation of a piezoelectrically actuated bistable laminate in terms of blocking force and free-deflection will be presented. Piezoelectric creep of the structure under open loop control will be experimentally observed and the actuator response correlated with the governing constitutive equation (eq. 6.2) presented by Jung [18] and the system time constant calculated in section 6.3.

6.2 Experimental Setup

6.2.1 Composite manufacture and actuator attachment.

An unsymmetric $[0/90]_T$ carbon fibre/epoxy composite measuring 150x150x0.32 mm, similar to that examined by Schultz [5], was manufactured using a standard composite lay-up procedure and cure cycle as described in Chapter 2. The laminate was manufactured using unidirectional HTA(12k)/913 carbon fibre pre-preg sheet and a cure temperature of 125°C. Once the layers had been placed a thermocouple was inserted between the pre-preg plies to monitor the laminate temperature during the cure cycle.

The piezoelectric actuator used was the Smart Materials (M-8557-P1) as in Chapters 3 and 4 with an active area of 85x57mm and an electrode spacing of 0.5 mm. The material used for the piezoelectric fibres was PZT-5A. The maximum operating voltage was 1500V with a maximum reported free strain of 0.1–0.135% at 1500V [28].

A two-part epoxy was used to bond the MFC actuator to the laminate. The surfaces of the actuator and carbon fibre composite were roughened to provide better mechanical adhesion and then cleaned using isopropryl alcohol before a small quantity of the adhesive was evenly spread on both surfaces. Care was taken that as thin a film as possible was applied to ensure good strain transfer between the actuator and composite. Once the actuator was located centrally on the laminate surface, the actuator and composite were subjected to a clamping force of 200N to keep the composite and actuator flat and in good contact for 24hrs while the epoxy cured.

Due to the applied load during bonding the actuator was bonded to the laminate whilst held flat, with the direction of the main actuator strain (and its piezoelectric fibres) aligned along the axis of curvature as shown in Fig. 6.4. The actuator-composite lay-up is therefore $[0_{MFC}/0/90]_T$. Fig. 6.4 shows the composite with the actuator attached. As discussed in Chapter 4, the additional structural stiffness of the MFC resulted in a reduction in the observed maximum deflection (D_{max}) of the final active laminate. However the composite was still bi-stable and exhibited two stable states (State A and State B), as shown in Fig. 6.4.

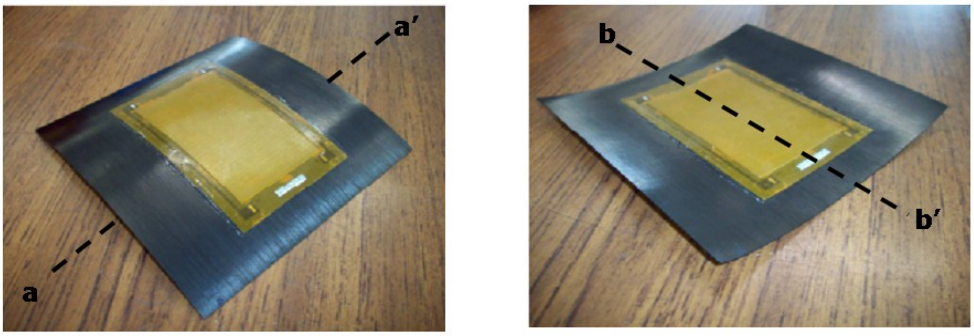

Fig.6.4: MFC location and axis of curvature in states A and B of a $[0_{MFC}/0/90]_T$ laminate with axes of curvature denoted by a-a' and b-b' for each state.

6.2.2 Measurement of blocking force.

The blocking force of an actuator is defined as the maximum force exerted by an actuator when placed in a perfectly unyielding clamp [29]. To determine the relationship between applied voltage and blocking force the test rig shown in Fig 6.5 was designed to allow force measurement in an Instron 1122 mechanical test machine. The rig consisted of two smooth nylon rails screwed into an aluminium top-plate which was in turn supported by four round aluminium columns. These columns bolted into an aluminium base-plate which was bolted to an Instron mounting boss. The laminate support rails and the cross-head of the Instron load cell were machined from nylon to provide electrical isolation of testing equipment from the applied voltage (up to 1400V).

A function generator was used to provide sinusoidal AC input-signals of varying amplitudes to a power amplifier (TREK PZD700 piezo driver) set to provide 200V output voltage per volt input. All signals were positively DC-biased by half the amplitude, hence all signals cycled from zero volts to a maximum voltage of 1400V to maintain polarity of the MFC.

The laminate was placed on the support rails in State A (as in Fig. 6.5) with no applied voltage and the cross-head of the Instron was adjusted to contact the top of the laminate with a contact force of less than 0.05N. A test frequency of 0.01Hz was selected for characterisation of blocking force, since this produced a corresponding force which alternated from 0N (at 0V) to a maximum force at the maximum applied voltage with limited phase difference between applied force and measured load. The applied AC voltage and resulting force were logged for 150 seconds then the input disconnected and the sample allowed to relax to its pre-test state.

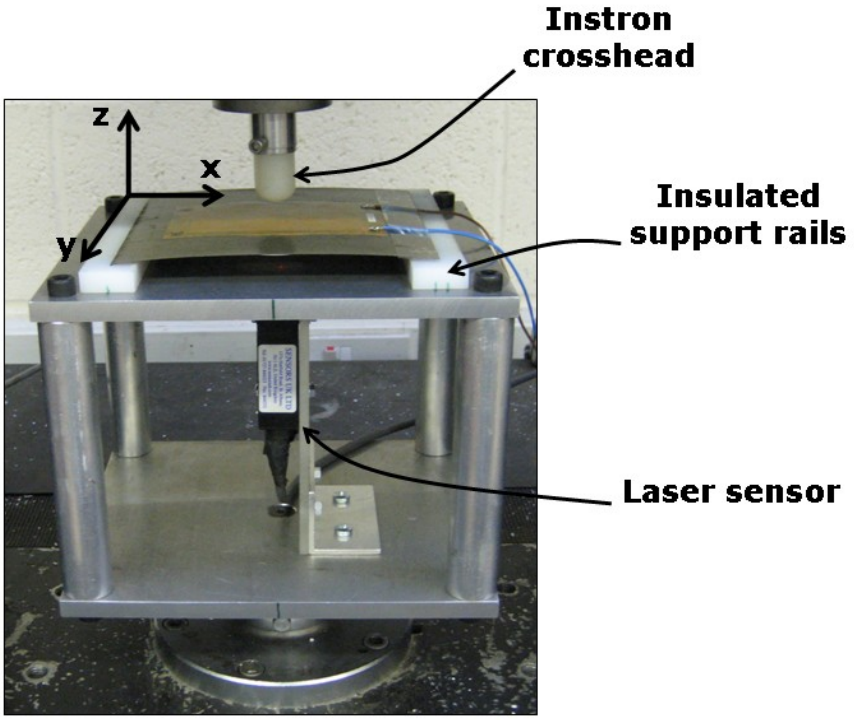

Fig.6.5: Experimental test rig to measure blocking force and free-deflection showing experimental coordinate system and key components.

The laminate was snapped into each of its stable states manually and electrically discharged after each experimental run to ensure that no residual charge effects influenced subsequent testing. This test procedure was repeated with the input voltage adjusted to measure the blocking force from 200-1400V in 200V increments. Coupled force and voltage data was then transferred into Microsoft Excel® for further analysis.

6.2.3 Measurement of free deflection

Free deflection is the actuator deflection in the absence of any restraining force [29]. The test rig described in section 3.2.2 was modified to include a Nippon LAS 5010 V laser measurement system (see Fig. 6.5) to measure the centre point free deflection of the laminate as a function of MFC drive-voltage. In order to remove mechanical constraint the nylon cross-head used during the blocking force measurement was moved away from the laminate surface. Gravitational load did act to reduce free deflection although due to the low mass and comparatively short unsupported span of the laminate gravitational effects are not thought to be significant.

The laser was calibrated using a scribe table to define a datum plane which was co-planar with the support surfaces of the nylon rails. System resolution of the LAS 5010V was 10 µm over a 50 mm range. With the laminate in State A, laminate centre displacement (w) [m] and MFC-drive voltage (V) were simultaneously logged using an analogue data logger with a sampling rate of 1Hz. The deflection (d) is defined as the change in laminate centre displacement (w) at MFC-drive voltage V relative to the undeformed value (w_0) original position at 0V as shown in Fig. 6.6.

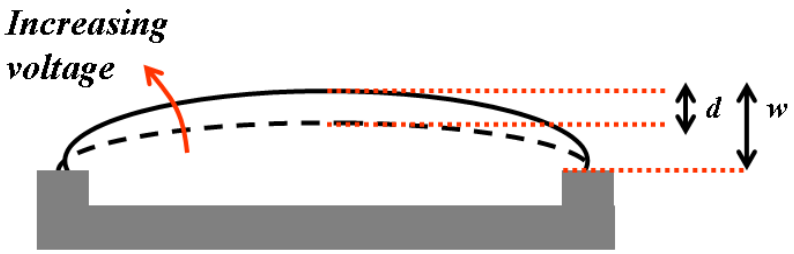

Fig.6.6: Laminate deflection (d) measures increase in laminate centre displacement (w) caused by MFC actuation strain.

MFC drive voltage was increased as a series of monotonic step inputs from 0 to 1400 V in increments of 200 V. At each 200 V increment the voltage was held constant for 60 s to allow any time dependent creep characteristics to subside and laminate displacement to reach a steady state value. Laminate deflection and drive voltage data was then transferred into Microsoft Excel®.

6.3 Results and discussion

The experimental measurements generated by the two experiments described in sections 6.2.2 and 6.2.3 will now be described. Section 6.3.1 describes results of blocking force measurement where the cross-head is fixed and in contact with the laminate. The observed linear relationship between drive voltage and blocking force is explained by use of the engineers beam equation.

Section 6.3.2 describes the measured free-deflection values and details the observed creep behaviour of the system. Time dependent creep in measured laminate deflection is correlated with previously published [18] constitutive equations. These blocking force and free deflection data are then combined to generate a 'force-generation versus displacement' diagram in section 6.3.3.

6.3.1 Blocking force

Figure 6.7 shows that blocking force increases with applied drive-voltage at a rate of 1.47×10^{-3} NV^{-1} from an initial value of 0N to a maximum value of 2.1N at 1400V. The relationship between MFC drive-voltage and blocking force is shown to be linear with a correlation factor (R^2) of 0.99 between experimental data and a linear trend line.

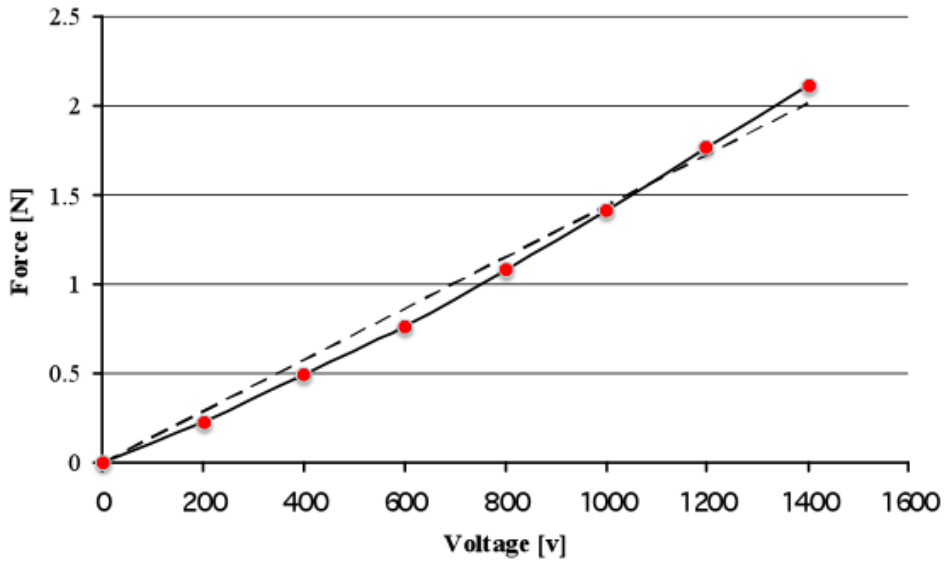

Fig.6.7: Blocking force as a function of MFC drive-voltage.

The linear relationship can be understood by a mechanical assessment of the laminate support case. Due to the fixed cross-head position and static nature of blocking force testing, the laminate may be considered as a 2D beam subject to a mid-span point load. Assuming that the supporting edges of the laminate behave as though they are pin-jointed and are free to slide in the *x*-direction, the laminate may be considered as simply supported as shown in Fig. 6.8.

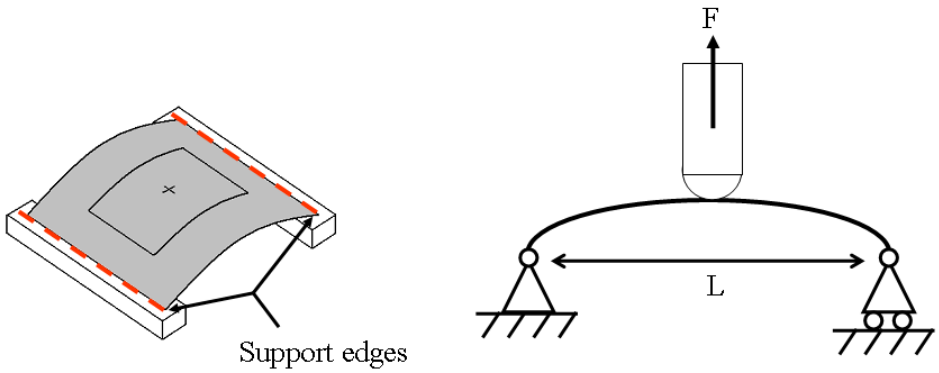

Fig.6.8: Actuated bistable laminate during blocking force testing showing supported edges of the laminate (a) and representative support case for beam equation (b).

From the beam equation [30] for a beam of span L, stiffness E, thickness t with a second moment of area I, it can be seen from equation 6.2 [30] that there is a linear relationship between the strain (ε) at the upper surface of the beam (where the piezoelectric is attached) and applied load (F) in Newtons.

$$\varepsilon = \frac{FLy}{4EI} \tag{6.2}$$

where y is the distance of the actuator from the laminate neutral axis [m]. Considering equation 6.2 it can be seen that the influence of the piezoelectric material is to induce an actuation strain at the upper surface of the laminate which in turn develops the force (F) which will be directly proportional to the piezoelectric strain and hence to the drive-voltage.

The observed linear relationship between laminate deflection and MFC drive-voltage validates the proposed linear model for piezoelectric coupling within the finite element model of the MFC described in Chapter 3. To further confirm this finding the measured free-deflection data will be presented in the following section.

6.3.2 Free deflection

Fig. 6.9 shows the centre free deflection (w) of the MFC-actuated laminate in State A as shown in Fig. 6.6. Laminate displacement 1s and 60s after the application of drive-voltage are shown in Fig. 6.9 and are marked as w_0 and w_{60} respectively. As MFC drive-voltage increases the induced actuation strain leads to an increase in the curvature of the laminate, leading to an increase in free deflection.

Laminate deflection one second after drive voltage application (w_0) increases to 7.37mm at 1400V from the initial undeformed laminate profile. Deflection creep is evident in the free-deflection measurements as w_{60} increases to 7.80mm at 1400V, 0.43mm more than the equivalent w_0 value. It is observed that free-deflection increases linearly with increased drive-voltage with an increase in w_0 of 0.0054mmV^{-1}. Deflection 60 seconds after MFC drive-voltage (w_{60}) increases by 0.0056mmV^{-1}.

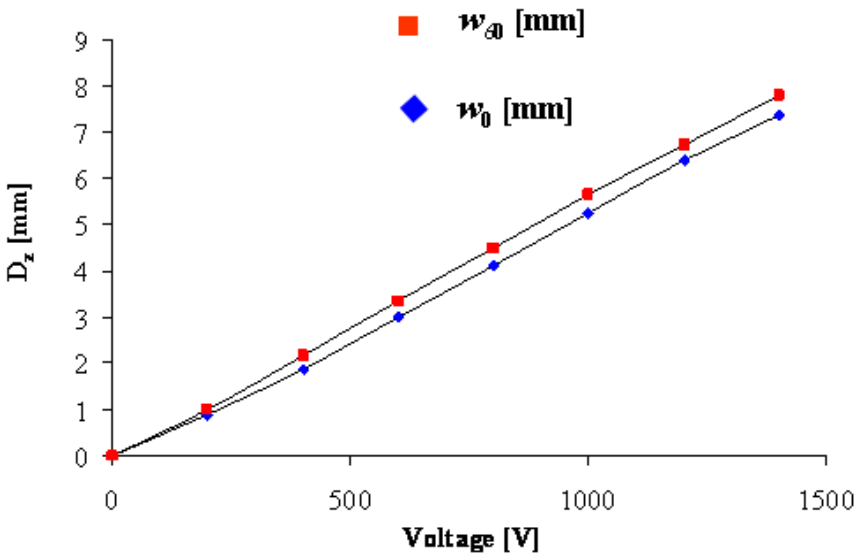

Fig.6.9: Free-deflection of laminate 0.1s (w_0) and 60 seconds (w_{60}) after voltage application.

In this single State A mode the piezoelectric-laminate combination is in many ways similar to THUNDER and LIPCA actuators [31], which are curved laminated piezoceramic. THUNDER and LIPCA actuators are curved due to differing coefficients of thermal expansion of individual layers in their laminated construction in a similar way to the curved composite laminate being measured in the present work. These actuators also demonstrate linear relationship between deflection and applied voltage or electric field [31].

It is not possible to use equation 6.2 to explain the linear relationship as the edges of the laminate are free to move and hence laminate curvature varies which prevents the use of the engineers beam bending equation.

There is some creep (drift) of the measured value of laminate centre deflection, after initial application of a drive-voltage and the resulting initial deflection, deformation continues before approaching a steady state value asymptotically as time progresses. The creep response has a logarithmic shape over time [18] and is commonly observed when piezoelectric materials are subjected to conventional open-loop actuation as described in section 6.1.

The magnitude of the observed creep (w_{60}-w_0) increases with increased applied voltage (Fig. 6.9) as greater domain wall motion and phase switching (section 6.1) would be expected at higher drive-voltages and electric fields [26]. This increase in creep magnitude results in an increased gradient of the w_{60} line compared to the w_0 line in Fig 6.9.

The observed creep response was found to have a logarithmic shape with respect to time and agrees well with equation 6.3 [18].

$$w(t) = w_0\left[1 + \gamma \log(\frac{t}{0.1})\right] \tag{6.3}$$

where $w(t)$ is the laminate deflection at time t [s] for any fixed input voltage [m], x_0 is a nominal constant displacement value (namely the displacement 0.1 s after applying the input voltage) [m] and γ is the system creep factor which determines the logarithmic creep rate (percent change per time decade). The initial rate of creep, and the speed at which initial rate of creep decays (γ), is seen to vary with MFC drive-voltage however no clear trend in γ is observed within this data set.

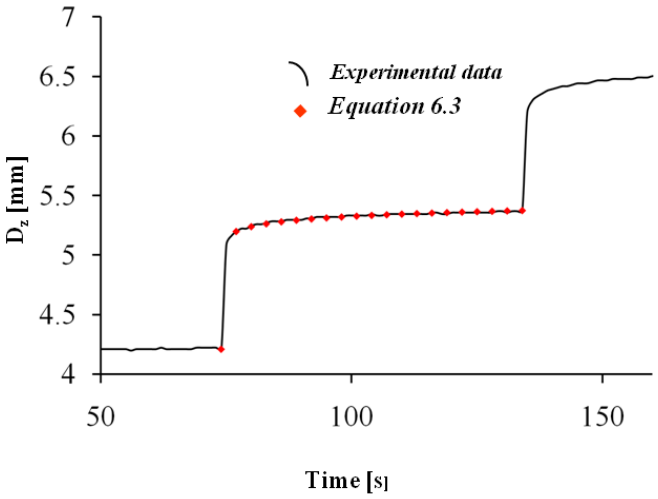

Fig.6.10: Experimental measured data for of laminate deflection for 200V, 400V and 600V with data points showing equation 6.3 describing laminate deflection for 400V drive-voltage fitted to the experimental data with a time constant of 0.027.

As an example of creep prediction, Fig. 6.10 shows time deflection data for 200, 400 and 600V, showing the creep in laminate centre deflection. As an example, equation 6.3 is shown fitted to the data for 400V with a creep factor of 0.027 providing a good fit for between analytical and experimental data. The creep factor was determined by graphical fitting of the experimental data to a plot of *w(t)* versus $\log_{10}(t/0.1)$. Typical γ values for deflection creep within the data for drive-voltages between 200-1400V vary from 0.01 to 0.05 with no strong correlation between γ and drive voltage.

6.3.3 Force-displacement characteristic

While the maximum actuator deflection is known with no applied force ('free deflection') and the maximum generated force is known with no actuator deflection ('blocking force'), laminate response to simultaneous deflection and force may be estimated using a "force-generation versus displacement" diagram [29]. If x_{free} is the free deflection, F the applied load and Δw is actual deflection under combined electrical and mechanical loading, the relationship between them is given by equation 6.4 [29].

$$\Delta w = x_{free} - \frac{F}{k_{actuator}} \tag{6.4}$$

where $k_{actuator}$ is the stiffness of the actuator (N/mm) and Δw is actuator displacement (mm). From equation 6.4, when Δw=0 the blocking force F is $k_{actuator} \cdot x_{free}$ and when F=0 the displacement Δw is x_{free}.

Fig. 6.11 is a force generation versus displacement graph constructed using the free deflection and blocking force data presented in sections 3.3.1-3.3.2. The intercept points on the load-axis (x) as a function of voltage correspond to the blocking force data in Fig 6.8, while the intercept points on the deflection axis (y) correspond to the free deflection data in (Fig. 6.9).

For conditions of simultaneous displacement and force generation, (such as the actuator pushing against a spring of stiffness k_s) a line based on equation 6.4 is drawn between the free-deflection and blocking force measurements of the actuator for each voltage. Since the gradient of the lines in Fig. 6.11 are $-1/k_{actuator}$ the near constant gradient suggests that the measured stiffness of the laminate does not change significantly with applied voltage.

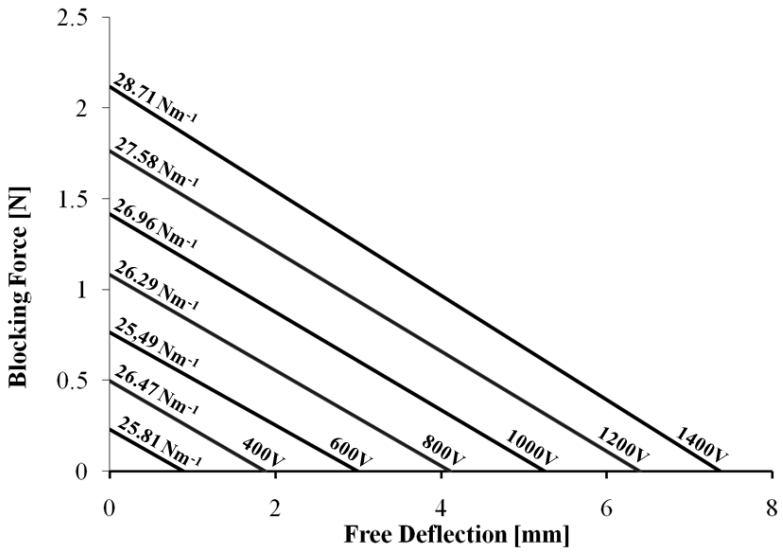

Fig.6.11: Force generation versus free-deflection of the actuated bistable laminate for a range of MFC drive-voltages with laminate stiffness at each voltage shown.

6.4 Conclusion

This chapter has characterised the actuator properties of a bistable carbon fibre composite with an MFC actuator bonded to its upper surface. An unsupported piezoelectric-laminate combination was evaluated in terms of its blocking force and free deflection capabilities.

The key conclusions drawn from the work presented in this chapter are:

- The blocking force of the piezoelectric laminate is directly proportional to the applied actuation voltage as predicted by the engineers beam equation.
- The Free-displacement of the piezoelectric laminate is also directly proportional to the applied actuation voltage though significant displacement creep is observed.
- The observed creep is caused by piezoelectric creep under open loop control and is correlated with previously published constitutive equations for time dependent creep in piezoelectric ceramics.

Linear relationships between both blocking force and free displacement with MFC drive-voltage were observed when the laminate was actuated within a single stable state. Maximum blocking force at 1400V was measured as 2.11N with a maximum free deflection of 7.80mm at 1400V. These data suggest that thin MFC actuated bistable laminates are better suited to lightly loaded structures due to the low maximum blocking force.

However the large free-deflection observed in Fig. 6.9 indicate that significant shape control of bistable laminates is possible within a single stable state. This shape control could prove useful in altering the height and profile of an adaptive bump to realise the proposed advantages in aerodynamic drag reduction noted by Stanewsky [32]. The ability to vary shape continuously within a single stable state in addition to the larger structural deformation created by snap-through could support the use of MFC actuated bistable composites for construction of an adaptive bump.

Significant deflection creep of the actuated laminate was measured as an increase in free-deflection without an increase in drive-voltage. This creep was attributed to the well known creep behaviour of the piezoelectric material within the MFC actuator when driven under open-loop control. If necessary, precise control of position could be achieved by closed-loop control of MFC drive-voltage.

The measured creep characteristics were fitted to previously presented equation for piezoelectric creep response and the creep time constant was found to vary in the range 0.01-0.05 for drive voltages of 200-1400V. No clear trend in creep time constant was found with increasing drive-voltage.

The force-displacement characteristic of the actuated laminate was also determined and the actuator stiffness for the laminate was found to remain approximately constant for all tested drive-voltages.

This chapter has shown that the linear piezoelectric constants used within the finite element model presented in Chapter 3 are sufficient to model the observed actuator behaviour. Furthermore piezoelectric creep has been measured and correlated with analytical predictions. The force-deflection capability of an MFC actuated bistable laminate has been characterised in terms of its free-deflection and blocking force.

In the following chapter the insights gained in each of the previous six chapters will be implemented in the design of an adaptive bump. The finite element model for actuated bistable composite laminates presented in Chapter 4 will be extended to predict the cured shape and snap-through voltage of an MFC actuated bistable bump.

6.5 Reference list

1. Brunner, A. J., Birchmeier, M., Melnykowycz, M. M., and Barbezat, M. (2009). "Piezoelectric Fiber Composites as Sensor Elements for Structural Health Monitoring and Adaptive Material Systems." Journal of Intelligent Material Systems and Structures, 20(9), 1045-1055.
2. Sodano, H. A., Park, G., and Inman, D. J. (2004). "An investigation into the performance of macro-fiber composites for sensing and structural vibration applications." Mechanical Systems and Signal Processing, 18(3), 683-697.
3. Choi, S. C., Park, J. S., and Kim, J. H. (2007). "Vibration control of pre-twisted rotating composite thin-walled beams with piezoelectric fiber composites." Journal of Sound and Vibration, 300(1-2), 176-196.
4. Sohn, J. W., Choi, S. B., and Lee, C. H. (2009). "Active vibration control of smart hull structure using piezoelectric composite actuators." Smart Materials & Structures, 18(7).
5. Schultz, M. R., and Hyer, M. W. (2003). "Snap-through of unsymmetric cross-ply laminates using piezoceramic actuators." Journal of Intelligent Material Systems and Structures, 14(12), 795-814.
6. Bilgen, O., Kochersberger, K. B., and Inman, D. J. (2008). "An experimental and analytical study of a flow vectoring airfoil via macro-fiber-composite

actuators." Proceedings of SPIE - The International Society for Optical Engineering, SPIE, San Diego, CA, United states. Vol.6930.

7. Sohn, J. W., Kim, H. S., Choi, S. B., and Kim, K. S. (2006). "Experimental investigation of smart hull structures based on macro fiber composite actuators." Key Engineering Materials, Trans Tech Publications Ltd, 326-328(2). 1419-1422.

8. Dano, M. L., Gakwaya, M., and Julliere, B. (2008). "Compensation of thermally induced distortion in composite structures using macro-fiber composites." Journal of Intelligent Material Systems and Structures, 19(2), 225-233.

9. Agrawal, B. N., and Elshafei, M. A. (1997). "Shape control of composite material plates using piezoelectric actuators." Proceedings of SPIE - The International Society for Optical Engineering, SPIE, Adelaide, SA, Australia, Vol. 3241. 300-311.

10. Park, J. S., and Kim, J. H. (2004). "Suppression of aero-thermal large deflections and snap-through behaviors of composite panels using macro fiber composite actuators." Smart Materials and Structures, 13(6), 1448-1459.

11. Schultz, M. R., Hyer, M. W., Williams, R. B., Wilkie, W. K., and Inman, D. J. (2006). "Snap-through of unsymmetric laminates using piezocomposite actuators." Composites Science and Technology, 66(14), 2442-2448.

12. Gude, M., and Hufenbach, W. (2006). "Design of novel morphing structures based on bistable composites with piezoceramic actuators." Mechanics of Composite Materials, 42(4), 339-346.

13. Portela, P., Camanho, P., Weaver, P., and Bond, I. (2008). "Analysis of morphing, multi stable structures actuated by piezoelectric patches." Computers & Structures, 86(3-5), 347-356.

14. Bowen, C. R., Butler, R., Jervis, R., Kim, H. A., and Salo, A. I. T. (2007). "Morphing and shape control using unsymmetrical composites." Journal of Intelligent Material Systems and Structures, 18(1), 89-98.

15. Binette, P., Dano, M. L., and Gendron, G. (2009). "Active shape control of composite structures under thermal loading." Smart Materials & Structures, 18(2).

16. Williams, R. B., Grimsley, R. B., Inman, D. J., and Wilkie, W. K. (2002). "Manufacturing and mechanics-based characterization of macro fiber composite actuators." American Society of Mechanical Engineers, Aerospace Division (Publication) AD, New Orleans, Louisiana, USA. Vol. 67. 79-89.

17. Betts, D. N., Salo, A. I. T., Bowen, C. R., and Kim, H. A. (2010). "Characterisation and modelling of the cured shapes of arbitrary layup bistable composite laminates." Composite Structures, 92(7), 1694-1700.

18. Jung, H., and Gweon, D. G. (2000). "Creep characteristics of piezoelectric actuators." Review of Scientific Instruments, 71(4), 1896-1900.

19. Changhai, R., and Lining, S. (2005). "Hysteresis and creep compensation for piezoelectric actuator in open-loop operation." Sensors and Actuators A: Physical, 122(1), 124-130.

20. Jaffe, B., and cook, W. R. (1971). "Piezoelectric ceramics." Academic Press, London, UK. ISBN:0-123-79550-8

21. Jung, H., Shim, J. Y., and Gweon, D. G. (2001). "Tracking control of piezoelectric actuators." Nanotechnology, 12(1), 14-20.

22. Tsurumi, T., Sasaki, T., Kakemoto, H., Harigai, T., and Wada, S. (2004). "Domain contribution to direct and converse piezoelectric effects of PZT

ceramics." Japanese Journal of Applied Physics, Part 1: Regular Papers and Short Notes and Review Papers, 43(11 A), 7618-7622.

23. Huang, H., and Tianshu, Z. (2002). "Stress- and Strain-relaxation in Lead Zirconate Titanate based ceramics." Mat. Chem and Phys, 75, 186-189.

24. Chen, P. J., and Montgomery, S. T. (1980). "Macroscopic theory for the existence of the hysteresis and butterfly loops in ferroelectricity." Ferroelectrics, 23(3-4), 199-207.

25. Haertling, G. H. (1999). "Ferroelectric ceramics: History and technology." Journal of the American Ceramic Society, 82(4), 797-818.

26. Cross, L. E. (2000). "Domain and phase change contributions to response in high strain piezoelectric actuators." Fundamental Physics of Ferroelectrics 2000, 535, 1-15.

27. Georgiou, H. M. S., and Mrad, R. B. (2008). "Dynamic electromechanical drift model for PZT." Mechatronics, 18(2), 81-89.

28. Deraemaeker, A., Nasser, H., Benjeddou, A., and Preumont, A. (2009). "Mixing Rules for the Piezoelectric Properties of Macro Fiber Composites." Journal of Intelligent Material Systems and Structures, 20(12), 1475-1482.

29. Cain, M., and Stewart, M. (2001). "The measurement of blocking force." Rep. No. MATC(A) 48, National Physical Laboratory, Teddington, UK.

30. Gere, J. M. (2006). "Mechanics of Materials." Thomson, Toronto, Canada. ISBN: 0-534-55397-4

31. Yoon, K. J., Shin, S., Park, H. C., and Goo, N. S. (2002). "Design and manufacture of a lightweight piezo-composite curved actuator." Smart Materials and Structures, 11(1), 163-168.

32. Stanewsky, E. (2001). "Adaptive wing and flow control technology." Progress in Aerospace Sciences, 37(7), 583-667.

Chapter 7 - Design and characterisation of adaptive bump demonstrator

As described in Chapter 1 significant improvements in aerodynamic performance can be achieved by introducing adaptive bumps on flow control surfaces of commonly used aerofoils [1]. Therefore in this chapter the finite element modelling procedures developed in Chapters 2, 3 and 4 will be extended to allow design of a laboratory demonstrator for a novel piezoelectrically actuated adaptive bump.

Section 7.1 describes the concept design process for the demonstrator and presents the chosen adaptive bump design. Section 7.2 will detail the formulation and solution of the finite element model used to predict the cured shape and snap-through behaviour of the demonstrator. The FE model will then be used to determine appropriate dimensions of bistable component and to predict the deflections and snap-through voltages expected during experimental characterisation.

The manufacturing process and experimental techniques used to measure cured shape and snap-through voltage of the adaptive bump are detailed in section 7.3 with results compared to FE predictions and discussed in section 7.4.

7.1 Demonstrator concept design

This section details several key design choices during the design process of an adaptive bump demonstrator which was identified in Chapter 1 as of significant research interest for aerodynamic flow control in civil aircraft. These design choices were key in determining the reason for the final demonstrator form.

Fig.7.1 shows the proposed central bistable segment within a unidirectional composite laminate. The elliptical shape was chosen as it was felt that rectangular or polygonal segments would introduce significant stress concentrations around the corner regions. It is hoped that by eliminating corners from the segment shape the stresses caused by the segmented layup will be distributed evenly across the entire joint. This is advantageous both for reduced modelling errors in regions of rapid stress gradient [2] and for the robustness of the demonstrator model.

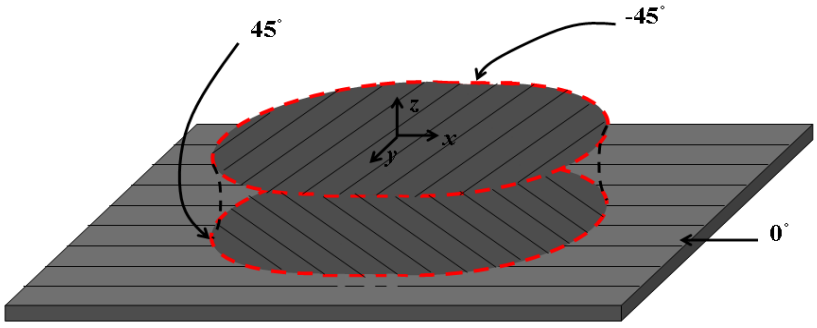

Fig.7.1: Elliptical bistable segment within a unidirectional host laminate with bistable section boundary highlighted and pre-preg lay-up schedule indicated.

The lay-up of the bistable segment was chosen so that the axis of curvature for both stable states would lie at equal but opposite angles to the host laminate fibre direction. This simple step ensured that the anisotropic stiffness of the host structure did not cause the maximum laminate deflection of the two stable states to be significantly different. Fig 7.3 shows the axis of curvature for the bistable segment in State A (A-A′) and State B (B-B′) with the angle between those axes and the host laminate fibre direction (θ).

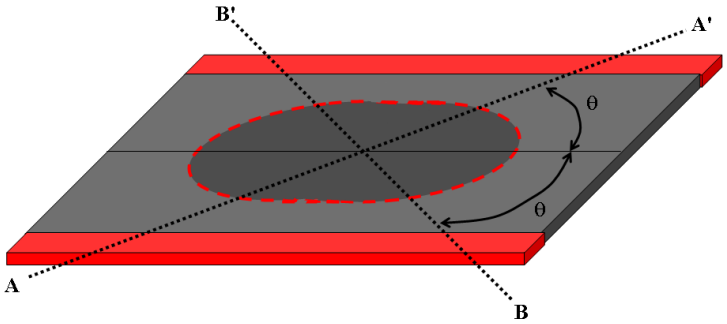

Fig.7.2: Axis of curvature for the $[-45/45]_T$ segment in State A (A-A') and State B (B-B'), angle (θ) between these axes and the host laminate fibre direction with laminate edges to be bonded to support rails indicated in red.

In order to simulate the integration of this adaptive bump into an aerospace structure the regions highlighted red in Fig. 7.2 will be bonded to rigid support rails to simulate attachment of the adaptive structure to a stringer or rib as is standard in aviation fuselage and wing structures. Fig. 7.3 indicates the expected bump profiles along the line A-A' and the large difference in central deflection which will result from transition between the two stable states.

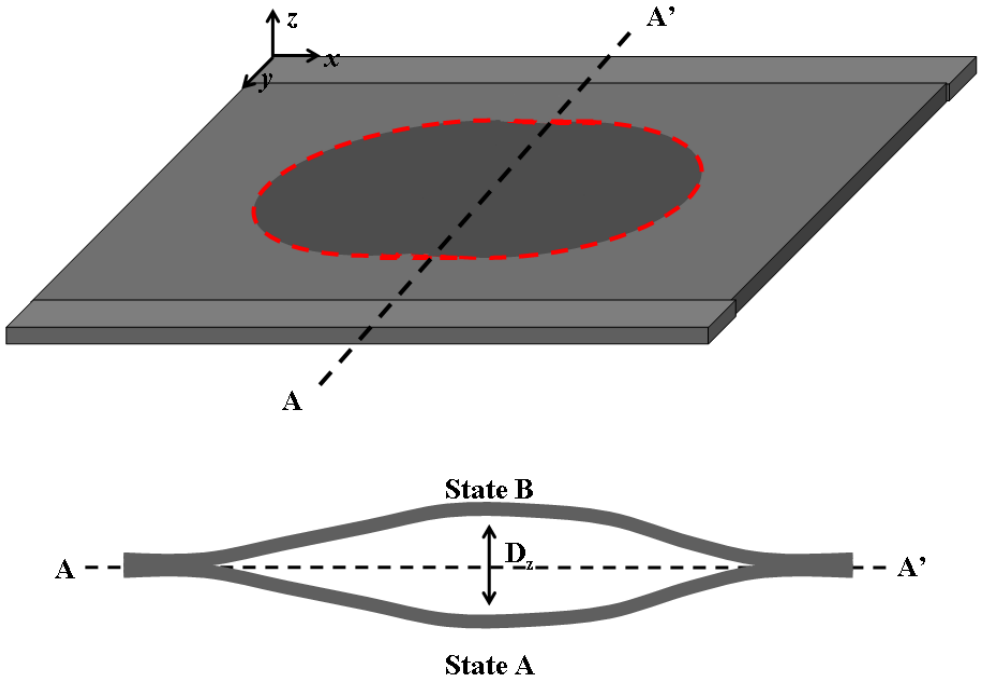

Fig.7.3: Cross section of bump profile in State A and State B along the line A-A' showing laminate deflection D_z.

Fig.7.4 shows the manufactured demonstrator bonded to the support rails with the bistable segment highlighted. It should be noted that the resin layer formed during composite

manufacture is uppermost in Fig. 7.4 and hence State A corresponds to the state where the centre point of the bump is below the level of the support rails.

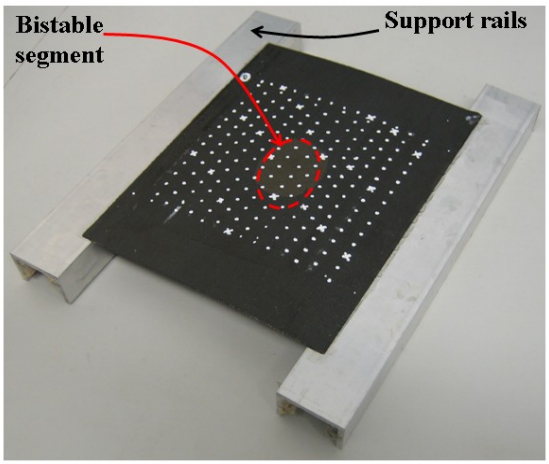

Fig.7.4: Adaptive bump demonstrator bonded to aluminium support rails, with bistable segment highlight by red dashed line.

This section has detailed the motivation for demonstrator concept design and highlighted the reasoning behind several key elements of the demonstrator. In the following section the finite element model used to design the final demonstrator model and predict its operational capabilities will be described.

7.2 Finite element modelling of adaptive bump structure

In this section the finite element model used to design a lab-scale demonstrator of an MFC actuated adaptive bump will be described. Several models were solved to enable laminate dimensions to be determined which created two stable states yet allowed snap-through at a drive voltage within the operational range (0-1500V) of a Smart Materials MFC8507-P1 actuator.

7.2.1 Composite model definition

To model the composite elements of the bistable bump, 20-node quadratic layered brick elements were used (SOLID186) in order to better capture the curved laminate geometry and allow accurate resolution of through thickness stress components, highlighted as important in Chapter 2. As described in Chapter 4 the layer thicknesses and elastic constants of the M21/T700 unidirectional pre-preg material shown in table 4.1 and table 4.2 were used in the layer thickness definitions within the SOLID186 element.

Several 'primitive' volumes were defined and subsequently combined using Boolean operations to create appropriately shaped volumes to represent the bistable and unidirectional segments of the composite laminate within the finite element model. The volumes created by these Boolean operations are shown in Fig. 7.5.

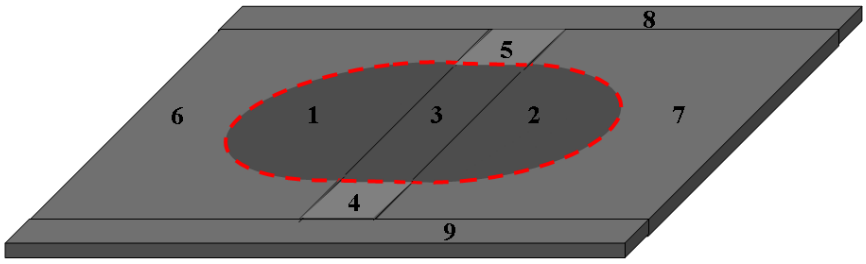

Fig.7.5: Nine volumes used to represent unidirectional composite laminate (volumes 4-9) and elliptical $[-45/45]_T$ bistable segment (volumes 1-3).

Layer sequence for both unidirectional and bistable composite segments were defined as section definitions within the SOLID186 element definition. Section definitions specify layer thickness, orientation and material within the layered element. When meshing a volume, these

parameters may be varied by selecting a section definition appropriate to the lay-up in that volume.

In defining the SOLID186 elements used within the adaptive bump model three section definitions were used. Layer thicknesses for all three sections definitions were assumed to match those previously measured for laminates with ply orientations of $[\theta/\theta\text{-}90/\text{resin}]_T$ as shown in table 4.1. Layer sequence for the unidirectional host laminate was chosen to be $[0/0/\text{resin}]_T$ so that the excess resin layer observed in the manufactured laminates was captured within the FE model. Bistable segments of the lay-up were defined with layer sequence of $[45/\text{-}45/\text{resin}]_T$.

When meshing the two semicircular segments (volumes 1 and 2 in Fig.7.5) it was found that the *VSWEEP* command used to mesh the volumes of revolution caused the *z*-axis of the elements in each volume to lay in opposing directions. An additional section lay-up with layer sequence ($[\text{-}45/45/\text{resin}]_T$) was defined so that the layer sequence was consistent within the global coordinate system. The *VSWEEP* command is an automatic meshing tool which creates volume elements based on the mesh defined for an initial area. The volume mesh is then swept through the volume until the target area, which lies opposite the initial area, has been meshed.

Once each segment within the laminate model had been assigned a section definition, element side lengths were selected so that nodes on adjacent volume boundaries were coincident. Fig. 7.6 shows the initial dimensions of the laminate model.

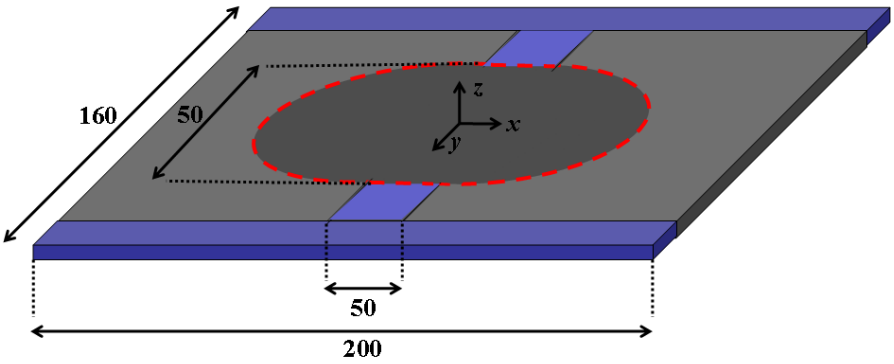

Fig.7.6: Initial dimensions in mm of segmented laminate model with model global coordinate system.

All volumes shaded grey in Fig 7.6 were meshed using the *VSWEEP* command within Ansys while those shaded blue were meshed using traditional mapped hexahedral meshing

automatically generated by the *VMESH* command. Element size is controlled by the element side lengths of each line in the volume to be meshed, therefore careful definition of the each volume is essential. Fig. 7.7 shows the initial area, target area and element side length constraints used by VSWEEP when meshing the semicircular segments of the laminate. Ansys code files used to control this process may be seen in Appendix 3.

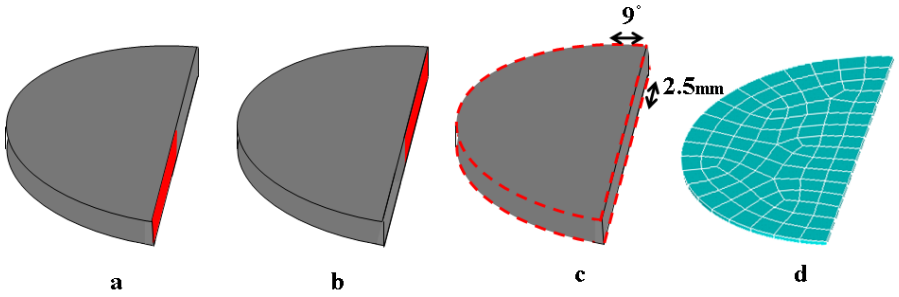

Fig.7.7: Initial area (a), target area (b) and element side length constraints (c) used by VSWEEP to produce final mesh (d).

The complete composite laminate was meshed using a total of 2082 SOLID186 elements with all elements being quadrilateral and having an aspect ratio of less than 10. The final mesh for the entire composite laminate can be seen in Fig. 7.8 which shows a well ordered mesh with smooth transitions in element size and no degenerate element shapes. Mesh density of the MFC was increased so that the complex stress state resulting from the actuator crossing the boundary between two segments of the lay-up was well captured.

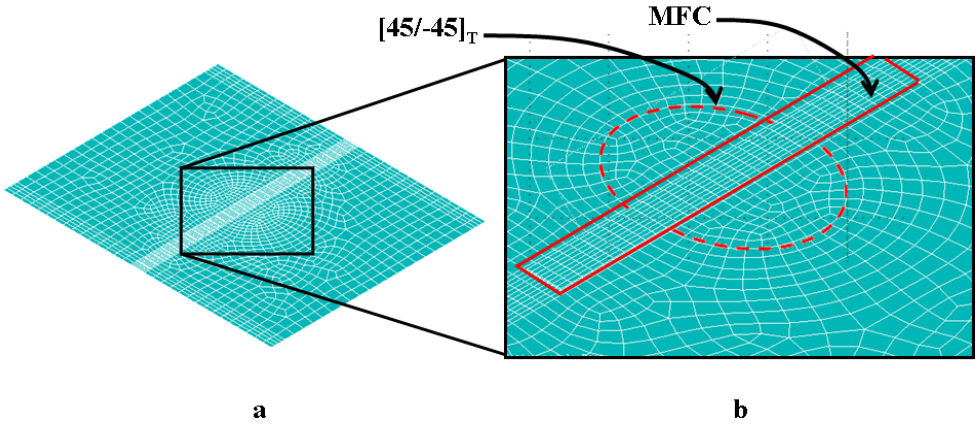

Fig.7.8: Meshed composite laminate model consisting of 2082 SOLID 186 elements (a) with close up of bistable region (b).

Once all volumes were meshed with appropriate section definitions defined all adjacent key points and nodes were merged using the *NUMMRG* command to ensure accurate stress transfer between volumes during load application. Finally, all composite elements were selected and their element coordinate systems defined as shown in Fig 7.7 to ensure correct layer orientation.

7.2.2. Adaptive model definition

Once the composite model was defined, a single MFC actuator (Smart Materials Corporation, MFC8507-P1) volume was added to the model and meshed with 20-node quadratic coupled field brick elements (SOLID226) as shown in Fig. 7.9. This volume was centrally located with element dimensions selected to match those of the underlying composite model for all tested models.

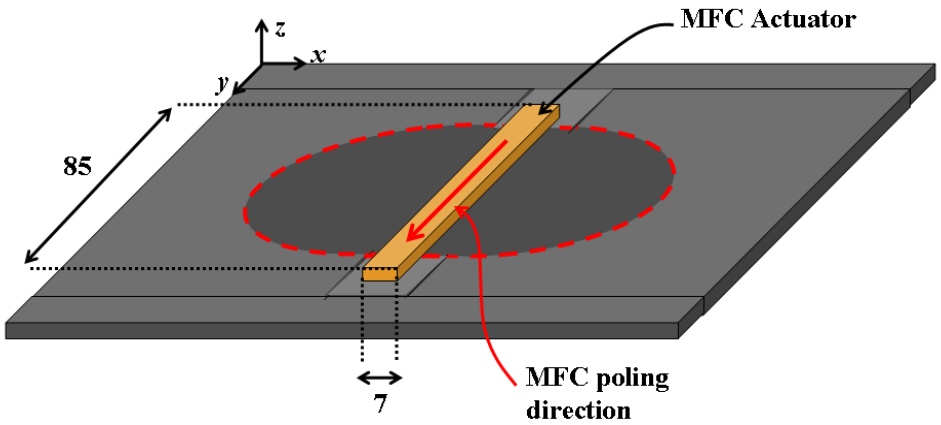

Fig.7.9: MFC actuator centrally located on the upper surface of the composite laminate, showing poling direction of PZT fibres.

The 8507-P1 actuator has an active area measuring 85mm×7mm×0.3mm with the PZT fibres and poling direction running parallel with the long axis of the actuator as seen in Fig. 7.8. This actuator was chosen so that maximum actuation strain could be generated in the *y*-direction while limiting undesired transverse actuation strain caused by the d_{31} piezoelectric coupling during application of the offset voltage, as discussed in Chapter 4.

Electrical constraints described in Chapter 3 section 3.1 were applied to the MFC volume to ensure generated electric field was aligned with the poling direction of the material. An offset voltage was applied to the MFC volume to counteract the stress state caused by thermal contraction of the composite laminate. Using equation 4.1 (section 4.3) the offset voltage (V_0)

required to counteract the imposed thermal stress in the MFC created by the underlying $[-45/45/resin]_T$ laminate was calculated to be 265462V.

The node at the origin of the global coordinate system was mechanically constrained from translation within the plane of the laminate (*xy*-plane) and a small initial displacement of -1mm applied in the *z*-direction as shown in Fig. 7.10a. This small initial displacement was necessary to force the model to converge into stable State B after application of the thermal load.

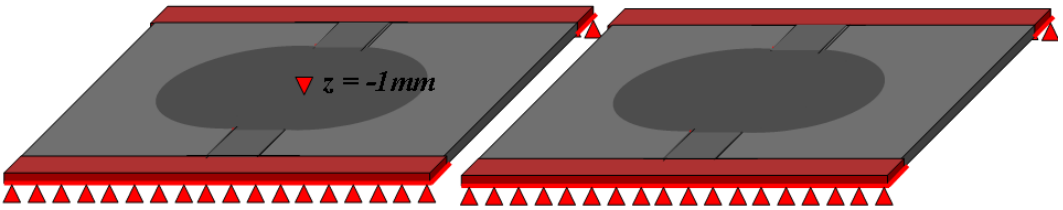

Fig.7.10: Mechanical constraint of FE model with central and edge constraints highlighted during thermal load step (a) and during electrical load step (b).

Nodes located within the two 5mm wide strips between y = 0mm and 5mm and between y = 155mm and 160mm (highlighted red in Fig. 7.10) were also constrained from translation in *z*-direction. This constraint set was chosen to simulate the conditions experienced by the demonstrator as it was bonded to the support rails, but prior to the adhesive curing. The in-plane translational degrees of freedom (x & y) within these two strips were left unconstrained so that model was able to deform in a similar manner to the curved demonstrator as it is pressed into contact with the flat support rails.

With the appropriate electrical and mechanical constraints imposed on the model the thermal load could be applied and the model solved. The following section describes the solution procedure to predict cured shape and snap-through voltage of the adaptive bump model.

7.2.3. Model solution

As described in Chapter 4, the solution was run as a geometrically non-linear structural analysis so that element stiffness matrices were calculated using the deformed and rotated nodal coordinate systems. This important step ensures that the changes in laminate stiffness caused by the out of plane deformations are accurately captured by the model.

All composite elements within the model were selected using the *ESEL* command and a temperature constraint of -158K applied to mimic the cool down from a cure temperature of 179˚C to a room temperature of 21˚C. Laminate deformation at the end of this load step can be seen in Fig. 7.11a.

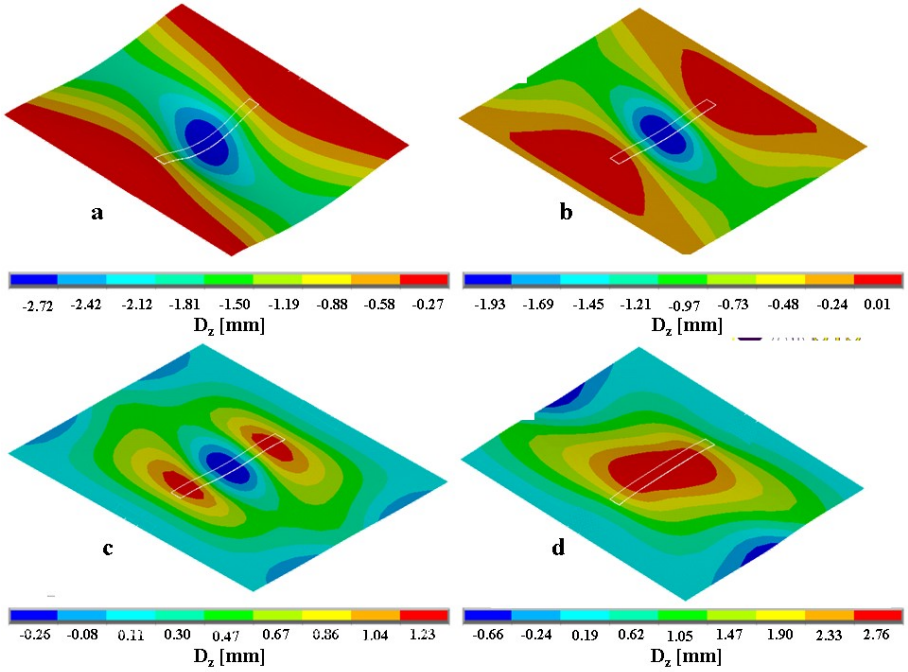

Fig.7.11: Surface plots of nodal displacement in z-direction [mm] for the adaptive bump model after the thermal load step (a), in stable State B (b), during MFC actuation (c) and after snap-though in stable State A (d) with legend displayed for each plot.

To enable solution settings to be varied between load steps each load step was defined and solved individually using the *TIME*, *NSUBSTP*, *KBC* and *SOLVE* commands as seen in the following excerpt from appendix 3:

```
TIME,1                  ! Sets time at end of load step
NSUBST,100,,,,          ! Divides load step into100 substeps
KBC,0                   ! Sets to ramped load step
ESEL,s,,,all
ESEL,u,mat,,2           ! Selects only SOLID186 elements
BFE,all,temp,1,-158     ! Temperature change of -158K
ALLSEL                  ! Reselects all elements in model
SOLVE                   ! Solves current load step
```

Once thermal loading was complete the *LNSRCH* solution option was implemented to improve solution stability and aid convergence during subsequent load steps. As discussed in Chapter 4 section 4.3 the use of the line search convergence control is not the preferred

method for analysis of snap-through buckling [2], however it is the only implementable stabilisation tool available for this coupled field analysis within Ansys V11.0.

Mechanical boundary conditions were altered to represent a perfect bond between the support rails and the laminate. The nodal locations in the *x*-direction of the two 5mm strips indicated in Fig. 7.11b were fixed so that mechanical boundary conditions imposed on the model during MFC actuation matched experimental conditions. The *z*-displacement imposed at the global coordinate system origin was removed after the thermal load step had solved. Once this central constraint was removed and the model solved, the adaptive bump converged to the State B configuration which is defined as the shape in which the excess resin layer lies on the convex face of the laminate (fig. 7.11b).

To simulate application of MFC drive-voltage the voltage constraint applied at y = 42.5mm was changed from the V_0 value of 265462V to the constraint voltage (V_c) of 10462V to create a change in electric field of 3MVm^{-1} within the MFC volume. This change in drive-voltage caused an actuation strain within the laminate, reducing curvature and hence maximum laminate deflection as seen in Fig. 7.11c.

In models for which snap-through occurred during this load step the voltage constraint was returned to the initial value (V_0) to allow the laminate to settle into State A as seen in Fig. 7.11d. If snap-through did not occur this step was omitted.

It was found that the line search convergence control technique was adequate to allow Ansys to fully predict the snap-through event within the adaptive bump model. It is thought that the smaller structural deformations and increased mechanical constraint caused by the clamped boundary conditions cause a more progressive snap-through than that observed in free-laminates. It is likely that the lack of a discontinuous load-displacement path in this more tightly constrained analysis allows the line search technique to converge to the correct stable state.

Despite a more gradual transition between states, a clear reversal of curvature was shown between consecutive substeps during the model solution as seen in Fig. 7.11c and 7.11d. The snap-through voltage was recorded as the drive-voltage at which this reversal of global curvature first occurred.

7.2.4 Demonstrator design

In this section the method used to determine appropriate laminate dimensions for the physical demonstrator will be described.

In order to determine the maximum achievable structural deflection of the adaptive bump when actuated using a single Smart Materials 8507-P1 MFC actuator the model described in the preceding sections was solved with laminate dimensions as shown in Fig. 7.5. This preliminary analysis showed the presence of a stable State B but did not predict snap-through to occur within the operational range of the MFC actuator (i.e. 0-1500V).

When increased drive voltage was applied to the model, snap-through did occur and when the drive voltage returned to the initial offset voltage (V_0) the model remained in a stable State A configuration. Once it was confirmed that the adaptive bump would exhibit two stable states the dimensions of the bistable segment (highlighted by the red dashed line in fig. 7.12) were reduced incrementally until snap-through occurred at a drive voltage of 1200V (80% of maximum operational drive-voltage). This conservative target drive-voltage was selected to allow for a functioning demonstrator to be produced even if the model predictions under estimate experimental snap-through voltage.

It was found that reduction of the bistable segment length in the *y*-direction below 40mm caused State B to become unstable and so this value was the minimum feasible segment length. However whilst segment dimension in the *x*-direction (width) remained at 100mm predicted snap-through voltage remained outside the MFCs operational range. The segment width was therefore reduced in order to reduce the predicted snap-through voltage.

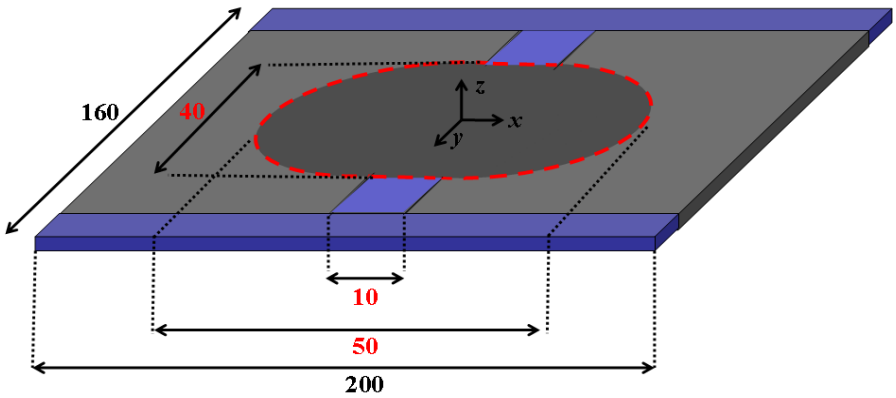

Fig.7.12: Final dimensions of adaptive bump demonstrator with segment dimensions which were varied during laminate design shown in red.

After several iterations it was found that in order to achieve maximum laminate deflection yet still snap-through at a predicted MFC drive voltage of less than 1350V the bistable segment of the adaptive bump must be of the dimensions shown in Fig. 7.12. The segment length was reduced to 40mm while the segment length was halved to 50mm. This iterative design process allowed design of a physical demonstrator but would also lend itself to automation as part of an optimisation study. Unfortunately such a study is beyond the scope of the present work.

7.3 Manufacture and experimental work

Section 7.3.1 describes the techniques used in the manufacture of the localised adaptive bump demonstrator, with the image correlation techniques used to measure the cured shape of the two stable states described in section 7.3.2. Experimental setup and procedure used to measure the snap though voltage of the demonstrator is described in section 7.3.3.

7.3.1 Demonstrator manufacture

Once the final dimensions of the composite laminate were determined, as described in section 7.2.4, the unidirectional T700/M21 pre-preg material was cut to size. In order to prepare the elliptical segments two rectangular coupons measuring 50mm × 40mm were cut so that fibre angle lay at 45˚ to the major axis of the rectangle. The semicircular shapes were marked on the pre-preg backing paper using a pair of compasses before a 40mm diameter PTFE rod was positioned to act as a cutting guide as shown in Fig. 7.13a. Once both semicircular cuts were complete the elliptical segment was ready for use.

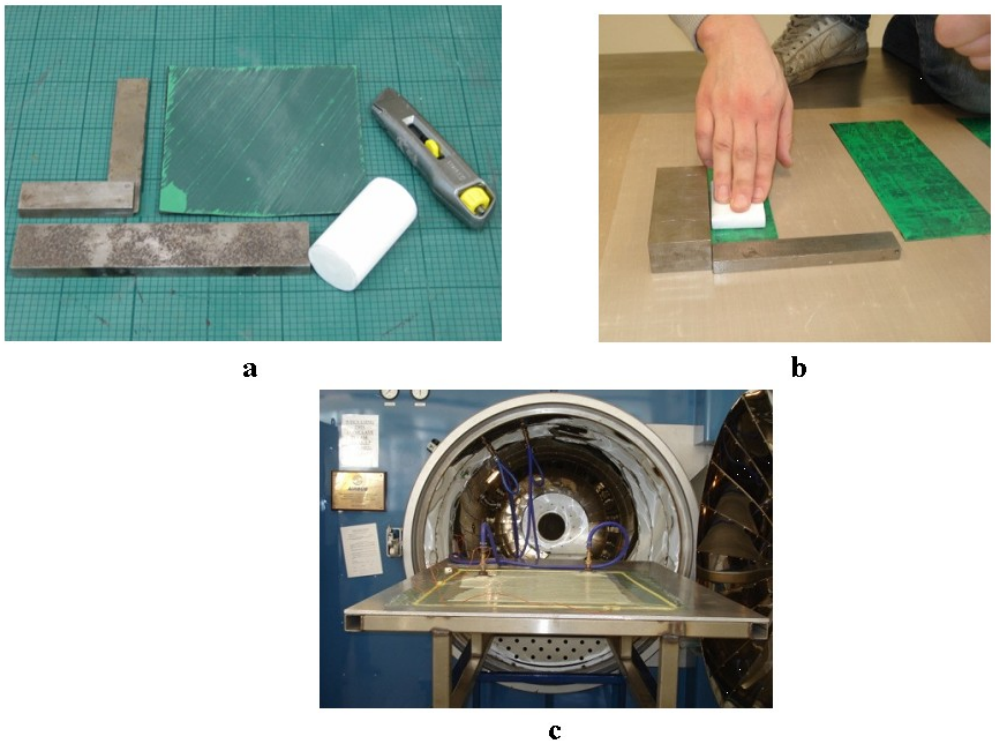

Fig.7.13: Photographs showing equipment used to cut pre-preg segments (a), lay-up and compaction (b) and completed vacuum bag ready for the autoclave (c).

To make the unidirectional plies of the host laminate two rectangular coupons measuring 180mm × 220mm were cut with fibre angle running parallel to the major axis of the rectangle (Fig. 7.13a). To allow addition of the bistable segment an elliptical segment was cut from each coupon with the centre of the segment positioned at the coupons centre.

Once all segments were cut to size the plies were laid onto an aluminium lay-up table coated in release film and the laminate compacted using PTFE rollers as seen in Fig. 7.13b. The laminates were then placed under release film before a breather layer was added and a vacuum bag sealed over the laminates. The vacuum bag containing the laminate can be seen before entering the autoclave in Fig. 7.13c.

The laminates were cured at 180˚C using a single dwell cure cycle as specified for the M21 resin system before being allowed to cool to room temperature. Once cooled the vacuum bag was removed and the laminate was trimmed to final dimensions using a liquid cooled diamond saw.

In order to mount the MFC actuator to the tool-side (without excess resin layer) of the laminate the bond region was lightly roughened using emery paper before being cleaned with isopropryl alcohol. The MFC actuator was also cleaned and a thin layer of two part epoxy adhesive applied to both bond surfaces. The laminate edges and aluminium support rails indicated in Fig. 7.14 were prepared in the same fashion and a thin layer of epoxy applied to both surfaces. The inset of Fig. 7.14 shows the location of the MFC actuator on the underside of the demonstrator.

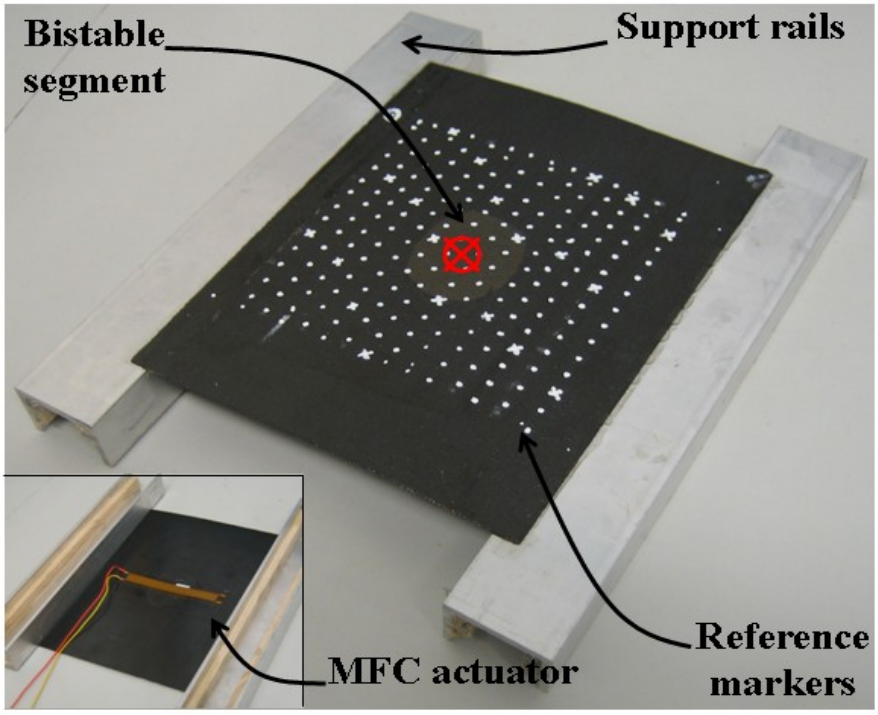

Fig.7.14: Localised bump demonstrator bonded to support rails showing reference dots applied to the resin layer to allow motion capture, central bistable segment and *inset* showing underside of demonstrator with MFC actuator bonded to the smooth side of the laminate.

The MFC and support rails were then positioned as required before a clamping load of 200N was applied to ensure full contact of bond surfaces. The clamp remained in place for 24hrs to allow the epoxy to fully cure. The laminate was bonded to the support rails so that the tool-side of the laminate, and hence the MFC were positioned on the lower surface, hence in Fig. 7.14 the excess resin layer is on the uppermost surface. The textured surface prevented the use of adhesive reference markers as used in Chapter 2 and 4, therefore reference markers were painted onto the laminate surface as seen in Fig. 7.14.

7.3.2 Measurement of cured shape using motion capture

The cured shape of the demonstrator was measured using the motion capture techniques described in section 2.2 of Chapter 2 to provide full-field surface profiles for both the stable states.

A number of dots (203 in total) were placed over an area measuring 120mm × 120mm centred about the laminate centre point as shown in Fig. 7.14 to act as reference markers for the motion capture analysis. This reduced measurement area was chosen to ensure sufficient point

density to fully capture features surrounding the edges of the bistable segment and reduce errors associated with surface interpolation from raw coordinates.

As in section 2.2 three cameras were positioned in an umbrella arrangement so that their viewing planes were not coplanar as recommended by Nigg [3] and all reference markers were visible to each camera. In order to best capture the shape of both stable states two of the cameras were repositioned between measurements of each state. With the camera positions set, the camera views were restricted to just outside of a 100mm × 100mm× 40mm calibration object similar to that seen in the inset of Fig. 2.4 to give a viewing area of 1440 × 1152 pixels. Short video clips were taken with each camera before the demonstrator was replaced so that the area of interest lay at the centre of the calibrated volume and a short video clip taken.

The digital images were exported to the motion capture software Peak Motus® (v. 8.5, Vicon, USA) where pixel locations of calibration frame vertices and reference markers were combined as described in section 2.2 to produce raw coordinates for each of the 203 reference marker locations.

These irregularly spaced spatial coordinates were imported into Matlab R2007A and interpolated using a spline based surface interpolation method [4] to create regularly spaced coordinates describing the interpolated surface for comparison with the FE-predicted coordinates.

This section has described the measurement of the cured shape; the following section describes the techniques used to measure snap-through voltage of the adaptive bump demonstrator.

7.3.3 Measurement of snap-through voltage

In order to determine the MFC drive-voltage required to cause the demonstrator to snap-through from stable State B to State A, the experimental setup shown in Fig. 7.15 was used. With the demonstrator support rails clamped in position a monotonic step change in drive voltage was applied from zero volts up to the test voltage via two single-core copper wires soldered to the MFC and secured to the table.

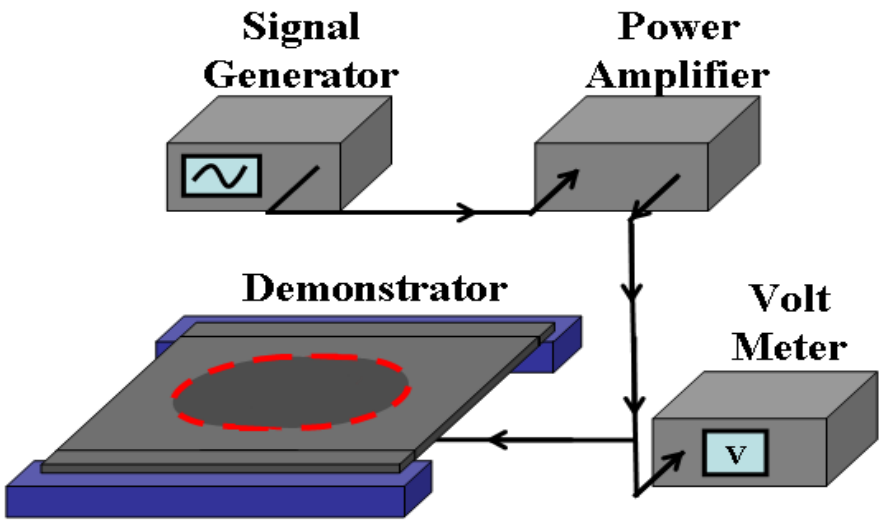

Fig.7.15: Block diagram of experimental set up showing signal generator (a), Power amplifier (b), voltmeter (c) and demonstrator (d).

A function generator was used to provide a DC step-input to a power amplifier (TREK PZD700 piezo driver) which was manually calibrated to provide an output voltage of 200±0.1V for a 1V input signal. Amplifier output stepped from zero volts up to the desired test voltage and held the test voltage for a period of 60 seconds for each test. Drive voltage was then returned to zero and the actuator disconnected from the power supply before the laminate was manually snapped into each stable state once before being reset to the starting condition and electrically discharged to ensure that no residual charge influenced system characteristics.

Drive voltage was increased in increments of 200V over the range 0-1400V but snap-through was not observed within this voltage range.

Additional high voltage testing was carried out using a stand-alone power amplifier (Glassman PS/FC30P04.0-22, Glassman High Voltage Inc, High Bridge, NJ) with drive voltages in the range 1400 - 1900V. Using the amplifier voltage controller a step change from zero volts to the desired test voltage was applied as before. While not rated for use beyond 1500V the MFC actuator remained functional despite repeated application of voltages in excess of this nominal maximum rating. However despite the increased drive-voltage snap-through was not observed within this range of drive-voltage.

Despite the expanded range of applied drive voltage snap-through was not observed under MFC-actuation alone so an additional mechanical load was applied to reduce drive voltage required to induce snap-through.

Bowen [5] has demonstrated that by combining mechanical loads with MFC actuation snap-through may be induced in bistable laminates. A single calibrated mass of 250g was placed at the centre of the bistable segment before the application of drive voltage was repeated using the setup shown in Fig. 7.15. As before, drive-voltage was increased in increments of 200V from 0V until snap-through was observed at 1220V, the minimum voltage required to induce snap-through was determined by binary search in the range 1100-1300V with 5V the smallest increment between test voltages. To ensure that inconsistencies in mass placement did not influence the snap-through voltage the search was repeated six times with the result repeated exactly on each occasion.

The measured snap-through voltage is the minimum voltage required to produce snap-through immediately upon application of drive-voltage, due to displacement creep of the MFC (discussed in section 6.1.2) snap-through occurred after extended drive voltage application at lower drive-voltages.

In order to examine the bump deformation induced by MFC actuation, detailed measurement of laminate deflection at different drive voltages were taken. The following section describes the measurement procedure used to verify that the demonstrator was in fact deforming under MFC actuation.

7.3.4 Measurement of laminate profile using laser profilometry

To gain insight into the deformation created by the MFC in the absence of applied mechanical load measurements of laminate deflection along the line x = 0mm and y = 0mm (shown in Fig. 7.16) were taken at drive voltages in the range 0-1400V. Measurements were taken using a Scantron Proscan 2000 laser profilometer setup to take 1400 height measurements over a scan length of 140mm centred about the origin of the global coordinate system. Measurement resolution for laminate deflection was 1μm with measurement points spaced at 100μm intervals.

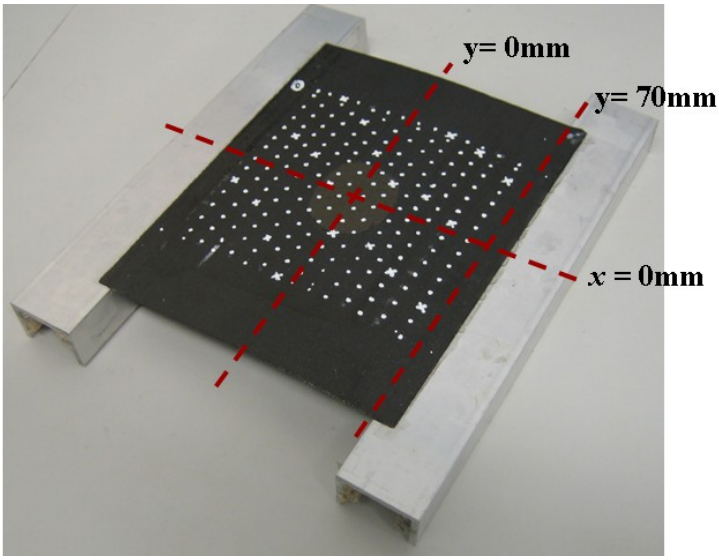

Fig.7.16: *x* = 0mm and *y* = 0mm lines scanned using laser profilometer to assess bump profile and the *y* = 70mm line used to normalise scan data.

Using the experimental setup seen in Fig. 7.15 drive voltages in the range 0-1400V were applied to the MFC in 200V increments. Drive voltage was applied as a monotonic step change immediately before scanning began, with each scan taking approximately 2seconds. A second scan was taken 5seconds later which showed some displacement creep as explained in Chapter 6. Laminate deflection along the x = 0mm line was normalized with respect to the measured deflection at y = 70mm (seen in Fig. 7. 16) as this point was bonded to the support rail and hence fixed. Laminate deflection along the y = 0mm line was normalized with respect to the measured laminate deflection at the global origin for each voltage so that for each experimental voltage line scans of laminate profile were coincident at this point. Once normalized values were exported the Microsoft Excel®.

A 6^{th} order polynomial trend line was fitted to the 1400 experimental data points to indicate laminate profile at each experimental drive-voltage. Maximum laminate deflection was extracted from the raw coordinates and plotted against the corresponding drive voltage. In the following section the results of experimental characterization of the adaptive bump demonstrator will be compared to the FE predicted behaviour.

7.4 Results and discussion

The experimental measurements generated by the three experiments described in section 7.3 will now be described and compared to those predicted using the finite element model described in section 7.2. Section 7.4.1 describes the cured shape of the laminate and how the predicted surface profile differs from that measured by motion capture techniques.

Section 7.4.2 describes the change in laminate deflection with applied MFC drive voltage as measured by laser profilometry before the snap-through behaviour of the demonstrator is compared to that predicted by FE modelling.

7.4.1 Cured shape

The motion capture measurements made of laminate deflection for the adaptive bump are now compared to the FE-predicted bump profile. Fig. 7.17 shows interpolated surfaces based on both FE-predicted and experimentally measured surface coordinates. Additionally in Fig. 7.17b and 7.17d the interpolated surface plot of measured laminate profile is shaded according to the total error between the FE-predicted coordinates and the measured values at that point.

Finite element predictions of the overall shape and major axis of curvature of both stable states (Fig. 7.17a and 7.17c) capture the laminate surface very well, although in both cases the bump profile predicted is longer in the *y*-direction with a less pronounced peak than is observed in experimental measurements.

The differences in bump profile are clearly shown by examining the error plots seen in Fig. 7.15 b and 7.15d. The absolute error in *mm* between FE-predictions and experimental data reach their maximum values in the locations where the MFC crosses the boundary between the bistable segment and the unidirectional host laminate. This rapid variation of error shows that the curvature of the two surfaces is significantly different, the relative changes in both error plots in these regions confirms that FE-predicted bump profile is wider in the *y*-direction.

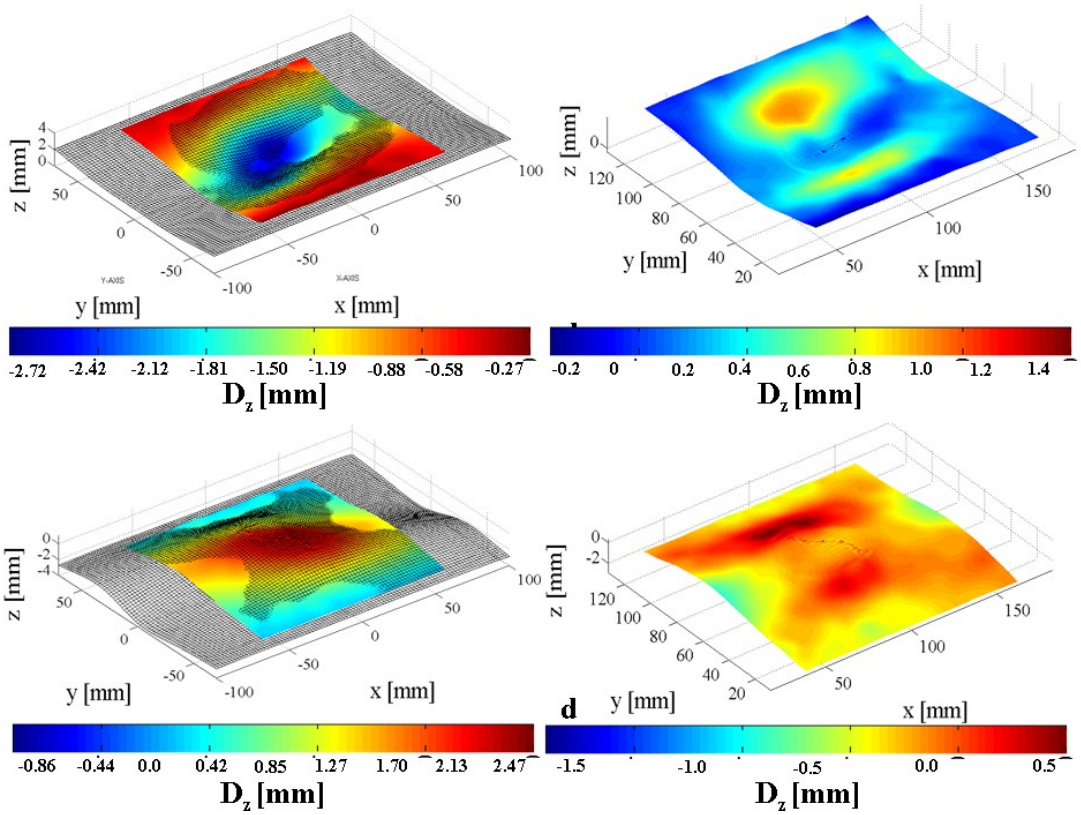

Fig.7.17: Interpolated surface plots of 203 experimentally measured coordinates with FE-predicted mesh overlaid showing State A (a) with interpolated surface plot shaded according to error of FE compared to experiment (b). Interpolated surface plot and error plot for State B are shown in (c) and (d) respectively.

In addition to this change in bump profile the predicted value of maximum laminate deflection for State B of 2.76mm is 0.29mm higher than the measured value of 2.47mm. The prediction error of 11.7% shows that quantitative agreement between predicted and measured cured shape for State B is very good and of similar accuracy as the previously presented work in Chapter 4. Quantitative agreement between measured and predicted laminate deflection within State A is excellent with maximum laminate deflection matching to within 0.2mm and a peak error of 0.8mm.

7.4.2 Laminate deformation with applied drive-voltage

In order to determine the extent of laminate deflection in response to MFC drive-voltage the line scans of laminate deflection along the x = 0mm and y = 0mm lines (shown in Fig. 7.16) are presented in Fig 7.18. Bump deflection along the x = 0mm line for MFC drive-voltages of 0V, 600V and 1400V are shown in Fig. 7.18a with the line scans along the y = 0mm for the same MFC drive-voltages shown in Fig. 7.18b.

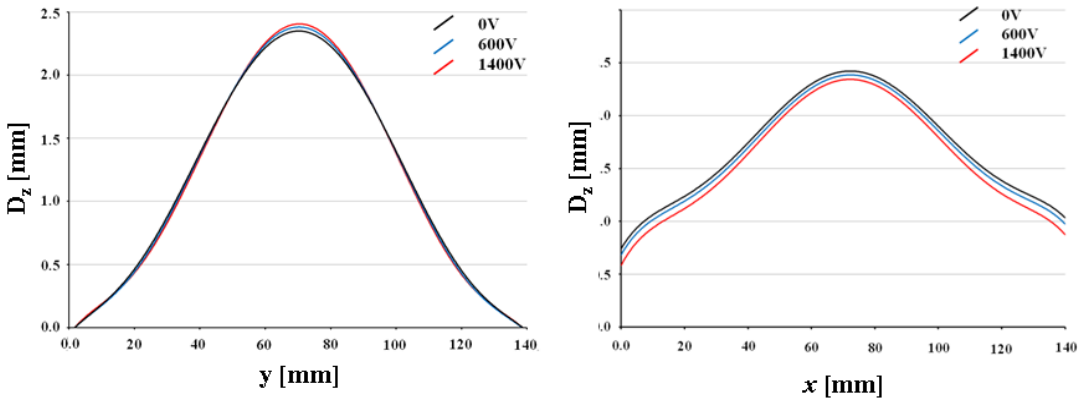

Fig.7.18: 6th order polynomial trend line for 1400 data points describing laminate surface profile along the *y* = 0mm line (left) and *x* = 0mm line (right) at MFC drive-voltage of 0V, 600V and 1400V.

Bump profile along the *x* = 0mm line is shown to the be a rounded curve with smooth transitions which would be well suited to use as an aerodynamic flow control surface and closely matches the bump profile shown in Stanewsky [1]. Bump profile along the *y* = 0mm line is also a smooth curve but is of more complex form than the "bell curve" of the *x* = 0mm profile.

It can also be seen that bump width in the *x*-direction remains largely unchanged with increasing MFC drive-voltage with the profile simply being translated as the bump reduces curvature in the *y*-direction.

Fig 7.18a shows bump deflection for 0V, 600V and 1400V only to maintain clarity of presentation, but maximum bump deflection at all test drive-voltages are shown in Fig. 7.19. A linear trend line fitted to the maximum bump deflection data is shown along with experimental data points in Fig. 7.17 and indicates that for drive voltages in the range 0-1400V the data is well described by the linear voltage-deflection relationship observed in Chapter 6. The rate of change of bump deflection with increasing MFC drive-voltage was measured as $-0.0404\mu mV^{-1}$ across the experimental voltage range. The observed rate of change in maximum bump deflection as a function of MFC drive-voltage is three orders of magnitude lower than that predicted by the FE-model.

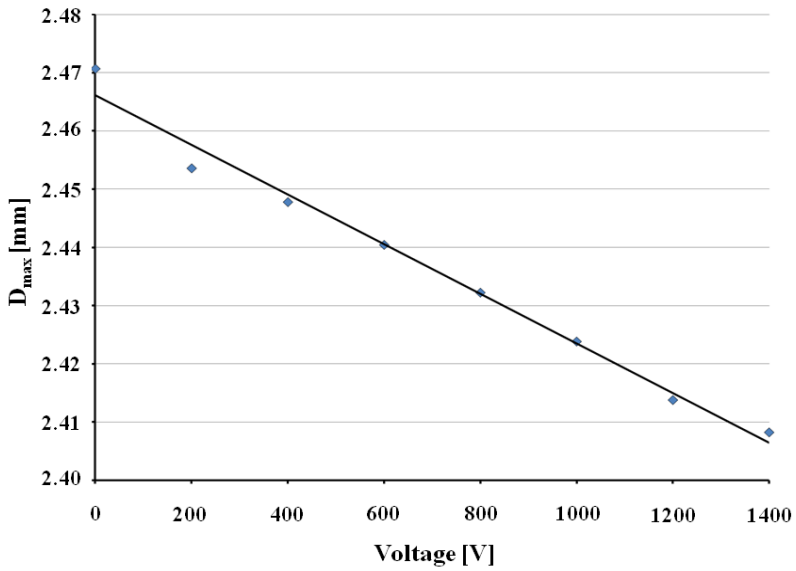

Fig.7.19: Maximum laminate deflection (Dmax) measured by laser profilometry for drive-voltages in the range 0V – 1400V.

Given the validation undertaken of the MFC model in Chapters 3, 4 and 6 this large discrepancy between predicted and observed laminate deflection may indicate that the specific actuator used was faulty or was damaged during the manufacturing process.

In light of this significant difference in bump deflection induced by MFC actuation between FE-predicted value for snap-through voltage is likely to differ significantly to that observed in experiment. In the following section the experimentally determined snap-through voltage will be presented and possible reasons for the discrepancy between FE-predictions and experimental measurements will be discussed.

7.4.3 Snap-through behaviour

This section will compare the FE-predicted snap-through behaviour and that observed in experiment before examining possible causes for the observed discrepancy between finite element predictions and experimental measurements for results presented in this section as well as those presented in sections 7.4.1 and 7.4.2.

The finite element model described in section 7.2 was used to predict snap-through behaviour of the adaptive bump demonstrator under MFC actuation, with predicted snap-through voltage of 1320V. However, as noted in section 7.3.3 the adaptive bump demonstrator did not snap-through under MFC actuation alone even at MFC drive-voltages of up to 1900V.

In order to cause snap-through of the demonstrator an additional mechanical load was necessary. This additional load was applied by placing a mass at the centre of the laminate as indicated in Fig. 7.14. This additional mass reduced the observed bump deflection and so reduced the MFC drive-voltage necessary to induce snap-through.

With a mass of 250g in position, the resulting 2.45N force reduced the snap-through voltage to 1170V, which is similar to the FE-predicted snap-through voltage without additional mechanical load. Despite excellent agreement between FE-predictions and experimental measurements for cured shape discussed in section 7.4.1, and the previously demonstrated accuracy of the presented FE-model for prediction of snap-through voltage in MFC actuated bistable laminates, snap-through behaviour of the adaptive bump demonstrator was not well predicted. Seven possible reasons for this discrepancy have been identified:

(i) Additional mechanical stress in composite from manufacture of demonstrator

(ii) Deviations in bistable segment dimensions and compositions from assumed values

(iii) Mechanical constraint applied to FE-model over constrains model

(iv) Malfunctioning MFC actuator

(v) Bending stiffness of MFC model higher than that of MFC actuator

(vi) Localised variations in stress State And electric field distribution within MFC

(vii) Single offset voltage for MFC volume which spans two different lay-up segments

Each of these potential sources of prediction error will now be examined.

In development of the adaptive bump concept the introduction of more complex mechanical boundary conditions was necessary to better represent the support conditions experienced when embedded in an aerospace structure. It is possible that by bonding the laminate to the support rails additional unrecognized stresses may have been introduced within the laminate or within the MFC. It is well known that piezoelectric materials exhibit different actuation capabilities when pre-stressed compared to unstressed conditions [6]. Therefore it is possible that additional stresses introduced during bonding of the laminate to the support rails could significantly influence actuator behaviour.

Variation in bistable segment dimensions caused by hand manufacture of the pre-preg segments may also have influenced experimental outcomes. Although great care was taken to ensure accurate cutting of the pre-preg material for both bistable and unidirectional segments,

it was seen that small voids were present at the boundary between these two lay-up segments. After curing these voids were no longer visible as the curing process had filled the voids with resin. These resin rich areas and the deviation from assumed laminate geometry they indicate may cause the observed stable states of the composite laminate to differ from those predicted by the FE-model.

In addition, the presence of significant volumes of neat resin may significantly alter the development of residual stresses and the transfer of actuation stress between bistable and unidirectional laminate sections. These fine scale geometric and compositional effects could not be included in the FE-model, however the author suggests that the errors introduced would not significantly reduce predictive accuracy of the model.

The extremely small change in bump deflection in response to MFC actuation could indicate that the composite laminate was significantly stiffer than is predicted by the FE-model, however the mechanical boundary conditions chosen to simulate constraint provided by the support rails was appropriate for the type of analysis undertaken.

It is also possible that the dramatic difference between predicted and experimentally observed bump deflection could be due to a malfunction of the specific actuator used in this study or to damage caused to the actuator during the manufacture or attachment of wiring. A reduction in actuator performance could easily account for the observed deviation of demonstrator performance from that predicted using the FE-model.

As previously observed in Chapter 4, the three dimensional stiffness matrix used to describe the MFC volume overestimates actuator bending stiffness as compared to approximations made using three-dimensional finite element modelling of a representative volume element [7]. The increase in actuator stiffness could explain the flatter and wider bump profile predicted by the presented FE-model (seen in Fig. 7.17). Increased actuator bending stiffness could also result in reduced snap-through voltage.

It is unlikely that increased bending stiffness is a major source of error in this case as the MFC actuator radius of curvature is far greater than that seen in the actuated bistable laminates described in Chapter 4. If increased actuator bending stiffness were a significant source of error it is likely that models of more highly curved actuators would show the greatest errors compared to experimental measurements.

When examining the finite element model for anomalous results or indications of non-representative behaviour, areas of increased stress and accompanying variations in localized

electric field within the MFC volume were observed. The locations of these variations in stress are shown in Fig. 7.20a and lie directly over the intersection between the bistable segment and the unidirectional host laminate.

Stress along the poling direction of the MFC (σ_z) shows values of approximately equal magnitude but of opposite polarity in the region of the MFC bonded to the bistable segment compared to that bonded to the host laminate as seen Fig. 7.20a. It is likely that the difference in σ_z in these regions is a direct result of a single offset voltage being applied to the MFC. While the initial stress state within the MFC varies between these regions when actuated, the magnitude of (σ_z) in both of these regions changes in a similar manner as expected. This indicates that while prediction of cured shape may be affected bump deflection in response to MFC drive-voltage should not be affected by the variation in σ_z.

A similar pattern of variation in γ_{xy} is seen in Fig. 7.20b with positive shear within the region bonded to the bistable segment approximately three times the magnitude, but of opposite polarity to the minimum shear stress predicted.

More localised variations in transverse stress (σ_x and σ_y) and through thickness shear components (γ_{yz} and γ_{xz}) also occur near the lay-up boundary, although peak values do not vary significantly from the global mean for these components

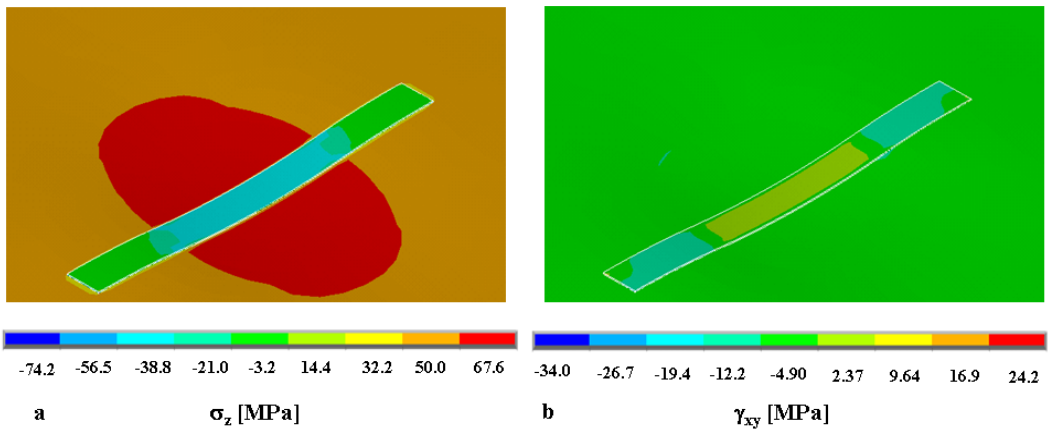

Fig.7.20: Plot of nodal stress components (σ_z) and (γ_{xy}) within the MFC volume in the region y = 20mm after application of offset voltage with bump in State B configuration.

The predicted variations in the stress state within the MFC volume are linked with localised changes to the electric field strength in the *y*-direction as seen in Fig. 7.21a. Electric field strength in the *y*-direction of the MFC volume varies by approximately ±10% from the global mean value of $6.7\times10^{6}\text{Vm}^{-1}$ within the MFC in the y = 20mm and y = -20mm regions. In

addition field strength in the x and z-directions also vary in these regions as seen in Fig. 7.21b with localised spikes in field strength in both field components two orders of magnitude higher than the global mean values, which are both less than $0.8\times10^{6}\mathrm{Vm}^{-1}$.

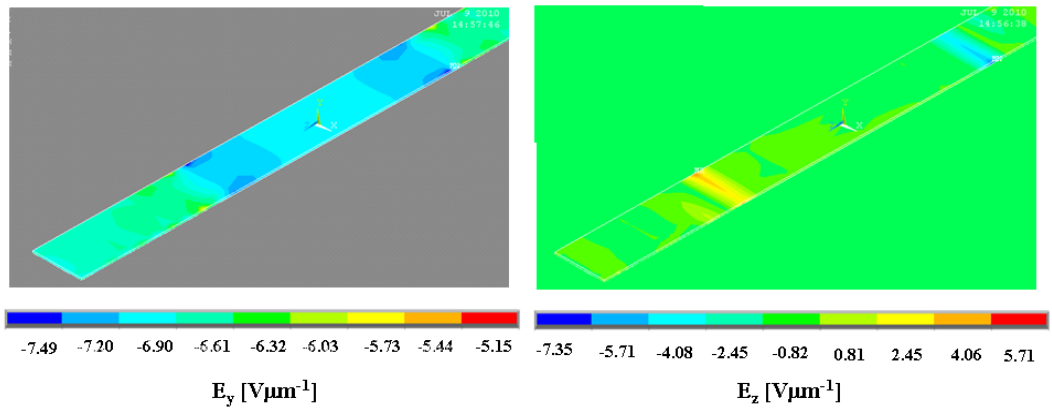

Fig.7.21: Plot of electric field within the MFC model volume in the *y*-direction (a) and in the *z*-direction (b) in the region *y* = 20mm after application of offset voltage with bump in State A configuration.

The deviation from constant electric field shown in Fig. 7.21 clearly contradicts the assumptions implicit in the formulation of the MFC model of a constant electric field which is aligned with the poling direction. However, while this variation in field strength in the *y*-direction has negatively influenced predictive accuracy of cured shape, it is not likely to have influenced the strain induced within the MFC model in response to changes in applied electric field.

It is possible that the observed variations in stress within the MFC have significantly altered the deformation behaviour of the MFC volume and that of the adaptive bump model by reducing MFC curvature to predict a wider flatter bump profile as seen in Fig. 7.16. This change in the initial bump profile would necessarily alter the predicted snap-through voltage. The variations in MFC stress State and electric field strength at the boundaries between bistable and unidirectional laminate segments may be a source of error within the FE-model, the extent to which it influences predictive accuracy is unclear.

The offset voltage used for the MFC volume was calculated based upon the thermal contraction and ply stiffness of the 45 degree ply which is uppermost on the bistable segment. However the MFC is in fact attached to an area of laminate spanning the bistable segment and the unidirectional segment. By calculating the offset voltage required based upon layer

properties of the bistable segment, the offset voltage applied could be overestimated in regions bonded to the unidirectional host laminate.

Calculation of offset voltage for actuators bonded across the boundary between two different lay-up segments present significant challenges in defining how the offset voltage and imposed stress within the MFC volume varies in these regions. This approach would require significant investigation to ensure that appropriate offsets were found.

Using an aggregated value for offset voltage based on the mean thermal stress imposed upon the MFC volume could provide a viable alternative to using the offset voltage required for the bistable segment alone. In this case, an aggregated offset voltage would be lower than the value of 265462V used within the present model. This reduction of offset voltage would decrease the predicted snap-through voltage. While variation of the offset voltage does significantly alter the predicted snap-through voltage, in the case of the adaptive bump demonstrator it is likely that the value used within the FE-model is an overestimate and hence would cause FE-predicted snap-through voltage to be higher than the measured value. Given the discrepancy between prediction and experiment, at this time data is not available to assess the validity of the chosen offset voltage.

7.6 Conclusions

In this chapter the design of an adaptive localised bump based on bistable composite laminates actuated by macrofibre composite actuators was presented.

The key conclusions drawn from the work presented in this chapter are:

- Bistable composite laminates can be used to created bumps suitable for reduction of aerodynamic drag on civilian aircraft.
- The finite element model presented in Chapter 4 is extended to accurately predict the cured shape of a piezoelectrically actuated adaptive bump to within 12% of experimentally measured values.
- Snap through was not achieved at the FE-predicted actuation voltage, however when mechanical loading was added, snap-through occurred.

Design and characterisation of the adaptive bump demonstrator has shown that sufficient bump height for use in drag reduction applications [1] within civil aviation applications is achievable using embedded bistable segments within a unidirectional host laminate. It is hoped that further refinement of composite lay-up and increased sized of bistable segment could further increase achievable bump height to enable the use of the proposed mechanism for yaw control [8].

Despite excellent agreement between finite element predictions of the cured shape of the adaptive bump in both stable deformation states, the snap-through voltage was not well predicted. Further assessment of bump deflection in response to MFC actuation showed that measured laminate deflection was three orders of magnitude lower than that observed in bistable laminates examined in Chapter 4. Although several areas of experimental uncertainty were identified which may contribute to predicted behaviour deviating from that observed in experiment, the author feels it is likely that the severely reduced degree of laminate deflection indicates actuator malfunction.

Unfortunately within the time scale of this project repeating the manufacturing process has not been possible, although the author feels that future investigations into the adaptive bump concept would prove prediction of snap-through voltage using the presented FE-model to be of similar accuracy as shown in Chapter 4.

The presented model has significantly extended the predictive capability of commercial finite element models in the design of piezoelectrically actuated bistable composite structures. The present model accurately predicts the cured shape of an MFC actuated adaptive bump suitable for aerodynamic reduction with excellent agreement with experiment. The model also correctly predicts the bistability of the adaptive bump after the MFC is bonded in place. Finally snap-through under MFC actuation is predicted and the cured shape of the second stable deformation State accurately predicted. While quantitative agreement between predicted and experimentally observed snap-through voltage was not achieved the presented model is suitable for prototype design of MFC actuated morphing structures based on bistable composite laminates and has therefore satisfied the primary research objective of this thesis as described in chapter 1.

In the following chapter a summary of the key findings of each chapter of this thesis is presented before areas for future work are discussed.

7.7 Reference list

1. Stanewsky, E. (2001). "Adaptive wing and flow control technology." *Progress in Aerospace Sciences*, 37(7), 583-667.

2. ANSYS Inc. 2007. Structures with geometric nonlinearities. Chapter 3. Ansys Theory Reference V11.0

3. Nigg, B. M., and Cole, G. K. (2007). "Optical methods." *Biomechanics of the musculo-skeletal system*, W. Herzog, ed., John Wiley and Sons, Chichester, 362-391.

4. Sandwell, D. T. (1987). "Biharmonic Spline Interpolation of Geos-3 and Seasat Altimeter Data." *Geophysical Research Letters*, 14(2), 139-142.

5. Bowen, C. R., Butler, R., Jervis, R., Kim, H. A., and Salo, A. I. T. (2007). "Morphing and shape control using unsymmetrical composites." *Journal of Intelligent Material Systems and Structures*, 18(1), 89-98.

6. Berlincourt, D. (1981). "Piezoelectric ceramics: Behaviour and applications." *J. Acoust. Soc. Am.*, 70(6), 1586-1595.

7. Dano, M. L., Gakwaya, M., and Julliere, B. (2008). "Compensation of thermally induced distortion in composite structures using macro-fiber composites." *Journal of Intelligent Material Systems and Structures*, 19(2), 225-233.

8. Natarajan, A., Kapania, R. K., and Inman, D. J. (2004). "Aeroelastic optimization of adaptive bumps for yaw control." *Journal of Aircraft*, 41(1), 175-185.

Chapter 8 – Thesis summary and future work

In section 8.1 of this chapter a brief summary of the work undertaken and the key findings of each of the preceding chapters will be presented before section 8.2 outlines interesting areas for future work.

8.1 Chapter summaries

Chapter 1 presents the motivation which has lead the author and many other investigators to study structural morphing within the context of aviation applications. A survey of published work on morphing aerodynamic flow control structures is presented with the schemes presented categorised into large, medium and small scale schemes to aid clarity.

It is concluded that due to the established aerodynamic benefits and the lack of prototype testing present in the literature that the development of an adaptive localised bump for use as a novel aerodynamic control surface should be the research focus of this thesis. It is also concluded that the operational capabilities of piezoelectrically actuated bistable composite laminates make this emerging technology well suited to use in the development of an adaptive bump.

To enable design of an adaptive bump prototype for proof of concept studies, the need for a robust finite element design tool is identified. The analytical work presented in Chapters 2-6 was therefore focussed on developing the theoretical and experimental understanding of bistable composite laminates and piezoelectric actuators to facilitate design of an adaptive bump prototype, which was presented in Chapter 7.

The underlying theory of bistable composite laminates, piezoelectric ceramics and macro fibre composite actuators were also presented in Chapter 1 to aid understanding of subsequent chapters.

Chapter 2 presented measurements of laminate composition for bistable laminates with $[\theta/90\text{-}\theta]_T$ lay-up schedule using optical microscopy techniques in conjunction with digital image processing. The resulting data identified average ply thicknesses and laminate architecture which deviated by up to 6% from the idealised laminate composition. The presence of an excess resin layer on one side of the laminate was also identified.

The cured shapes of a 150x150mm $[-30/60]_T$ and a 75x75mm $[0/90]_T$ bistable laminates were measured using video motion capture and laser profilometry techniques. These data showed

peak deflection (D_{max}) was not equal in both stable states, but rather a dominant state was observed in which D_{max} was greater; this state was designated State A with the secondary states denoted State B. State A corresponded with the excess resin layer being at the concave surface of the curved laminate. Localised reversal of curvature near the edges and corners of the laminates were observed.

A finite element (FE) model which included the observed laminate composition was described and used to predict peak deflection (D_{max}) of both State A and State B to within 12.5% of experimental values. The presented FE model captured the inequality in State A and State B deflection unlike previous methods for predicting laminate deflection. In addition the inclusion of measured laminate composition allowed the model to converge to State A without need of imposed imperfections to aid convergence which is not possible using idealised laminate composition.

The observed reversal of curvature in edge and corner regions of the bistable laminates was predicted by the model and shown to be related to localised increases in the through thickness stress components σ_z, γ_{xz} and γ_{yz}. This finding highlights the need for finite element analysis of bistable composites as these through thickness stress variations are not possible to predict using the laminated plate theory prevalent in the analysis of bistable laminates.

Chapter 3 develops a homogenised solid model of the macro fibre composite actuators used in this thesis by creating three-dimensional matrices describing elastic, dielectric and piezoelectric constants. A finite element model of the MFC actuator was constructed using the derived material properties and predictions of actuator performance experimentally validated.

Tip deflection of an aluminium beam caused by MFC-actuation was accurately predicted over a range of MFC-drive voltages from 0V-400V. In addition the change in actuator stiffness of a passive actuator caused by varying electrical boundary conditions was also successfully predicted, which has not been demonstrated by previous models.

Chapter 4 describes a finite element model for prediction of cured shape and snap-through voltage for an MFC actuated bistable laminate. The MFC model described in Chapter 3 was combined with the bistable composite model of Chapter 2 and appropriate mechanical and electrical constraint applied to model device behaviour. The cured shape of two MFC actuated bistable laminates was measured using video motion capture techniques before snap-through voltage was experimentally determined.

The finite element model described was shown to predict the cured shape of bistable laminates well with maximum laminate deflection predicted to within 16% of measured values for both experimental samples. Snap-through voltage was extremely well predicted with snap-through occurring at voltages within 5% of predicted values in both cases. The presented finite element model has significantly improved previous coupled field models for MFC actuated bistable composite elements and as shown in Chapter 7, may be extended to predict the behaviour of more complex morphing structures.

Chapter 5 presented experimental measurement of laminate deflection under imposed thermal loading. Significant non-linearities in the temperature-deflection characteristic were observed and correlated with previously presented data on the temperature dependent elastic constants of epoxy resin systems. The finite element model presented in Chapter 2 was extended to predict laminate deflection with predicted values in good agreement with experiment in the range 20-110°C. Even when the laminate was heated to cure temperature significant residual curvature remained and it was suggested that this residual curvature results from stress fields created by chemical, mechanical and thermal effects during the cure process.

Chapter 6 presented experimental characterisation of a bistable carbon fibre composite with an MFC actuator bonded to its upper surface in terms of its blocking force and free deflection. Linear increases in both blocking force and free deflection with increasing MFC drive-voltage were observed which provides supporting evidence for the validity of the linear piezoelectric constants used in the MFC model definition.

Significant deflection creep was observed during prolonged voltage application. This creep was measured and compared to well established models for piezoelectric creep, creep rate varied in the range 0.01 – 0.05 although no trend in creep rate with increased drive voltage was shown.

In Chapter 7 the finite element model developed in Chapter 4 was extended to predict cured shape and snap-through voltage for an MFC-actuated bistable bump. The presented FE-model was then used to design a composite laminate with embedded bistable segment suitable for actuation using a commercially available MFC actuator (Smart Materials GmbH MFC8507-P1).

The FE-model was used to dimension the bistable segment in order to achieve predicted snap-through well within the MFCs actuation range while still achieving adequate laminate deflection. Once laminate design was finalised the adaptive bump demonstrator was manufactured and snap-through voltage and cured shape measured.

Finite element predictions of cured shape agreed with the motion capture and laser profilometry measurements to within 12%. Although slight differences in laminate curvature were observed the presented model predicted the cured shape within both deformation states with sufficient accuracy to serve as a prototype design tool. Laminate deflection with increasing MFC drive-voltage and snap-through voltage was not well predicted for the demonstrator presented in this work. Due to the large differences between demonstrator behaviour and previous MFC-actuated composite structures it is thought that manufacturing factors or actuator malfunction are responsible for this large discrepancy between predicted and observed snap-through behaviour.

Although this work has successfully developed understanding and finite element modelling capabilities to aid in prototype design of an adaptive bump based on bistable composite laminates, there remains many area of interesting research. Section 8.2 will detail published work resulting from this thesis and section 8.3 will identify some of the key topics which could form part of future research efforts.

8.2 List of Publications

Complete manuscripts for the journal papers listed may be found in Appendix 4.

Journal papers

(i) Peter F. Giddings, C.R. Bowen, R. Butler, H.A. Kim. Characterisation of actuation porperties of piezoelectrically actuated bistable composite laminates. Composites: Part A 39 (2008) 697-703

(ii) Peter F. Giddings, C. R. Bowen, Aki I.T. Salo, H. A. Kim, A. Ive. Bistable composite laminates: Effects of laminate composition on cured shape and response to thermal load. Composite Structures 92 (2010) 2220–2225

Conference papers

(i) Peter F. Giddings, C. R. Bowen, Aki I. T. Salo, H. A. Kim, 2009. Bistable composite laminates - effects of laminate composition on cured-shape and response to thermal load. *In*: *15th International Conference on Composite Structures*, 1-5 June 2009, Porto, Portugal.

(ii) Peter F. Giddings, C. R. Bowen, H. A. Kim, 2009. A coupled field finite element model to predict actuation properties of piezoelectrically actuated bistable composites. *In*: *ICCM-17: 17th International Conference on Composite Materials*, 27-31 July 2009, Edinburgh, UK.

(iii) Peter F. Giddings, C. R. Bowen, H. A. Kim, 2008. Characterisation of force-deflection behaviour of piezoelectrically actuated bistable composite laminate under two-axis constraint. *In*: *3rd International Conference on Smart Materials, Structures and Systems - Emboding Intelligence in Structures and Integrated Systems, CIMTEC 2008*, June 8-13 2008, Sicily, Italy.

8.3 Future work

Future work could include the following:

(i) A further investigation into the assumption of a reduced resin layer Young's modulus, as used in the finite element model (Chapter 2) should form part of future work. Not only is this assumption key to model accuracy but at present no published work has examined the role of surface texture on residual thermal stresses within layered solids. This may have applications to the study of environmental stress placed on building components as well as further enhancing understanding of composite behaviour.

(ii) An investigation of the influence of laminate composition on the snap-through load of bistable laminates could prove useful and would complement the characterisation of cured shape presented within Chapter 2.

(iii) Inclusion of the temperature dependent materials properties of epoxy resin systems would improve prediction accuracy of laminate deflection in response to thermal loads. It is not thought that implementing these changes within the present model would significantly improve prediction of cured shape. However, as indicated in Chapter 5, prediction of laminate deflection during service conditions would be significantly improved.

(iv) The thermal characterisation shown in Chapter 5 could also be extended to capture laminate deflection throughout the expected service temperature range for a civil aircraft fuselage. This data is vital in assessing the feasibility of bistable composite components for morphing structures, although due to facilities restrictions this was not achievable within this project.

(v) The identification of remnant laminate curvature even after reheating to cure temperature could prove useful in the quantification of the residual stresses created by chemical shrinkage, differential curing and moisture absorption effects. A more detailed study of the observed remnant curvature described in Chapter 5 may lead to improvements in manufacturing processes and reduction in the dimensional variance often seen in thin composite components.

(vi) Further development of the homogenised MFC model should centre on the validation of the compliance and permittivity matrices. Full micro-scale finite element

modelling is at present the most attractive method for predicting the relative permittivity of the active layer and the compliance of the actuator as a whole. By fully modelling all features of the MFC actuator the complex poling and electric field effects which influence permittivity could be accurately assessed. In addition, the developed FE model could be used to determine the relationship between device capacitance and active layer properties which at present is not possible.

(vii) Further improvements of prediction of cured shape and snap-through voltage for MFC actuated bistable laminates may be possible by precisely quantifying ply thickness, and ply-orientation for each experimental sample as well as the piezoelectric constants specific to each actuator. However this approach is not feasible in an industrial setting where the additional time and cost would render it inappropriate.

(viii) The challenges associated with the use of the offset voltage to correct for the unrepresentative thermal stresses placed on the MFC volume are not fully soluble within Ansys V11.0. Because element birth and death procedures are not currently compatible with SOLID 226 elements, thermal stresses will continue to cause discrepancies between prediction and experiment. Hence, an investigation of other commercial finite element packages may result in improved solution methodologies. If more robust coupled field analysis proves possible using alternative FE packages implementation of the Arc Length method for convergence control would also allow full prediction of snap-through under MFC actuation.

(ix) The finite element model presented in Chapter 7 has shown that prototype design is possible using the proposed method. However, to further improve modelling accuracy and better understand the mechanisms which control cured shape and snap-through of composite laminates with embedded bistable segments incremental testing and validation of the finite element modelling approach would be desirable. Due to time constraints of this project this was not possible however future work could include analysis and validation of the influence of bistable segment dimensions, shape and lay-up. The influence of MFC placement across laminate segment boundaries with specific reference to the localised changes in stress and electric field caused by rapidly changing stresses in that region could also help investigator gain insight into actuator behaviour.

(x) A more extensive experimental investigation into bump profile would also allow validation of the finite element model with laminate composition at the boundary between lay-up segments being included within the FE formulation. Optimum laminate design and MFC placement and orientation could also be investigated using the FE model and experimental techniques presented within this thesis.

(xi) An investigation of directly embedding piezoelectric fibres within the carbon fibre/epoxy pre-preg may lead to reduced manufacturing variance and allow novel actuation schemes not achievable using MFC actuators bonded to the laminate surface.

While there remain many areas of work open to investigation relating to the design and analysis of an MFC actuated adaptive bump based on bistable composite laminates, the presented work has significantly advanced understanding and analytical capability in this field.

Appendix 1

Ansys APDL code file used to model cured shape of 75mm ×75mm [0/90]T laminate seen in Fig. 2.8.

Throughout lines surrounded by '!***' denote sections of code with specific purpose and lines starting with '!' give specific comment on the purpose of that line of code only. All values are specified in stadard SI units throughout this appendix and appendix 2 and 3.

```
!
*******************
*
! Creates model of 70x70mm square 0/90 laminate
!
*******************
***
! Author: P.F.Giddings en1pfg@bath.ac.uk
!
*******************
***
! Exits from previous work
FINISH
! Deletes previous variables/arrays
*DEL,ALL
! Changes working directory
/CWD,'C:\Ansys\Porto models\0 90 lam'

! Clears current data and reads default start.ans file
/CLEAR,START

/FILNAME,70mm bistable CFRP laminate
/TITLE,Validation model: Basic
/UNITS, SI
!
*******************
***
! Enter pre-processor mode
!
*******************
***
/PREP7
SHPP,ON
! Define Element1 as 3D layered orthotropic solid, with X,Y,Z DOF
ET,1,SOLID186

keyopt,1,3,1
keyopt,1,8,1
sectype,1,shell
! Sets layer thicknesses from experiment
secdata,0.000255,1,90
secdata,0.000234,1,0
secdata,0.000027,2,0
tref,0
! ------------------------
------
! Define material properties
! ------------------------
------
! Material (1): T800/M21 UD prepreg 0.25mm thick
! Taken from Airbus data sheet
! ------------------------
------MP,ex,1,172e9

MP,ey,1,8.9e9
MP,ez,1,8.9e9
MP,gxy,1,4.2e9
MP,gxz,1,4.2e9

MP,gyz,1,0.0225e9
MP,prxy,1,0.35

MP,prxz,1,0.35

MP,pryz,1,0.01

MP,dens,1,1072

! Defines CTE for X as longitudinal value
MP,ALPX,1,-0.9e-7
! Defines CTE for Y&Z as trasverse value
MP,ALPY,1,2.65e-5
MP,ALPZ,1,2.65e-5
!*******************
**
! excess resin layer effective properties
!*******************
**
MP,ex,2,1.5e9
MP,prxy,2,0.4
```

```
MP,alpx,2,9e-5
! ------------------------------
! Create model
! ------------------------------
BLock,0,75e-3,0,0.516e-3,0,75e-3
VSEL,S,,,1
! Mesh type: Mapped where possible, no smart size.
MSHKEY,2

LESIZE,5,2.5e-3

Lesize,12,2.5e-3

Lesize,1,,,1
! aligns element coordinate system z-axis to line 23
VEORIENT,1,thin
! Set selected volume attributes to MAT=1,ET=1,Cartesian
VATT,1,,1,0
VMESH,ALL
allsel
!------------------------------
!Apply temperature change
!------------------------------
! Select nodes at Y=0, then constrain DOF by symmetry
NSEL,S,LOC,X,37.5e-3$
DSYM,SYMM,XNSEL, all
!Applies central pinned constraint
Nsel,S,LOC,Z,37.5e-3
NSEL,R,LOC,X,37.5e-3
nsel,R,loc,y,0
D,ALL,UX,,,,,UY,UZ
allsel
Nsel,S,LOC,Z,37.5e-3
NSEL,R,LOC,X,37.5e-3
NSEL,R,LOC,Y,0.1e-3,0.516e-3
D,ALL,UX,,,,,UZ
allsel
!Defines first loadstep for solution
Time,1
! Sets load step as 10 seconds
NSUBST,20,,,,
! Sets to ramped load step
KBC,0
NSEL,ALL
!Applies 1 deg temp change to aid initial convergence Tunif, -1

lswrite,1
Time,158
NSUBST,50,,,,
KBC,0
NSEL,ALL
Tunif, -158
lswrite,2
!Applies displacement constraint to induce snap-through
time,159

nsubst,50
kbc,0
Nsel,S,LOC,x,75e-3
NSEL,a,LOC,X,0
!NSEL,r,LOC,z,0
NSEL,r,loc,y,0
D,ALL,Uy,3e-3
NSEL,all

lswrite,3
!Removes displacement constraint
time,160

nsubst,20
kbc,0
Nsel,S,LOC,x,75e-3
NSEL,a,LOC,X,0
!NSEL,r,LOC,z,0
NSEL,r,loc,y,0
Ddele,all,all
nsel,all
lswrite,4
!**********************
! Enter solution mode
!**********************
!Enter solution mode and solves each substep
/solu
ANtype,static,new
!Activates non-linear geometric option
NLGEOM, On
autots,on
CNVTOL,U,,,,,1e-6
outres,all,2
LSSOLVE,1,4,1
save
FINISH
!**********************
!writes 3d coordinates of surface to file
!**********************
/post1
```

```
!Select results to write to file
set,2,,

nsel,s,loc,y,0
*get,LNG,node,,count
allsel
*DIM,nodeinfo1(1),,LNG,11
*DIM,offset1(1),,LNG,3
*vget,nodeinfo1(1,1),node,1,NLIST,,,,0
*vget,nodeinfo1(1,2),node,1,loc,x,,,0
*vget,nodeinfo1(1,3),node,1,loc,z,,,0
*vget,nodeinfo1(1,4),node,1,u,x,,,0
*vget,nodeinfo1(1,5),node,1,u,y,,,0
*vget,nodeinfo1(1,6),node,1,u,z,,,0
*VOPER,nodeinfo1(1,7),nodeinfo1(1,2),add,nodeinfo1(1,4)
*VSCFUN,offset1(1,1),min,nodeinfo1(1,7)
*vabs,1,0
*voper,nodeinfo1(1,8),nodeinfo1(1,7),sub,offset1(1,1)
*VOPER,nodeinfo1(1,9),nodeinfo1(1,3),add,nodeinfo1(1,6)
*VSCFUN,offset1(1,2),min,nodeinfo1(1,9)
*vabs,1,0
*voper,nodeinfo1(1,10),nodeinfo1(1,9),sub,offset1(1,2)
*VSCFUN,offset1(1,3),min,nodeinfo1(1,5)
*vabs,1,0
*voper,nodeinfo1(1,11),nodeinfo1(1,5),sub,offset1(1,3)
! opens .txt file, writes nodeloc 3D array into it. Need to know MATLAB format
*CFOPEN,xla,csv
*vwrite,nodeinfo1(1,8)
(1x, F7.6)
*CFCLOS
*CFopen, yla,csv
*vwrite,nodeinfo1(1,11)
(1x, F7.6) *CFCLOS
*CFopen, zla,csv
*vwrite,nodeinfo1(1,10)
(1x, F7.6)
*CFCLOS
FINISH
```

Appendix 2

Ansys ADPL code file used to model cured shape and snp-through voltage of $[-30/60/MFC]_T$ laminate seen in Fig. 4.6.

```
! ************************

! Creates model of 150x150mm square -15/75 laminate

! ************************

! Author: P.F.Giddings en1pfg@bath.ac.uk

! ************************

FINISH

*DEL,ALL

/CLEAR,START

/FILNAME,150mm_30_60_thesis

/TITLE,Validation model: Basic

/UNITS, SI

! ************************

! Enter pre-processor mode

! ***************************

/PREP7

SHPP,ON
! Define Element1 as 3D layered orthotropic solid, with X,Y,Z DOF

ET,1,SOLID186

keyopt,1,3,1

keyopt,1,8,1

!Define three layer matching experimental values

sectype,1,shell

secdata,0.000255,1,-30

secdata,0.000234,1,60

secdata,0.000027,5,0

tref,0

!Define element 2 as 3D coupled field brick with X,Y,Z&Volt DOF

ET,2,solid226,1001

!Define element 3 as 3D structural solid with X,Y,Z DOF

ET,3,solid186

keyopt,3,3,0

! ----------------------------------------

! Define material properties

! ----------------------------------------

! Material (1): T800/M21 UD prepreg 0.25mm thick cured

! Aligns material axes with element axes

! Taken from Airbus data sheet Pa

! ----------------------------------------

MP,ex,1,172e9

MP,ey,1,8.9e9

MP,ez,1,8.9e9

MP,gxy,1,4.2e9

MP,gxz,1,4.2e9

MP,gyz,1,0.0225e9

MP,prxy,1,0.35

MP,prxz,1,0.35

MP,pryz,1,0.01

MP,dens,1,1072

MP,ALPX,1,-0.9e-7

MP,ALPY,1,3e-5

MP,ALPZ,1,3e-5

! ----------------------------------------

! Material (2): Dummy MFC actuator z-z poled (Nrm)

! ----------------------------------------

MP,dens,2,2000

!Sets relative permittivity at constant strain

MP,PERX,2,2712

MP,PERY,2,1.7

MP,PERZ,2,737

! Defines CTE for MFC

MP,ALPX,2,6.96e-6

MP,ALPY,2,1e-25

MP,ALPZ,2,2.2e-5

MP,REFT,2,0

!defines anisotropic compliance matrix

TB,ANEL,2,1,,1

tbtemp,0

TBDATA,1,0.065,-0.0205,-0.0106

TBDATA,7,0.065,-0.0106

TBDATA,12,0.034

TBDATA,16,0.165

TBDATA,19,0.173

TBDATA,21,0.173

!sets the piezoelectric strain matrix using d31 and d33 values from Smart Mats

TB,PIEZ,2,,,1

TBMODIF,1,1,0

TBMODIF,1,2,0

TBMODIF,1,3,-2.1e-20

TBMODIF,2,1,0

TBMODIF,2,2,0

TBMODIF,2,3,-2.1e-20

TBMODIF,3,1,0

TBMODIF,3,2,0

TBMODIF,3,3,4.67e-20
```

```
TBMODIF,4,1,0

TBMODIF,4,2,0

TBMODIF,4,3,0

TBMODIF,5,1,0

TBMODIF,5,2,0

TBMODIF,5,3,0

TBMODIF,6,1,0

TBMODIF,6,2,0

TBMODIF,6,3,0

 ! ---------------------------------------

! Material (3): MFC actuator z-z poled

! ---------------------------------------

MP,dens,3,2000

MP,PERX,3,712

MP,PERY,3,1.7

MP,PERZ,3,737

MP,ALPX,3,6.96e-6

MP,ALPY,3,1e-25

MP,ALPZ,3,2.2e-5

MP,REFT,3,0

!*

TB,ANEL,3,1,,1

tbtemp,0

TBDATA,1,0.065e-9,-0.0205e-9,-0.0106e-9

TBDATA,7,0.065e-9,-0.0106e-9

TBDATA,12,0.034e-9

TBDATA,16,0.165e-9

TBDATA,19,0.173e-9

TBDATA,21,0.173e-9

!*

TB,PIEZ,3,,,1

TBMODIF,1,1,0

TBMODIF,1,2,0

TBMODIF,1,3,-2.1e-10

TBMODIF,2,1,0

TBMODIF,2,2,0

TBMODIF,2,3,-2.1e-10

TBMODIF,3,1,0

TBMODIF,3,2,0

TBMODIF,3,3,4.67e-10

TBMODIF,4,1,0

TBMODIF,4,2,0

TBMODIF,4,3,0

TBMODIF,5,1,0

TBMODIF,5,2,0

TBMODIF,5,3,0

TBMODIF,6,1,0

TBMODIF,6,2,0

TBMODIF,6,3,0

! excess resin layer effective properties

MP,ex,5,1.5e9

MP,prxy,5,0.4

MP,alpx,5,9e-5

! ---------------------------------------

! Create model

! ---------------------------------------

BLock,0,46.5e-3,0,-0.516e-3,0,150e-3

BLock,46.5e-3,103.5e-3,0,-0.516e-3,0,150e-3

BLock,103.5e-3,150e-3,0,-0.516e-3,0,150e-3

Block,46.5e-3,103.5e-3,0,0.29e-3,32.5e-3,117.5e-3

! Define volume 1- 1st strip of laminate

VSEL,S,,,1

LESIZE,5,,,10

Lesize,12,2.5e-3

Lesize,1,,,1

VEORIENT,1,thin

VATT,1,,1,0

VMESH,ALL

allsel

! Define volume 2- laminate under MFC

VSEL,S,,,2

MSHKEY,2

LESIZE,19,,,20

Lesize,23,2.5e-3

Lesize,18,,,1

VEORIENT,2,thin

VATT,1,,1,0

VMESH,ALL

allsel

! Define volume 1- 3rd strip of laminate

VSEL,S,,,3

MSHKEY,2

LESIZE,31,,,10

Lesize,35,2.5e-3

Lesize,30,,,1

VEORIENT,3,thin

VATT,1,,1,0

VMESH,ALL

allsel

! Defines MFC volume

VSEL,S,,,4

MSHKEY,2

LESIZE,43,,,20

Lesize,47,2.5e-3

Lesize,42,,,1

VEORIENT,4,thin

VATT,2,,2,0

VMESH,ALL

allsel

!Merges all coincedent Key points, nodes and areas
```

nummrg,all,1e-6

allsel

!--

!Apply temperture change

!--

Nsel,S,LOC,Z,75e-3

NSEL,R,LOC,X,75e-3

NSEL,R,LOC,Y,-0.5e-3,0.5e-3

D,ALL,Ux,,,,,uz

allsel

Nsel,S,LOC,Z,75e-3

NSEL,R,LOC,X,75e-3

nsel,R,loc,y,-0.516e-3

D,ALL,UX,,,,,UY,UZ

allsel

! Applies displacement constraint to aid convergence

Nsel,S,LOC,Z,150e-3

NSEL,R,LOC,X,0

nsel,R,loc,y,0

D,ALL,UY

allsel

Nsel,S,LOC,Z,0

NSEL,R,LOC,X,150e-3

nsel,R,loc,y,0

D,ALL,UY

allsel

!Applies electrical constraint

NSEL,s,loc,z,32.5e-3

nsel,r,loc,x,45e-3,105e-3

nsel,r,loc,y,0,0.5e-3

d,all,volt,0

allsel

NSEL,s,loc,z,37.5e-3

nsel,r,loc,x,45e-3,105e-3

nsel,r,loc,y, 0,0.5e-3

cp,1,volt,all

allsel

NSEL,s,loc,z,42.5e-3

nsel,r,loc,x,45e-3,105e-3

nsel,r,loc,y,0,0.5e-3

cp,2,volt,all

allsel

NSEL,s,loc,z,47.5e-3

nsel,r,loc,x,45e-3,105e-3

nsel,r,loc,y,0,0.5e-3

cp,3,volt,all

allsel

NSEL,s,loc,z,52.5e-3

nsel,r,loc,x,45e-3,105e-3

nsel,r,loc,y,0,0.5e-3

cp,4,volt,all

allsel

NSEL,s,loc,z,57.5e-3

nsel,r,loc,x,45e-3,105e-3

nsel,r,loc,y,0,0.5e-3

cp,5,volt,all

allsel

NSEL,s,loc,z,62.5e-3

nsel,r,loc,x,45e-3,105e-3

nsel,r,loc,y,0,0.5e-3

cp,6,volt,all

allsel

NSEL,s,loc,z,67.5e-3

nsel,r,loc,x,45e-3,105e-3

nsel,r,loc,y, 0,0.5e-3

cp,7,volt,all

allsel

NSEL,s,loc,z,72.5e-3

nsel,r,loc,x,45e-3,105e-3

nsel,r,loc,y,0,0.5e-3

cp,8,volt,all

allsel

NSEL,s,loc,z,75e-3

nsel,r,loc,x,45e-3,105e-3

nsel,r,loc,y,0,0.5e-3

cp,9,volt,all

allsel

NSEL,s,loc,z,77.5e-3

nsel,r,loc,x,45e-3,105e-3

nsel,r,loc,y,0,0.5e-3

cp,10,volt,all

allsel

NSEL,s,loc,z,82.5e-3

nsel,r,loc,x,45e-3,105e-3

nsel,r,loc,y,0,0.5e-3

cp,11,volt,all

allsel

nsel,s,loc,z,87.5e-3

nsel,r,loc,x,45e-3,105e-3

nsel,r,loc,y,0,0.5e-3

cp,12,volt,all

allsel

nsel,s,loc,z,92.5e-3

nsel,r,loc,x,45e-3,105e-3

nsel,r,loc,y,0,0.5e-3

cp,13,volt,all

allsel

nsel,s,loc,z,97.5e-3

nsel,r,loc,x,45e-3,105e-3

nsel,r,loc,y,0,0.5e-3

cp,14,volt,all

allsel

nsel,s,loc,z,102.5e-3

nsel,r,loc,x,45e-3,105e-3

nsel,r,loc,y,0,0.5e-3

```
cp,15,volt,all

allsel

nsel,s,loc,z,107.5e-3

nsel,r,loc,x,45e-3,105e-3

nsel,r,loc,y,0,0.5e-3

cp,16,volt,all

allsel

nsel,s,loc,z,112.5e-3

nsel,r,loc,x,45e-3,105e-3

nsel,r,loc,y,0,0.5e-3

cp,17,volt,all

allsel

nsel,s,loc,z,117.5e-3

nsel,r,loc,x,45e-3,105e-3

nsel,r,loc,y,0,0.5e-3

cp,18,volt,all


allsel

! ------------------------------

! Enters solution mode and solves each substep at a time

! ------------------------------

/solu

ANtype,static,new

NLGEOM, On

autots,on

outres,all,all

Time,1

NSUBST,100,,,,


KBC,0


Esel,s,,,all

Esel,u,mat,,2

BFE,all,temp,1,-1

allsel

solve

Time,158

NSUBST,50,,,,

KBC,0

Esel,s,,,all

Esel,u,mat,,2

BFE,all,temp,1,-160

allsel

!applies offset voltage

nsel,s,loc,z,117.5e-3

nsel,r,loc,x,45e-3,105e-3

nsel,r,loc,y,0,0.5e-3

D,all,volt,476590

allsel

solve

!Enables line search convergence control

lnsrch,on

neqit,1000

Esel,s,mat,,2

mpchg,3,all

allsel

Time,159

nsubstp,1

kbc,1

solve

!Removes displacement constraints

Time,160

NSUBST,100,,,,

KBC,0

Nsel,S,LOC,Z,75e-3

NSEL,R,LOC,X,75e-3

!nsel,R,loc,y,0

Ddele,ALL,UY

allsel

solve

!Applies 600V MFC drive-voltage

Time,161

nsubstp,20

kbc,0

nsel,s,loc,z,117.5e-3

nsel,r,loc,x,45e-3,105e-3

nsel,r,loc,y,0,0.5e-3

D,all,volt,374590


allsel

solve

!Applies 750V MFC drive voltage

Time,162

nsubstp,100

kbc,0

nsel,s,loc,z,117.5e-3

nsel,r,loc,x,45e-3,105e-3

nsel,r,loc,y,0,0.5e-3

D,all,volt,349590


!D,all,volt,221590

allsel

solve

save

FINISH

! ------------------------------------

! Select surface nodes

! ------------------------------------

/prep7

cmsel,s,plate,,

nsel,s,loc,x,0

nsel,a,loc,x,4.65e-3

nsel,a,loc,x,9.3e-3

nsel,a,loc,x,13.95e-3

nsel,a,loc,x,18.6e-3
```

```
nsel,a,loc,x,23.25e-3

nsel,a,loc,x,27.9e-3

nsel,a,loc,x,32.55e-3

nsel,a,loc,x,37.2e-3

nsel,a,loc,x,41.85e-3

nsel,a,loc,x,46.5e-3

nsel,a,loc,x,52.2e-3

nsel,a,loc,x,57.9e-3

nsel,a,loc,x,63.6e-3

nsel,a,loc,x,69.3e-3

nsel,a,loc,x,75e-3

nsel,a,loc,x,80.7e-3

nsel,a,loc,x,86.4e-3

nsel,a,loc,x,92.1e-3

nsel,a,loc,x,97.8e-3

nsel,a,loc,x,103.5e-3

nsel,a,loc,x,108.15e-3

nsel,a,loc,x,112.8e-3

nsel,a,loc,x,117.45e-3

nsel,a,loc,x,122.1e-3

nsel,a,loc,x,126.75e-3

nsel,a,loc,x,131.4e-3

nsel,a,loc,x,136.05e-3

nsel,a,loc,x,140.7e-3

nsel,a,loc,x,145.35e-3

nsel,a,loc,x,150e-3

seltol,1e-6

nsel,r,loc,y,0

*get,LNG,node,,count

*DIM,node1(1),,20187,13

*DIM,offset1(1),,20187,3

*DIM,offset2(1),,20187,3

*DIM,offset3(1),,20187,3

*VGET,node1(1,13),node,1,nsel,,,,0

*vmask,node1(1,13)

*VGET,node1(1,1),node,1,loc,x,,,,0

*vmask,node1(1,13)

*VGET,node1(1,2),node,1,loc,z,,,,0

allsel

finish

! ---------------------------------------

! calculate and print nodal displacement

! ---------------------------------------

/post1

set,4,8

cmsel,s,plate,,

nsel,s,loc,x,0

nsel,a,loc,x,4.65e-3

nsel,a,loc,x,9.3e-3

nsel,a,loc,x,13.95e-3

nsel,a,loc,x,18.6e-3

nsel,a,loc,x,23.25e-3

nsel,a,loc,x,27.9e-3

nsel,a,loc,x,32.55e-3

nsel,a,loc,x,37.2e-3

nsel,a,loc,x,41.85e-3

nsel,a,loc,x,46.5e-3

nsel,a,loc,x,52.2e-3

nsel,a,loc,x,57.9e-3

nsel,a,loc,x,63.6e-3

nsel,a,loc,x,69.3e-3

nsel,a,loc,x,75e-3

nsel,a,loc,x,80.7e-3

nsel,a,loc,x,86.4e-3

nsel,a,loc,x,92.1e-3

nsel,a,loc,x,97.8e-3

nsel,a,loc,x,103.5e-3

nsel,a,loc,x,108.15e-3

nsel,a,loc,x,112.8e-3

nsel,a,loc,x,117.45e-3

nsel,a,loc,x,122.1e-3

nsel,a,loc,x,126.75e-3

nsel,a,loc,x,131.4e-3

nsel,a,loc,x,136.05e-3

nsel,a,loc,x,140.7e-3

nsel,a,loc,x,145.35e-3

nsel,a,loc,x,150e-3

seltol,1e-6

nsel,r,loc,y,0

*vmask,node1(1,13)

*VGET,node1(1,3),node,1,U,x,,,0

*vmask,node1(1,13)

*VGET,node1(1,4),node,1,U,Y,,,0

*vmask,node1(1,13)

*VGET,node1(1,5),node,1,U,z,,,0

!find nodal locations

*vmask,node1(1,13)

*voper,node1(1,6),node1(1,3),add,node1(1,1)

*vmask,node1(1,13)

*voper,node1(1,7),node1(1,5),add,node1(1,2)

!find minimum nodal coordinates

*VSCFUN,offset1(1,1),min,node1(1,6)

*VFILL,offset1(2,1),ramp,offset1(1,1),0

*VSCFUN,offset2(1,1),min,node1(1,4)

*VFILL,offset2(2,1),ramp,offset2(1,1),0

*VSCFUN,offset3(1,1),min,node1(1,7)

*VFILL,offset3(2,1),ramp,offset3(1,1),0

!normalize displacements

*vmask,node1(1,13)
```

```
*voper,node1(1,8),node1(1,6),sub
,offset1(1,1)

*vmask,node1(1,13)

*voper,node1(1,9),node1(1,4),sub
,offset2(1,1)

*vmask,node1(1,13)

*voper,node1(1,10),node1(1,7),su
b,offset3(1,1)

! opens .txt file, writes nodeloc
3D array into it.

*CFOPEN,xla_30,csv

*vwrite,nodeinfo1(1,8)

(1x, F7.6)

*CFCLOS

*CFopen, yla_30,csv

*vwrite,nodeinfo1(1,11)

(1x, F7.6)

*CFCLOS

*CFopen, zla_30,csv

*vwrite,nodeinfo1(1,10)

(1x, F7.6)

*CFCLOS

/eof
```

Appendix 3

Ansys APDL code file used to design and model adaptive bump demonstrator seen in Fig. 7.15.

```
! ************************

! Creates model of 150x150mm square -15/75 laminate

! ************************

! Author: P.F.Giddings en1pfg@bath.ac.uk

! ************************

FINISH

*DEL,ALL

/CLEAR,START

/FILNAME,150mm CFRP circular Bump 2

/TITLE,Validation model: Basic

/UNITS, SI

! ************************

! Enter pre-processor mode

! ************************

local,11,0,0,0,0,0,0,0

/PREP7

SHPP,ON

ESYS,11

ET,1,SOLID186

keyopt,1,3,1

keyopt,1,8,1

sectype,1,shell

secdata,0.000027,5,0

secdata,0.000234,1,45

secdata,0.000255,1,-45

tref,0

sectype,2,shell

secdata,0.000255,1,-45

secdata,0.000234,1,45

secdata,0.000027,5,0

tref,0

sectype,3,shell

secdata,0.000027,5,0

secdata,0.000234,1,0

secdata,0.000255,1,0

tref,0

ESYS,11

ET,2,solid226,1001

! ----------------------------------------

! Define material properties

! ----------------------------------------

! Material (1): T700/M21 UD prepreg 0.25mm thick

! Taken from Airbus data sheet Pa

! ----------------------------------------

MP,ex,1,148e9

MP,ey,1,7.8e9

MP,ez,1,7.8e9

MP,gxy,1,3.8e9

MP,gxz,1,3.8e9

MP,gyz,1,0.0225e9

MP,prxy,1,0.35

MP,prxz,1,0.35

MP,pryz,1,0.01

MP,dens,1,1072

MP,ALPX,1,-0.9e-7

MP,ALPY,1,3e-5

MP,ALPZ,1,3e-5

! ----------------------------------------

! Material (2): Dummy MFC actuator z-z poled (Nrm)

! ----------------------------------------

MP,dens,2,2000

MP,PERX,2,7.12

MP,PERY,2,1.7

MP,PERZ,2,737

MP,ALPX,2,-0.9e-7

MP,ALPY,2,1e-25

MP,ALPZ,2,3e-5

MP,REFT,2,0

!*

TB,ANEL,2,1,,1

tbtemp,0

TBDATA,1,0.065,-0.0205,-0.0106

TBDATA,7,0.065,-0.0106

TBDATA,12,0.034

TBDATA,16,0.165

TBDATA,19,0.173

TBDATA,21,0.173

!*

TB,PIEZ,2,,,1

TBMODIF,1,1,0

TBMODIF,1,2,0

TBMODIF,1,3,-2.3e-19

TBMODIF,2,1,0

TBMODIF,2,2,0

TBMODIF,2,3,-2.3e-19

TBMODIF,3,1,0

TBMODIF,3,2,0
```

TBMODIF,3,3,4.67e-19

TBMODIF,4,1,0

TBMODIF,4,2,0

TBMODIF,4,3,0

TBMODIF,5,1,0

TBMODIF,5,2,0

TBMODIF,5,3,0

TBMODIF,6,1,0

TBMODIF,6,2,0

TBMODIF,6,3,0

!*

MP,dens,3,2000

MP,PERX,3,2712

MP,PERY,3,1.7

MP,PERZ,3,737

MP,ALPX,3,-0.9e-7

MP,ALPY,3,1e-25

MP,ALPZ,3,3e-5

MP,REFT,3,0

!*

TB,ANEL,3,1,,1

tbtemp,0

TBDATA,1,0.065e-9,-0.0205e-9,-0.0106e-9

TBDATA,7,0.065e-9,-0.0106e-9

TBDATA,12,0.034e-9

TBDATA,16,0.165e-9

TBDATA,19,0.173e-9

TBDATA,21,0.173e-9

!*

TB,PIEZ,3,,,1

TBMODIF,1,1,0

TBMODIF,1,2,0

TBMODIF,1,3,-2.1e-10

TBMODIF,2,1,0

TBMODIF,2,2,0

TBMODIF,2,3,-2.1e-10

TBMODIF,3,1,0

TBMODIF,3,2,0

TBMODIF,3,3,4.67e-10

TBMODIF,4,1,0

TBMODIF,4,2,0

TBMODIF,4,3,0

TBMODIF,5,1,0

TBMODIF,5,2,0

TBMODIF,5,3,0

TBMODIF,6,1,0

TBMODIF,6,2,0

TBMODIF,6,3,0

! ----------

! excess resin layer effective properties

! ----------

MP,ex,5,1.5e9

MP,prxy,5,0.4

MP,alpx,5,9e-5

! ----------

! Create model

! ----------

!Defines key points for semi circles

K,1,-5e-3,0,0

K,2,-5e-3,0,20e-3

k,3,-5e-3,0.516e-3,0

k,4,-5e-3,0.516e-3,20e-3

! Defines Area 1

A,1,2,4,3

! Defines axis of revolution for semicircle 1

K,5,-5e-3,0,0

k,6,-5e-3,0.516e-3,0

! Defines key points, area and axis of semi circle2

K,7,5e-3,0,0

K,8,5e-3,0,-20e-3

k,9,5e-3,0.516e-3,0

k,10,5e-3,0.516e-3,-20e-3

A,7,8,10,9

K,11,5e-3,0,0

k,12,5e-3,0.516e-3,0

!creates primitive volumes for segmented laminate

BLOCK,-100e-3,-5e-3,0,0.516e-3,-70e-3,70e-3

BLOCK,5e-3,100e-3,0,0.516e-3,-70e-3,70e-3

block,-5e-3,5e-3,0,0.516e-3,-80e-3,80e-3

block,-5e-3,5e-3,0,0.516e-3,-20e-3,20e-3

VROTAT,1,,,,,,5,6,-180,1

VROTAT,2,,,,,,11,12,-180,1

! Performs Boolean operations to combine primitives

VSBV,1,5,,delete,keep

vsbv,2,6,,delete,keep

vsbv,3,4,,delete,keep

allsel

! Defines element sizes for each volume within segmented laminate

!volume 5 sizing

lesize,3,2.5e-3,,

lesize,59,2.5e-3,,

lesize,60,,9

lesize,61,,9

lesize,2,,,1

!volume 6 sizing

lesize,62,2.5e-3,,

lesize,5,2.5e-3,,

lesize,66,,9

lesize,65,,9

```
lesize,6,,,1

!volume 4 sizing

lesize,55,2.5e-3,,

lesize,56,2.5e-3,,

lesize,49,1e-3,,

lesize,46,1e-3,,

lesize,50,,,1

!volume 1 and 7 sizing

lesize,68,2.5e-3,,

lesize,71,2.5e-3,,

lesize,74,2.5e-3,,

lesize,18,2.5e-3,,

lesize,70,2.5e-3,,

lesize,25,,,15

lesize,15,,,15

lesize,22,,,15

lesize,12,,,15

lesize,31,,,20

lesize,17,,,20

lesize,39,1e-3,,

lesize,36,1e-3,,

lesize,38,,,1

lesize,35,,,1

! ------------------------------------

! Mesh laminaet model

! ------------------------------------

vsel,s,,,4

vsel,a,,,5

vsel,a,,,6

VATT,,,1,0,1

veorient,4,thin

veorient,5,thin

veorient,6,thin

vsweep,all

allsel

vsel,s,,,1

vsel,a,,,7

vatt,,,1,0,3

veorient,1,thin

veorient,7,thin

vsweep,all

allsel

!volume 8 and 2 sizing

lesize,75,2.5e-3,,

lesize,76,2.5e-3,,

lesize,70,2.5e-3,,

lesize,73,2.5e-3,,

lesize,34,1e-3,,

lesize,37,1e-3,,

lesize,38,,,1

lesize,35,,,1

vsel,s,,,2

vsel,a,,,8

vatt,,,1,0,3

veorient,2,thin

veorient,8,thin

vmesh,all

allsel

! ------------------------------------

! Define and mesh MFC volume

! ------------------------------------

block,-4e-3,4e-3,0.516e-3,0.816e-3,-42.5e-3,42.5e-3

lesize,84,2.5e-3,,

lesize,81,1e-3,,

lesize,80,,,1

vsel,s,,,3

vatt,2,,2,0

veorient,3,line,84

vmesh,all

allsel

! ------------------------------------

! Define and mesh outer laminate portions

! ------------------------------------

block,-100e-3,-5e-3,0,0.516e-3,70e-3,80e-3

lesize,97,2.5e-3,,

lesize,91,,,15

lesize,92,,,1

block,5e-3,100e-3,0,0.516e-3,70e-3,80e-3

lesize,109,2.5e-3,,

lesize,105,,,15

lesize,101,,,1

vsel,s,,,9,10,1

vatt,,,1,0,3

vmesh,all

allsel

block,-100e-3,-5e-3,0,0.516e-3,-80e-3,-70e-3

lesize,119,2.5e-3,,

lesize,114,,,15

lesize,111,,,1

block,5e-3,100e-3,0,0.516e-3,-80e-3,-70e-3

lesize,133,2.5e-3,,

lesize,124,,,15

lesize,125,,,1

vsel,s,,,11,12,1

vatt,,,1,0,3

vmesh,all

allsel

!Define element section definitions

esel,s,,,1,358,1

emodif,all,secnum,1

allsel

esel,s,,,359,1852,1
```

```
emodif,all,secnum,3

allsel

esel,s,,,2125,2354,1

emodif,all,secnum,3

allsel

! Merge all coincident key points and nodes

nummrg,kp

nummrg,node

allsel

! Reorient element coordinate systems

esel,s,,,all

Esel,s,type,,1

emodif,all,esys,11

eorient,lsyl,negy,180

allsel

!-------------------------------------

!Constrain model

!-------------------------------------

nsel,s,loc,z,70e-3,80e-3

nsel,a,loc,z,-80e-3,-70e-3

nsel,r,loc,y,0

d,all,uy,0

allsel

nsel,s,loc,z,0

nsel,r,loc,x,0

nsel,r,loc,y,0

D,all,ux,,,,,uz,uy

allsel

! Apply electrical constraint

nsel,s,loc,z,-42.5e-3

nsel,r,loc,x,-5e-3,5e-3

nsel,r,loc,y,0.5e-3,0.9e-3

D,all,Volt,0

allsel

nsel,s,loc,z,-32.5e-3

nsel,r,loc,x,-5e-3,5e-3

nsel,r,loc,y,0.5e-3,0.9e-3

cp,2,volt,all

allsel

nsel,s,loc,z,-22.5e-3

nsel,r,loc,x,-5e-3,5e-3

nsel,r,loc,y,0.5e-3,0.9e-3

cp,3,volt,all

allsel

nsel,s,loc,z,-12.5e-3

nsel,r,loc,x,-5e-3,5e-3

nsel,r,loc,y,0.5e-3,0.9e-3

cp,4,volt,all

allsel

!nsel,s,loc,z,-5e-3

!nsel,r,loc,x,-5e-3,5e-3

!nsel,r,loc,y,0.5e-3,0.9e-3

cp,5,volt,all

allsel

nsel,s,loc,z,0

nsel,r,loc,x,-5e-3,5e-3

nsel,r,loc,y,0.5e-3,0.9e-3

cp,6,volt,all

allsel

!nsel,s,loc,z,5e-3

!nsel,r,loc,x,-5e-3,5e-3

!nsel,r,loc,y,0.5e-3,0.9e-3

cp,7,volt,all

allsel

nsel,s,loc,z,12.5e-3

nsel,r,loc,x,-5e-3,5e-3

nsel,r,loc,y,0.5e-3,0.9e-3

cp,8,volt,all

allsel

nsel,s,loc,z,22.5e-3

nsel,r,loc,x,-5e-3,5e-3

nsel,r,loc,y,0.5e-3,0.9e-3

cp,9,volt,all

allsel

nsel,s,loc,z,32.5e-3

nsel,r,loc,x,-5e-3,5e-3

nsel,r,loc,y,0.5e-3,0.9e-3

cp,10,volt,all

allsel

nsel,s,loc,z,42.5e-3

nsel,r,loc,x,-5e-3,5e-3

nsel,r,loc,y,0.5e-3,0.9e-3

!Apply offset voltage

D,all,volt,265462

allsel

! ------------------------------------

! Solves model ste by step

! ------------------------------------

/solu

ANtype,static,new

NLGEOM, On

autots,on

outres,all,all

Time,1

NSUBST,10,,,,

KBC,0

Esel,s,,,all

Esel,u,mat,,2

BFE,all,temp,1,-1

allsel

solve

! Applies displcement constraint to aid convergence

Time,2

NSUBST,20,,,,
```

```
KBC,0
nsel,s,loc,z,0
nsel,r,loc,x,0
nsel,r,loc,y,0
D,all,ux,,,,,uz
d,all,uy,-3e-3
allsel
solve
Time,3
NSUBST,100,,,,
KBC,0
Esel,s,,,all
Esel,u,mat,,2
BFE,all,temp,1,-50
allsel
solve
NSUBST,100,,,,
KBC,0
Esel,s,,,all
Esel,u,mat,,2
BFE,all,temp,1,-158
allsel
solve
! Implements Line search convergence control
lnsrch,on
NSUBST,100,,,,
KBC,0
! Removes Displcement constraint
nsel,s,loc,z,0
nsel,r,loc,x,0
nsel,r,loc,y,0
ddele,all,uy
allsel
nsel,s,loc,z,70e-3,80e-3
nsel,a,loc,z,-80e-3,-70e-3
nsel,r,loc,y,0
d,all,uy,0
d,all,ux,%_fix%
allsel
solve
Time,5
neqit,100
Esel,s,mat,,2
mpchg,3,all
allsel
solve
! Applies MFC drive voltage
Time,6
NSUBST,50
KBC,0
nsel,s,loc,z,42.5e-3
nsel,r,loc,x,-5e-3,5e-3
nsel,r,loc,y,0.5e-3,0.9e-3
D,all,volt,10642
allsel
solve
!Removes MFC drive voltage after snap-through
Time,7
NSUBST,20
KBC,0
nsel,s,loc,z,42.5e-3
nsel,r,loc,x,-5e-3,5e-3
nsel,r,loc,y,0.5e-3,0.9e-3
D,all,volt,265642
allsel
solve
```

Appendix 4

On the following pages the journal papers which the author has published as part of this thesis in peer reviewed journals are included as they appear in print.